Computational and experimental studies of mixing for industrial multiphase processes

Maltby, Richard

Award date:
2020

Awarding institution:
University of Bath

Computational and experimental studies of mixing for industrial multiphase processes

Richard Peter Maltby

A thesis submitted for the degree of Doctor of Philosophy

University of Bath

Department of Chemical Engineering

June 2019

Declaration of any previous submission of the work

The material presented here for examination for the award of a higher degree by research has not been incorporated into a submission for another degree.

Candidate's signature:

Declaration of Authorship

I am the author of this thesis, and the work described therein was carried out by myself personally, with the exception of Chapter 5 where no more than five percent of the work was carried out by other researchers as follows:

The meshing and defeaturing of the BioMOD tank and impeller geometry used in the computational fluid dynamic models presented in Chapter 5 was performed in collaboration with postdoctoral researcher Dr Shuai Tian.

Candidate's signature:

The work presented in Chapter 5 is based on the following published research article:

Maltby, R., Tian, S. and Chew, Y.M.J., 2018. Computational studies of a novel magnetically driven single-use-technology bioreactor: A comparison of mass transfer models. *Chemical Engineering Science*, 187, pp.157–173.

Table of Contents

List of Figures

Figures from published sources have been reproduced under the following license numbers:

Figure 2-1 and Figure 2-2: **4611810760536**

Figure 2-3 and Figure 2-4: **4611810980754**

Figure 8-1: **4612391158502**

List of Tables

Nomenclature

a	Specific interfacial area (m^{-1})
A_p	Specific particle area (m^{-1})
B_B	Birth due to breakup ($m^{-3}\ s^{-1}$)
B_C	Birth due to coalescence ($m^{-3}\ s^{-1}$)
C	Molar concentration (mol m^{-3})
C^*	Saturation concentration (mol m^{-3})
C_D	Drag coefficient (-)
$C_{\varepsilon 1}$, $C_{\varepsilon 2}$, C_μ	k-ε constants (-)
d_b	Bubble diameter (m)
D_B	Death due to breakup ($m^{-3}\ s^{-1}$)
D_C	Death due to coalescence ($m^{-3}\ s^{-1}$)
D_c	Column diameter (m)
d_f	Fringe spacing (m)
$D_{G,L}$	Interphase drag force (N m^{-3})
D_i	Impeller diameter (m)
D_L	Molecular diffusivity ($m^2\ s^{-1}$)
d_p	Particle diameter (m)
ER	Eddy ratio (-)
F	Mass flow rate (kg s^{-1})
f	Size fraction (-)
f_d	Doppler frequency (s^{-1})
F^{TD}	Turbulent dispersion force (N m^{-3})
F_B, F_{CT}, F_{CB}	Calibration factors (-)
g	Gravitational acceleration (m s^{-2})
$g(\ ;\ )$	Specific breakup rate ($m^3\ s^{-1}$)
h_f	Critical film thickness (m)
h_0	Initial film thickness (m)
K	Proportionality constant
k	Turbulent kinetic energy ($m^2\ s^{-2}$)
k_L	Mass transfer coefficient (m s^{-1})
M	Molar mass (kg mol^{-1})
m	Mass (kg)
N	Number of groups (-)
n	Number density (m^{-3})
N_i	Impeller rotational speed (RPM)
N_{O_2}	Oxygen transfer rate (mol $m^{-3}\ s^{-1}$)
N_P	Power number (-)
N_p	Number of particles (-)
P	Power consumption (W)
p	Pressure (Pa)
p'	Modified pressure (Pa)
Q	Volumetric flow rate ($m^3\ s^{-1}$)
$Q(\ ;\ )$	Specific coalescence rate ($m^3\ s^{-1}$)
r	Radius (m)
Re	Reynolds number (-)
S	Source terms (N m^{-3})
s	Mean surface renewal rate (s^{-1})
Sc	Schmidt number (-)
Sh	Sherwood number (-)
t	Time (s)
t_c	Contact time (s)
t_{ij}	Rupture sime (s)
u, v, w	Velocity (m s^{-1})
U_T	Terminal rise velocity (m s^{-1})
v	Kinematic viscosity ($m^2\ s^{-1}$)
V	Volume (m^3)
v_b	Slip velocity (m s^{-1})
V_p	Volume of particles (m^3)
v_s	Superficial gas velocity (m s^{-1})
W_i	Impeller blade width (m)
X	Coalescence mass matrix (-)
x	Mass fraction (-)
x, y, z	Distance (m)

α	Volume fraction (-)
α, β	Exponential factors
ε	Eddy dissipation rate ($m^2\ s^{-3}$)
η_{ij}	Collision efficiency (-)
θ	Beam angle (°)
θ^T	Collisions due to buoyancy ($m^3\ s^{-1}$)
θ^T	Collisions due to turbulence ($m^3\ s^{-1}$)
λ	Wavelength (m)
μ	Dynamic viscosity (Pa s)
μ_{eff}	Effective viscosity (Pa s)
μ_T	Turbulent viscosity (Pa s)
ξ	Dimensionless eddy size (-)
ρ	Mass density ($kg\ m^{-3}$)
σ	Surface tension ($N\ m^{-1}$)
$\sigma_\varepsilon, \sigma_k$	k-ε constants (-)
τ	Shear stress (Pa)
τ_{ij}	Contact time (s)
χ	Dimensionless energy (-)

Subscripts

G	Gas phase
L	Liquid phase
i, j, k	Bubble group

Abbreviations

AFF = Adaptive force field

ASM = Algebraic stress model

CAD = Computer aided design

CARPT = Computer automated radioactive particle tracking

CCS = Carbon capture and storage

CFD = Computational fluid dynamics

CIP = Cleaning in place

CM = Classes method

CQMOM = Conditional quadrature method of moments

CT = Computed topography

DNS = Direct numerical simulation

DO = Dissolved oxygen

DQMOM = Direct quadrature method of moments

E-E = Euler-Euler

E-L = Euler-Lagrange

IBC = Impeller boundary condition

I/O = Inner/outer

LCA = Lifecycle assessment

IS = Immersed solids

LDV = Laser Doppler velocimetry

LES = Large eddy simulation

LIF = Laser induced fluorescence

MRF = Multiple reference frame

MUSIG = Multiple size group

PIV = Particle image velocimetry

QMOM = Quadrature method of moments

RANS = Reynolds averaged Navier-Stokes

SIP = Sterilisation in place

SM = Sliding mesh

SS = Source-sink

SST = Shear stress transport

SUT = Single-use-technology

TKE = Turbulent kinetic energy

VOF = Volume of fluids

VOS = Volume of solids

vvm = Volume of gas per volume of liquid per minute

Acknowledgements

I would like to gratefully acknowledge the continual support of my lead supervisor Professor John Chew, who has provided indispensable encouragement and advice throughout the process of performing and writing up the work contained within this thesis.

I am very grateful to the postdoctoral researchers who have provided support and advice during the duration of my PhD project, namely Will Lewis, Vincent Lister, Shuai Tian and Olivier Camus.

I would also like to acknowledge the support of the directors and administrative staff of the Centre for Sustainable Chemical Technologies (CSCT) for providing a framework for this PhD to be conducted, and the Engineering and Physical Sciences Research Council (EPSRC) for part-funding the project. Further acknowledgement is due to all fellow of the members of CSCT cohort 14 for providing many moments of enjoyment throughout the PhD process.

I am also grateful to all of the industrial collaborators involved in the work detailed in this thesis. This includes all of the other active members of the BioMOD consortium (CPI, BPES, and NAREC) and the associated funding bodies.

I would like to acknowledge the efforts of all of the technical and administrative staff in the Department of Chemical Engineering, without whom it would not be possible to effectively perform this work. Further thanks for the support of Paul Frith, whose mechanical expertise has enabled the experimental apparatus used in this work to be designed and constructed efficiently and to a high standard.

Finally, I would like to thank my family and friends who have been accommodating and supportive during the course of undertaking this PhD project.

Abstract

The main aim of this PhD project is to develop computational and mathematical models to describe industrial-scale gas-liquid flows using the computational fluid dynamics (CFD) software ANSYS CFX. Two particular industrial applications are studied, namely industrial biotechnology and sugar refining. The models are based on a comprehensive literature review covering the use of CFD modelling in gas-liquid stirred tank systems. Where there is no consensus in literature for the preferred choice of model, different available options have been compared. The CFD model has been applied to a novel single-use-technology bioreactor, which has been designed and operated as part of an industrial collaboration. The 1,000 L cubic reactor incorporates a single floor-mounted magnetically-driven impeller and fourteen individual gas spargers, meaning that the mixing characteristics cannot be evaluated using traditional design correlations. The hydrodynamic model has been solved over a range of different stirrer rotational speeds and air flow rates. The flow patterns have been shown to change from buoyancy dominant to impeller dominant between 200 and 300 RPM, accompanied by a much greater distribution of the gas phase. The mass transfer performance, reported in terms of volume-averaged $k_L a$, is modelled using five different mass transfer models existing in literature and compared to experimental measurements. There is a large spread of $k_L a$ values predicted by the different models, with the experimental value sitting within these predictions. However, due to the limited access to take experimental measurements within the full-scale system, laboratory-scale validation is also performed against multiple parameters in a 9.4 L square-bottomed glass tank. The liquid-phase velocity, measured using laser Doppler velocimetry, provides a reasonable fit to an equivalent model of the validation tank at stirrer speeds of 100 to 400 RPM, whereas a qualitative analysis of the gas dispersion shows a good match between the model and experiments. The bubble size distribution is approximated experimentally using a watershed function applied to multiple images. As with the full-scale system, the measured $k_L a$ falls within the range of values predicted by the model. Two of the models are found to provide a good fit to the experimental $k_L a$ measurement, with the slip velocity matching the measured $k_L a$ most accurately across the full-scale and validation tanks. However, the model considerably over-predicted the $k_L a$ in the validation tank at 400 RPM, which is proposed to predominantly result from the specification of the population balance parameters based on the full-size bioreactor, where the influence of the impeller action in bubble break-up mechanisms is reduced.

The CFD modelling work has shown that the bubble size is a much more significant factor in interphase mass transfer than the mass transfer coefficient, which remains relatively constant across different conditions, and therefore using sub-millimetre bubbles, i.e. microbubbles, may lead to vastly improved mass transfer. This has been investigated experimentally by using a commercially available microbubble pump to measure the mass transfer of oxygen from air to water in three different geometry tanks with varying volumes of water from 7.62 to 200 L. The results show that the $k_L a$ is independent of the tank geometry as the microbubbles are observed to be dispersed evenly throughout each tank. Furthermore, introducing mechanical agitation is shown to provide no improvement in mass transfer, since microbubbles have a much greater stability than larger bubbles, meaning that stirring costs may be reduced for many applications. The pump is also shown to create a significant supersaturation of oxygen in the liquid due to the high pressure in the pumping circuit and within the individual microbubbles, which is also beneficial for interphase mass transfer. The mass transfer rate achieved per volume of gas is significantly improved by using the microbubble pump, however the large pumping capacity of the pump is likely to limit its applicability for many larger-scale mass transfer processes.

CFD modelling developed has also been applied to an industrial-scale continuous gas-liquid contactor used during the carbonatation process, which is a clarification step in the refining of cane sugar. The hydrodynamic model shows that the column is operating in the churn-turbulent bubbling regime under normal operating conditions. This means that the liquid-phase is well mixed and there are no significant concentration gradients between the top and the bottom of the column. The mass transfer is shown to improve with increasing gas flow rate up to 0.7 t hr^{-1}, however the shear stress also increases significantly within the operating range, resulting in a predicted optimum gas flow rate in the region of 0.5 t hr^{-1}.A model of the complex series of reactions occurring during carbonatation has been developed within the CFD software environment. The model has been used to predict the local and outlet concentration profiles under two distinct phases of column operation, with and without excess calcium hydroxide present from start-up, and for a range of different operating conditions. The reaction model has been validated against a laboratory-scale model system, consisting of a closed system of water and calcium hydroxide, which is continually bubbled with carbon dioxide gas. The model provides a good fit to experimental measurements of the pH and both solid and dissolved carbonate concentrations for three different gas flow rates, although the fit is less good at higher hydroxide concentration.

1 Introduction

Multiphase flows are an important feature across a wide range of industrial processes such as oxidation, chlorination and sulfochlorination, the majority of which are limited by the rate of mass transfer between the gas and liquid phases (Azbel, 1981). Gas-liquid flows are often utilised for interphase mass transfer processes in large bubble column contactors or stirred tank reactors, where a species is transferred between the gas and the liquid phases. This may be the stripping of an unwanted component from a liquid stream or the transfer of a reacting species from the gas to the liquid. Two phase flows may also occur during transport processes, such as the extraction of crude oil and natural gas, and may be utilised to give desirable qualities such as porosity or texture in many consumer products.

One area where interphase mass transfer is especially important is the bioprocessing industry, where a constant supply of dissolved oxygen is required for growing cultures of cells via aerobic conditions. This is achieved by sparging the growing media broth with air and using mechanical agitation to distribute and break down the gas bubbles, increasing the rate of mass transfer. Mammalian cells, which are typically used for high value products, generally have a fairly low oxygen demand and high shear sensitivity, and are therefore grown in relatively small volumes with low levels of mechanical agitation. However, bacterial and yeast fermentations, which are typically used for the production of lower-value bulk products such as alcohols, organic solvents and enzymes, often have a very high oxygen demand and must be grown to high cell concentration in order to produce commercially viable product volumes. Microbial cells are much less shear sensitive, and therefore can be exposed to more extreme stirring conditions which promote bubble break-up, giving a high interfacial area for mass transfer.

Industrial-scale two-phase processes have traditionally been specified based upon design equations and correlations for well-characterised systems with known ratios of dimensions, with the majority of existing two-phase systems following these known design parameters. However, in recent years the development of computational fluid dynamics (CFD) techniques applicable to two-phase flows, in parallel with large increases in available computational power, have allowed for the efficient design and evaluation of non-standard equipment computationally. The steps involved in developing a CFD model are common between all simulations, and have been well described by Andersson et al. (2011). The key stages have been summarised in Figure 1-1 in the form of a flow chart. They require a two

or three-dimensional geometry to be developed and divided into a number of discreet computational cells. The required physical and reaction models, fluid properties and boundary conditions are applied, and the model solved using the specified numerical scheme until a specified set of convergence criteria are met. More complex models are required when working with complex systems including multiphase flows, moving mechanical parts and chemical reactions.

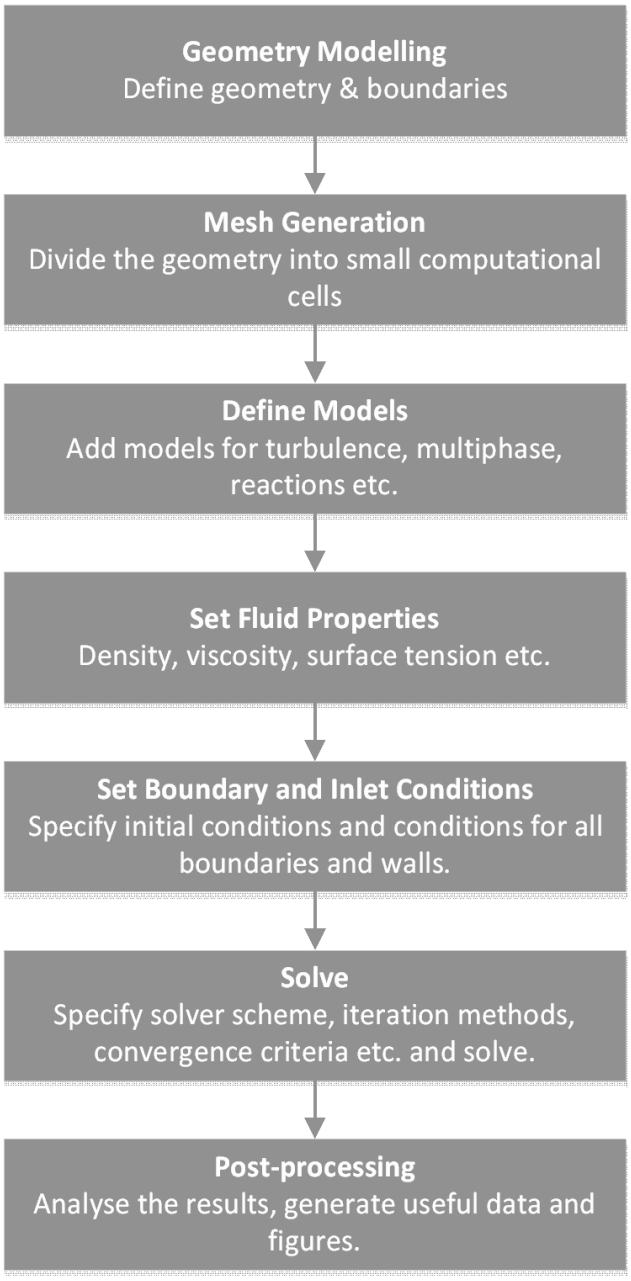

Figure 1-1: Flowchart of the typical steps involved in developing a CFD model. Applicable to CFD modelling in any common software package, and adapted from the general textbook resource of Andersson et al. (2011).

1.1 Scope of Research

This research is primarily concerned with the CFD modelling of two industrial-scale two-phase systems: a single-use-technology (SUT) bioreactor and a carbonatation vessel. The SUT bioreactor is a novel system that is very different to existing equipment, and therefore requires extensive characterisation to understand the hydrodynamic and mass transfer performance. This research presented in this thesis will identify the current trends in the computational modelling of two-phase flows and apply them to the relevant systems within the limitations of the available models within the ANSYS CFX software. This does not include the development of new fundamental CFD models, however existing techniques may be adapted and evaluated for specific applications. Similarly, this work has not been conducted to create a new appraisal of all of the modelling options available, such as the choice of discretisation scheme or solver numerical scheme, which have been well scrutinised elsewhere in literature. Both applications modelled are highly dependent on the interphase mass transfer of a species from the gas phase to the liquid phase, and evaluating the performance of various mass transfer models that are compatible with CFD model outputs will form an important part of this thesis.

The second industrial application of CFD modelling in this thesis is applied to a carbonatation vessel, also known as a saturator, which is used during the refining of cane sugar. The design of the vessel is reasonably similar to other gas-liquid contactors characterised in literature, however the carbonatation process has not been previously been described in the context of CFD modelling. There is a complex series of aqueous-phase chemical reactions occurring, which are driven by the interphase mass transfer of carbon dioxide gas. The model developed to represent this system will build upon published studies relating to analogous carbon capture and storage applications in geological systems. This thesis includes a novel attempt to model the reacting system in three-dimensions within a commercial CFD environment. Due to the already considerable complexity of the system described, the modelling of solid particles within the reacting system as a distinct third phase will not fall within the scope of this work, with the relevant assumptions clearly stated within the chapter.

The experimental work in Chapters 6 and 9 is presented to provide evidence in support of the CFD models applied to the industrial-scale case studies. The experiments in Chapter 6 are performed using established techniques that have previously been applied to similar

two-phase models. Performing experimental validation work in-house allows for a greater control of the conditions evaluated than using published studies, and gives a better understanding of the parameters that the presented results are representing. The experimental work presented in Chapter 9 builds on the hydrodynamic analysis previously presented by developing a representative experimental system for the series of reactions that occur during the carbonatation process. The experimental and analytical procedure applied will be specifically developed for this model system, using commercially available, calibrated electrode probes.

The research in this thesis relating to microbubbles stands as a purely experimental investigation within a relatively new and fast-developing area of research, and is inspired by the findings of the preceding CFD modelling work in respect to the influence of bubble size on mass transfer performance. The scope of this chapter is limited to investigating the potential for using a commercially available microbubble generator for the intensification of gas-liquid mass transfer, although there are numerous other current and potential applications of microbubble technology acknowledged in the introduction to Chapter 7. Whereas the image processing technique relating to microbubbles is based on pre-existing MATLAB functions, the sizing apparatus is newly commissioned, and therefore requires sensitivity analyses in order to provide confidence in the calculated size distributions. The techniques developed here can be used as a basis for further studies of microbubble flows.

1.2 Structure of the Thesis

This thesis is divided into several chapters, detailing various aspects relating to industrial aspects of two-phase flows. Chapter 2 provides a critical review of the available literature surrounding the design and CFD modelling of industrial two phase systems, specifically stirred tanks and bubble columns. Available mathematical techniques are introduced and evaluated based on their current and historical applications within the published body of literature. The aims and objectives of the thesis are defined in Chapter 3. Chapter 4 provides numerical details of the various mathematical models applied throughout subsequent chapters of this thesis. These can be used as a reference for the CFD modelling work presented in all later chapters.

Chapter 5 details the development and subsequent application of a CFD model for the novel single-use-technology BioMOD bioreactor. Similarly, Chapter 8 presents the development of a CFD model including a liquid-phase reaction model for a gas-liquid carbonatation vessel currently used during the refining of cane sugar. Each of these chapters include details of the physical geometry, simplifications made and the relevant mathematical models and boundary conditions applied. Results are then presented for a range of different operating conditions, with any further reaction models specific to that chapter also explained and applied.

Each of these modelling chapters is immediately followed by an accompanying chapter presenting the relevant experimental validation. This includes details of the experimental design, procedures equipment used. The experimental results in each validation chapter are compared to a comparable CFD model and related to the industrial-scale findings.

- Chapter 6 provides experimental validation relevant to chapter 5.
- Chapter 9 provides experimental validation relevant to chapter 8.

Chapter 7 details the characterisation and evaluation of a commercial microbubble pump, which is assessed for its applicability to the intensification of mass transfer processes. Whilst this chapter is entirely experimental in nature, the context follows directly from the preceding two chapters relating to the BioMOD bioreactor, and builds upon the hypothesised relationships between the mass transfer rate and bubble size. Finally, the key findings from all of the different sections of the thesis are discussed and summarised in Chapter 10, with recommendations for future work proposed to build upon the research presented in this thesis presented in Chapter 11.

2 Literature Review

This section reviews the current state of the published literature regarding the design and CFD modelling of gas-liquid contacting systems, in particular the modelling of stirred tank systems and gas-liquid contactors such as bubble columns and airlift reactors which are relevant to the industrial applications detailed in this thesis. This will help to establish a current literature consensus on available modelling techniques, as well as identifying areas where no clear consensus on modelling methods currently exists. This literature review will also help to identify gaps in the literature that the present work may seek to address. Further consideration to the literature specific to the content of each chapter is included in the relevant 'Introduction' sections of future chapters.

2.1 Design Considerations for Gas-Liquid Systems

Traditionally, gas-liquid contacting systems have been designed and specified based upon well-established empirical correlations for known ratios of dimensions and operating conditions, as summarised for stirred tank systems by Joshi et al. (1982). Commonly used parameters include the power number, a dimensionless term which can be used to characterise the resistance to the impeller when rotating within a process fluid. It generally holds a fixed value for each impeller type under turbulent mixing conditions, as presented by Doran (1995) for several common impeller designs. Correlations are also available for laminar and transitional flow regimes. The single-phase power consumption for turbulent flow can be calculated based on the power number using equation (2-1).

$$P = N_P \rho {N_i}^3 {D_i}^5 \tag{2-1}$$

where P is the power consumption, N_P is the power number, ρ is the fluid density, N_i is the impeller rotational speed and D_i is the impeller diameter.

The power consumption in gas-liquid stirred tanks is generally lower than liquid-phase stirred tanks due to the formation of gas cavities from trailing vortices that are generated in the low pressure region behind the impeller blades, which in turn reduces the drag force acting upon the rotating impeller (Van't Riet and Smith, 1973). The power consumption in gas-liquid stirred tanks can be calculated from the ungassed power consumption using charts or correlations such as those developed by Hughmark (1980), which are shown to be

representative for a wide range of different operating conditions. The correlation for disc turbines is given by equation (2-2). By combining this with equation (2-1) it is clear that the power requirements do not scale linearly with tank size, with larger tanks requiring very a large power input to achieve the same levels of mixing achieved at the pilot scale.

$$\frac{P_G}{P} = 0.1\left(\frac{Q_G}{N_i V}\right)^{-0.25}\left(\frac{{N_i}^2 {D_i}^4}{g W_i V^{0.4}}\right)^{-0.2} \tag{2-2}$$

where P_G is the two-phase power consumption, Q_G is the volumetric gas flow rate, V is the liquid volume, g is the gravitational acceleration and W_i is the impeller blade width.

The mass transfer in gas-liquid contacting systems is often reported in terms of the parameter $k_L a$, which is a combination of the liquid phase mass transfer coefficient, k_L, and the specific interfacial area, a. This is often used due to the relative ease in which it can be experimentally determined (Garcia-Ochoa et al., 2010), although care must be taken when comparing reported values due to sensitivities in the measurement process and variations in the values calculated by the different measurement techniques. Additionally, the $k_L a$ can be predicted for standard tank designs using equations of the form of equation (2-3) (Van't Riet, 1979), where α and β are exponents that may fall within the ranges $0.4 < \alpha < 1$ and $0 < \beta < 0.7$. This gives a relatively wide range of uncertainty when predicting mass transfer via design correlations, and a further large degree of non-linear scaling with respect to the hydrodynamic conditions and tank volume. Similarly, the value of the proportionality constant, K, is shown to vary significantly between different studies.

$$k_L a = K\left(\frac{P_G}{V}\right)^{\alpha} {v_s}^{\beta} \tag{2-3}$$

where v_s is the superficial gas velocity.

All of the correlations discussed above are only applicable for the relevant tank and impeller design, meaning that the mixing and mass transfer performance of non-standard equipment is often difficult to predict, thus limiting the wider implementation of novel mixing equipment. One of the most widely applied standard designs for biological applications is the Rushton turbine, which uses a single six-bladed disc impeller suspended

within a cylindrical, baffled vessel based on the specified dimensions presented in Figure 2-1. Common ratios of dimensions applied to tanks of this design include; $D_i = C_i$, $D_T = H_L$, $D_i = {}^1/_3\, D_T$ and W_{BF} no more than one tenth of W_T in order to maximise the mixing efficiency and ensure the applicability of the correlations discussed above (Doran, 1995).

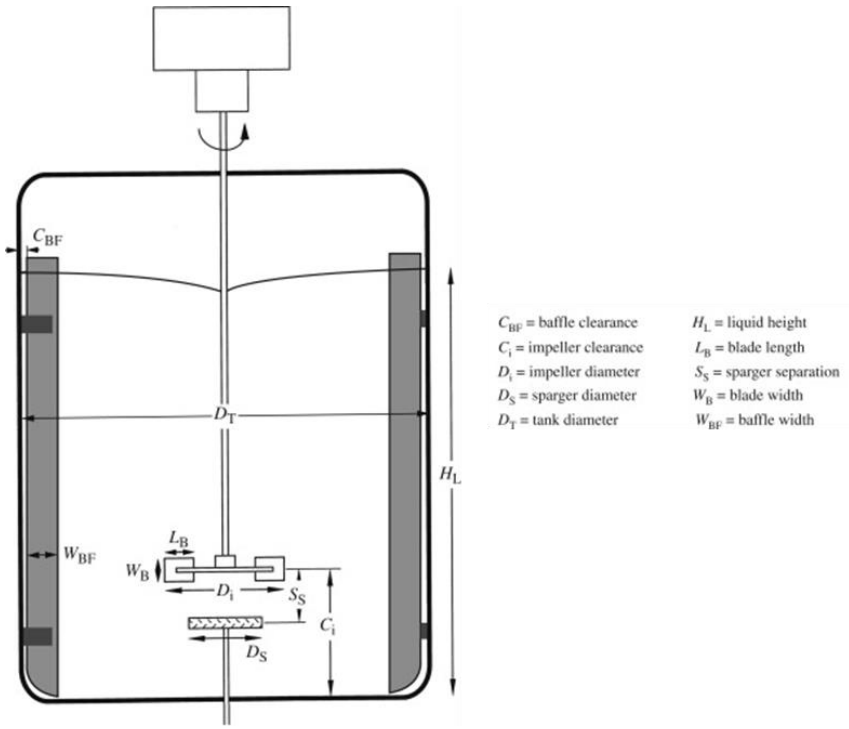

Figure 2-1: Diagram of a typical single-impeller stirred tank system. Adapted from Doran (1995).

It is clear from all of the correlations presented above that the key parameters involved in the design of traditional gas-liquid contacting equipment such as the power input and the mass transfer rate do not scale linearly with vessel size. This means that the scale-up of mixing equipment can often be difficult, with larger vessels often not achieving the performance expected from the pilot scale or requiring impractically large power input to do so. Doran (1995) explains how the scale-up of stirring equipment based on maintaining the same mixing time is generally not possible, citing an example where a 100 times increase in reactor volume would require approximately 2000 times the power input to maintain the same mixing time. Alternative scale-up methods employed in stirred tank design include maintaining constant volumetric power input, stirrer speed, impeller tip speed or Reynolds number. It is not possible to keep more than one of these parameters the same for any fixed geometry type. This is demonstrated by Table 2-1 (Catapano et al., 2009), which shows that adopting any single one of these techniques to achieve a 1000

times increase in reactor volume is expected to lead to very different mixing conditions due to the large variations in the other parameters listed.

Table 2-1: Ratio of characterisitic parameters for various scale-up strategies for increasing the volume of a stirred tank from 10 L to 10 m^3. Adapted from Catapano et al. (2009).

Scale-up Criterion	P	P/V	N_i	$N_i \times D_i$	Re
Equal P/V	10^3	1	0.22	2.15	21.5
Equal N_i	10^5	10^2	1	10^2	10^2
Equal tip speed	10^2	0.1	0.1	1	10
Equal Re	0.1	10^{-4}	0.01	0.1	1

A further difficulty when designing gas-liquid contacting systems relates to the different two-phase flow regimes that occur with various gassing and stirring conditions. These are summarised in Figure 2-2 (Doran, 1995), which shows that either an increase in stirrer speed or a decrease in the gas flow rate will affect the dispersion of the gas phase within the vessel, and thus the mass transfer performance. The changing rheology of many fermentation broths is expected to further complicate the relationship between the gas and liquid phases during the course of a fermentation process.

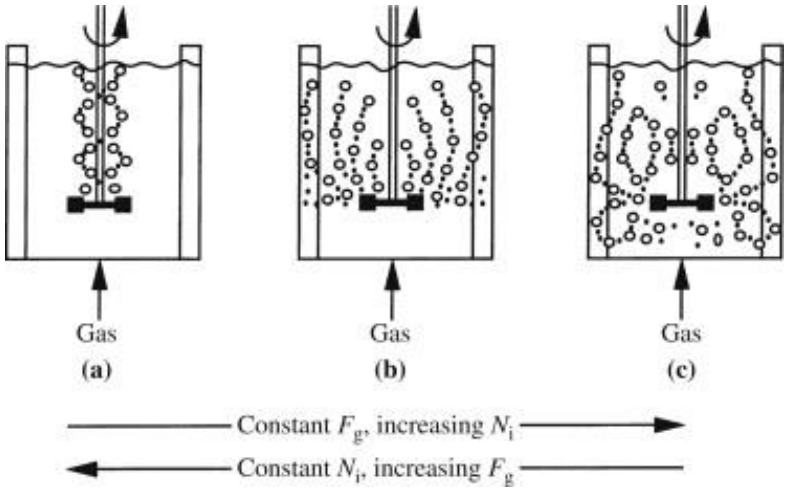

Figure 2-2: Typical gas dispersion patterns in a sparged stirred tank with radial flow impeller, Doran (1995).

The two-phase flow regime is similarly important when considering the flow in unstirred systems such as pipe flow and bubble columns, including the column design studied in Chapter 8. Once again, the relationship between the different flow regimes is well-correlated empirically through flow regime maps for vertical pipe flow (Hewitt and Roberts,

1969) and bubble columns (Shah et al., 1982). The different flow regimes that may be observed in bubble columns are presented in Figure 2-3**.** At lower gas flow rates, the bubble size distribution is said to be relatively narrow, with bubbles rising with a uniform velocity, known as the homogeneous or bubbly flow regime. In contrast, the churn turbulent (heterogeneous) regime is characterised by unsteady flow patterns with a much broader range of bubble sizes present, propagated by the presence of large spherical cap bubbles which drive the flow patterns due to their high rise velocity. The maximum diameter of bubbles found in this regime is reported to be in the region of 0.15 m (Shah et al., 1982), with the majority of industrial bubble columns claimed to operate in this regime. The use of CFD modelling to characterise such systems – where a much greater degree of detail about the flow patterns and bubbling regime can be deduced – is described in Section 2.3.

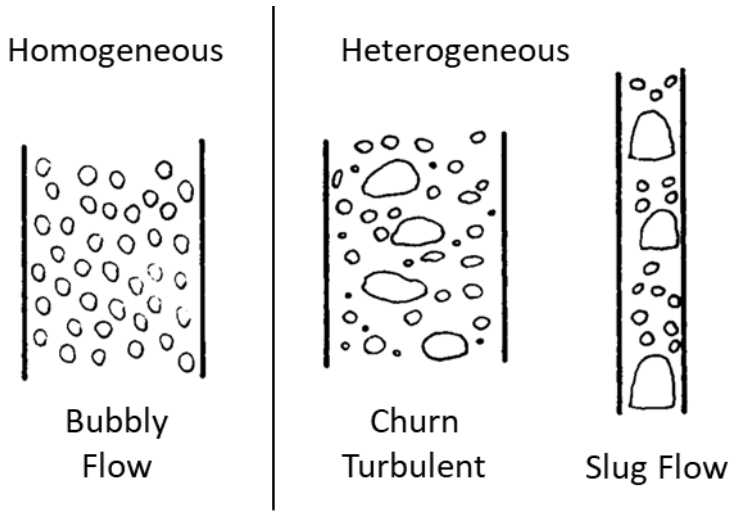

Figure 2-3: Diagram representing the different two-phase regimes encountered for industrial-scale bubble columns. Adapted from Shah et al. (1982).

The relationship between homogeneous and heterogeneous flow patterns has been quantified for pure water or with low surfactant concentrations, as presented in Figure 2-4 (Shah et al., 1982). The figure suggests that a transition between bubbling regimes can be achieved by increasing the gas flow rate in the column. It also shows that the slug flow regime is mostly applicable to narrow columns regardless of the gas flow rate, where the bubble size approaches the column diameter. The bubbling regime can also be significantly influenced by the gas sparger design, liquid flow direction and additional phases present in the column (Besagni et al., 2018). Since there is no impeller-induced distribution of the gas phase, the sparging in bubble columns is typically much more distributed than for the

stirred tank systems considered previously, where sparging is usually performed directly beneath the impeller.

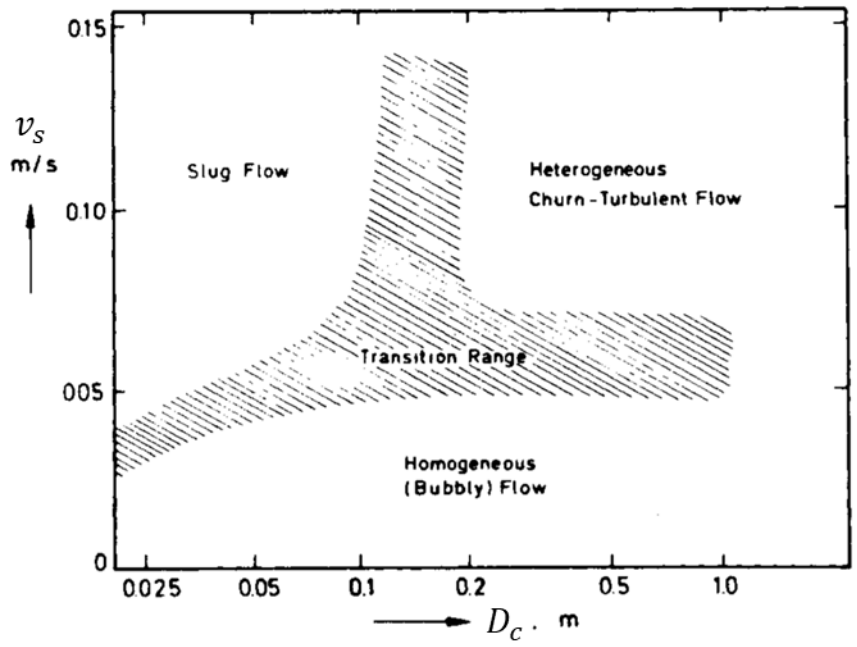

Figure 2-4: Flow regime map for industrial scale bubble columns, Shah et al. (1982).
v_s = superficial gas velocity, D_c = column diameter.

Mass transfer in bubble columns has been investigated for a number of different operating conditions and fluid pairings, with a variety of different correlations developed, as summarised by Shah et al. (1982) and Besagni et al. (2018). One of the most commonly referenced correlations was developed by Akita and Yoshida (1973), and is described by equation (2-4). As with the stirred tank correlations, the mass transfer performance does not scale linearly with the column diameter, however it may be considered to be independent of column height for the range of aspect ratios covered by this relationship.

$$\frac{k_L a \, {D_c}^2}{D_L} = 0.6 \left(\frac{v_L}{D_L}\right)^{0.5} \left(\frac{g {D_c}^2 \rho_L}{\sigma}\right)^{0.62} \left(\frac{g {D_c}^3}{{v_L}^2}\right)^{0.31} {\alpha_G}^{1.1} \tag{2-4}$$

where D_L is the molecular diffusivity of the solute in the liquid, v_L is the kinematic viscosity of the liquid, σ is the surface tension and α_G is the gas volume fraction.

The gas volume fraction can be calculated via further correlations, along with the bubble diameter which is another important operating parameter that features in some similar

correlations. As with the stirred tank design equations, these correlations are only applicable for standard cylindrical column designs and within a strict set of operating limits. Computational modelling can therefore be a useful tool in the design and optimisation of unstirred gas-liquid contactors, especially for non-standard designs and uncommon process fluids.

2.2 CFD Modelling of Stirred Tank Systems

Due to the difficulty in the design and scale-up of two-phase systems described in Section 2.1, the use of CFD modelling has emerged as a valuable tool for the design of stirred tank equipment. The detail and complexity of models has increased since the pioneering stirred tank studies were published, in combination with vast increases in computing power over the past 25 years. Initially, CFD techniques have been applied to well-characterised systems such as the Rushton turbine in order to develop more representative models of the physical process. However, as CFD techniques have became more established, they have been applied to a much wider array of applications such as different impeller types, two-phase and three-phase flows. This section will detail the development of CFD stirred tank models over time, providing an in-depth chronological evaluation of the published studies which have applied CFD modelling to gas-liquid stirred tank systems.

2.2.1 Single-Phase CFD Modelling of Stirred Tanks

A series of comprehensive review articles investigating the use of CFD simulations relating to stirred tank systems up to 2011 has been published by Joshi et al. (2011a; 2011b). This period covers the development and implementation of the majority of the most commonly used CFD techniques, with the significant improvement in computational ability with time allowing for greater complexity in models and application to be considered. The first published stirred tank CFD studies were reported by Harvey and Greaves (1982a; 1982b). At this time, computing resources were not advanced enough to model the complexities of impeller-fluid interactions directly. The action of the impeller was therefore modelled using an impeller boundary condition (IBC) technique, where a smooth interface surrounding the impeller was created and experimentally determined boundary conditions for velocity and turbulence were applied. This method is not ideal as it requires the accurate measurement of several flow parameters and is only applicable for the measured conditions. Later developments have allowed for the direct modelling of the impeller geometry, starting with

the source-sink (SS) model first applied by Pericleous and Patel (1987), which applied a momentum source term to the impeller surface, and a momentum sink at the baffles.

Other impeller motion techniques divide the geometry into a rotating region (the rotor) which includes the impeller and a stationary region (the stator) which includes the tank walls and baffles. Examples include the inner-outer (Brucato et al., 1994) and the snapshot (Ranade and Dommeti, 1996) techniques. The multiple reference frame (MRF) technique, first applied to stirred tank simulations in the early 1990's by Luo et al. (1993), uses a smooth interface between the rotor and the stator and applies a rotational source term to the fluid in the rotor region. This technique has become a popular choice for stirred tank studies following its introduction, since it offers a good compromise between solution accuracy and computing load, and is applicable to both steady-state and transient models. Sliding mesh (SM) techniques use a similar mesh setup to the MRF method, however the entire rotor region is physically rotated in space between each timestep modelled. This approach was first applied to stirred tanks by Murthy et al. (1994), and has subsequently been applied to numerous single phase simulations, see Joshi et al. (2011a). Since the mesh is varied with respect to time, these models must be solved using a transient solver scheme, which requires the convergence of the model at each timestep, further increasing the computational load over steady-state techniques such as MRF.

Much like for the impeller motion techniques, early CFD simulations were limited in their choice of turbulence model by the available computing resources. Although it is possible to solve the unsteady three-dimensional Navier-Stokes equations directly (a technique known as direct numerical simulation, DNS), this would require a very fine computational mesh and excessive computational expense due to the requirement to resolve the simulation down to the Kolmogorov time and length scales (Andersson et al., 2011). The majority of early simulations used Reynolds averaged Navier Stokes (RANS) models, with variations of the k-ε model by far the most popular (see Joshi et al. (2011a)). RANS models use Reynolds decomposition techniques to separate the instantaneous velocity and pressure fields into fluctuating and time-averaged terms, and can therefore be solved using a steady-state solver. This offers significant savings in computational time by iterating the solution towards a final time-averaged state. Other variations using the RANS closure models such as k-ω and shear stress transport (SST) models have also been applied to single phase

modelling. Furthermore, several modifications on the k-ε model have been proposed, often using modified model constants as described by Joshi et al. (2011a).

A more recent alternative to the RANS closure model is the large eddy simulation (LES) technique, where the largest eddies in the fluid are modelled directly via the three-dimensional Navier-Stokes equations, and the influence of smaller eddies is modelled using an approximation called a subgrid-scale model. This provides a good approximation of the overall flow patterns since they are largely dictated by the larger eddies, however the problem must be solved as transient and three-dimensional due to the explicit simulation of the large eddies (Andersson et al., 2011). Initially, LES was applied to stirred tank systems using a Lattice-Boltzmann discretisation scheme (Eggels, 1996; Derksen and Van den Akker, 1999), with the first finite volume approach applied several years later by Yeoh et al. (2004). This study showed that the LES model can provide improved predictions when compared to RANS models in single phase problems, providing a good fit to experimental data for overall flow patterns and local features such as trailing vortices.

For single-phase simulations, there has been a clear trend towards the use of the sliding mesh technique in combination with large eddy simulation models as computing power has increased (Joshi et al., 2011a). However, this trend has not necessarily translated to two-phase modelling as discussed in Section 2.2.2 due to the greater complexity and computational demands involved in the modelling of multiphase flows.

2.2.2 Liquid-Gas CFD Modelling of Stirred Tanks

A comprehensive chronological list of published studies covering the use of CFD to model sparged gas-liquid stirred tank systems is presented in Table 2-2. The first model to be published in this field is presented by Gosman et al. (1992), along with modelling for a dispersed solid phase, both using the Euler-Euler 'two fluids' reference frame. Whilst containing many of the key elements that future studies would incorporate, such as the use of a RANS turbulence model and coupling of the gas and liquid phases through interfacial drag forces, this model does not provide a good prediction of two-phase flow. This has since been attributed to the large mesh used to model the fluid domain, necessitated by the limited computing resources of the time, and the use of a very small fixed bubble diameter of 0.5 mm. There is also no experimental validation of the model presented by Gosman et al. (1992), whereas the vast majority of later publications have attempted to

validate their results against a range of different measured parameters including liquid and gas velocity, gas holdup, mixing time and bubble diameter as described in Table 2-2.

The vast majority of publications listed in Table 2-2 are for cylindrical, baffled stirred tanks in either single or multiple impeller configurations, with the gas sparged directly onto the impeller blades. This is not surprising since these are the designs most commonly applied during traditional two-phase process design due to the wide availability of empirical data discussed in Section 2.1. This is particularly apparent when considering earlier CFD studies, where the focus of the research tends to be on developing new and accurate CFD codes rather than designing new equipment. In this case it is desirable to use a well-characterised test case, often with published experimental data for validation. With the exception of Bakker and Van den Akker (1994), who studied three different impeller designs, all geometries investigated up to 2003 used a single Rushton impeller in a cylindrical baffled tank of known dimensions such as those presented in Figure 2-1. Subsequent investigations have studied different impeller designs (Khopkar et al., 2003; Lane et al., 2005) and multiple impeller designs (Kerdouss et al., 2006), however the use of rigid cylindrical vessels has been the tank design investigated in all but two published studies, namely Appa et al. (2014) and Witz et al. (2016) who used horizontal half drum and cubic tank geometries respectively.

Frame of Reference

The analysis in Table 2-2 allows for a number of key developments in the evolution of two-phase stirred tank models to be identified. The dispersed phase is in general introduced in either an Euler-Euler (E-E) or Euler-Lagrange (E-L) frame of reference. The Euler-Euler method (Ishii, 1975) treats the two phases as interpenetrating fluids, with the momentum and continuity equations solved for each phase (Andersson et al., 2011). In gas-liquid flows, the two phases are strongly coupled by interfacial drag forces. In contrast, the Euler-Lagrange method treats the dispersed phase as discreet particles, whose movement is tracked over time and which can undergo momentum, mass and energy transfer with the continuous phase. This method is considered to be accurate at low volume fractions, however at high volume fractions the requirement for a closure for inter-particle interactions from the high number of collisions occurring make computational demands very high (Andersson et al., 2011). For this reason, the great majority of gas-liquid stirred tank studies presented in Table 2-2 use the Euler-Euler reference frame. A single attempt to

use the volume of fluids (VOF) method for describing the gas distribution was made by Zamankhan (2010). This method tracks the location of the interface between the two phases based on the volume fraction of each computational cell, however the clear difficulty and computational expense of tracking the entire gas-liquid interface in industrial-scale bubbly systems makes this an impractical choice.

Unlike for single-phase modelling, where more advanced methods for modelling turbulence such as LES have become popular, the k-ε model remains overwhelmingly the most widely applied turbulence model for two-phase stirred tank flows. This is a widely applied RANS turbulence model, which is often considered to provide a good compromise between accuracy and computational expense for large-scale CFD simulations (Andersson et al., 2011). The RANS-based SST model has also been applied to a small number of the cases presented in Table 2-2. Of the published studies identified, only three have attempted to use the LES turbulence model for gas-liquid stirred tank studies, namely Arlov et al. (2008), Zhang et al. (2008) and Zamankhan (2010). Of these studies, only Zhang et al. (2008) has provided a comparison of the LES and k-ε turbulence models, with the LES model showing improved performance when compared to published velocity and gas holdup data. Furthermore, the LES study of Zamankhan (2010) used the VOF reference frame with a very low volumetric aeration rate to the order of 10^{-3} vvm (volume of gas per volume of liquid per minute), and is therefore not applicable to industrial scale applications with high gas fractions due to the greater extent of gas-liquid interface that requires modelling. Notably, the modelling of gas-liquid stirred tanks using LES has not been revisited in the literature since 2010, suggesting little appetite or necessity for its introduction.

Impeller Motion

The motion of the impeller is another key parameter to be considered in the specification of a stirred tank system. Early studies did not have the required computing power available to directly model the interactions between the fluids and the impeller wall, instead applying the IBC or source-sink methods. The snapshot technique was also used in several earlier two-phase studies, as shown in Table 2-2. However, since the mid-2000s, the two most popular methods for modelling impeller motion have emerged as the Multiple Reference Frame and Sliding Mesh methods. Both of these techniques separate the fluid domain into rotating and stationary regions with a smooth interface between them as

described in Section 2.2.1. These models have been compared by Jahoda et al. (2009) for a pitched-blade impeller with a fixed bubble size of 4mm. Comparing to experimental measurements of homogenisation and mixing times, it was concluded that the MRF method offers acceptable results with very significant savings in computational time. However, a difference in the flow patterns between the methods can be observed for a low gas flow rate. An alternative method for modelling the impeller motion that has emerged recently is the Immersed Solids (IS) method, which uses two entirely overlapping meshes to describe the tank and the impeller, thus eliminating the need for a computational interface. This method is not applicable to the vast majority of stirred tank simulations listed in Table 2-2, where the gas is sparged directly onto the impeller, due to documented limitations in the way that the solid in the current implementation interacts with the dispersed gas phase (ANSYS Inc., 2016). However the model has not been investigated with regards to gas-liquid systems with distributed sparging prior to the work detailed in this thesis.

Bubble Size

As with several of the key parameters required for two-phase stirred tank modelling, the definition of the bubble size was initially limited by the available computational power. Many of the early studies shown in Table 2-2 were restricted to using a single bubble size, despite the known existence of a distribution of bubble sizes in most gas-liquid systems. There is a large degree of variability in the values of the fixed bubble size specified, with the majority being in the region of 1 to 6 mm in diameter. Some early studies also used a technique called the bubble number density (BND), first applied to stirred tank systems by Bakker and Van den Akker (1994), which uses the local gas volume fraction and estimates of the breakup and coalescence frequency based on local flow conditions to correlate a value for the bubble diameter. Similarly, some studies have attempted to predict the local bubble diameter based on the correlation of Hinze (1955), which uses the fluid properties and the local energy dissipation rate to predict the maximum bubble diameter.

A more complete method of approximating the bubble diameter can be achieved through population balance modelling, where bubble coalescence and break-up are modelled directly based upon the local two-phase conditions. The two types of population balance models most commonly applied are the classes method (CM), the most common form of which identified in Table 2-2 is the multiple size group (MUSIG) model implemented into ANSYS CFX, and variants of the quadrature method of moments (QMOM) model. These will

be discussed in detail in Section 2.2.3. Population balance modelling was first introduced to gas-liquid stirred tank systems by Laakkonen et al. (2007) using CM, with the majority of subsequent studies opting to include a population balance model. However, several recent studies have still been performed using a constant bubble size, most likely in the interests of computational efficiency, as demonstrated by Table 2-2.

Drag Model

Whereas many of the above modelling considerations have a clear preferred choice in the literature, it is also clear from Table 2-2 that there is no current consensus on the selection of an interfacial drag model between the gas and liquid phases. The Schiller-Naumann correlation, and modifications upon it, was one of the first drag models to be implemented in two-phase stirred tank systems. It was developed with consideration of a single non-deformable spherical particle. Various extensions or modifications of this model have been applied in CFD modelling, such as Tomiyama (1998) which accounts for more bubbling regimes but not effects relating to a high concentration of bubbles (dense gas phase), and Tzounakos et al. (2004) which has been applied to non-Newtonian (power law) fluids. Other correlations such as the Ishii-Zuber (Ishii and Zuber, 1979) and Grace (Clift et al., 1978) models have been applied in later years in order to account for both the differing bubble morphology and the dense gas phase present in aerated systems. The Brucato drag model (Brucato et al., 1998), and various modifications upon it, have also proved to be popular since first being introduced to aerated stirred-tank systems by Lane et al. (2002). This model is correlated from experimental data for solid particles in turbulent flow, and like the Schiller-Naumann correlation does not account for bubble deformation. Similarly, Scargiali et al. (2007) described the bubble drag in terms of the terminal rise velocity of a single bubble.

Table 2-2: A chrononological analysis of published studies using CFD modelling applied to gas-sparged stirred tank systems.
BND = Bubble Number Density, CM = Classes Method, MUSIG = Multiple Size Group, QMOM = Quadrature Method of Moments, DQMOM = Direct Quadrature Method of Moments, CQMOM = Conditional Quadrature Method of Moments, E-E = Euler-Euler, E-L = Euler-Lagrangian, VOF = Volume of Fluid, IBC = Impeller Boundary Condition, MRF = Multiple Reference Frame, I/O = Inner/Outer, VOS = Volume of Solids, SM = Sliding Mesh, AFF = Adaptive Force Field, ASM = Algebraic Stress Model, LES = Large Eddy Simulation, SST = Shear Stress Transport.

Authors	**Geometry and Application Details**	**Bubble Diameter**	**Reference Frame**	**Drag Model**	**Impeller Motion**	**Turbulence Model**
Gosman et al. (1992)	Cylindrical, baffled, single Rushton impeller. Volume = 20 L. No validation data.	0.5 mm	E-E	mod. Schiller-Naumann	IBC	k-ε
Bakker and Van den Akker (1994)	Cylindrical, baffled, three impeller and two sparger configurations. Volume = 69 L. Validated for gas holdup and bubble size.	BND	One-way coupled	mod. Schiller-Naumann	IBC	ASM
Ranade and Van den Akker (1994)	Cylindrical, baffled, single Rushton impeller. Volume =21 L. Validated for liquid velocity (LDV), TKE and gas holdup.	6 mm	E-E	Grace	Snapshot	k-ε
Morud and Hjertager (1996)	Cylindrical, baffled, single Rushton impeller. Volume = 15 L. Validated for liquid and gas velocity (LDV) and gas holdup.	Unspecified	E-E	Ishii-Zuber	Source-sink	k-ε
Ranade and Deshpande (1999)	Cylindrical, baffled, single Rushton impeller, focussing on trailing vortex. Volume = 21 L. Qualitative comparison to experiments.	2 mm	E-E	Unspecified	Snapshot	k-ε
Ranade et al. (2001)	Cylindrical, baffled, single Rushton impeller. Volume = 50 L. Validated for gas and liquid velocity (PIV) and TKE.	Unspecified	E-E	Schwarz and Turner	Snapshot	k-ε
Lane et al. (2002)	Cylindrical, baffled, single Rushton impeller.	BND	E-E	Brucato	MRF	k-ε

	Volume = 785 L. Qualitative comparison to experiments.					
Deen et al. (2002)	Cylindrical, baffled, single Rushton impeller. Volume = 14 L. Comparison of different drag models and bubble sizes with 2-phase PIV.	4 mm, 2 mm	E-E	Schiller-Naumann, Ishii-Zuber	SM	k-ε
Wang and Mao (2002)	Cylindrical, baffled, single Rushton impeller. Volume = 72 L. Validated for liquid velocity (hot-wire anemometry) and gas holdup.	Hinze correlation	E-E	Ishii-Zuber	Snapshot	k-ε
Khopkar et al. (2003)	Cylindrical, baffled single, pitch-blade impeller. Volume = 5.4 L. Validated for liquid and gas velocity (PIV) and TKE.	4 mm	E-E	Brucato	Snapshot	k-ε
Lane et al. (2005)	Cylindrical, baffled, multiple single-impeller configurations. Volume = 785 L. Validated for bubble diameter and gas holdup. A modified Brucato drag model is proposed.	BND	E-E	mod. Brucato	SM	k-ε
Khopkar et al. (2005)	Cylindrical, baffled, single Rushton impeller. Volume = 6.3 L. Validated for flow patterns (CARPT) and gas holdup.	4 mm	E-E	Brucato	Snapshot	k-ε
Wang et al. (2006)	Cylindrical, baffled, single Rushton impeller. Volume = 72 L. Validated for gas holdup.	Hinze correlation	E-E	Ishii-Zuber	I/O	k-ε
Kerdouss et al. (2006)	Cylindrical, baffled, dual Rushton impeller. Volume = 39 L. Validated for bubble diameter and gas holdup.	BND	E-E	Schiller-Naumann	MRF	k-ε
Khopkar and Ranade (2006)	Cylindrical, baffled, single Rushton impeller. Volume = 72 L. Validated for gas holdup, with a focus on drag model development.	4 mm, 3 mm	E-E	mod. Schiller-Naumann, Brucato	Snapshot	k-ε

Laakkonen et al. (2007)	Cylindrical, baffled, single Rushton impeller. Volume = 14 L and 200 L. Validated for bubble diameter and gas holdup.	CM - MUSIG	E-E	Tomyara	MRF	k-ε
Murthy et al. (2007)	Cylindrical, baffled, self-inducing pitch-blade impeller. Volume = 98 L. Validated for gas induction rate and has holdup.	3 mm	E-E	Morsi and Alexander	MRF	k-ε
Montante et al. (2007)	Cylindrical, baffled, single Rushton impeller. Volume = 10 L. Validated for liquid and gas velocity (PIV).	U_T = 12 m s^{-1}	E-E	Scargiali	SM	k-ε
Scargiali et al. (2007)	Cylindrical, baffled, single Rushton impeller. Volume = 72 L. Qualitative comparison to experiments.	2 mm, 3 mm, 4mm	E-E	Scargiali	SM	k-ε
Kerdouss et al. (2008)	Cylindrical, unbaffled lab bioreactor (New Brunswick BioFlow 110) with axial impeller. Volume = 2 L. Validated for $k_L a$.	3 mm, CM	E-E	Ishii-Zuber	MRF	k-ε
Arlov et al. (2008)	Cylindrical, baffled, single Rushton impeller. Single and two-phase. Volume = 21 L. Validated for liquid flow patterns.	1.5 mm, 2 mm	E-L	Schiller-Naumann	VOS	LES
Montante et al. (2008)	Cylindrical, baffled, single Rushton impeller. Volume = 10 L. Validated for liquid and gas velocity (PIV) and bubble diameter.	CM - MUSIG	E-E	Brucato	SM	k-ε
Khopkar and Tanguy (2008)	Cylindrical, baffled, dual Rushton impeller with varying impeller heights. Volume = 143 L. Validated for gas holdup.	3.5 mm	E-E	Brucato	MRF	k-ε

Moilanen et al. (2008)	Cylindrical, baffled, multiple single-impeller configurations. Volume = 200 L. Validated for gas holdup, TKE, $k_L a$ and bubble diameter.	BND, CM - MUSIG	E-E	Tzounakos	MRF	SST
Zhang et al. (2008)	Cylindrical, baffled, single Rushton impeller. Volume = 72 L. Validated for liquid velocity (hot-film anemometry) and gas holdup.	Hinze correlation	E-E	Brucato	I/O	k-ε, LES
Jahoda et al. (2009)	Cylindrical, baffled, single pitch-blade impeller. Volume = 19 L. Validated for homogenisation time and power characteristics.	4 mm	E-E	Schiller-Naumann	MRF, SM	k-ε
Zhang et al. (2009)	Cylindrical, baffled, triple impeller bioreactor. Volume = 20 L. Compared to mass transfer correlations.	CM - MUSIG	E-E	Ishii-Zuber	Source-sink	k-ε
Gimbun et al. (2009)	Cylindrical, baffled, single Rushton impeller. Volume = 14 L and 200 L. Validated for liquid and gas velocity (PIV) and dissolved oxygen.	3.5 mm, QMOM	E-E	Ishii-Zuber	MRF	k-ε
Petitti et al. (2010)	Cylindrical, baffled, single Rushton impeller with ring and porous spargers. Volume = 196 L. Validated for gas holdup and bubble diameter.	QMOM	E-E	Scargiali	MRF	k-ε
Ahmed et al. (2010)	Cylindrical, baffled, dual Rushton impeller. Volume = 5 L. Validated for overall gas holdup, mixing time and power number.	CM - MUSIG	E-E	Brucato	MRF	k-ε
Zamankhan (2010)	Cylindrical, baffled, single Rushton impeller. Volume = 14 L. Qualitative comparison to experimental PIV and imaging data.	N/A	VOF	N/A	SM	LES

Selma et al. (2010)	Cylindrical, baffled, dual Rushton impeller. Volume = 39 L. Validated for gas holdup and bubble diameter. Comparison of different population balance closures.	CM, DQMOM	E-E	Schiller-Naumann	MRF	k-ε
Iranzo et al. (2011)	Cylindrical, baffled, quadruple Rushton and pitch-blade impellers. Volume = 100,000 L. Very high viscosity liquid (500 times greater than water). No validation data.	20 mm	E-E	Grace	MRF	SST
Taghavi et al. (2011)	Cylindrical, baffled, dual Rushton impeller. Volume = 150 L. Validated for power consumption.	Unspecified	E-E	Zadghaffri and Moghaddas	MRF	k-ε
Kaiser et al. (2011)	Cylindrical, unbaffled single-use bioreactor with micro-porous sparger. Volume = 2L. Validated for $k_L a$ and mixing time.	0.4 mm	E-E	Schiller-Naumann	MRF	k-ε
Ranganathan and Sivaraman (2011)	Cylindrical, baffled, dual Rushton impeller. Volume = 39 L. Validated for gas holdup, bubble diameter and $k_L a$.	CM – MUSIG, Inhomogeneous MUSIG	E-E	Brucato	MRF	k-ε
Liu et al. (2011)	Cylindrical, baffled, single Rushton impeller. Volume = 6.3 L. Validated for gas holdup using γ-CT scans.	CM - MUSIG	E-E	Schiller-Naumann	MRF	k-ε
Buffo et al. (2012)	Cylindrical, baffled, single Rushton impeller. Volume = 196 L. Validated for bubble diameter.	DQMOM	E-E	Scargiali	MRF	k-ε
Sungkorn et al. (2012)	Cylindrical, baffled, single Rushton impeller. Volume = 10 L. Validated for liquid velocity (PIV) and bubble diameter.	CM	E-L	mod. Schiller-Naumann	AFF	Lattice-Boltzmann

Yang et al. (2013)	Cylindrical, baffled with one elliptical and two hydrofoil blade impellers and variable temperature gas sparging. Volume = 145 L. Validated for gas holdup.	CM - MUSIG	E-E	Grace	MRF	k-ε
Elqotbi et al. (2013)	Cylindrical, baffled, single Rushton impeller. Volume = 5 L. Includes Monod-type bioreaction model and compared to cell growth data.	2 mm	E-E	mod. Schiller-Naumann	MRF	k-ε
Petitti et al. (2013)	Cylindrical, baffled, single Rushton impeller. Volume = 196 L. Validated for dissolved oxygen concentration and bubble diameter.	CQMOM	E-E	Scargiali	MRF	k-ε
Morchain et al. (2014)	Cylindrical, baffled, single Rushton impeller. Volume = 70 L and 70,000 L. Validation of power consumption and gas holdup. Includes Monod-type reaction model.	1 mm	E-E	Schiller-Naumann	SM	k-ε
Wang et al. (2014)	Cylindrical, baffled, dual radial impeller. Volume = 5 L. Validated for gas holdup and liquid velocity (LDV).	CM - MUSIG	E-E	Ishii-Zuber	MRF	k-ε
Kálal et al. (2014)	Cylindrical, baffled, single Rushton impeller. Volume = 19 L. Validated for power number and bubble diameter.	CM - MUSIG	E-E	mod. Schiller-Naumann, Ishii-Zuber, Brucato, Scargiali	MRF	k-ε
Gelves et al. (2014)	Cylindrical, baffled, triple Rushton impeller and novel six-component stirrer designs. Volume = 180 L. No validation data.	CM	E-E	mod. Schiller Naumann	MRF, SM	k-ε

Appa et al. (2014)	Horizontal half-drum geometry, two baffles, two-blade radial impeller. Volume = 60 L. Validated for mass transfer coefficient.	Constant, CM	E-E	Schiller-Naumann	MRF, SM	k-ε
Bao et al. (2015)	Cylindrical, baffled, multiple three-impeller configurations. Volume = 134 L. Validated for gas holdup.	CM -MUSIG	E-E	Grace	MRF	k-ε
Yang et al. (2015)	Cylindrical, baffled, dual dislocated-blade impellers. Volume = 12 L. Validated for power number	4 mm	E-E	mod. Schiller-Naumann	MRF	k-ε
Chen et al. (2016)	Cylindrical, baffled, dual blade turbine and pitch-blade impellers. Volume = 62 L. Optimisation of geometry parameters using a multiobjective evolutionary algorithm. Validated for gas holdup.	4 mm	E-E	Tomiyama	MRF	k-ε
Gimbun et al. (2016)	Cylindrical, baffled, single Rushton impeller. Volume = 14 L. Validated for liquid and gas velocity (PIV).	Three-way coupled QMOM	E-E	Ishii-Zuber	Unspecified	k-ε
Basavarajappa and Miskovic (2016)	Cylindrical. Baffled, single Rushton impeller (196 L) and unbaffled floatation tank (170 L). Validated for gas holdup and bubble diameter.	QMOM	E-E	Brucato	MRF	k-ε
Wutz et al. (2016)	Cylindrical, baffled, three (2.3 L) and four (80 L) radial impellers. Validated for $k_L a$.	Correlation	E-L	Tomiyara	SM	k-ε
Witz et al. (2016)	Cubic, unbaffled, triple Rushton impeller. Volume = 150 L and 40,000 L. Validated for gas holdup and $k_L a$.	Collision model	E-L	Tomiyara	Modified bounce-back	LES

Bach et al. (2017)	Cylindrical, unbaffled, single axial impeller. Volume = 150 to 350 L. Bubble diameter varied to fit $k_L a$ data. 23 fermentation conditions covering a range of rheology. Validated for tracer concentration, bubble diameter, $k_L a$ and power number.	Data fitting	E-E	Grace	MRF, SM	k-ε
Vlaev et al. (2018)	Cylindrical, baffled, dual Rushton impeller. Submerged membrane for bioreactor operation. Volume = 5 L. Validated for wall shear using non-Newtonian model fluid.	2 mm, 4 mm	E-E	Schiller-Naumann	MRF	k-ε
Maltby et al. (2018)	Cubic, unbaffled single-use bioreactor with floor-mounted impeller. Volume = 1,000 L. Validated against $k_L a$.	CM - MUSIG	E-E	Ishii-Zuber	Immersed Solid	k-ε

2.2.3 Population Balance Modelling

Population balance modelling has become a commonly applied technique for describing the bubble size distribution in two-phase simulations. The bubble size distribution is particularly important for mass transfer applications as the rate of mass transfer is directly dependent on the local bubble size through the interfacial surface area. Population balance modelling became popular for stirred tank studies following the work of Laakkonen et al. (2007), and now forms an important factor in the majority of sparged stirred tank studies, as can be seen from Table 2-2. The two widely used methods for predicting the bubble size distribution within two-phase systems are variations upon the quadrature method of moments (QMOM) and the classes method (CM). These can be found as built-in options in commercial software such as ANSYS CFX and Fluent. The scope of this thesis is limited to those models available in the commercial software ANSYS CFX, as explained in Chapter 3.

The CM approach was first developed by Kumar and Ramkrishna (1996), and requires the user to provide a framework for the bubble size distribution by specifying the range of bubble sizes and number of classes to be used. These values are used to discretise the bubble size parameter into a number of classes, before explicitly solving the population balance equations as described in Section 4.3 with the inclusion of additional models for the breakup and coalescence of bubbles. This method allows the full distribution of bubble sizes to be directly modelled, within the fixed user-specified discretisation. However, this model can lead to a large number of additional equations being solved, especially when a high degree of discretisation is required, leading to a large computational expense (Selma et al., 2010).

The QMOM method was first developed by McGraw (1997) to describe the dynamic evolution of aerosols, based upon the pre-existing method of moments technique. Instead of explicitly solving the population balance for various bubble sizes, it uses the quadrature approximation of a probability density function to generate a much smaller set of partial differential equation. The direct quadrature method of moments (DQMOM) technique (Fan et al., 2004; Marchisio and Fox, 2005) extends QMOM to include an additional parameter which describes the variation in velocity field experienced by bubbles of different sizes, and has also been successfully applied to several stirred tank studies as described in Table 2-2. Finally, the conditional quadrature method of moments (CQMOM) extension has been applied by Petitti et al. (2013) to describe both the bubble size and gas-phase chemical

composition for a stirred tank simulation that includes mass transfer. In a direct comparison of the CM and DQMOM methods, Selma et al. (2010) found that both models compared well to each other and to experimental data for two-phase bubble column and stirred tank models, outperforming previously published monodispersed bubble models. The DQMOM model is claimed to achieve this with a much lower computational load, however the full population distribution is not described by this model.

The most common implementation of CM is the multiple size group (MUSIG) model as implemented into the commercial software ANSYS CFX, and applied within this thesis as described in Section 4.3. Table 2-3 summarises the published studies applying the classes method to gas-liquid stirred tank systems, including details of the maximum bubble diameter used, number of classes specified and the breakup and coalescence models used when provided. The number of discreet groups used in these studies varies from 7 to 24, whereas the maximum bubble diameter specified is usually in the region of 10 to 15 mm, which was first proposed by Laakkonen et al. (2007), although it was noted that a small number of individual bubbles of up to 25 mm were identified experimentally. Few published models beyond the initial explorative studies have taken the step of optimising the parameters defined for CM, in particular the upper and lower bubble size limits and the number size groups, despite the high computational load when compared to monodispersed models and the DQMOM method.

Table 2-3: A chronological analysis of the gas-liquid stirred tank CFD simulations to include population balance modelling via the classes method.
* denotes modified model constants based on experimetnal data

Authors	Maximum diameter (mm)	Number of Groups	Breakup Model	Coalescence Model
Laakkonen et al. (2007)	10, 15	20	Luo and Svendsen	Hagesaether*
Kerdouss et al. (2008)	12	7, 9, 11, 13	Luo and Svendsen	Hagesaether
Montante et al. (2008)	15	16	Luo and Svendsen	Prince and Blanch
Moilanen et al. (2008)	16.53	10	Luo and Svendsen	Hagesaether*
Zhang et al. (2009)	-	-	Luo and Svendsen	Prince and Blanch
Ahmed et al. (2010)	11	10	Luo and Svendsen	Prince and Blanch
Selma et al. (2010)	10	10, 15, 25	Luo and Svendsen	Hagesaether
Ranganathan and Sivaraman (2011)	10	21	Luo and Svendsen	Prince and Blanch
Liu et al. (2011)	10	20	Luo and Svendsen	Prince and Blanch
Sungkorn et al. (2012)	4.5	15	Luo and Svendsen	Sommerfeld
Yang et al. (2013)	-	-	Luo and Svendsen	Prince and Blanch
Wang et al. (2014)	15	20	Luo and Svendsen	Prince and Blanch
Kálal et al. (2014)	16	24	Luo and Svendsen	Prince and Blanch
Appa et al. (2014)	-	11	Luo	Luo
Bao et al. (2015)	-	-	Luo and Svendsen	Prince and Blanch

By far the most commonly applied breakup and coalescence models used are the Luo and Svendsen (Luo and Svendsen, 1996) and Prince and Blanch (Prince and Blanch, 1990) models respectively, the numerical details of which can be found in sections 4.3.1 and 4.3.2. Their popularity is likely to have been deepened through their status as the only pre-defined models available in the popular ANSYS CFX commercial software package (ANSYS Inc., 2016), with the numerical details of the population balance being relatively complex to implement through user-defined functions. Despite this, other models have been successfully applied, such as the Hagesaether coalescence model. This models the coalescence of bubbles as the product between the coalescence probability as proposed by Hagesaether et al. (2000) and the frequency of collisions through turbulence first proposed

by Saffman and Turner (1956), which is also included as part of the Prince and Blanch formulation. Other mechanisms of bubble collision are not considered for this model. The coalescence model applied by Sungkorn et al. (2012) combines the stochastic particle collisions modelled by Sommerfeld (2001) with the Prince and Blanch model, however it is only applicable to Euler-Lagrange models, where individual bubble collisions can be directly modelled.

An extension of the standard homogeneous MUSIG model as described in Section 2.2.2 is the inhomogeneous MUSIG model. Instead of assuming that all bubble classes share the same velocity field, the gas phase is divided into a specified number of velocity fields – typically much fewer than the number of size groups – in addition to the discretisation of the bubble size. These velocity fields allow smaller and larger bubbles to follow different flow paths, however each velocity field modelled adds additional computational demand. The development and implementation of this technique into the ANSYS CFX software is described by Krepper et al. (2008) for a well-established two-phase test case consisting of bubbly flow in a vertical pipe. The authors suggest that the inhomogeneous model may improve the understanding of application-specific phenomena such as the separation of differently sized bubbles in vertical pipe flows, however an improvement in results over the homogenous MUSIG model is not proven. It has also been applied to a multi-impeller gas-liquid stirred tank model by Ranganathan and Sivaraman (2011), using two velocity fields and 21 size groups. The results of this study showed a difference between the predictions of the bubble size distribution when compared to the homogeneous MUSIG model, however no definitive improvement in the prediction of the gas-liquid flows within the stirred tank that can be inferred from the available experimental data.

2.2.4 Gas-Liquid Mass Transfer Modelling

The mass transfer of a species between the gas and liquid phases in two-phase processes can be described using film theory, which is an established method described in numerous chemical and process engineering references (Azbel, 1981; Doran, 1995; Coulson et al., 1999). By assuming that the film resistance on the gas side is negligible, due to good mixing within the low-viscosity gas bubble, the rate of transfer, $\mathrm{N}_{\mathrm{O}_2}$, can be assumed to be proportional to the concentration driving force via the term $k_L a$, as described by equation (2-5). This term represents the product of of the liquid side mass transfer coefficient, k_L, and the specific area for interfacial mass transfer, a.

$$N_{O_2} = \frac{dC}{dt} = k_L a(C^* - C) \tag{2-5}$$

where C is the concentration of dissolved oxygen and C^* is the saturation concentration.

For industrial applications, the mass transfer performance of processes and equipment is routinely reported in terms of $k_L a$, since it can be easily measured through a range of experimental techniques (Doran, 1995; Garcia-Ochoa et al., 2010). One of the most common techniques is known as the dynamic method, which measures the response in dissolved oxygen concentration to a change in gassing conditions, such as changing the sparged gas from nitrogen to air, using a dissolved oxygen electrode submerged within the liquid. Whilst this method can be straightforward and reliable, care must be taken to ensure that the system is sufficiently well mixed and that the probe response time or the formation of a boundary layer at the probe surface do not influence the calculated $k_L a$. Integrating equation (2-5) with respect to time leads to equation (2-6), which can be used to approximate the $k_L a$ from just two concentration measurements, however more accurate predictions can be achieved by solving this linearised equation graphically. For very high $k_L a$ applications, corrected expressions can be used to correct for slow probe response times via curve fitting algorithms (Garcia-Ochoa et al., 2010). The method can also be adapted for use with active fermentation processes.

$$ln\left(\frac{C^* - C_1}{C^* - C_2}\right) = k_L a(t_2 - t_1) \tag{2-6}$$

A sulphite oxidation technique can also be used to measure $k_L a$, where sodium sulphite is converted to sulphate in the presence of a metal catalyst. However, the use of sulphite methods is not recommended since the reaction kinetics are thought to be dependent on the operating conditions and the salts used will affect the bubble size and shape (Van't Riet, 1979). Finally, an oxygen balancing technique can be applied to fermentation systems under normal operating conditions by comparing the composition of the inlet and outlet gas streams, however the difference in oxygen concentration is too low to detect accurately in the absence of a fast aerobic process (Doran, 1995). $k_L a$ values required for industrial fermentation processes are typically between 72 and 900 hr^{-1} (Doran, 1995),

however care must be taken when comparing different reported values as the measured $k_L a$ may vary considerably depending upon the measuring technique used.

The individual terms k_L and a are difficult to individually determine experimentally, requiring techniques such as the Danckwerts plot method (Danckwerts, 1970), which requires the analysis to be repeated in multiple concentrations of a reacting system such as aqueous sodium sulphite (Linek et al., 2005). Furthermore, they can only be determined as overall tank-averaged values, meaning that useful details about the local variation in k_L and a may be missed, leading to dead spots in the reactor being overlooked. In contrast, CFD modelling allows for the individual prediction of k_L and a distributions throughout the tank, in addition to predicting the time-dependent concentration profiles described using equation (2-5).

There is a wide range of published expressions to describe the liquid-phase mass transfer coefficient based upon both liquid and gas phase properties as compiled by Kulkarni (2007), some of which are compatible with the outputs of CFD modelling. The most commonly applied of these models are derived from Higbie's penetration theory of interfacial mass transfer (Higbie, 1935), as described by equation (2-7). The parameter t_c represents the contact time between a fluid element from the bulk and the bubble surface, and is therefore not compatible with the outputs of CFD software without introducing further approximations.

$$k_L = \frac{2}{\sqrt{\pi}}\sqrt{\frac{D_L}{t_c}} \tag{2-7}$$

The first of the models based on Higbie's theory, which will be referred to in later chapters of thesis as the Penetration model, is derived by assuming that the contact time can be described using the Kolmogorov time scale, leading to equation (2-8). Along with the corresponding Kolmogorov length and velocity scales, this is used to describe the smallest eddies that exist in turbulent flow and can be described mathematically as $\sqrt{\frac{\nu_L}{\varepsilon}}$ (Andersson et al., 2011), where ε is the turbulent eddy dissipation rate.

$$k_L = \frac{2}{\sqrt{\pi}} \sqrt{D_L \sqrt{\frac{\varepsilon}{v_L}}} \tag{2-8}$$

Numerous variations upon the form of the model presented in equation (2-8) have been used in CFD simulations, replacing the proportionality constant of $\frac{2}{\sqrt{\pi}}$ with various alternative constants, derived from either theory or experimentation. For the ease of comparison, these models will be collectively referred to in this chapter only as the Eddy Model, as described by equation (2-9). One frequently used variation uses a proportionality constant, K, of 0.301, based on the work of Kawase et al. (1992). Other constants used are based on fitting this form of the equation to empirical values, including 0.523 (Linek et al., 2004), 0.592 (Prasher and Wills, 1973) and 0.7 (Appa et al., 2014).

$$k_L = K \sqrt{D_L \sqrt{\frac{\varepsilon}{v_L}}} \tag{2-9}$$

Another expression taking the general form of the Eddy Model was derived by Lamont and Scott (1970), and is often referred to as the Eddy Cell model. This uses a refinement of Higbie's penetration theory first proposed by Danckwerts (1951), who assumes that the mean rate of surface renewal is described by a constant s, and the chance of an element of fluid at the surface being replaced is independent of the element's age. This gives rise to equation (2-10). Lamont and Scott (1970) derived an expression for the surface renewal rate s by modelling the mass transfer into idealised eddies of sizes across the energy scale. This gives an equation with the same form as equation (2-9) but having a proportionality constant of 0.4.

$$k_L = \sqrt{D_L s} \tag{2-10}$$

An alternative model, also derived from Higbie's penetration theory, is the Slip Velocity model. This can be derived by assuming that t_c, the contact time from equation (2-7) can approximated by the ratio of the local bubble diameter, d_b, to the slip velocity between the gas and liquid phases, v_b, as described by equation (2-11).

$$k_L = \frac{2}{\sqrt{\pi}}\sqrt{\frac{D_L v_b}{d_b}} \tag{2-11}$$

An alternative approach to modelling the mass transfer coefficient is presented by Alves et al. (2004), based on the Frössling correlation (Frössling, 1938), which can be used to describe the Sherwood number as shown by equation (2-12). This model is referred to as the Rigid Model, since the Frössling correlation is empirically derived for single rigid spheres. This therefore requires that the bubbles may be sufficiently spherical for the correlation to apply, which is only true for small bubbles or in highly contaminated liquids (Alves et al., 2004).

$$Sh = \frac{k_L d_b}{D_L} = 2 + 0.6Re^{1/2}Sc^{1/3} \tag{2-12}$$

where Sh is the Sherwood number, Re is the Reynolds number and Sc is the Schmidt number.

Equation (2-12) can be rearranged to give equation (2-13) to describe the mass transfer coefficient, assuming that the influence of forced convection is much greater than the natural convection, thus ignoring the factor of 2 in equation (2-12).

$$k_L = 0.6\left(\frac{v_b}{d_b}\right)^{1/2}(D_L)^{2/3}{v_L}^{-1/6} \tag{2-13}$$

The final mass transfer model that will be considered in this thesis is the Surface Renewal Stretch model presented by Jajuee et al. (2006). This model combines aspects of both surface renewal and penetration theory, resulting in an expression for the mass transfer coefficient given by equation (2-14). It has been correlated against experimental data by the original authors with a high degree of accuracy reported, however it is yet to be applied to published CFD modelling studies.

$$k_L = \frac{2}{\sqrt{\pi}} \sqrt{D_L \sqrt{\frac{v_s g}{v_L}}} \tag{2-14}$$

A summary of the published CFD studies that implement interphase mass transfer modelling in simulations of mechanically stirred tanks is presented in Table 2-4. A similar comparison can be found in Table 2-5 for the simulation of bubble columns. All but one of the published studies in this table use a form of the Eddy model to describe the mass transfer process, sometimes in addition to other models used for comparison. However, the proportionality constant for the eddy model varies from 0.301 to $\frac{2}{\sqrt{\pi}}$, as shown in Table 2-4, representing a very large variation of up to 3.75 times the final $k_L a$ values obtained between the different forms.

Table 2-4: A chronological analysis of the gas-liquid stirred tank CFD simulations to include interphase mass transfer modelling.

Authors	**Mass Transfer Model(s)**
Bakker and Van den Akker (1994)	Eddy Model (K = 0.301)
Laakkonen et al. (2006)	Eddy Model (K = 0.301)
Kerdouss et al. (2008)	Eddy Model ($K = 2/\sqrt{\pi}$)
Moilanen et al. (2008)	Eddy Model (K = 0.3)
Gimbun et al. (2009)	Eddy Model (K = 0.4), Slip Velocity Model
Zhang et al. (2009)	Eddy Model ($K = 2/\sqrt{\pi}$)
Kaiser et al. (2011)	Eddy Model (K = 0.4)
Ranganathan and Sivaraman (2011)	Eddy Model (K = 0.4 & $2/\sqrt{\pi}$), Slip Velocity Model, Rigid Model
Buffo et al. (2012)	Eddy Model (K = 0.4)
Elqotbi et al. (2013)	Eddy Model ($K = 2/\sqrt{\pi}$)
Morchain et al. (2014)	Constant k_L
Appa et al. (2014)	Eddy Model (K = 0.7), Slip Velocity Model
Wutz et al. (2016)	Eddy Model (K = 0.78)
Bach et al. (2017)	Eddy Model ($K = 2/\sqrt{\pi}$)

There is also a smaller number of comparative studies presented in Table 2-4, in which two or more of the previously discussed mass transfer models are implemented for the same hydrodynamic conditions. Of these, Ranganathan and Sivaraman (2011) compare the greatest number of different mass transfer models for a dual-impeller stirred tank CFD model. Comparing to published experimental data (Alves, Maia and Vasconcelos, 2002; Alves, Maia, Vasconcelos, et al., 2002), they find a reasonable prediction of the local gas volume fraction and bubble size – both critical parameters in mass transfer estimation – however there is no distinct advantage observed by using the inhomogeneous MUSIG model over the homogeneous MUSIG model. The eddy cell and slip velocity models both provide a good fit to the measured values of the volume-averaged $k_L a$, with the eddy cell

model over-predicting by 8.3% and the slip velocity under-predicting by 16.7%. The other mass transfer models do not provide a good fit to the measured value despite using the same hydrodynamic results. However, the comparison between different mass transfer models is only presented for a single set of conditions, making it impossible to comment on the more universal applicability of the different models.

2.2.5 Experimental Validation of Stirred Tank Systems

The majority of studies presented in Table 2-2 provide validation data for at least one parameter, based either on original experiments or previously published experimental data upon which the modelled geometry and conditions are based. Some of the most common parameters used to validate these models include the liquid flow patterns, gas volume fraction, stirrer power consumption and mass transfer coefficient (as described in Section 2.2.4). The bubble size distribution is also regularly used to validate models when a population balance model is included. Several experimental techniques have been used to acquire data on these parameters, as presented in Table 2-2 and discussed in detail below.

Single phase stirred tank models have been routinely validated against the flow patterns using a variety of methods summarised by Mavros (2001). Simple imaging methods such as fluorescence imaging or the use of flow following particles can give good insights into the qualitative flow behaviour in the tank, however they do not provide the quantitative velocity profiles required for the validation of CFD models. Invasive flow measurement techniques such as Hot Wire Anemometry (Bertrand and Couderc, 1985; Lu and Ju, 1987) and Pitot Tube measurements (Wolf and Manning, 1966) have historically been used to take single-point velocity measurements in stirred tanks, however these require the physical insertion of the measuring device into the fluid flow, which may influence the flow patterns and cause issues when used close to rotating equipment, limiting the number of locations where they can be applied.

Two different non-intrusive methods, laser Doppler velocimetry (LDV) and particle image velocimetry (PIV), have been extensively applied to both single and two-phase stirred tanks. Both techniques require the flow to be seeded with small, neutrally buoyant reflective particles, and each can measure the velocity in two dimensions using a single set of optical equipment, or be expanded to three dimensions by incorporating a second set of optics. LDV is a point measurement technique, measuring the velocity components only at

the location of intersecting laser beams, with the external transmitting optics being moved to generate time-averaged two-dimensional flow fields. In contrast, PIV takes an ensemble measurement which means that velocity measurements for an entire plane (or volume for 3D PIV) are taken simultaneously. PIV therefore has the advantage of recording both the time-averaged and instantaneous flow patterns.

Both LDV and PIV methods can also be applied to two phase flows, however PIV requires additional camera equipment to distinguish between the gas and liquid phases (Deen and Solberg, 2000), whereas LDV has been shown to predominantly capture the liquid-phase velocity in a bubble column when operated in back-scattering mode (Mudde et al., 1998). The best fit to the velocity profiles for both phases achieved by Deen and Solberg (2000) was achieved using a combination PIV and laser induced fluorescence (LIF) technique, however the sampling time for the LDV measurements presented in this article was noted to be too low to accurately capture the time-averaged velocity. This resulted in representative but less smooth profiles being measured by LDV, which could be improved by using a greater sample size at each location. Despite this, a reasonable agreement between the LDV and PIV/LIF profiles for the liquid phase was achieved. Single camera PIV did not provide a good fit to the velocity profiles measured using the other methods. Khopkar et al. (2005) applied a further non-invasive technique known as computer automated radioactive particle tracking (CARPT) to a two-phase stirred tank system, where radioactive beads are tracked as they follow the liquid flows. A good agreement between experiment and model was achieved, however the setup used required 16 sensors to track the polypropylene beads, which at 1 mm are much larger than those used in LDV or PIV applications.

The dispersed gas phase can be used to qualitatively assess the accuracy of a stirred tank model by comparing the distribution of the gas phase within the vessel between the model and experimental observations. For clear-walled vessel, this can be achieved through low-cost imaging techniques using standard camera equipment. Quantitative measurements of the gas fraction have also been used in several of the stirred tank simulations included in Table 2-2. The overall gas holdup has been determined in many studies by measuring the difference in liquid height between aerated and unaerated conditions, however this can lead to quite large experimental uncertainty, especially when the liquid surface is not flat. Experimental measurement of the local gas distribution have been achieved by numerous

invasive techniques including suction probes (Alves, Maia and Vasconcelos, 2002) conductivity probes (Yang et al., 2013; Witz et al., 2016) and hot film anemometry (Zhang et al., 2008), all of which require the device to be physically inserted into the flow. A non-intrusive computed topography (CT) method has been applied by Khopkar et al. (2005), however the equipment costs for the multiple sensors used in this technique are very high.

Further to the gas volume fraction, the bubble size distribution has also been frequently used to validate stirred tank CFD models, in particular since the introduction of population balance modelling. The overall and local population size distributions can be determined through image processing techniques in clear walled vessels, as applied by (Laakkonen et al. (2007) and Kálal et al. (2014). Typically, a number of different images are analysed to give a sufficiently high number of bubbles in each region of interest. In contrast, a single point bubble size distribution can be measured using a capillary suction probe (Barigou and Greaves, 1991), as applied by Alves, Maia, Vasconcelos, et al. (2002) and Moilanen et al. (2008). This requires a probe to be inserted into the tank, with a continual suction rate applied to withdraw the two phases, which are measured as slugs flowing in a capillary tube. The works of Laakkonen et al. (2007) and Alves et al. (Alves, Maia and Vasconcelos, 2002; Alves, Maia, Vasconcelos, et al., 2002) have come to be used as test cases for a number of subsequent CFD studies in single impeller (Petitti et al., 2010; Petitti et al., 2013; Buffo et al., 2012; Basavarajappa and Miskovic, 2016) and dual impeller (Kerdouss et al., 2006; Selma et al., 2010; Ranganathan and Sivaraman, 2011) systems respectively, due to the high level of multi-parameter characterisations and detailed descriptions of the physical systems used.

2.3 CFD Modelling of Industrial Bubble Columns

Bubble column reactors are used in a wide variety of industrial processes, and as such their hydrodynamics have been extensively studied through experimentation and CFD modelling, as summarised in the recent review of Besagni et al. (2018). The modelling of two-phase bubble column systems predates the development of gas-liquid stirred tank models, since the computationally difficult challenge of modelling impeller motion is avoided. As early as the mid-1970's, computational modelling was being used as a tool to describe two-phase systems. For example, the two-dimensional finite difference model of Szekely et al. (1976), who attempted to develop a model system for the bubble-driven ladle systems used in steel processing. However, two-dimensional models are unable to

accurately capture complex unsteady behaviour such as plume oscillation, as demonstrated by Mudde and Simonin (1999), and full three-dimensional systems are therefore preferred to two-dimensional simulations or those seeking to exploit symmetry within the column.

The fundamental modelling techniques applied to bubble columns are similar to those applied to stirred tanks and discussed in Section 2.2.2. The choice of available turbulence models is largely the same, with RANS and LES models the most commonly applied in literature. Comparisons between the two models in three-dimensional simulations (Dhotre et al., 2008; Ekambara and Dhotre, 2010) found the k-ε model to be in reasonable agreement with experimental measurements for the majority of the flow characteristics observed, with the exception of some fluctuating velocities. Similarly, Tabib et al. (2008) compared the k-ε and LES models to the Reynolds's stress model (RSM), and concluded that the k-ε model was the preferred option for capturing average behaviours. As with stirred tank studies, there is no clear consensus in literature for the choice of an interphase drag model. The recent works within the Fletcher group at the University of Sydney (Mcclure et al., 2014; McClure, Aboudha, et al., 2015; McClure et al., 2016; Fletcher et al., 2017; McClure et al., 2018) represent the current state of CFD modelling for bubble column systems, with a stated focus towards industrial scale applications. The simulations covered in these studies include a wide range of gas flow rates, which cover both the bubbly flow and churning flow regimes, as represented by the instantaneous tracer velocity plots presented by McClure, Aboudha, et al. (2015).

2.3.1 Mass Transfer Modelling in Bubble Columns Using CFD

Due to the lack of mechanical agitation, there is a reduced potential for bubble breakage through turbulent interactions in bubble columns, and therefore a much larger and more uniform bubble size distribution may be expected in the bubbly flow regime. This means that there is still a relatively large number of studies using a constant bubble size assumption in preference to more computationally demanding population balance modelling. Furthermore, the more uniform hydrodynamic conditions mean that a reasonable fit to experimental data can be achieved using a constant volumetric mass transfer coefficient, k_L, such as the recent work of Fletcher et al. (2017). In addition, there have been attempts to model the mass transfer performance of bubble columns using some of the mass transfer models discussed in Section 2.2.4. A summary of the published CFD models of bubble columns to include mass transfer modelling is provided in Table 2-5.

Of the studies assuming a constant value of k_L, all of the values are of the same order of magnitude (10^{-4} m s^{-1}), although a wide range of constant bubble sizes is also used in conjunction with this assumption. The use of the Eddy Model is less widespread for bubble column applications than for stirred tanks, with the Slip Velocity model being applied most often. The Eddy Model was compared to the Slip Velocity model by Wang and Wang (2007) with a good agreement observed between the two models, however both models required some degree of modification of the proportionality constants to provide an exact fit to the experimental $k_L a$ data presented. Huang et al. (2010) compared several mass transfer models for an internal airlift reactor, with the Slip Velocity model providing a good fit to experimental data with no adjustments of the model constants, as did a design correlation based only on the local gas fraction and fixed fluid properties.

Table 2-5: A chronological analysis of CFD simulations of bubble columns which include interphase mass transfer models.

Author(s)	Geometry	Bubble Diameter	Mass Transfer Model
Cockx et al. (2001)	Rectangular Airlift	Constant	Slip Velocity
Krishna and Van Baten (2003)	Bubble Column	5 mm	Constant (k_L = 0.0004 m s^{-1})
Dhanasekharan et al. (2005)	External Loop Airlift	PBM	Eddy Model ($K = 2/\sqrt{\pi}$),
Ghadge et al. (2005)	Bubble Column	Correlation	Eddy Model ($K = 2/\sqrt{\pi}$),
Talvy et al. (2007)	Rectangular Airlift	Constant	Slip Velocity
Wang and Wang (2007)	Bubble Column	PBM	Slip Velocity, Eddy Model (K = 0.27)
Huang et al. (2010)	Airlift Loop	5 mm, 6 mm	Correlation, Slip Velocity, Eddy Model ($K = 2/\sqrt{\pi}$), Rigid
McClure, Kavanagh, et al. (2015)	Bubble Column	4 mm	Constant (k_L = 0.0004 m s^{-1})
McClure et al. (2016)	Bubble Column Bioreactor	5 mm	Constant (k_L = 0.0002 m s^{-1})
Fletcher et al. (2017)	Bubble Column	8 mm, 4 mm	Constant (k_L = 0.0004 m s^{-1})
McClure et al. (2018)	Bubble Column and Airlift	4 mm, 6 mm	Constant (k_L = 0.0003 m s^{-1}, 0.0004 m s^{-1})
M. Kim et al. (2018)	Slurry Bubble Column	Correlation	Rigid
Ndiaye et al. (2018)	Airlift Loop Photoreactor	3 mm	Slip Velocity

2.4 Summary of Literature Review

The design of gas-liquid contacting systems such as stirred tanks and bubble columns is traditionally achieved based upon empirical or semi-empirical correlations for well-characterised systems, which are not applicable to non-typical mixing applications such as

those studied in Chapter 5. However, in recent years computational fluid dynamic (CFD) modelling has emerged as a suitable tool for the design of gas-liquid systems, giving a greater understanding of the performance characteristics and two-phase flow behaviour occurring. This also presents an opportunity for the rational design of novel gas-liquid contacting systems, however the vast majority of CFD simulations of stirred tank systems identified in this literature review continue to focus on cylindrical, baffled vessels with well-characterised impeller designs.

A comprehensive review of the use of CFD modelling for gas-liquid stirred tank systems has been undertaken, from their development in the early 1990's to the present day. During this time, the complexity of the models has increased as the available computing power has increased, however a consensus on many of the key model choices can be made by reviewing the available literature as follows:

- Euler-Euler reference frame is the most suitable choice for describing the overall two-phase flow behaviour of stirred tank systems in a computationally efficient manner due to the unacceptably high computational requirements of modelling the bubbles as discreet particles (E-L) or tracking the entire gas-liquid interface (VOF) at the gas fraction and physical scale of the proposed systems.
- Multiple reference frame (MRF) or sliding mesh (SM) methods for impeller motion
- k-ε turbulence model (or modifications upon it)
- A population balance model should be used to describe the bubble size

However, there is no clear consensus in the literature for important two-phase phenomena such as the interphase drag model, with a wide range of different models applied with varying levels of detail and complexity. A relatively small number of CFD simulations of stirred tanks and bubble columns have also involved the modelling of interphase mass transfer between the gas and liquid phases via the term $k_L a$, which can be easily determined experimentally. However, there is once again no clear consensus on the choice of mass transfer model, with a wide range of different models and proportionality constants being applied. Five suitable models for the liquid phase mass transfer coefficient, k_L, have therefore been identified from literature for further consideration. The vast majority of CFD simulations have been validated against at least one parameter, with a wide variety of experimental techniques used as discussed in this review, highlighting the need for models developed to be validated against multiple experimental parameters.

3 Aims and Objectives

This thesis aims to apply the current preferred modelling choices within the limitations of the commercial CFD software ANSYS CFX, as identified via a review of the relevant literature, to industrial-scale two-phase flow systems. This will be used to improve the understanding of the complex hydrodynamic, mass transfer and reaction phenomena that are occurring in these systems. Methods for optimising mass transfer will be evaluated, including the potential use of microbubble technology as a replacement for traditional gas sparging. The hydrodynamic models developed should be applicable to industrial-scale gas-liquid systems, and be able to be solved in a time-efficient manner. The accuracy of the CFD modelling results will be evaluated by performing experimental validation in order to understand and comment on the ability of the models to describe the behaviour of the two-phase systems. Since there is limited access to take measurements and observations in the full-scale systems, this will be achieved by developing model systems at the laboratory scale and applying equivalent modelling techniques to them. The models will be validated against multiple experimental parameters in order to give the greatest possible confidence in the results generated.

The modelling work in support of the BioMOD project aims to provide a greater understanding of the fluid dynamic and mass transfer behaviour within a novel single-use-technology bioreactor design under different operating conditions by applying an experimentally validated computational modelling approach. This will be achieved by completing the following objectives:

- Identify and evaluate the current best practice in gas-liquid CFD modelling from the published body of literature.
- Develop a three-dimensional geometry and optimised mesh based on the specifications of the existing BioMOD bioreactor.
- Evaluate different options for modelling decisions where there is no clear preferred option in the literature, such as interphase drag and mass transfer models.
- Solve the optimised model for a range of different operating conditions in order to evaluate the performance characteristics of the BioMOD system.
- Develop a series of laboratory-scale experiments in order to generate data for the validation of the CFD model.

- Develop and solve an optimised three-dimensional CFD model of the validation system based on the optimised BioMOD model and solve for a range of different operating conditions.
- Compare the experimental and modelled data for the validation system and comment on the suitability of the models applied to the full-scale BioMOD reactor.

The investigation into the mass transfer performance of a commercially available microbubble generating pump aims to quantify the performance of the pump under typical operating conditions. The dependence of the mass transfer rate on the volume, geometry and the stirring conditions in the measurement system will be evaluated in an attempt to evaluate its applicability to industrial-scale mass transfer processes. This will be achieved by completing the following objectives:

- Develop and evaluate a process for characterising the size distribution of microbubbles produced by the pump for an air-water system.
- Run the microbubble pump using manufacturer recommended settings for a range of different volumes and geometries of tank, and evaluate the mass transfer performance by measuring the dynamic response in dissolved oxygen concentration to changes in the feed gas.
- Evaluate the influence that stirring has on the mass transfer performance in the various measuring tanks when compared to traditional gas sparging.

The modelling of the carbonatation process aims to develop a CFD model to evaluate the hydrodynamic and mass transfer performance of the existing process under a typical range of operating conditions. The analysis will include a reaction model that covers the interphase mass transfer of carbon dioxide gas, and the complex series of chemical reactions which lead to the formation of solid calcium carbonate, implemented within the CFD software environment. This work should allow for a number of recommendations about the performance and operation of the process to be made. This will be achieved by completing the following objectives:

- Develop a three-dimensional geometry and optimised mesh based on the physical details supplied by the process operators.
- Develop an appropriate hydrodynamic and mass transfer model based on the findings of the BioMOD reactor modelling and validation work, and solve under a range of carbon dioxide gas flow rates.

- Identify and implement a suitable and time-efficient reaction model that can be implemented within the CFD solver environment, and solve for a range of carbon dioxide flow rates, hydroxide concentrations and recycle conditions.
- Develop a suitable laboratory-based model system and accompanying analytical procedures to provide suitable data on the reactions that occur during the carbonatation process for model validation.
- Compare the modelled and experimental results for the laboratory system, and comment on the suitability of the reaction model and any simplifications applied.

4 Numerical Modelling

This chapter details the numerical models that have been implemented in the two-phase computational fluid dynamics (CFD) models presented in the following chapters. Alternative approaches to modelling various aspects of single and two-phase flows are discussed in the literature review presented in Chapter 2. CFD modelling is performed using the commercial software ANSYS CFX 17, which uses a finite volume discretisation scheme to divide the three-dimensional geometry into discrete volumes across which fluid dynamic parameters such as mass, momentum and energy are conserved. All of the multiphase models presented in this thesis are produced using the coupled multiphase solver, which solves all fluid dynamic properties iteratively within a single matrix of equations. High resolution advection and turbulence numerics are used to generate all results presented, giving second-order accurate solutions.

The theoretical basis for the CFD modelling presented in this thesis is the continuity and Navier-Stokes equations, which represent mass and momentum balance equations respectively over a control volume. An analogous energy balance is not included in this set of equations due to the assumption of isothermal operation in all models presented in this thesis. These balances are described for a single fluid by equations (4-1) and (4-2) using tensor notation, which allows for the three-dimensional system to be described by a single equation. Whereas it is possible to directly solve these equations for a discretised three-dimensional computational mesh, a solution method known as direct numerical simulation (DNS), it would require a very fine mesh and very small timestep due to the requirement to resolve the simulation down to the Kolmogorov time and length scales (Andersson et al., 2011). Therefore, an approximation of the Navier-Stokes equations is required in the form of a turbulence model to avoid excessive computational expense, especially for engineering-scale problems where large fluid domains are being considered.

$$\frac{\partial \rho}{\partial t} + \nabla \cdot (\rho \boldsymbol{u}) = 0 \tag{4-1}$$

$$\frac{\partial}{\partial t}(\rho \boldsymbol{u}) + \nabla \cdot (\rho\, \boldsymbol{u} \otimes \boldsymbol{u}) = -\nabla p + \nabla \cdot \boldsymbol{\tau} + \boldsymbol{S} \tag{4-2}$$

where $\boldsymbol{u}$ is the velocity vector, p is the pressure, $\boldsymbol{\tau}$ is the shear stress tensor and $\boldsymbol{S}$ represents the external source terms applied. The operator $\otimes$ represents the Kronecker product of two matrices.

4.1 Governing Equations

The continuity and momentum equations for the gas and liquid phases (k = G, L respectively) are shown for a two-phase Euler-Euler simulation as they are implemented for the two-phase modelling work in this thesis. The momentum balance equation shown is a simplification of the Navier-Stokes equations that is used for incompressible Newtonian fluids (Andersson et al., 2011).

$$\frac{\partial}{\partial t}(\alpha_k \rho_k) + \nabla \cdot (\alpha_k \rho_k \boldsymbol{u}_k) = 0 \tag{4-3}$$

$$\begin{aligned} \frac{\partial}{\partial t}(\alpha_k \rho_k \boldsymbol{u}_k) + \nabla \cdot \left(\alpha_k (\rho_k \boldsymbol{u}_k \otimes \boldsymbol{u}_k)\right) \\ = -\alpha_k \nabla p' + \nabla \cdot \left(\alpha_k \mu_{eff,k} \left(\nabla \boldsymbol{u}_k + \nabla \boldsymbol{u}_k{}^T\right)\right) \\ + \alpha_k (\rho_k - \rho_L)\boldsymbol{g} + D_{G,L} + F^{TD}{}_k + \boldsymbol{S}_k \end{aligned} \tag{4-4}$$

where p' is the modified pressure, μ_{eff} is the effective viscosity, $\boldsymbol{u}_k{}^T$ is the transpose of the matrix $\boldsymbol{u}_k$, $\boldsymbol{g}$ is the gravitational vector, $D_{G,L}$ is the interphase drag force and F^{TD} is the turbulent dispersion force.

The modified pressure field, which is shared between the gas and liquid phases, is shown in equation (4-5)**.**

$$p' = p + \frac{2}{3}\rho_L k \tag{4-5}$$

The k-ε turbulence model is used for two-phase modelling, and is the most widely used Reynolds averaged Navier-Stokes (RANS) model applied it CFD modelling. Reynolds decomposition techniques are used to separate the fluctuating and time-averaged velocity and pressure fields. The k-ε model is an example of a two-equation turbulence model, with the separate equations for the turbulent kinetic energy, k, and eddy dissipation rate, ε, given by equations (4-6) and (4-7) respectively. The selection of the k-ε turbulence model is based on a review of the published literature presented in Table 2-2 and a preliminary study of different turbulence models in a single-phase stirred tank, using three different

impeller types, which can be found in Appendix A. In each single-phase case, the LES model provides only a small improvement in the modelled results, with significantly higher computational load required to apply the model to two-phase meaning there are very few published examples for gas-liquid stirred tanks. Further advantages of using RANS models include the ability to solve problems using the steady state solver for conditions when a steady-state final solution is possible. The solution is iterated towards a steady-state condition using a pseudo-time parameter, however the transient development of the solution is not accurately described using this method.

$$\frac{\partial}{\partial t}(\alpha_L \rho_L k) + \nabla \cdot \left(\alpha_L(\rho_L \boldsymbol{u}_L k) - \left(\mu_L + \frac{\mu_{T,L}}{\sigma_k}\right)\nabla k\right) = \alpha_L(p' - \rho_L \varepsilon) \tag{4-6}$$

$$\frac{\partial}{\partial t}(\alpha_L \rho_L \varepsilon) + \nabla \cdot \left((\alpha_L \rho_L \boldsymbol{u}_L \varepsilon) - \left(\mu_L + \frac{\mu_{T,L}}{\sigma_\varepsilon}\right)\nabla \varepsilon\right) = \frac{\alpha_L \varepsilon}{k}(C_{\varepsilon 1} p' - C_{\varepsilon 2} \rho_L \varepsilon) \tag{4-7}$$

where μ is the dynamic viscosity, μ_T is the turbulent viscosity and σ_ε, σ_k, $C_{\varepsilon 1}$, $C_{\varepsilon 2}$ are constants.

The liquid-phase turbulent viscosity, $\mu_{T,L}$, is used as a closure for the turbulence model, as shown in equation (4-8), using a constant C_μ. No turbulence model is applied to the dispersed gas phase, with the gas phase turbulent viscosity, $\mu_{T,G}$, calculated using equation (4-9). The constants used in this turbulence model are included in Table 4-1.

$$\mu_{T,L} = \rho_L C_\mu \frac{k^2}{\varepsilon} \tag{4-8}$$

$$\mu_{T,G} = \frac{\rho_G}{\rho_L}\mu_{T,L} \tag{4-9}$$

Table 4-1: Constants used for the k-ε turbulence model.

$C_{\varepsilon 1}$	$C_{\varepsilon 2}$	σ_k	σ_ε	C_μ
1.44	1.92	1.00	1.30	0.09

The effective viscosity, μ_{eff}, for the liquid and gas phases is calculated from equations (4-10) to (4-12). An additional term, $\mu_{T,p}$, is introduced as an enhancement factor which takes into account the bubble-induced turbulence in two-phase flows (Sato and Sekoguchi, 1975).

$$\mu_{eff,L} = \mu_L + \mu_{T,L} + \mu_{T,p} \tag{4-10}$$

$$\mu_{T,p} = 0.6\rho_L \alpha_G d_b |\boldsymbol{u}_G - \boldsymbol{u}_L| \tag{4-11}$$

$$\mu_{eff,G} = \mu_G + \mu_{T,G} \tag{4-12}$$

A final source term is applied to the momentum equation to account for the dispersion of the gas phase due to turbulence in the liquid phase. This is known as the Favre-averaged turbulent dispersion force, F^{TD}, as described by equation (4-13). The implementation of this model using the CFX software, including the application to a stirred tank model, is described by Burns et al. (2004). Other source terms built-in to the ANSYS CFX software such as the lift and virtual mass forces are not considered for the applications presented in this thesis due to their reported minor influence for similar cases (Lane et al., 2002; Khopkar et al., 2005; Kerdouss et al., 2006; Gimbun et al., 2009). These effects have been quantified by Scargiali et al. (2007), with less than 5% variation in the overall gas holdup predicted by applying any of the additional interphase source terms.

$$F^{TD}{}_L = -F^{TD}{}_G = \frac{3}{4}\frac{C_D}{d_b}\alpha_G |u_G - u_L| \frac{\mu_{T,L}}{0.9}\left(\frac{\nabla \alpha_G}{\alpha_G} - \frac{\nabla \alpha_L}{\alpha_L}\right) \tag{4-13}$$

4.2 Interphase Drag Models

Three interphase drag models are to be compared within this thesis. Each describes an expression for the drag coefficient, C_D, which is used in the interfacial drag source term in the momentum equation, as described by equation (4-14). This force couples the velocity fields for the gas and liquid phases used in the Euler-Euler reference frame model.

$$D_{g,l} = \frac{3}{4}\frac{C_D}{d_b}\alpha_G \rho_L |u_G - u_L|(u_G - u_L) \tag{4-14}$$

4.2.1 Schiller-Naumann Drag Model

The Schiller-Naumann drag model is one of the simplest models available to couple the gas and liquid phases. The model was developed for flow around a single, spherical particle, and therefore assumes that there is no distortion of the bubble shape. This is generally only true for small bubbles or bubbles flowing in highly contaminated liquids (Alves et al., 2004). The Schiller-Naumann model is implemented in the CFX software using the conditional expression in equation (4-15).

$$C_D = max\left(\frac{24}{Re}(1 + 0.15Re^{0.687}), 0.44\right) \tag{4-15}$$

4.2.2 Grace Drag Model

The Grace drag model (Clift et al., 1978) is more complex, and accounts for the deformation of larger bubbles rising within a liquid. The model considers bubbles in the spherical, spherical-cap and elliptical regimes. However, since the model was developed for flow past a single bubble, the effect of densely populated regions of the gas phase are not accounted for without modification based on experimental observations. The drag coefficient when the bubble is in the spherical flow regime, $C_D(sphere)$, is calculated using the Schiller-Naumann correlation given in equation (4-15). The drag coefficient for bubbles in the spherical cap regime, $C_D(cap)$, is calculated using equation (4-16).

$$C_D(cap) = \frac{3}{8} \tag{4-16}$$

The drag coefficient for the elliptical bubble regime, also known as the distorted regime, is calculated using equations (4-17) to (4-20).

$$C_D(ellipse) = \frac{4}{3}\frac{g d_b}{{U_T}^2}\frac{(\rho_L - \rho_G)}{\rho_L} \tag{4-17}$$

where U_T is the terminal rise velocity of the bubble calculated from equations (4-18) to (4-20), with μ_{ref} as the dynamic viscosity of water at 25°C and 1 bar = 0.0009 Pa s.

$$U_T = \frac{\mu_L}{\rho_L d_b}\left(\frac{{\mu_L}^4 g(\rho_L - \rho_G)}{{\rho_L}^2\sigma^3}\right)^{-0.149}(J - 0.857) \tag{4-18}$$

$$J = 0.94H^{0.757} \quad IF \quad 2 < H \leq 59.3$$
$$J = 3.42H^{0.441} \quad IF \quad H > 59.3 \tag{4-19}$$

$$H = \frac{4}{3}\frac{g{d_b}^2(\rho_L - \rho_G)}{\sigma}\left(\frac{{\mu_l}^4 g(\rho_L - \rho_G)}{{\rho_L}^2\sigma^3}\right)^{-0.149}\left(\frac{\mu_L}{\mu_{ref}}\right)^{-0.14} \tag{4-20}$$

The local bubble regime for the discretised model is calculated using the conditional expression presented in equation (4-21), with the appropriate model implemented to yield the drag coefficient used in equation (4-14).

$$C_D = max\left(C_D(sphere), min\big(C_D(ellipse), C_D(cap)\big)\right) \tag{4-21}$$

4.2.3 Ishii-Zuber Drag Model

Like the Grace model, the Ishii-Zuber drag model (Ishii and Zuber, 1979) accounts for bubbles flowing in the spherical, spherical-cap and elliptical regimes, but also includes a modification to account for regions of dense gas phase, where bubble-bubble interactions are expected to influence the observed drag coefficient. The equation for the drag coefficient in the spherical cap regime used by the Grace model (equation (4-16)) has been modified to give a reduction in drag at high gas fractions, as shown in equation (4-22).

$$C_D(cap) = \frac{3}{8}(1 - \alpha_G)^2 \tag{4-22}$$

Similarly, the drag coefficient in the spherical bubble regime is described by the Schiller-Naumann correlation with the addition of a modified Reynolds number, Re_m, to account for regions of dense gas phase, as described by equation (4-24).

$$C_D(sphere) = \frac{24}{Re_m}\left(1 + 0.15{Re_m}^{0.687}\right) \tag{4-23}$$

$$Re_m = \frac{\rho_L|u_G - u_L|d_b}{\mu_L(1 - \alpha_G)^{-2.5\mu_*}} \quad , \quad \mu_* = \frac{\mu_G + 0.4\mu_L}{\mu_G + \mu_L} \tag{4-24}$$

Bubbles in the elliptical regime are described using equations (4-25) and (4-26), representing the most significant deviation from the Grace drag model.

$$C_D(ellipse) = \frac{2}{3}\left(\frac{g\Delta\rho {d_b}^2}{\sigma}\right)^{0.5} E(\alpha) \tag{4-25}$$

$$E(\alpha) = \frac{\left(1 + 17.67 f(\alpha)^{6/7}\right)}{18.67 f(\alpha)} \quad , \quad f(\alpha) = \frac{(1-\alpha_G)^{0.5}}{(1-\alpha_G)^{-2.5\mu_*}} \tag{4-26}$$

The conditional expressions presented in equation (4-27) are used to determine the local bubble regime within the discretised fluid domain when using the Ishii-Zuber drag model.

$$\begin{gathered} C_D = C_D(sphere) \quad IF \quad C_D(sphere) \geq C_D(ellipse) \\ C_D = min\big(C_D(ellipse), C_D(cap)\big) \quad IF \quad C_D(sphere) < C_D(ellipse) \end{gathered} \tag{4-27}$$

4.3 Population Balance Modelling

The bubble size distribution within a polydispersed fluid is modelled using the homogeneous multiple size group (MUSIG) model, which is an example of a classes method technique built in to the ANSYS CFX software. A summary of the published gas-liquid stirred tank models that include population balance models, and a discussion of their implementation can be found in Section 2.2.3. The general population balance equation used to describe the distribution of bubbles of mass m is presented in equation (4-28).

$$\frac{\partial}{\partial t} n(m,t) + \frac{\partial}{\partial x^i}\Big(u^i(m,t) n(m,t)\Big) = B_B - D_B + B_C - D_c \tag{4-28}$$

The terms on the right hand side of equation (4-28) represent the birth, B_B, and death, D_B, of bubbles due to bubble breakup and the birth, B_C, and death, D_C, of bubbles through coalescence. These terms can be calculated using equations (4-29) to (4-32) for the number fraction, n, of bubbles with mass m at time t.

$$B_B = \int_m^\infty g(\varepsilon; m) n(\varepsilon, t) d\varepsilon \tag{4-29}$$

$$D_B = n(m, t) \int_0^m g_g(m; \varepsilon) d\varepsilon \tag{4-30}$$

$$B_C = \frac{1}{2} \int_0^m Q(m - \varepsilon; \varepsilon)\, n(m - \varepsilon, t) n(m, t) d\varepsilon \tag{4-31}$$

$$D_C = n(m, t) \int_0^\infty Q(m; \varepsilon) n(\varepsilon, t)\, d\varepsilon \tag{4-32}$$

where $g(m; \varepsilon)$ represents the specific breakup rate of bubbles with mass m to form bubbles of mass ε and $m - \varepsilon$. Similarly, $Q(m; \varepsilon)$ represents the specific coalescence rate at which bubbles of mass m coalesce with bubbles of mass ε to form bubbles of mass $m + \varepsilon$.

The population balance equation is discretised into i groups, each with a number density of N_i, using equation (4-33). Assuming that all size groups share the same density and velocity fields, this can be integrated to give the expression for the size fraction, f_i, presented in equation (4-34).

$$N_i(t) = \int_{m_{i-1/2}}^{m_{i+1/2}} n(m, t)\, dm \tag{4-33}$$

$$\frac{\partial}{\partial t}(\rho_G \alpha_G f_i) + \frac{\partial}{\partial x_i}\left(\rho_G \alpha_G u_G^i f_i\right) = B_{Bi} - D_{Bi} + B_{Ci} - D_{ci} \tag{4-34}$$

The discretised break-up terms between size groups j and i, on the right hand side of equation (4-34) can be expressed by equations (4-35) and (4-36).

$$B_{Bi} = m_i \int_{m_{i-1/2}}^{m_{i+1/2}} B_C\, dm = \rho_G \alpha_G \left(\sum_{j>i} g(m_j; m_i) f_i \right) \tag{4-35}$$

$$D_{Bi} = m_i \int_{m_{i-1/2}}^{m_{i+1/2}} D_B \, dm = \rho_G \alpha_G \left(f_i \sum_{j<1} g(m_i; m_j) \right) \tag{4-36}$$

Similarly, the discretised form of the coalescence terms between size groups i, j and k can be expressed by equations (4-37) and (4-38).

$$B_{Ci} = m_i \int_{m_{i-1/2}}^{m_{i+1/2}} B_C \, dm = (\rho_G \alpha_G)^2 \left(\frac{1}{2} \sum_{j \le i} \sum_{k \le i} Q(m_j; m_k) X_{jki} f_i f_k \frac{m_j + m_k}{m_j m_k} \right) \tag{4-37}$$

$$D_{Ci} = m_i \int_{m_{i-1/2}}^{m_{i+1/2}} D_C \, dm = (\rho_G \alpha_G)^2 \left(\sum_j Q(m_i; m_j) f_i f_j \frac{1}{m_j} \right) \tag{4-38}$$

The term X_{ijk} is known as the coalescence mass matrix, calculated using equation (4-39), and represents the mass fraction resulting from collisions between bubbles of groups j and k into group i. The sum of X_{ijk} across all of the size groups must equal to 1.

$$\begin{aligned} X_{jki} &= \frac{(m_j + m_k) - m_{i-1}}{m_i - m_{i-1}} \quad IF \quad m_{i-1} < m_j + m_k < m_i \\ X_{jki} &= \frac{m_{i+1} - (m_j + m_k)}{m_{i+1} - m_i} \quad IF \quad m_i < m_j + m_k < m_{i+1} \\ X_{jki} &= 0 \quad IF \quad m_j + m_k < m_{i-1} \quad , \quad m_j + m_k > m_{i+1} \end{aligned} \tag{4-39}$$

The range of bubble sizes modelled by the MUSIG population balance model is defined by the user between the fixed limits d_{min} and d_{max}. This range is discretised into N equally spaced groups with a diameter of d_i using equation (4-40).

$$d_i = d_{min} + \frac{d_{max} - d_{min}}{N} \left(i - \frac{1}{2} \right) \tag{4-40}$$

4.3.1 Bubble Break-up Model

The break-up of bubbles is modelled using the Luo and Svendsen model (Luo and Svendsen, 1996). This model uses the turbulence in the liquid phase and probability functions to predict the breakup of bubbles of size group j to size group i. The model assumes isotropic turbulence and that the parent bubble will always form only two child bubbles. The model was developed from isotropic turbulence theory with no experimental parameters applied in the default form of the model, and was initially validated for turbulent air-water pipe flow. It has since been used in several stirred tank CFD models as summarised in Table 2-3. The specific break-up rate of bubbles in size group j into group i is calculated using equations (4-41) to (4-43).

$$g(m_i; m_j) = 0.293 F_B (1-\alpha_G) \left(\frac{\varepsilon_L}{{d_i}^2}\right)^{1/3} \int_{\xi_{min}}^{1} \frac{(1-\xi)^2}{\zeta^{11/3}} e^{-\chi}\, d\xi \tag{4-41}$$

$$\chi = \frac{6\left(\left(\frac{m_j}{m_i}\right)^{2/3} + \left(1-\left(\frac{m_j}{m_i}\right)\right)^{2/3} - 1\right)\sigma}{\rho_L {\varepsilon_L}^{2/3} {d_i}^{5/3} \xi^{11/3}} \tag{4-42}$$

$$\xi_{min} = \frac{ER_{min}\left(\frac{{v_L}^3}{\varepsilon_L}\right)^{1/4}}{d_i} \tag{4-43}$$

where F_B is a calibration factor which can be arbitrarily set by the user to improve the fit of the model to different experimental conditions, and has a default value of 1. χ is the dimensionless energy, ζ is the dimensionless size of eddies in the inertial subrange of the isotropic turbulence and ER_{min} is the minimum eddy ratio.

4.3.2 Bubble Coalescence Model

Bubble coalescence is modelled using the Prince and Blanch model (Prince and Blanch, 1990). This model is based on a three-step process for bubble coalescence consisting of bubble collision, trapping a thin film of liquid between the coalescing bubbles, the subsequent draining of the film until a critical thickness is reached and finally the film rupture to give a single bubble of size group j. The model presented below considers collisions occurring through two different mechanisms, collisions due to random motion

within turbulent flows, θ^T, and collisions due to buoyancy arising from the different rise velocity of bubbles of different sizes, θ^B. Collisions due to shear between regions of different velocity are not included in this formulation, but are also included in the original Prince and Blanch model. The model also considers the collision efficiency, η_{ij}, which compares the contact time, τ_{ij}, with the time required for film rupture, t_{ij}, to determine whether film rupture will occur. The specific coalescence rate between bubbles in size groups i and j are described through equations (4-44) to (4-47).

$$\begin{aligned} Q(m_i; m_j) &= \eta_{ij}(\theta^T + \theta^B) \\ &= e^{-t_{ij}/\tau_{ij}} \left(F_{CT} \frac{\sqrt{2}\pi}{4} {\varepsilon_L}^{1/2} (d_i + d_j)^2 \left({d_i}^{2/3} + {d_j}^{2/3} \right)^{1/2} \right. \\ &\quad \left. + F_{CB} \frac{\pi}{4} (d_i + d_j)^2 \left| U_{Tj} - U_{Ti} \right| \right) \end{aligned} \tag{4-44}$$

Where U_T is the rise velocity given by:

$$U_T = \left(\frac{2.14\sigma}{\rho_L d_i} + 0.505 g d_i \right)^{1/2} \tag{4-45}$$

F_{CT} and F_{CB} are calibration factors that can be used to give a better fit to experimental data. Both have a default value of 1.

The contact time and the time necessary for film rupture are calculated using equations (4-46) and (4-47). The terms h_0 and h_f represent the initial and critical thickness of the film between the coalescing bubbles, which are assumed to take the default values of 10^{-4} and 10^{-8} m respectively, and r represents the equivalent radius of a spherical bubble in size groups i and j.

$$\tau_{ij} = {\varepsilon_L}^{-1/3} \left(\frac{1}{2} \left(\frac{1}{r_i} + \frac{1}{r_j} \right) \right)^{-2/3} \tag{4-46}$$

$$t_{ij} = \left(\frac{\rho_L}{8\sigma \left(\frac{1}{r_i} + \frac{1}{r_j} \right)} \right)^{1/2} ln \left(\frac{h_0}{h_f} \right) \tag{4-47}$$

4.4 Mass Transfer Modelling

Mass transfer analysis is implemented into the CFD model either at the post-processing stage or as part of a species source term by consideration of the commonly reported parameter $k_L a$, where k_L is the volumetric mass transfer coefficient and a is the specific interfacial area between the gas and liquid phases. The form of each of the five mass transfer models considered in this thesis, as they are implemented within the CFD environment, are presented in Table 4-2. The theoretical basis for each of these models can be found in Section 2.2.4.

Table 4-2: Mass transfer models applied during CFD modelling.

Mass Transfer Model	Modelled Equation	Source Equation
Penetration Model	$\mathrm{k}_L = \frac{2}{\sqrt{\pi}}\sqrt{D_L\sqrt{\frac{\varepsilon\,\rho_L}{\mu_L}}}$	(2-7)
Eddy Cell Model	$\mathrm{k}_L = 0.4\sqrt{D_L\sqrt{\frac{\varepsilon\,\rho_L}{\mu_L}}}$	(2-9)
Slip Velocity Model	$\mathrm{k}_L = \frac{2}{\sqrt{\pi}}\sqrt{\frac{D_L v_b}{d_b}}$	(2-7)
Rigid Model	$\mathrm{k}_L = 0.6\left(\frac{v_b}{d_b}\right)^{1/2}(D_L)^{2/3}\left(\frac{\mu_L}{\rho_L}\right)^{-1/6}$	(2-12)
Surface Renewal Stretch Model	$\mathrm{k}_L = \frac{2}{\sqrt{\pi}}\sqrt{D_L\sqrt{\frac{v_s\,g\,\rho_L}{\mu_L}}}$	(2-13)

The specific interfacial area is considered as the ratio between the surface area and the volume of a spherical bubble, which is described by equation (4-48).

$$a = \frac{6\alpha_G}{d_b} \tag{4-48}$$

5 BioMODULE Modelling

The modelling work presented in this chapter is in support of a collaborative industrial project, with the aim of developing a single-use-technology (SUT) bioreactor that is suitable for use in the wider biopharmaceutical industry. Existing SUT bioreactors are typically limited to applications for the production of high-value pharmaceutical products and mammalian cells, as discussed in Section 5.1, and there is therefore a gap in the market for a low-cost reactor with a production volume and mass transfer capability to perform bacterial and algal fermentations to commercially significant concentrations. This project forms part of a wider industrial project named BioMOD (full title 'A Modular Bio-processing Platform for Competitive, High Quality Manufacturing'). The project consortium was led by the Centre for Process Innovation (CPI) and includes partners with interests in manufacturing (Pall Life Sciences), process control (Bioprocess Engineering Services, BPES) and lifecycle assessment (NAREC).

5.1 Introduction

The term 'single-use-technology' refers to a category of disposable bioprocessing equipment where traditional stainless steel equipment is replaced by pre-sterilised plastic components such as reactors, storage bags, piping and filters. These components are disposed of and replaced after use. Three distinct historical phases in the development of SUT concepts have been identified by Eibl et al. (2010). SUT concepts began in the 1960s, when certain glass laboratory equipment began to be replaced by plastic alternatives. For example, glass shaker flasks were replaced by shaken bags made of polypropylene and Teflon, with significantly improved aeration reported at the time (Falch and Heden, 1963). A second phase of SUT adoption occurred during the 1970s, when single-use hollow fibre membrane systems were developed (Knazek et al., 1972), and subsequently applied to successfully produce monoclonal antibodies up to the gram scale. The third phase of SUT development involves the implementation of disposable bioreactors for the pilot and production scale, beginning with the first wave-type bioreactors in the late 1990s (Singh, 1999) and leading to the wide range of commercially available bioreactors and peripheral equipment compiled in the recent review articles of Shukla and Gottschalk (2013), Lopes (2015) and Junne and Neubauer (2018). The wide range of different manufacturers offering SUT systems is a further indicator of the current interest in the field.

SUT bioreactors can be broadly divided into two categories; wave and stirred-type. Wave-type bioreactors use a rocking platform in order to achieve mixing through gentle agitation of a partially-filled polymer bag, with oxygen transfer occurring between the inflated headspace and the process fluid at the moving liquid surface (Brecht, 2009), providing very good conditions for the growth of animal, insect and plant cells (Singh, 1999), however the mass transfer is not high enough to sustain high-density concentrations of aerobic bacteria or yeast cells, and the maximum bag volume is also limited. Other recent developments of SUT bioreactor concepts include rotary oscillating and pneumatically driven designs, however these concepts are also unlikely to be able to achieve the high $k_L a$ conditions needed to sustain high-density microbial or algal fermentations.

Stirred tank SUT bioreactors work on a similar principal to fixed stainless steel bioreactors, and therefore experience many of the same difficulties with the scale-up of two-phase hydrodynamic conditions discussed in Section 2.1. They typically consist of a rigid steel frame, into which a pre-sterilised polymer bag is secured. Stirring and sparging apparatus are often kept as similar as possible to established bioreactor designs, with gas sparged directly onto shaft-driven impellers. However, this increases the complexity of the bag design due to the need for a rotating impeller shaft to intersect the bag and the use of a relatively complex cylindrical bag shape, often incorporating baffles. SUT alternatives to the vast majority of peripheral equipment typically associated with bioprocessing plants have been developed by SUT manufacturers, however the limited development of some SUT-compatible sensors and control equipment are currently limiting the degree of automation achievable in SUT processes (Lopes, 2015).

A recent and exhaustive list of current SUT bioreactor manufacturers has been compiled by Junne and Neubauer (2018), with large bioprocessing manufacturers including Sartorius Stedim Biotech (Dreher et al., 2014), Merck Millipore (Kaiser et al., 2011) and GE Life Sciences (Löffelholz et al., 2014) offering a range of options that have been characterised for various different applications. Commercial stirred SUT bioreactors are available with working volumes from the sub-litre level up to 2,000 litres. This upper level has not increased in the past decade, see Brecht (2009), and numbering-up of multiple units therefore remains the only viable option to achieve the production volumes of up to 20,000 litres achieved by stainless steel stirred tanks (Brecht, 2009). The possibility of using SUT bioreactors in continuous operation is proposed by Junne and Neubauer (2018), thus

opening up the possibility of using a lower physical reactor volume for high-volume production processes.

All of the SUT bioreactor concepts presented above offer excellent choice and flexibility for the production of low oxygen demand, shear sensitive cultures of animal, insect and plant cells. However, there is still a large potential for expanding the use of SUT concepts to aerobic bacterial or yeast fermentations, as discussed by Pollard and Kistler (2017). However, there are several issues that will need to be addressed before this becomes a commercial possibility, largely owing to the much greater oxygen demand from high density microbial fermentations. This is already achieved at the laboratory scale using high-throughput screening and scale-down devices such as the Sartorius (formerly TAP) Ambr 250 (Xu et al., 2017), which uses multiple 250 mL disposable stirred chambers controlled with a high degree of automation. Furthermore, successful microbial fermentations have been reported at the 30 L (GE Healthcare, 2013) and 50 L (Dreher et al., 2013; Dreher et al., 2014) scales, with modified baffles and high-speed overhead stirring used to achieve a reported $k_L a$ of up to 150 hr^{-1}. High cell density fermentations have also been achieved up to the 300 L scale in a high aspect ratio SUT fermenter (Jones, 2015) by enriching the sparged gas with oxygen (Galliher et al., 2011), however this approach provides additional cost and has potential safety implications when considering the potential for loss of bag integrity. Further challenges for the implementation of SUT for microbial fermentations include the increased cooling requirements, with cooling from internal structures such as baffles seen as a possible solution, and a necessity to reduce bag cost and complexity to achieve commercial viability (Pollard and Kistler, 2017).

The drivers and barriers behind the wider acceptance of SUTs and their perceived significance has been discussed by several sources (Pora and Rawlings, 2009; Ravise et al., 2009; Shukla and Gottschalk, 2013). The findings of a survey of Biopharmaceutical producers in 2009 (Kapp et al., 2010) showed that the largest perceived barriers to the introduction of SUT included existing investments in traditional technology, validation concerns and a lack of experience with the technology, although the latter of these was significantly reduced from the previous year. The key potential benefits of embracing SUT concepts have been extensively discussed by Lopes (2015), covering issues relating to the design, build and operation of SUT-based manufacturing facilities. These can be broadly summarised under the headings below.

Sterility and Cleaning: One of the most widely reported benefits of using SUT components is the reduced requirement for cleaning in place (CIP) and sterilisation in place (SIP). Since SUT components are manufactured and stored pre-sterilised using gamma radiation, there is no need to undergo CIP and SIP before each production run. The energy requirements for sterilisation, cleaning and materials are approximated, based on certain stated assumptions, by Rawlings and Pora (2009) for comparable SUT and stainless steel processes. The total energy required for the SUT facility is less than half that for the stainless steel process, with the vast majority of the energy required for preparing the stainless steel process attributed to CIP and SIP. Furthermore, there is much less process required for the validation and assurance of sterility when using pre-sterilised components, which is reported to result in significant savings in costs and labour (Lopes, 2015). It has been reported that the turnaround time between batches of product can be significantly improved when using SUT components (Kapp et al., 2010), with estimates of 8-10 hours for traditional stainless steel equipment reduced to just 1-2 hours using SUT components (Brecht, 2009).

Flexibility and Build Time: In addition to the reduced time between batches of the same product mentioned above, SUT facilities are reported to be able to switch between different products in a similar timeframe of 1-2 hours, instead of up to 3 weeks for traditional stainless steel facilities (Brecht, 2009). This is further improved by the use of flexible, re-routable single-use piping and the generally transportable nature of modular SUT processes. SUT concepts also allow for the rapid response to varying market demand, since the scale-up of processes is generally achieved through the numbering-up of modular SUT components with known performance characteristics (Kapp et al., 2010). A typical timeline for the design and build of an SUT production facility is provided by Lopes (2015), and compared to a similar stainless steel facility. The estimated build time is reduced from 4 years to 3 years, with the most significant time savings achieved through a reduction in construction time, however the ability to perform the qualification of modular equipment alongside the construction phase is also cited as a significant time saving benefit.

Economics: Economic benefits of SUT cover both capital and many recurring operating costs, as summarised by Lopes (2015) for a fully SUT facility and a hybrid facility, which combines SUT and traditional equipment, for the production of viral vaccine products. Capital costs are significantly reduced for all of the sub-categories identified, which include

costs relating to equipment purchase, design, construction and validation. This cost saving can be associated with the shorter build time discussed previously. A total reduction in capital costs of around 50% is claimed for both the hybrid and fully SUT facilities, however this value may be somewhat misleading as the ongoing cost of replacing SUT components is classified as an operating cost. The increase in expenditure on consumables through the replacement of SUT components is reported to be 233% for the hybrid facility, rising to 631% if only SUT components are used. However, this is offset against large reductions in utilities consumption through reduced cleaning requirements and lower labour costs leading to significant overall savings on the cost of the completed product.

Environmental: The environmental credentials of switching to SUT facilities are more difficult to evaluate, especially due to the large amounts of contaminated plastic waste produced. The disposal of this waste has been considered by the industry body Bio-Process Systems Alliance (BPSA, 2007a). A typical single use bag will be a composite made up from of multiple layers of FDA approved polymers such as polyethylene terephthalate (PET), polyvinyl chloride (PVC), polyvinyl acetate (PVA) and low-density polyethylene (LDPE). Typical ratios of polymeric materials in SUT bags are presented by (Brecht, 2009), consisting of five different layers made up from four materials. Added to the additional controls required for the disposal of contaminated waste, it is expected that any form of recycling or untreated landfill will not be a viable option. It is therefore concluded that the most suitable option for disposal is incineration with energy recovery, along with combined energy generation (BPSA, 2007a).

There have been a limited number of lifecycle assessment (LCA) studies reported for SUT facilities, although these have been largely limited to trade publications or equipment manufacturers. However, a peer-reviewed lifecycle approach has been published by GE healthcare (Pietrzykowski et al., 2013) to assess the production of monoclonal antibodies up to the 2,000 L scale. The environmental impact of comparable SUT and stainless steel fermenters is compared across three categories; ecosystem, human health and resources. The SUT production process was 30-40% less damaging than the traditional process, although this benefit was reduced as the production volume increased. A further lifecycle approach, albeit with a much narrower system boundary, was made by Rawlings and Pora (2009), covering the areas of sterilisation, cleaning and materials. This report predicted a 50% reduction in the energy use over a traditional bioprocessing plant.

As a relatively new development in a highly-regulated sector, there are still several challenges that SUT concepts must overcome if they are to become more widely accepted within the biopharmaceutical and particularly the industrial biotechnology sectors. A survey of manufacturers within the industry (Pora and Rawlings, 2009) has reported that a significant driver behind the adoption of SUT is the assurances of sterility for components such as SUT bioreactor bags, compared to the possibility of human error when cleaning and sterilising fixed equipment. However, some safety concerns have been raised over the possibility of extractables and leachables entering the process media from the plastic materials used to make SUT components (Lopes, 2015). Leachables are components that may enter the process media under normal conditions and are therefore of particular concern (BPSA, 2007b). The lack of standardisation between different manufacturers or regulatory guidance is identified as a further complication (Lopes, 2015), and could make processes susceptible to the fortunes and decisions of the component manufacturers, although the plastics used for SUT components have typically already been approved for food and drug administration (Eibl et al., 2010). The interaction of hydrophobic species with common SUT materials has been found to be significant in some scenarios (Altaras et al., 2007), with the effects considered to be highly process specific.

5.2 BioMOD Production Facility

The physical BioMODULE system, on which the following modelling work is based, is located in a newly refurbished unit at the Centre for Process Innovation (CPI) process development facility in Teesside, UK. During the course of the project, several trial fermentations have been performed by researchers at CPI using the 1,000 L fermenter shown in Figure 5-1, providing data for the evaluation and validation of the computational model presented in this chapter. It is clear from this image that there is limited access to monitor the hydrodynamic performance of the vessel during operation due to the rigid frame and requirement to maintain bag integrity and sterility, and CFD modelling is therefore an important tool for understanding the mixing and flow characteristics of the fermenter under different conditions. Furthermore, additional validation experiments have been performed at the University of Bath using laboratory scale techniques as detailed in Chapter 6 in order to validate the hydrodynamic and mass transfer models used with the maximum possible access for measurements and observations.

Figure 5-1: BioMOD production facility at CPI, Wilton, UK.
Image courtesy of Stephen Wright, CPI.

5.3 Domain Definition and Simplifications

The fluid region of the reactor is represented as a 1 × 1 × 1 meter cubic geometry. Between the corners of the reactor, the distributed sparger inlets and the four-bladed impeller, there exists a single plane of symmetry, as shown in Figure 5-2. The reactor uses a floor-mounted, magnetically driven impeller, the geometry of which is shown in Figure 5-3. It has four large vertical blades, with an additional four curved internal vanes intended to promote recirculation of the liquid phase. Air is introduced into the domain through 14 individual candle spargers, located in two rings around the impeller; eight in an inner ring and six in an outer ring. This combination of sparging and mixing devices is preferred so that the bag can be supplied with the pre-sterilised impeller and spargers already installed, and can therefore be packed, stored and installed efficiently. Furthermore, bag integrity can be improved by removing the need for an impeller shaft to penetrate the bag. However, due to these compromises the reactor design is clearly very different from the aeration and stirring mechanisms applied in traditional bioprocessing equipment, and therefore the flow characteristics and mass transfer mechanisms are expected to also be very different to existing technologies, and can therefore not be characterised using existing correlations for stirred tanks.

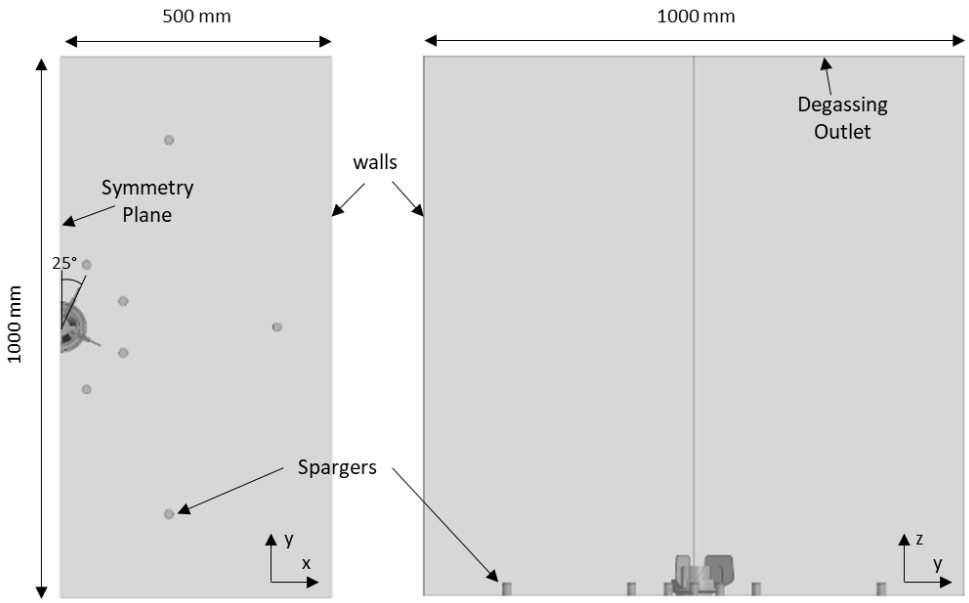

Figure 5-2: Modelled geometry for the 1,000 L BioMOD SUT bioreactor.

In the modelled domain used, the impeller is offset by an angle of 25° to the symmetry in order to minimise the interactions between the impeller blades and the internal boundary, which is modelled using a single instance of rotational periodicity around the central axis of the tank. The impeller geometry has been imported from pre-existing CAD files, with mild defeaturing and curvature removal applied in order to optimise model performance and reduce the number of mesh cells required to discretise the impeller region. The inner walls of the tank are modelled as smooth walls, with the assumption than any folding or rippling of the polymeric bag is minimised during installation, and that wall roughness is not significant in dictating the flow patterns. All solid walls in this domain are modelled using the no-slip boundary condition with respect to the liquid phase, and free-slip with respect to the gas phase. The liquid surface is modelled using the degassing boundary condition, which acts as a wall with no-shear condition with respect to the liquid phase and an outlet with respect to the gas phase.

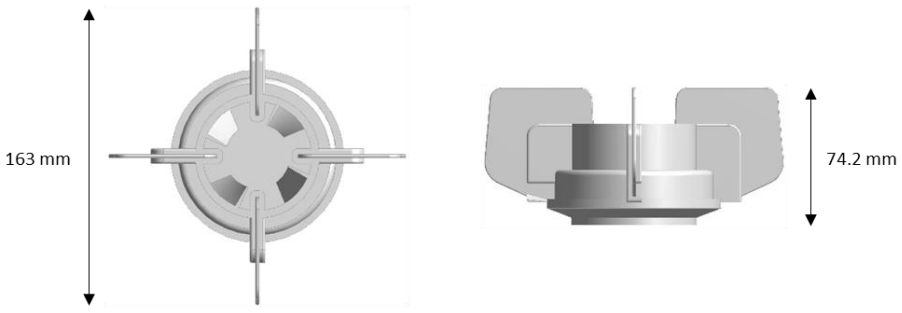

Figure 5-3: Geometry of the single-use impeller used with the BioMOD bioreactor.

The impeller motion is modelled using a novel application of the Immersed Solids (IS) method. This method is not universally applicable to two-phase systems due to limitations in the way that the dispersed phase interacts with the solid wall (ANSYS Inc., 2016). This method allows for the fluid and impeller regions to overlap, meaning that that there is no interface required between the rotating and stationary regions, significantly improving the mesh quality and model stability. The influence that applying this method has on the computational results for the BioMOD reactor, in comparison to the MRF technique, has been found to be negligible since there are only limited interactions between the impeller blades and the gas phase when compared to traditional sparged reactors such as Figure 2-1. The volume averaged $k_L a$ values, calculated using the eddy cell model at 400 RPM and assuming a 1 mm constant bubble size, match to within 1.72% when the same conditions are modelled using the IS and MRF methods.

5.4 Meshing

The fluid region is discretised using a fully structured hexahedral mesh within the ANSYS ICEM software package. A structured mesh is chosen for this geometry due to the relative ease with which the cubic geometry can be discretised, and based on the consensus that structured meshes can give better numerical properties for lower computational load (Andersson et al., 2011). The mesh is finest in the regions close to the impeller and air spargers, where the velocity gradients are expected to be the greatest. The solid region which forms the impeller is meshed separately using an unstructured tetrahedral mesh. A structured mesh is not suitable for this region due to the complex geometry of the impeller. A mesh dependency study is performed using five meshes of increasing density, as presented in Table 5-1. The meshes are evaluated with water as the continuous phase and air as the dispersed phase, with a fixed bubble diameter of 1 mm and introduced equally through the spargers at a rate of 0.1 vvm (based on the full 1 m^3 geometry). The mean size of a single mesh cell for the tank region ranges from 6.5 cm^3 for Mesh 1 to 0.72 cm^3 for Mesh 5. This is much larger than the size of a single bubble, and therefore justifies the use of the Euler-Euler reference frame, which treats the dispersed phase as a continuum rather than discreet particles. For this reason, other discretisation schemes such as Euler-Lagrange and Volume of Fluids would be expected to require much finer grids to give mesh-independent results.

Table 5-1: Mesh dependency study for the 1,000 L SUT bioreactor.
1 mm constant bubble diameter.

Mesh	Number of Elements			$k_L a$ (hr^{-1})	
	Total	Stationary region	Impeller region	Eddy Cell	Slip Velocity
1	209,555	154,294	12,320 + 42,941	56.31	106.8
2	431,914	349,794	18,144 + 63,976	54.58	153.6
3	821,909	693,064	23,400 + 105,445	60.73	177.9
4	997,828	844,316	23,400 + 130,112	62.29	170.1
5	1,548,956	1,375,456	23,400 + 150,110	62.22	168.4

The volume-averaged $k_L a$ is selected as a criterion for assessing the independence of the model from the mesh used, due to the importance of the mass transfer performance on the operation of the SUT bioreactor and the dependence of the different mass transfer models on both fluid dynamic and two-phase parameters. Both the slip velocity and eddy cell models – each of which is calculated from very different fluid dynamic parameters, see section 2.2.4 – show that there is a convergence of $k_L a$ towards the finer meshes. The variation between meshes 4 and 5 is less than 1% of the value for the highest density mesh, suggesting that mesh 4 represents an optimal trade-off between solution accuracy and computational load. The selected mesh (Mesh 4) is shown in Figure 5-4 for the tank and impeller regions. The mesh refinement in the regions of the impellers and gas spargers can also be identified from Figure 5-4.

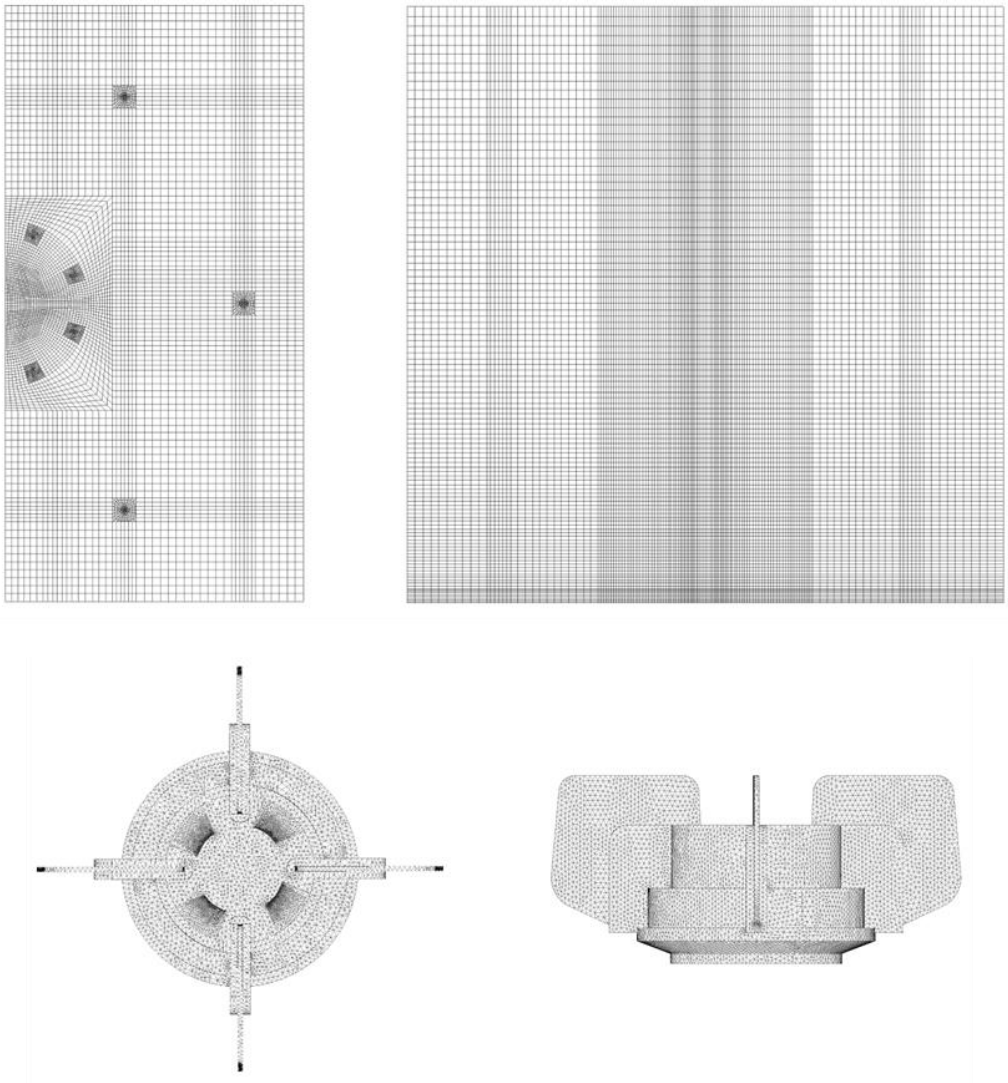

Figure 5-4: Optimised mesh for the tank (top) and impeller (bottom).

5.5 Population Balance Model Optimisation

The population balance model described in section 4.3 is implemented into the BioMODULE fluid dynamic model to describe the range of bubble sizes that occur within the fluid domain. The range of bubble sizes and number of size groups are user-defined inputs for the MUSIG model, and therefore require optimisation to ensure that the solution is not being constrained by the model definition. The bubble diameter is expected to be reduced by the action of the impeller via the break-up mechanism, and the minimum bubble diameter is therefore set to 0 mm in order to ensure that this is captured effectively. The maximum bubble diameter is increased in 3 mm increments between 3 and 12 mm, with an initial estimate of 12 size groups applied. The hydrodynamic model is solved for each size range for a 'base case' setup with a stirrer speed of 400 RPM and

aeration rate of 0.1 vvm. The size distribution at the liquid surface – where the bubbles are expected to be the largest – is presented in Figure 5-5. For figures a) and b), the size distribution is considered to be constrained by the input range since the majority of bubble diameters at the surface are in groups close to the maximum allowed size. In contrast, the distribution in Figure 5-5 d) is limited to the lower end of the permitted range, meaning that distribution loses resolution. The optimal size range is therefore determined to be 0-9 mm (Figure 5-5 c), which captures the entire range of bubble sizes expected to occur within the reactor volume whilst maintaining a good definition between groups – with the maximum population in a single group of 33% of the total.

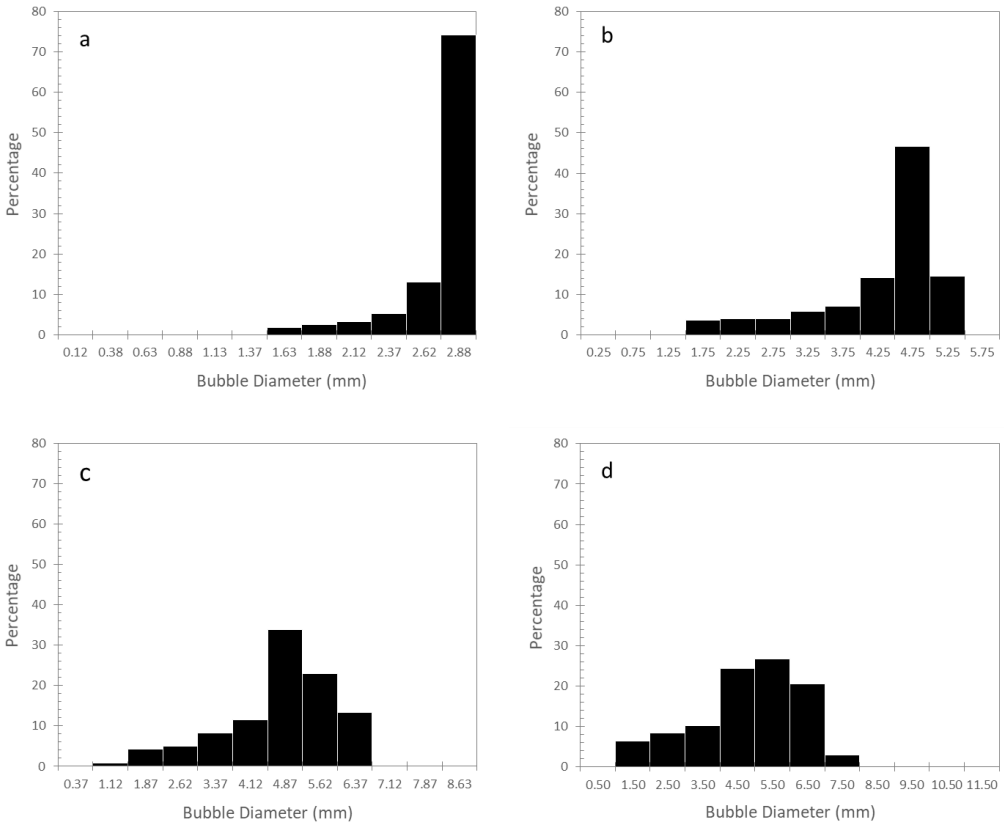

Figure 5-5: Bubble size distributions at the liquid surface for different MUSIG ranges.
a) 0-3 mm, b) 0-6 mm, c) 0-9 mm, d) 0-12 mm.

The hydrodynamic model with a MUSIG size range of 0-9 mm is also solved with 18 and 24 size groups. This will help to ensure that the resolution of the size discretisation is sufficient to capture the necessary detail required for the hydrodynamic and mass transfer models. The volume-averaged $k_L a$ values for the eddy cell and slip velocity models are presented in Table 5-2, and show very little difference between the different numbers of size groups applied. This means that increasing the number of size groups above 12 does not

significantly improve the accuracy or the model, and the additional computational expense to model additional size groups is therefore not justified.

Table 5-2: Volume-averaged $k_L a$ values for different numbers of population balance size groups. (MUSIG size range 0-9 mm).
Time for solution based on the time taken to reach 1,000 iterations using 16 cores. [Intel Xeon E5-2670 v2 CPUs, 64 GB RAM].

Number of Groups	Average $k_L a$ (hr^{-1})		Time for Solution (hrs)
	Eddy Cell	Slip Velocity	
12	17.603	30.261	8.26
18	17.440	29.376	10.44
24	17.965	30.507	13.43

5.6 Evaluation of Drag Models

The interphase drag is the closure method used for coupling the gas and liquid phase momentum balances in the Euler-Euler frame of reference. The force exerted by one phase on the other is given by equation (4-14), with the drag coefficient C_D described using one of several available drag models. For low Reynolds number flows around a single, spherical bubble, the drag coefficient can be described using Stokes law. However, at higher Reynolds numbers, or in flows with a large fraction of discreet bubbles, empirical correlations such as those studied in this section may be required to accurately describe the interphase drag. Many correlations such as the Grace and Ishii-Zuber models also account for the deformation and oscillation of larger bubbles at high Reynolds numbers (Re > 200), where much more complex definitions of C_D are required (Andersson et al., 2011). As discussed in Section 2.2.2, there is no consensus in literature on the most appropriate interfacial drag model to use for two-phase stirred tank models. Evaluation of three existing interfacial drag models has been performed with the optimised mesh and MUSIG parameters for the 'base case' simulation with a stirrer speed of 400 RPM and aeration rate of 0.1 vvm. The Schiller-Naumann, Ishii-Zuber and Grace drag models have been implemented as described in Section 4.2.

A comparison of the volume-averaged values of the $k_L a$ calculated via the slip velocity and eddy cell models in Table 5-3 shows very little difference between the predicted $k_L a$ values for the two models despite the differences in the drag models. However, a comparison of the volume-averaged bubble size and air fraction, also included in Table 5-3, show that the predicted air fraction is lower for the Schiller-Naumann model and the mean bubble

diameter is smaller than the other two models. This divide is unsurprising since the Schiller-Naumann drag model is developed for single spherical bubbles, whereas the other two models both account for bubble deformation, with the Ishii-Zuber model also and high gas fraction bubbly flows.

Table 5-3: Volume-averaged hydrodynamic parameters using different drag models. Time for solution based on the time taken to reach 1,000 iterations using 16 cores. [Intel Xeon E5-2670 v2 CPUs, 64 GB RAM].

	$k_L a$ (hr^{-1})		Gas Holdup (-)	Bubble Diameter (mm)	Time for Solution (hrs)
	Slip Velocity	**Eddy Cell**			
Ishii-Zuber	30.1676	17.2063	0.00798548	3.3289	8.26
Grace	29.3141	16.1283	0.00771291	3.30744	8.31
SN	29.5512	15.3338	0.00589361	2.84884	8.13

A comparison of the local air fraction and bubble diameter is also presented in Figure 5-6 from the centre to the wall of the tank at a height of 0.5 m within the tank. As with the volume-averaged values, the Grace and Ishii-Zuber models have much more similar profiles than the Schiller Naumann model. Of the two, the Ishii-Zuber model predicts a slightly higher air fraction and bubble diameter than the Grace model, however the two models can be said to give similar results for both parameters. This analysis shows that more complex models such as the Ishii-Zuber or Grace models – both of which account for bubble deformation - are required to more accurately capture the interfacial drag. Considering the similarity between these two models as described in Table 5-3 Figure 5-6, the Ishii-Zuber drag model has been selected for use in the subsequent modelling work presented in this thesis due to the comparable performance with the Grace model and more extensive number of applications in literature studies (see Table 2-2), giving it a greater weight of validated applications to similar two-phase systems.

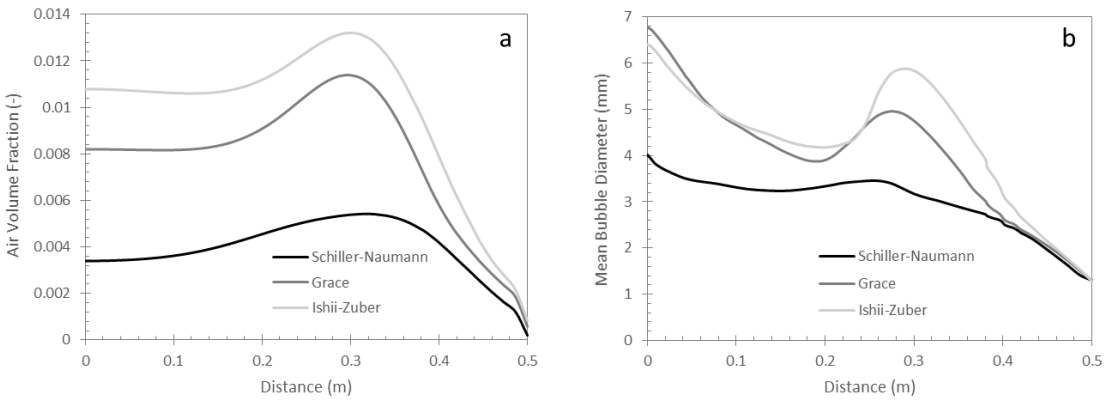

Figure 5-6: Comparison of hydrodynamic results using different interphase drag models. a) air fraction, b) mean bubble diameter.

5.7 CFD Modelling Results

The computational fluid dynamic model for the BioMOD SUT bioreactor described above has been solved for a 'base case' scenario of 400 RPM stirrer speed and 0.1 vvm aeration rate, which is based on typical operating conditions for production runs performed at CPI. Five different mass transfer models are also applied to the solution in order to identify the most suitable model for use with SUT equipment. Although several of the models have previously been applied to CFD simulations, there have been few comparative studies between the models. The finalised CFD model is then used to explore and optimise the reactor performance under different operating conditions. All models presented in this chapter have been solved with convergence criteria of 10^{-4} for the root-mean-squared (RMS) residuals of momentum and turbulence parameters, and a maximum permitted imbalance of 0.01 for all parameters including the bubble size. A second-order accurate, high-resolution numerical scheme has been used for all models with a fixed pseudo-timestep of 0.005 s used to generate the steady-state solutions.

5.7.1 Hydrodynamic Results

The hydrodynamic results for the base case model can be used to gain a better understanding of the mixing characteristics of the BioMOD reactor under typical operating conditions. The liquid and gas flow patterns in the reactor are compared in Figure 5-7 a) and b) respectively for a stirrer speed of 400 RPM and volumetric aeration rate of 0.1 vvm, along with the distribution of air for the central cut plane. There is a good distribution of the gas phase within the tank, as signified by the light blue colours in the contour plots, which reduces the chances of dead-zones developing at the base-case stirrer speed. The

vector arrows show that there is a significant recirculation of the liquid phase in the lower half of the tank, driven by the action of the impeller, and a significant rise of the gas phase in the upper section of the tank driven by the buoyancy of the gas bubbles. This slip velocity observed between the two phases, as identified from the differences between the two sets of vector arrows, is expected to lead to significant mass transfer according to the slip velocity model, equation (2-7).

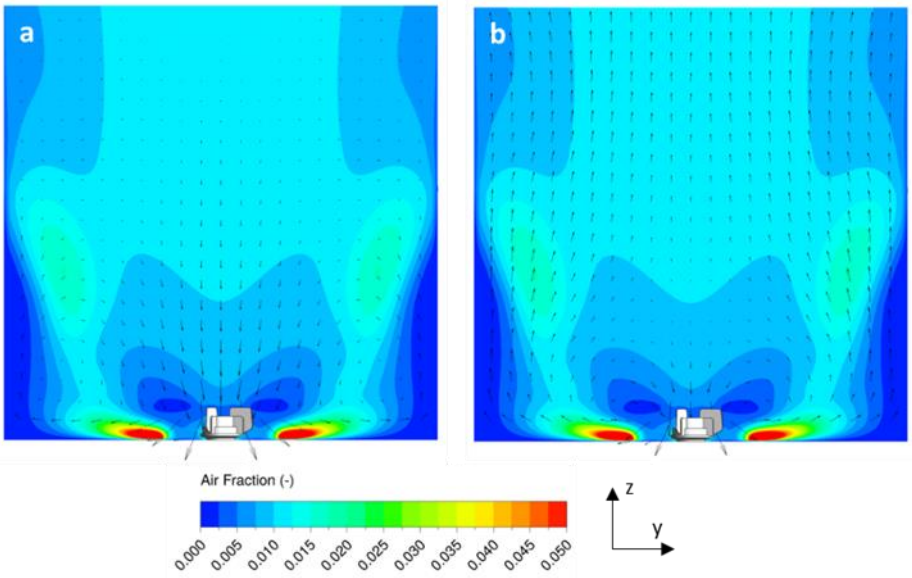

Figure 5-7: Vector plots of the liquid (a) and gas (b) phase velocity. Both are overlaid on the same the air fraction contour plot for a vertcal cut-plane at the centre of the SUT bioreactor at 400 RPM and 0.1 vvm.

The changing bubble size within the bioreactor can be assessed by plotting the bubble size distribution for cut planes at different heights in the tank, as shown in Figure 5-8. The bubbles at the inlet are assumed to have a uniform size, as shown in Figure 5-8 a), however this has quickly developed to give a distribution of bubble sizes either side of this value by a height of 100 mm, 10% of the filled tank height. This shows that the bubble coalescence and breakup models applied within the MUSIG framework are both in effect in the lower region of the tank. The breakup mechanism is assumed to be driven by the influence of the impeller, whereas significant coalescence is expected to occur close to the sparger candles due to the proximity of several gas bubbles. The distribution of bubble sizes then continues to shift towards the larger bubbles as the height within the reactor is increased, as the coalescence of bubbles becomes the dominant influence. Due to the strong dependence of the mass transfer rate on the bubble size, described through the interfacial area, it is therefore expected that the mass transfer will be highest towards the bottom of the tank.

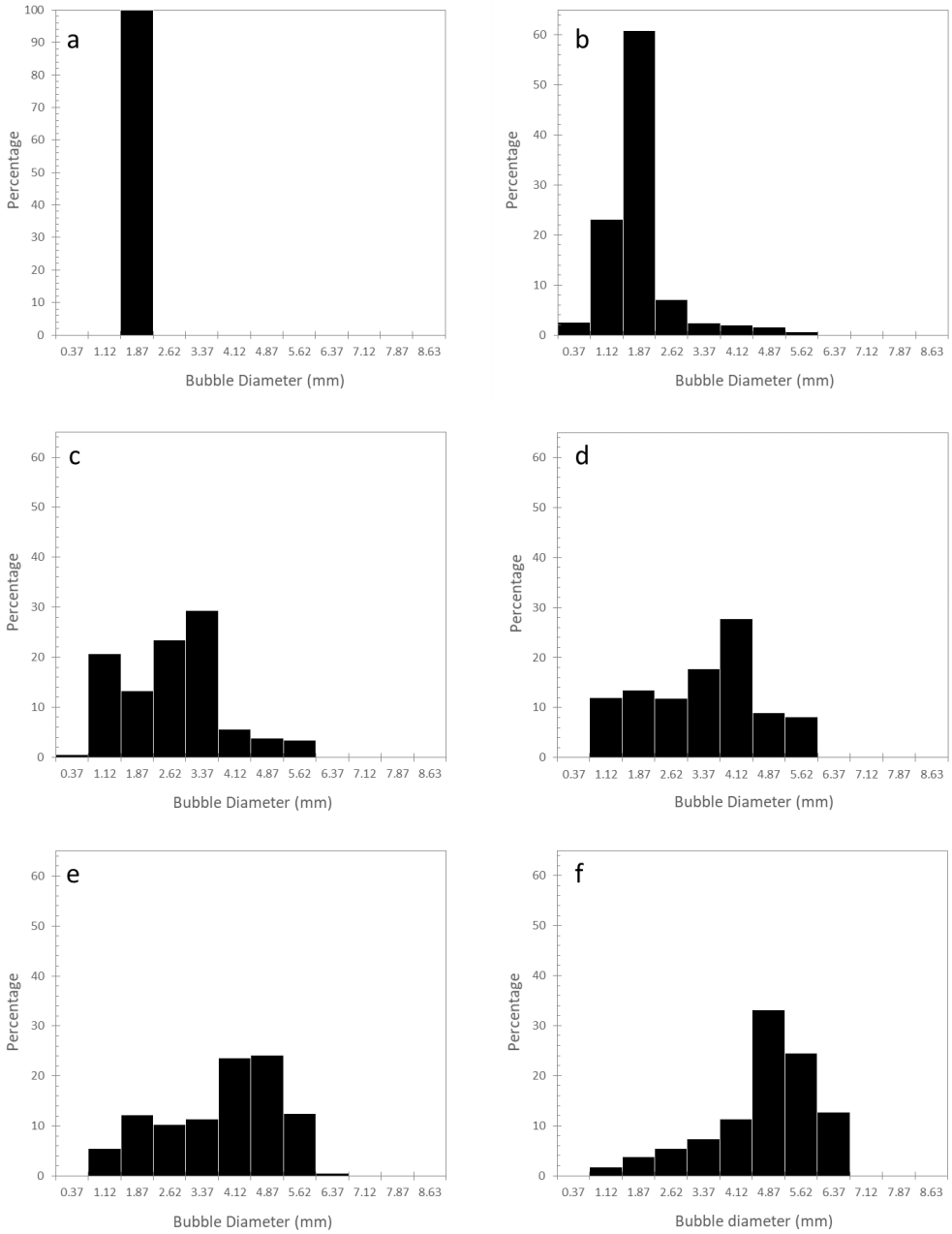

Figure 5-8: Bubble size distributions at horizontal cut-planes of increasing height within the SUT bioreactor at 400 RPM and 0.1 vvm.
a) Inlet, b) 100 mm, c) 250 mm, d) 500 mm, e) 750 mm, f) 1,000 mm.

5.7.2 Mass Transfer Modelling

Five CFD-appropriate models for the mass transfer coefficient, k_L, have been identified from literature, as described in Section 2.2.4. These are evaluated for the 'base case' conditions and compared to experimental $k_L a$ values measured in water using the dynamic method (see Section 2.2.5) by researchers at CPI. Repeated measurements at different locations within the SUT bioreactor fall within the range of 35 to 40 hr^{-1} for the base case

conditions, as represented by the solid lines in Figure 5-9. The dashed lines represent ± 20% of the midpoint of the measured experimental range. The computational results are generated by calculating the volume-averaged $k_L a$ for the entire 1 m^3 geometry and are therefore not necessarily representative of local $k_L a$ values. However, this does provide a good comparison to experimental results generated using the dynamic method, in which the dissolved levels of oxygen are measured within the tank, which will represent a combined effect of oxygen transfer throughout the liquid volume for a well-mixed system, since the dissolved oxygen will be transported by the liquid flow patterns.

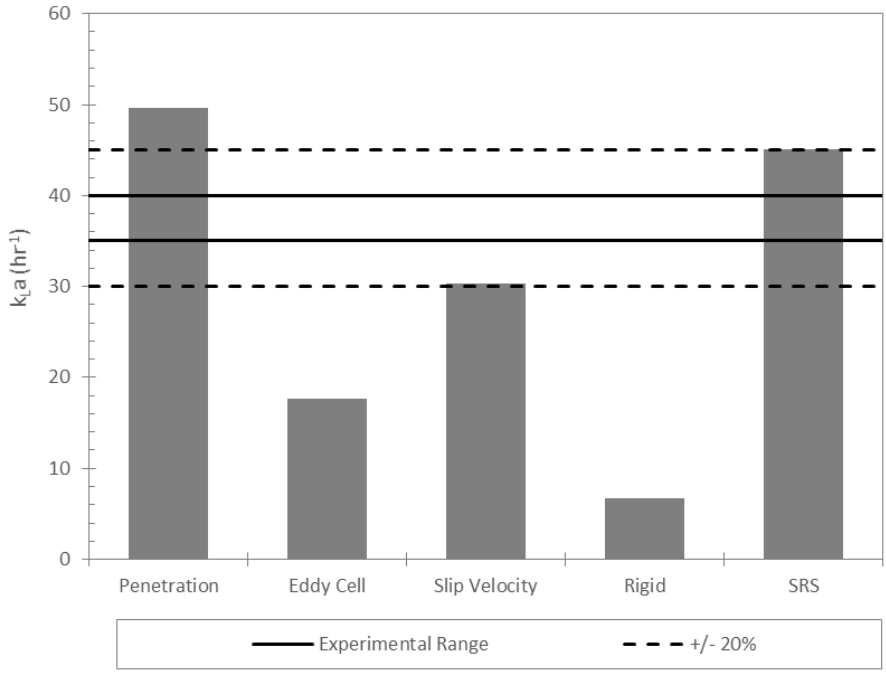

Figure 5-9: Comparison of $k_L a$ values using different mass transfer models with experimental measurements at 400 RPM and 0.1 vvm.

The range of $k_L a$ values predicted by the various mass transfer models is very large, with a greater than seven-times difference between the minimum and maximum predicted values, however the experimental values do fall within the range predicted by the models. The worst fit is provided by the rigid model, which under-predicts the mid-point of the experimental range by 5.6 times. The slip velocity and surface renewal stretch models both predict the $k_L a$ to within ±20% of the mid-point of the experimental range, with the slip velocity model under-predicting and the surface renewal stretch model over-predicting the measured values. The penetration model also provides a reasonably close fit to the 20% limit. Furthermore, the experimental values fall between the limits predicted by the eddy

cell and penetration models, which both have the same form but with different proportionality constants. This suggests that this form of the eddy model may be applicable to computational models of SUT systems with a modified proportionality constant to account for the non-standard design of the bioreactor.

5.7.3 Stirrer Speed Optimisation

In order to better characterise the performance of the bioreactor, a parametric sweep of the stirrer speed has been performed between 0 and 500 RPM, the physical upper limit imposed on the system due to lift generated by the impeller and the risk of magnetic decoupling at high speeds. The aeration rate is maintained at 0.1 vvm, as in the base case previously studied, and the same optimised MUSIG parameters are applied. Each model is initialised from a pre-converged solution and solved using high-resolution (second-order accurate) numerics to the same convergence criteria as the base case model.

The liquid and gas velocity vector plots are shown in Figure 5-10 and Figure 5-11 respectively. The application of the Euler-Euler reference frame means that the two phases occupy different velocity fields, and therefore follow different flow patterns, however they are strongly coupled by the interphase drag force, as seen in the similarity in the major flow features between the phases. Between 0 and 200 RPM, the dominant factor driving the flow is the buoyancy of the gas phase, which leads to a strong upward velocity for each phase at the centre of the tank, where the majority of the gas spargers are located. There is a mild recirculation of the liquid phase within the vessel, with down-flow at the walls to account for the displaced fluid at the centre of the tank. In contrast, there is no appreciable recirculation of the gas phase at lower stirrer speeds, with the gas leaving the domain at the liquid surface, meaning that the residence time of the gas phase in the reactor is low, and therefore the mass transfer is likely to be limited. In contrast, the liquid-phase flow patterns at 300 RPM show a change in the dominant flow feature, with significant radial dispersion at the bottom of the tank caused by the impeller action and strong recirculation close to the impeller. These features become more pronounced as the impeller speed increases, signifying a greater degree of mixing. The gas-phase also shows some recirculation close to the impeller at 400 and 500 RPM. This will help to increase the amount of impeller-bubble interactions, and therefore reduce the bubble size in the lower section of the tank.

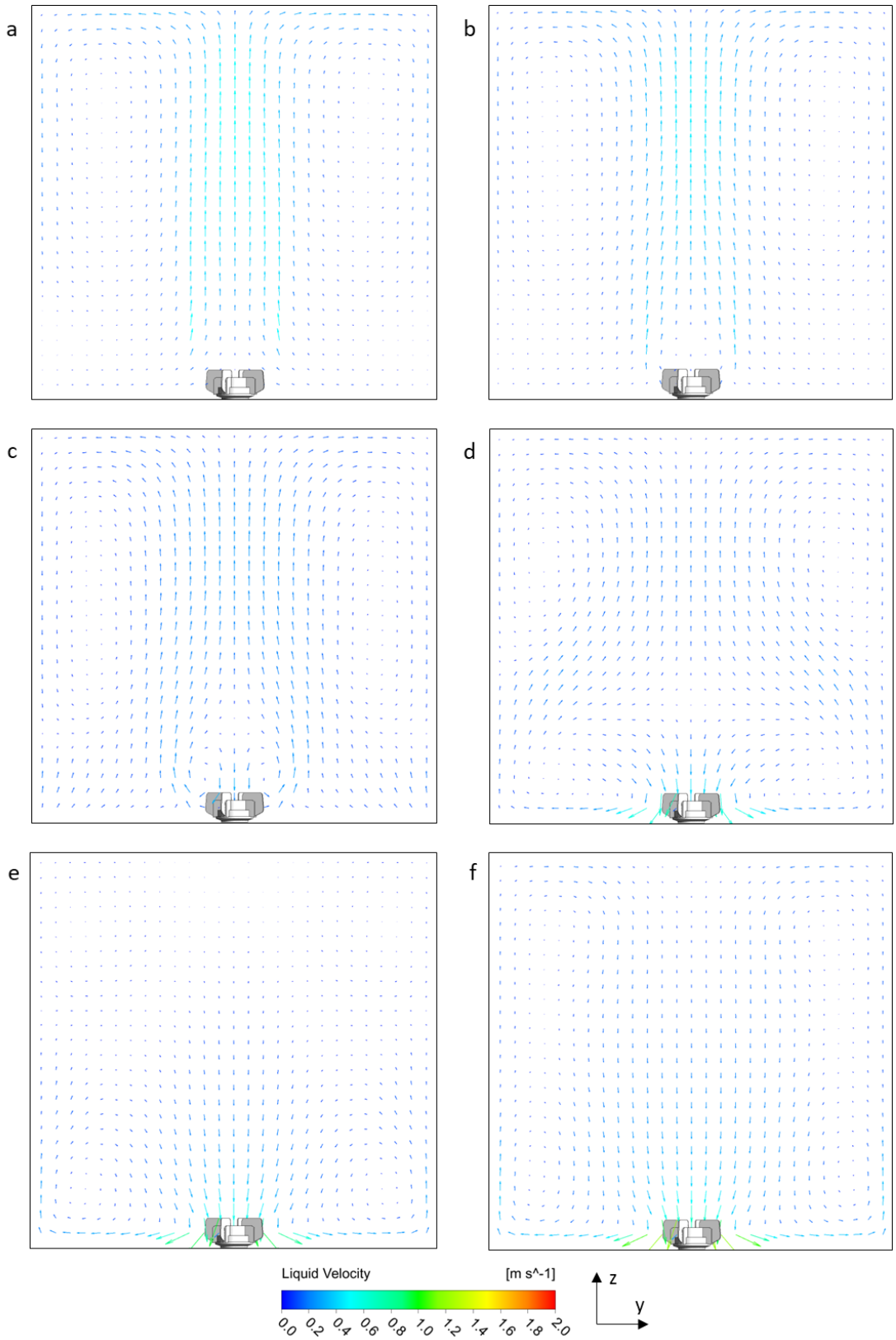

Figure 5-10: Liquid-phase velocity vector plots at a vertical cut-plane through the centre of the SUT bioreactor at increasing stirrer speeds.
a) 0 RPM, b) 100 RPM, c) 200 RPM, d) 300 RPM, e) 400 RPM, f) 500 RPM.

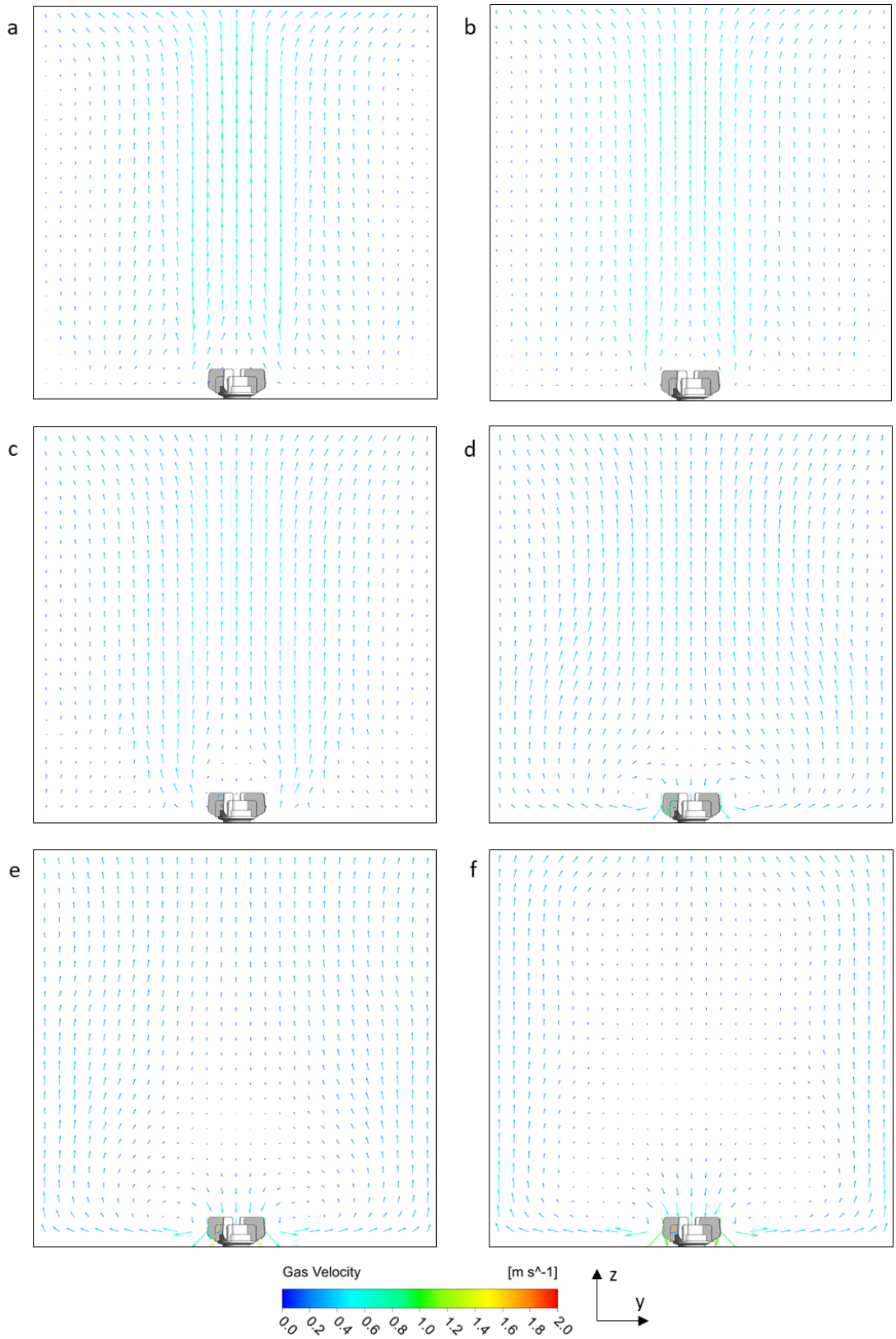

Figure 5-11: Gas-phase velocity vector plots at a vertical cut-plane through the centre of the SUT bioreactor at increasing stirrer speeds.
a) 0 RPM, b) 100 RPM, c) 200 RPM, d) 300 RPM, e) 400 RPM, f) 500 RPM.

The change in dominance between the buoyancy of the gas phase and the influence of the impeller is reflected in the dispersion of the gas phase, as shown in Figure 5-12 across the range of stirrer speeds modelled. At 200 RPM and below, there are large areas of the vessel where there is little to no gas phase present – represented by the dark blue colours on the contour plots – which means that interphase mass transfer will not be occurring in these locations. This increases the likelihood of dead zones developing within the reactor, where the dissolved oxygen is completely consumed by the biomass growing in a location, restricting further growth. In contrast, there is a much more even distribution of the gas phase at stirrer speeds of 300 RPM and above, where the action of the impeller provides high enough radial momentum to overcome the rise of the gas phase and disperse the majority of the gas bubbles from the inner sparger ring radially outwards. This effect increases slightly up to the maximum speed of 500 RPM, with less dark blue visible in the bottom corners and at the walls of the reactor.

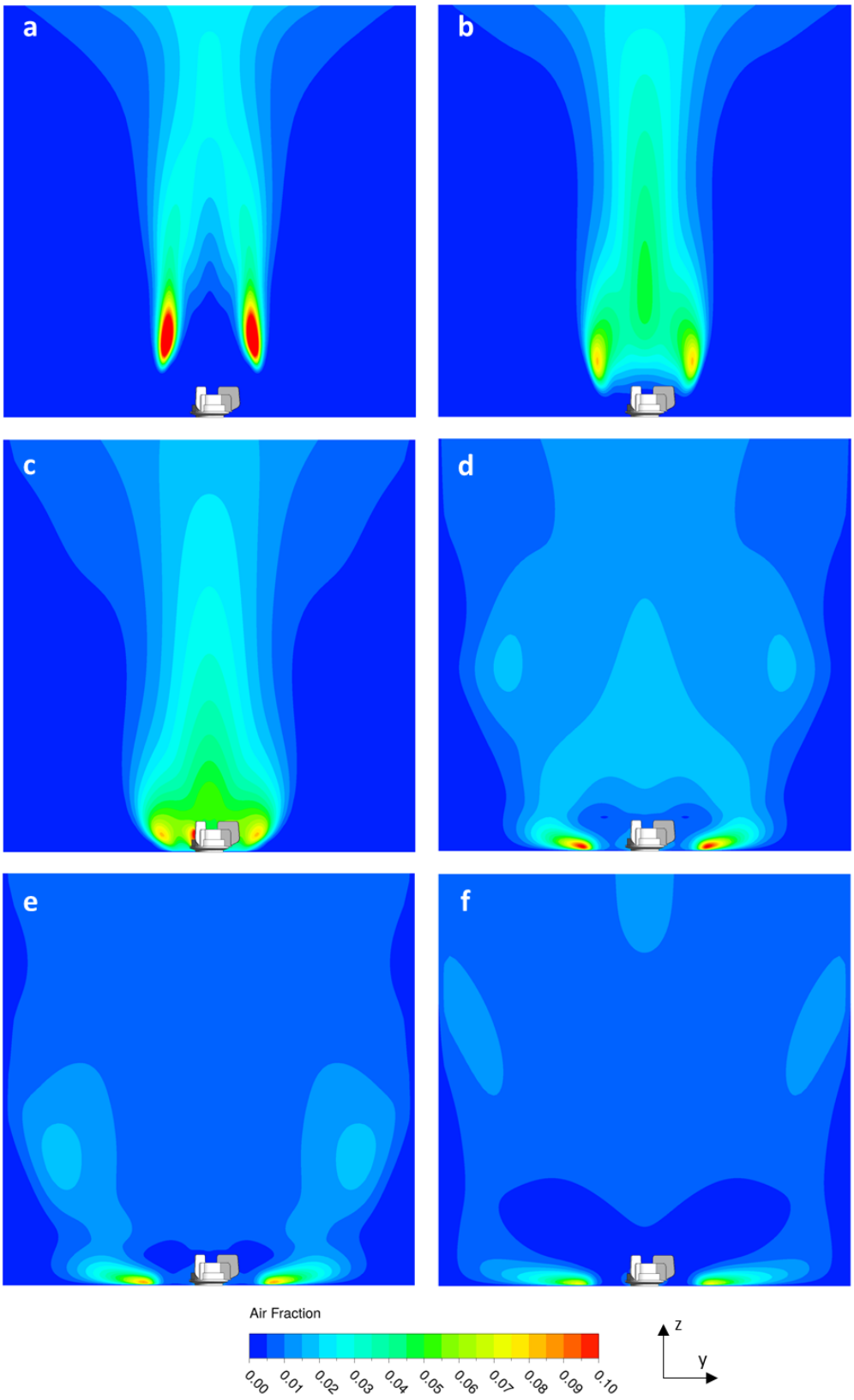

Figure 5-12: Air fraction contour plots for a vertical cut-plane through the centre of the SUT bioreactor at increasing stirrer speeds.
a) 0 RPM, b) 100 RPM, c) 200 RPM, d) 300 RPM, e) 400 RPM, f) 500 RPM.

Equation (4-41) proposes that the breakup of bubbles is dictated by the levels of turbulence in the continuous phase. This can be represented in terms of the turbulent kinetic energy (TKE), the parameter k in the k-ε model, as shown in Figure 5-13 for the different stirrer speeds modelled. Each image in this figure is presented with its own colour bar due to the very different magnitudes of TKE generated under the different conditions. For example, the maximum TKE modelled in the domain at 100 RPM is 0.140 $m^2 s^{-2}$, whereas the same impeller system can generate a maximum TKE of 3.76 $m^2 s^{-2}$ when operating at 500 RPM. For each condition except the 0 RPM case, where the impeller does not influence the fluid flows, the location of the maximum turbulence occurs at the tip of the impeller blades, suggesting that the impeller is the dominant feature influencing bubble break-up. For 0 and 100 RPM, the distribution of TKE throughout the domain is fairly uniform, albeit at a relatively low magnitude. In contrast, the distribution of TKE at stirrer speeds of 200 RPM and above is highly localised to the region close to the impeller. This shows that the influence of the impeller in causing bubble break-up is limited to a relatively small region, and with the distributed gas sparging employed by the BioMOD system it is likely that this effect will not influence the bubble size for the outer sparger ring.

The distribution of bubble sizes for a horizontal cut-plane at half of the filled height for the different stirrer speeds is presented in Figure 5-14. The distribution of bubble sizes between 0 and 200 RPM (Figure 5-14 a-c) show very little variation, covering the same range of bubble sizes and having a similar profile. Only a small proportion of the gas phase has maintained the inlet bubble size, with all other bubbles occupying larger size groups, showing that bubble coalescence is a significant factor within the BioMOD reactor. Figure 5-14 d) shows that the distribution at 300 RPM is much more weighted towards the smaller bubbles, with around 40% of the bubble population occurring within the first three size groups. At higher stirrer speeds, the distribution of bubble sizes is further weighted towards the smaller groups, with relatively few bubbles in size group seven and above, suggesting that further increasing the impeller-induced turbulence can lead to significant bubble size reductions. Furthermore, the increased distribution of the gas phase at higher stirrer speeds means that the potential for coalescence of the air bubbles is reduced due to the reduced chance of bubble collisions, as required by equation (4-44). However, in all profiles there is a large proportion of bubbles with diameters greater than the inlet size, which is expected to increase with height within the tank due to further bubble coalescence.

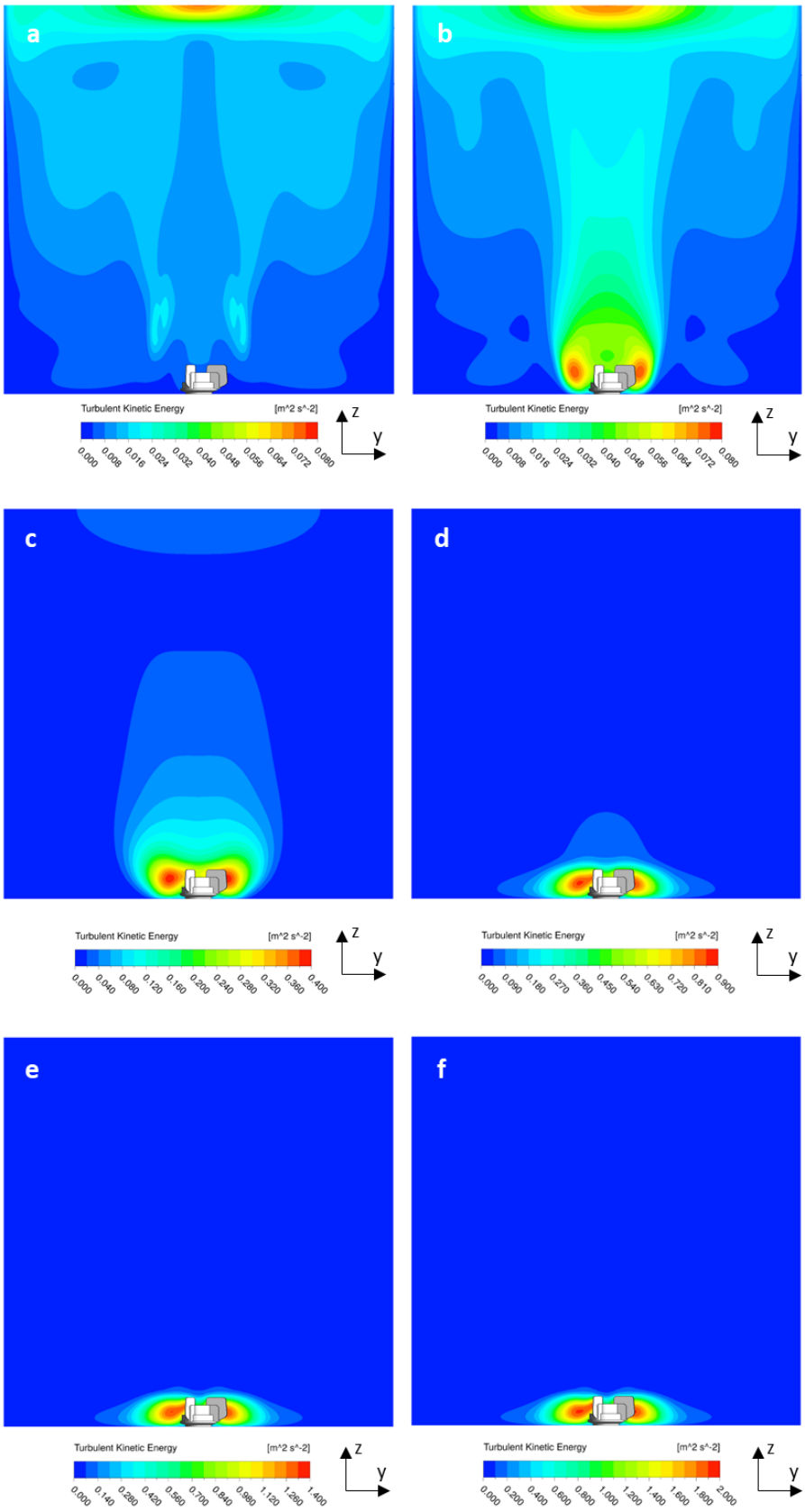

Figure 5-13: Liquid-phase turbulent kinetic energy contour plots for a vertical cut-plane through the centre of the SUT bioreactor at increasing stirrer speeds.
a) 0 RPM, b) 100 RPM, c) 200 RPM, d) 300 RPM, e) 400 RPM, f) 500 RPM.

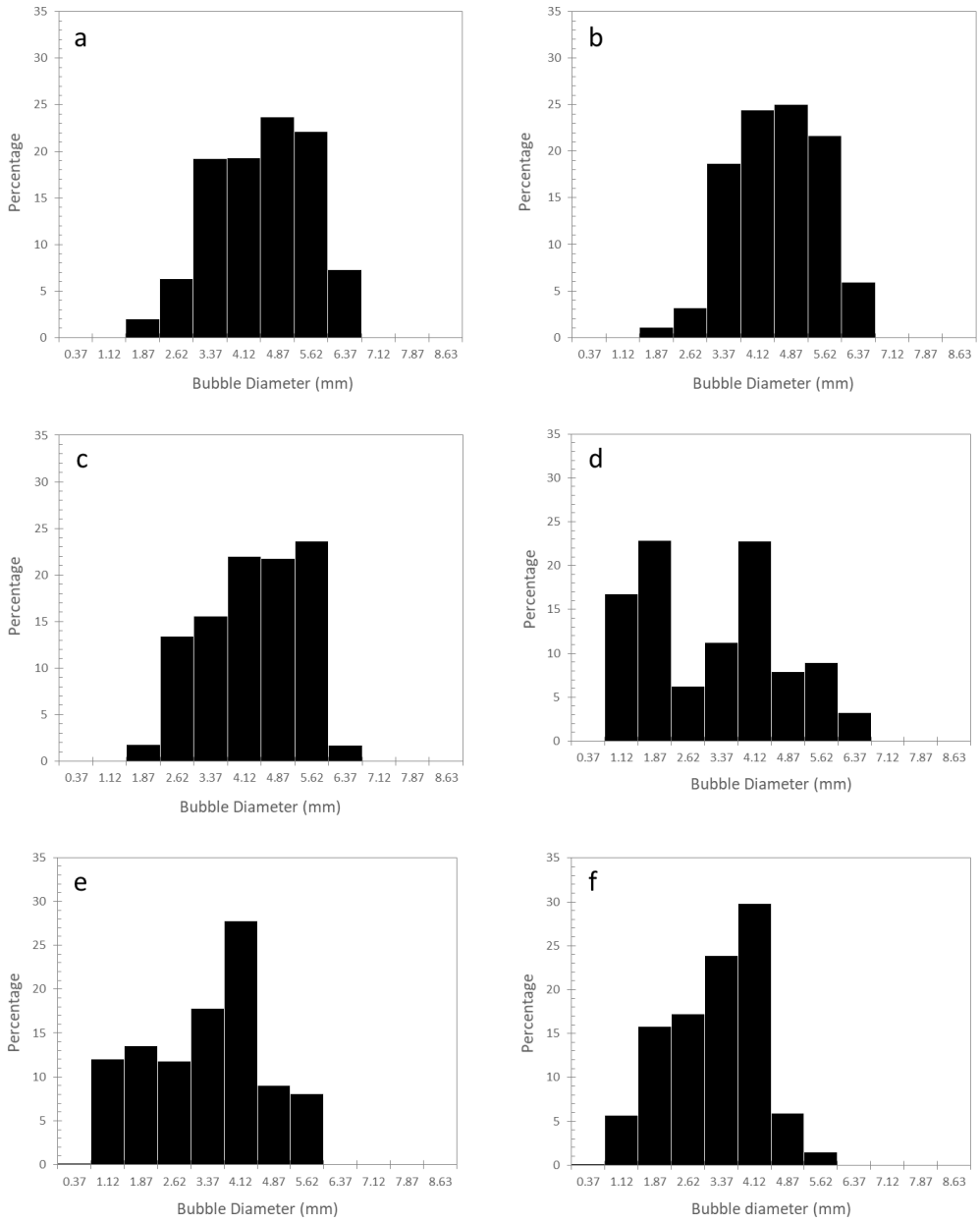

Figure 5-14: Bubble size distribution for a horizontal cut-plane at a height of 500 mm for different stirrer speeds and an aeration rate of 0.1 vvm.
a) 0 RPM, b) 100 RPM, c) 200 RPM, d) 300 RPM, e) 400 RPM, f) 500 RPM.

The combined influence of the improved gas distribution, hydrodynamic conditions and reduced bubble size leads to an increase in the volume averaged $k_L a$ with stirrer speed for all of the mass transfer models previously evaluated, as shown in Figure 5-15. Each model presents a similar trend, with an approximately linear increase in $k_L a$ between 100 and 500 RPM. This means that despite the relatively small impeller-to-tank size ratio and distributed air sparging, the impeller action is able to generate significant improvements in interphase mass transfer. The order of the different models with regard to the average $k_L a$ remains

largely unchanged across the range of stirrer speeds, with only the penetration and surface-renewal-stretch models switching order at 200 RPM. The penetration and eddy cell models, which share the same form with different proportionality constants, show a steeper relative increase between 100 and 200 RPM when compared to the other models, however the gap between all of the different models remains largely unchanged across the range.

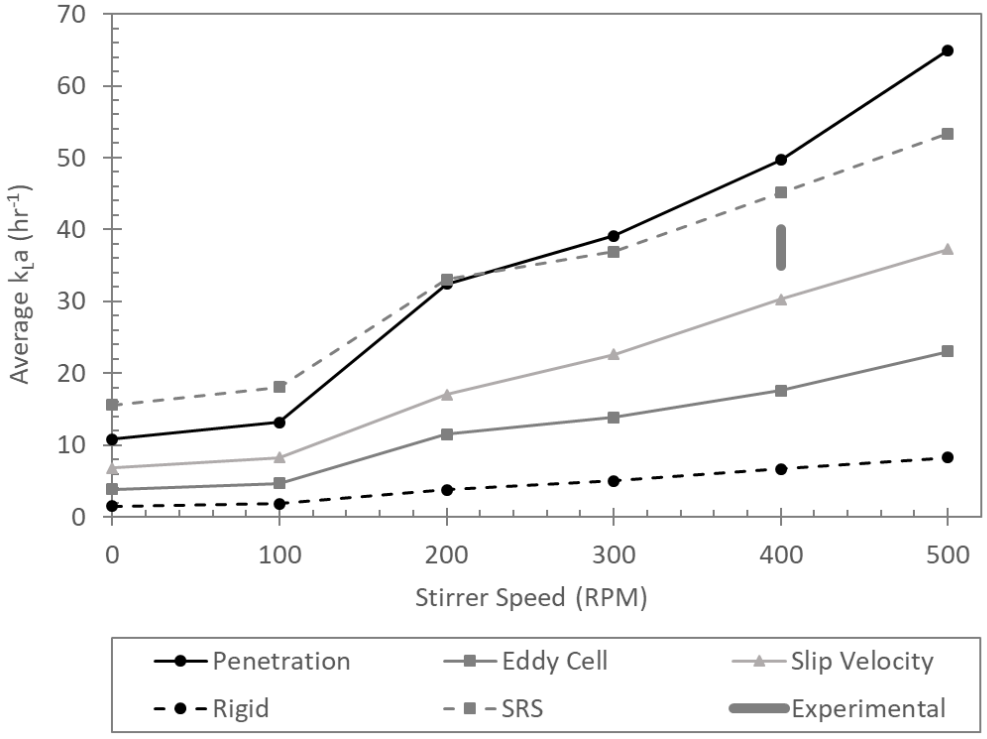

Figure 5-15: Volume-averaged $k_L a$ values between 0 and 500 RPM stirrer speed for different mass transfer coefficient models.

The values presented in Figure 5-15 represent the volume-averaged values of the combined term $k_L a$, which is representative of the values that can be easily determined through experimental techniques, and therefore provides a useful method for evaluating different models and conditions. However, using CFD modelling it is also possible to explore the individual influence of the terms k_L, the mass transfer coefficient, and a, the interfacial area, at various locations throughout the reactor. Figure 5-16 provides a detailed comparison of how the $k_L a$ and k_L values are distributed within the reactor volume for the slip velocity (left) and penetration (right) models for the 'base case' conditions. The variation in $k_L a$ profiles between the models is large when compared to the work of Gimbun et al. (2009), where the same models are compared for traditional 14 and 200 L baffled stirred tanks. It is proposed that these designs have a much more even distribution of turbulence throughout the reactor volume when compared to the BioMOD reactor due

to the size and location of the impeller. For the BioMOD reactor, the $k_L a$ is highest close to the floor-mounted impeller for both models (Figure 5-16 a), where the highest levels of turbulence are generated. The shape of the $k_L a$ contours for each model approximately match the outline of the gas fraction contours (Figure 5-7), however the magnitude of the $k_L a$ for the slip velocity model is greater throughout the bulk of the reactor volume.

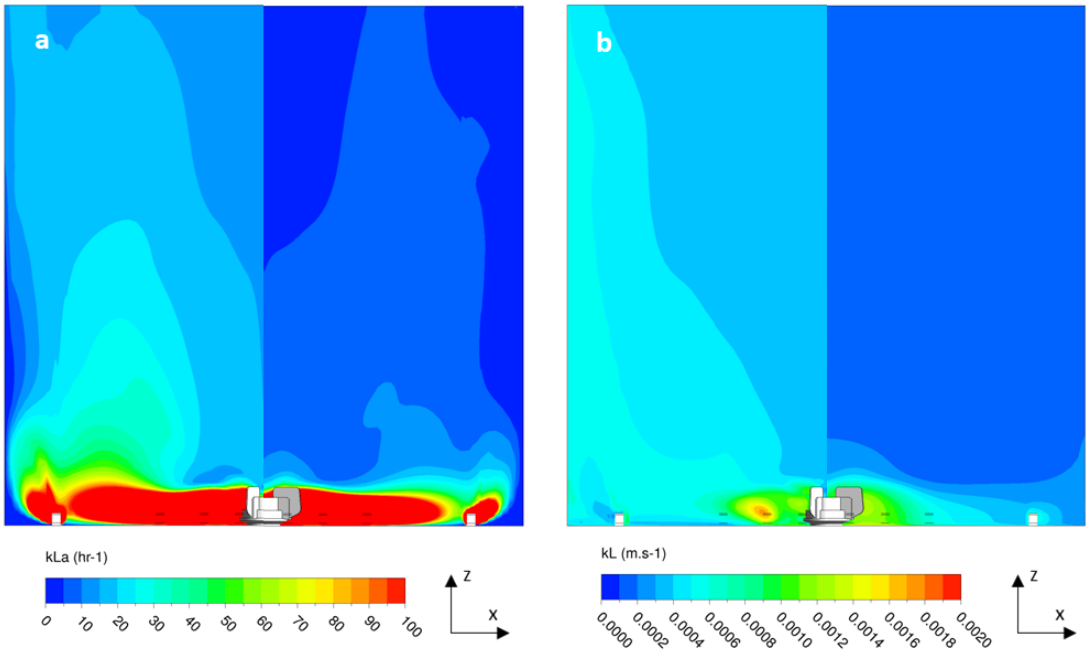

Figure 5-16: Comparison of contour plots for the slip velocity (left) and eddy cell (right) mass transfer models at a central cut-plane.
a) $k_L a$ (range limited to 100 hr^{-1}), b) k_L.

The difference between the two $k_L a$ plots for the different models is due to the distribution of k_L values within the reactor volume, which are isolated in Figure 5-16 b). These are based solely on mixing parameters, and therefore do not directly depend on the local air fraction. As seen in the $k_L a$ profiles, the mass transfer coefficient for the eddy cell model (right) is much more localised around the impeller than the slip velocity model (left). This is because the eddy cell model is based upon the turbulent eddy dissipation, which like the TKE is highly weighted towards the impeller at higher stirrer speeds. In contrast, the slip velocity is dependent upon the difference in velocity between the liquid and gas phases. Whereas this is also very high close to the impeller, where large velocity gradients are generated, there is also a significant slip velocity throughout the reactor due to the buoyancy-driven flow of the dispersed phase.

The order of the magnitude of the slip velocity and eddy cell models in this study is reversed from the findings of Ranganathan and Sivaraman (2011) for a multi-impeller system. Such designs have a much more even distribution of turbulence throughout the vessel, leading to higher predictions using the eddy cell model than have been predicted in this study. However, the shape of the $k_L a$ distribution is still similar between the two cases, regardless of the magnitude of the $k_L a$. This is in contrast to the k_L values presented in Figure 5-16 b), which shows that the slip velocity predicts a higher k_L throughout the majority of the vessel. This is because the majority of the turbulent energy imparted to the liquid phase in the non-standard geometry modelled here occurs in the region close to the impeller, making this region critical to the eddy cell model. Unlike the traditional stirred tanks studied by Gimbun et al. (2009) and others, there are large regions where the slip velocity between the two phases is more significant than the eddy dissipation, since the impeller action is confined to a small area of the reactor. Therefore, this suggests that it is necessary to include non-standard systems when evaluating different mass transfer models for stirred tanks to ensure that selected models are appropriate in multiple flow regimes.

The relative dependence of the overall $k_L a$ values on the individual values of k_L and a is compared between 0 and 500 RPM in Figure 5-17 for a volumetric aeration rate of 0.1 vvm. Both of the mass transfer models show a very flat profile in comparison to the specific area, with the slip velocity model showing a step-change between 200 and 300 RPM where the gas distribution significantly improves, increasing the proportion of the tank where a slip velocity may exist. In contrast, there is very little change in the volume-averaged mass transfer coefficient for the eddy cell model despite the wide range of hydrodynamic conditions previously presented. This may be exaggerated by the BioMODULE design since the turbulence parameters for the majority of the tank are largely unaffected by the impeller action. This means that the $k_L a$ profiles presented are predominantly a result of the increasing interfacial area – influenced by a greater gas holdup and reduced bubble size – with stirrer speed.

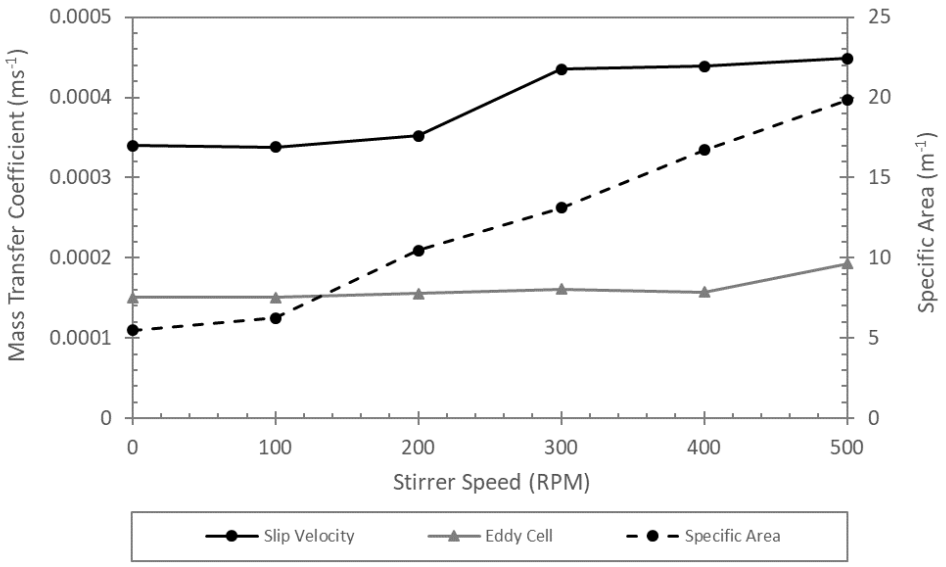

Figure 5-17: Comparison of modelled k_L values for the slip velocity and eddy cell models and the specific interfacial area at stirrer speeds of 0 to 500 RPM.

Due to the strong dependence of the mass transfer rate on bubble size rather than hydrodynamic conditions suggested by Figure 5-17, it is proposed that very high $k_L a$ values may be achieved by introducing very small air bubbles to the domain, regardless of the stirring conditions. This hypothesis has led to the investigations in Chapter 7, where the mass transfer potential of microbubbles has been explored with a long-term view to their applicability for bioprocessing applications such as the BioMOD reactor, as an alternative to mechanical agitation.

5.7.4 Aeration Rate Optimisation

The volumetric aeration rate supplied to the BioMOD reactor is currently limited to approximately 0.1 vvm by the candle sparger system, however CFD modelling can be used to predict the mass transfer performance of the reactor under different aeration conditions that would require a modification of the sparging system to achieve experimentally. For this analysis, the aeration rate is varied between 0.025 and 0.2 vvm (25 to 200 L min^{-1}) for a fixed stirrer speed of 400 RPM. The distribution of the gas phase within the reactor is presented in Figure 5-18 for the different aeration rates. Each contour is presented alongside its own colour bar, since the magnitude of the local volume fraction is highly dependent on the inlet aeration rate. Despite this, the distribution of the gas phase between the different aeration rates is very similar, suggesting that the impeller action remains the dominant force influencing the flow patterns throughout the range studied.

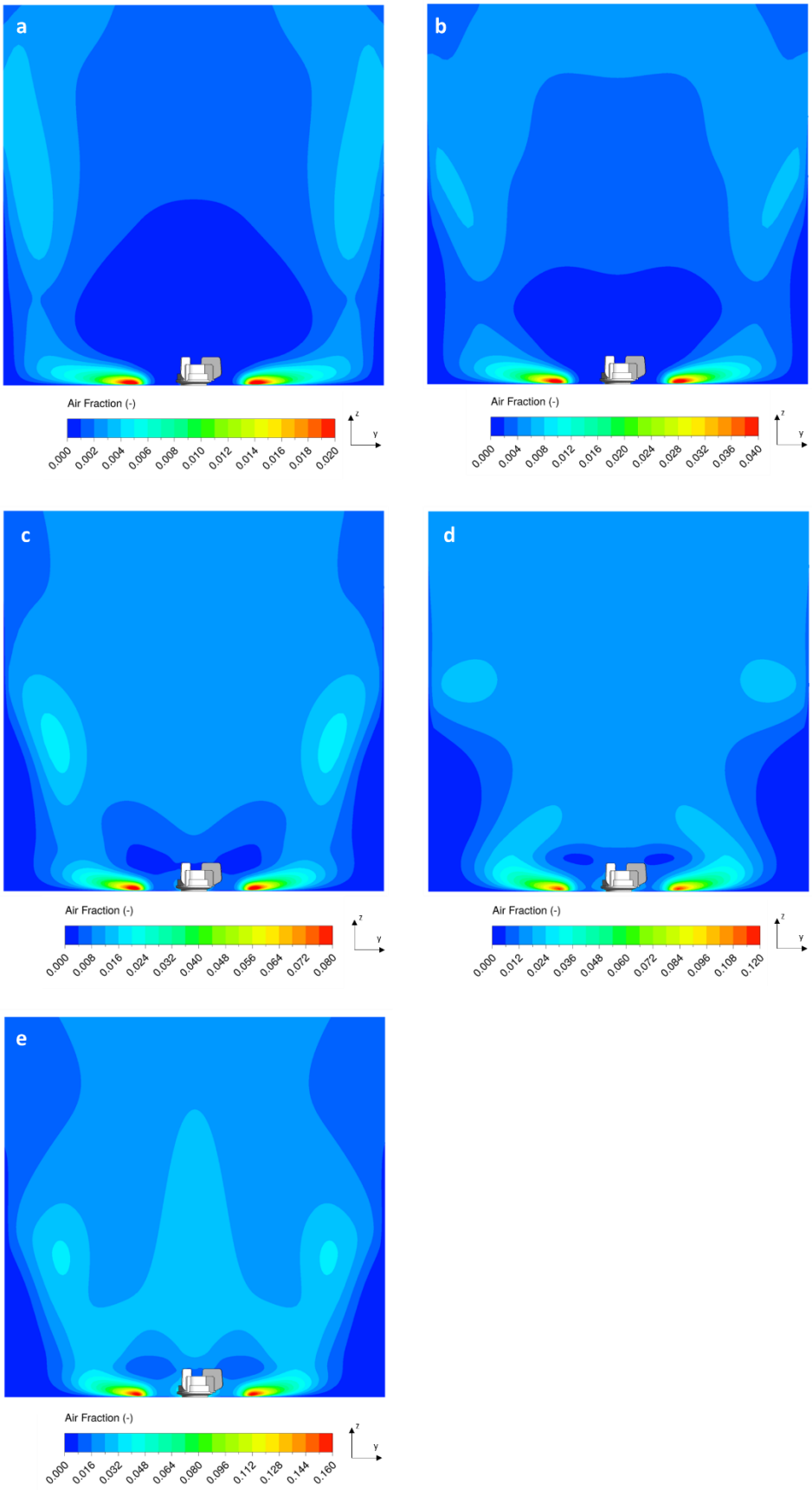

Figure 5-18: Air volume fraction contour plots for a vertical cut-plane through the centre of the SUT bioreactor at increasing aeration rates.
a) 0.025 vvm, b) 0.05 vvm, c) 0.1 vvm, d) 0.15 vvm, e) 0.2 vvm.

The distribution of bubble diameters within the BioMOD reactor across the same range of gas flow rates is shown in Figure 5-19. For the higher aeration rates, the maximum bubble size within the fluid domain increases as the chance of bubble collisions is increased. The distribution of bubble sizes shows the effect of bubble coalescence is dominant within the majority of the reactor, with the dark orange and red colours occurring towards the top of the cut-plane at higher aeration rates. Similarly, there is a relatively localised region close to the impeller where the bubble size remains very small for all conditions due to the action of the impeller in promoting bubble break-up.

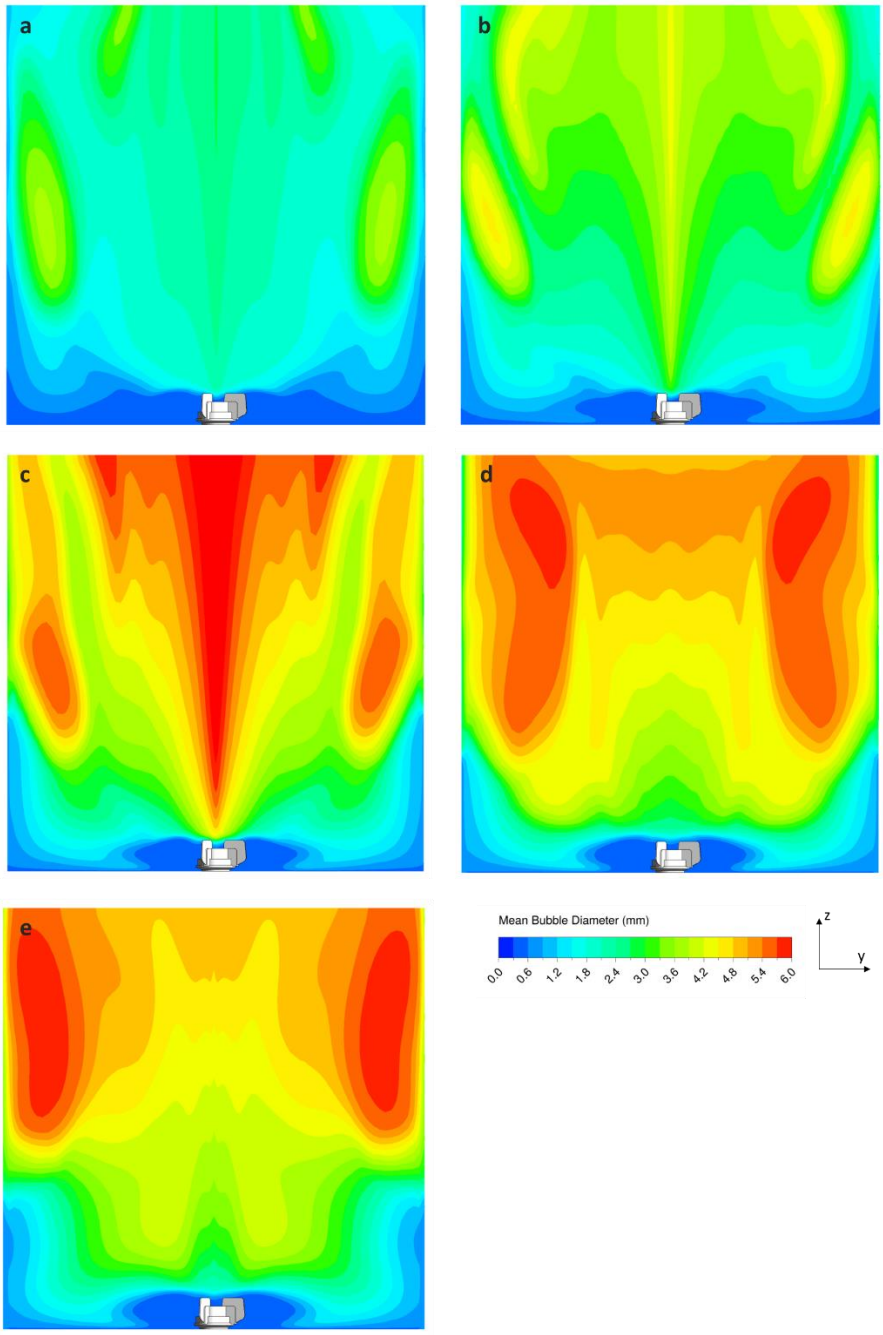

Figure 5-19: Mean bubble diameter contour plots for a vertical cut-plane through the centre of the SUT bioreactor at increasing aeration rates.
a) 0.025 vvm, b) 0.05 vvm, c) 0.1 vvm, d) 0.15 vvm, e) 0.2 vvm.

The volume averaged $k_L a$ for a range of air flow rates between 0.025 and 0.2 vvm is compared in Figure 5-20 for the mass transfer models previously considered. Each of the models shows an approximately linear increase in volume-averaged $k_L a$ with aeration rate across the modelled range, despite the increased levels of bubble coalescence at higher aeration rates. As with the stirrer speed optimisation, there is no significant change in the

order or shape of the curves for the different models between the different aeration conditions. Stirred industrial fermenters are can be operated with a volumetric aeration rate of 1 vvm or higher (Doran, 1995), which means that there is a greater volume of gas available for mass transfer to take place. Extrapolating the results for the eddy cell model linearly from the points presented in Figure 5-20 means that the $k_L a$ could be increased as high 148 hr^{-1} by using similar vvm values, however this assumes a linear trend may exist far in excess of the modelled range, whereas a physical maximum is expected to exist due to changes in the bubbling regime. Furthermore, it would require a significant redesign of the spargers and tubing system in order to accommodate the vastly increased air flow rate, and higher running costs to facilitate the increased gas supply.

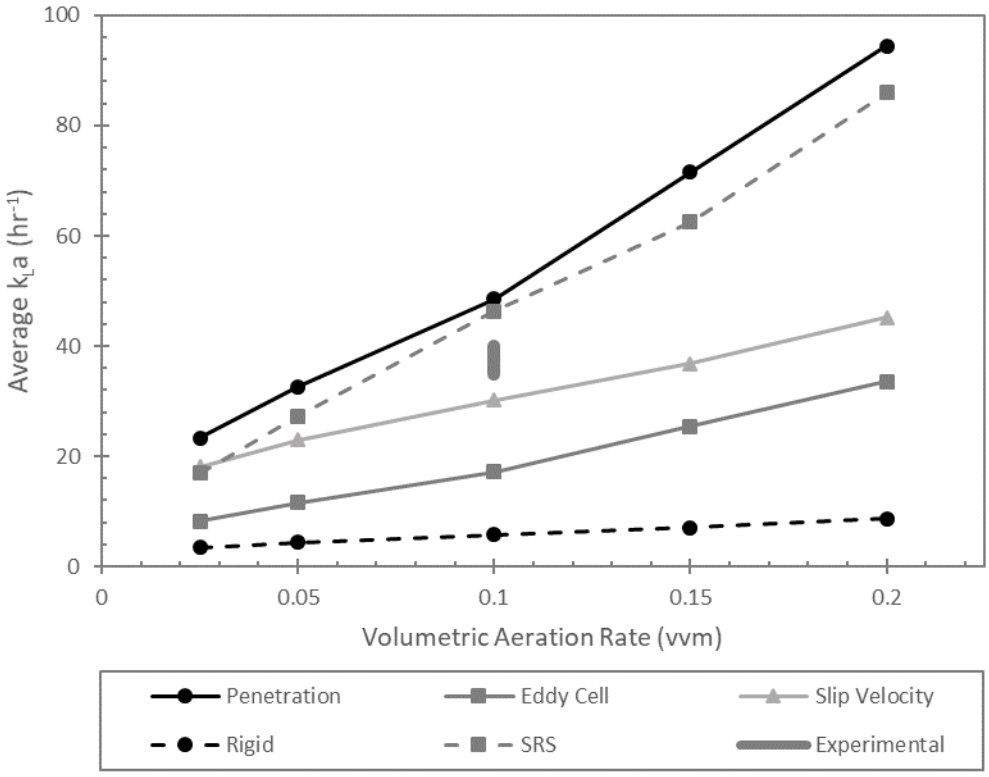

Figure 5-20: Volume-averaged $k_L a$ values between 0.025 and 0.2 vvm aeration rate for different mass transfer coefficient models.

5.8 Summary

This chapter has detailed the development of a steady-state CFD model of a novel 1,000 L single-use-technology bioreactor, which has been developed and operated as part of a wider industrial consortium. The design incorporates a cubic geometry with a floor-mounted magnetically driven impeller and distributed gas sparging through porous spargers at 14 individual locations across the tank floor. This means that the hydrodynamic characteristics of the reactor are not well understood, and cannot be approximated using existing correlations. The model developed uses a novel application of the immersed solid method for modelling the motion of the impeller, which significantly simplifies the mesh and increases the solver stability with minimal influence on the results due to limited interactions between the gas phase and the impeller blades in the design studied. Turbulence is modelled using the k-ε turbulence model, with the Ishii-Zuber model identified at the most suitable for the interphase drag force. The bubble size distribution is modelled using the multiple size group (MUSIG) model due to the importance of accurately defining the bubble size on mass transfer. The specified values of the bubble size range and the number of size groups has been optimised for the modelled system.

The CFD model has been solved for a range of different stirrer rotational speeds and air flow rates based upon the conditions achievable in the operational vessel, and covering a wide range of operating regimes. Analysis of the flow patterns, gas distribution and the bubble size distributions show that there is significant bubble breakup caused by the action of the impeller at rotational speeds of 300 RPM and above, which causes the gas phase to be dispersed throughout the whole of the vessel. In contrast, the buoyancy effect of the gas phase causes the gas bubbles to rise directly to the liquid surface at speeds of 200 RPM and below, with little influence of the impeller action on the gas distribution or flow patterns. Increasing the air flow rate above the currently used maximum value of 0.1 vvm is predicted to significantly improve the mass transfer rate, with typical stainless steel fermenters often operating at higher aeration rates, however this is likely to require a re-design of the current sparging system.

The mass transfer of oxygen from the gas to the liquid phase is characterised in terms of the parameter $k_L a$, which is a combination of the liquid-phase mass transfer coefficient, k_L, and the specific interfacial area, a. Five different models for k_L have been identified and compared with experimental measurements made by researchers at CPI under ‘base

case' operating conditions of 400 RPM stirrer speed and 0.1 vvm aeration rate. The experimental values fall within the range of values predicted by the different models, however the spread of predicted values is very large. The best fit to the experimental data was achieved by the slip velocity, penetration and surface renewal stretch models, which under and over-predict the measured range of values by a similar amount (±20%). These models are calculated from different parameters such as liquid and gas phase velocity or turbulence parameters, and the fact that the measured values fall within the range predicted by these models suggests that the CFD model is predicting multiple parameters with reasonable accuracy. Separating the values of k_L and a from the model under different stirring conditions shows that the specific interfacial area, which is dependent on the gas volume fraction and the bubble size, is by far the most significant factor in changing the modelled $k_L a$ with different stirring conditions.

6 Validation of the BioMODULE Model

Due to the limited access to take measurements within the 1,000 L BioMOD reactor, multi-parameter validation of the CFD models applied to the BioMOD reactor in Chapter 5 has been performed at the laboratory scale. The work presented in this chapter is not a like-for-like recreation of the BioMOD setup, rather it is intended to provide conditions that are sufficiently similar to the BioMOD system to provide comparable environments, whilst also producing data for validation across a wide range of different flow regimes. The range of stirrer speeds used is therefore selected based on the flow regimes observed in the validation tanks, rather than attempting to scale-down the conditions within the BioMOD reactor. This validation is based on multiple parameters, namely the liquid-phase velocity, gas dispersion, bubble size and mass transfer rate across a range of stirrer speeds. Performing experimental validation against several parameters and under different flow regimes ensures that several of the significant model outputs can be evaluated, giving a greater degree of confidence in the model applied to the BioMOD system than for single parameter validation. This chapter will also allow for the ability to comment on the applicability of the selected models at different scales of size and for different flow regimes, and therefore the universal applicability of the model for scale-up and scale-down applications can be assessed.

6.1 Introduction

As identified in Table 2-2, there is a wide range of different techniques that have been applied to measure the liquid-phase velocity in stirred tank systems. From the options compared in Section 2.2.5, two-dimensional back-scattering LDV is selected as the most appropriate method for measuring the liquid-phase velocity profiles for the validation experiments presented in this chapter, due to the relatively modest equipment requirements to extend the system to two-phase flow. The operating principles of backscattering LDV are shown in Figure 6-1 (Dantec Dynamics, n.d.). For each velocity component (x, y, z coordinates) measured, two intersecting laser beams, one with a slightly shifted wavelength, are transmitted from the optical probe so that they intersect at a location within the flow known as the measurement volume. The intersection of the two beams causes an interference pattern consisting of a series of parallel lines with known spacing of d_f, the fringe spacing, which can be calculated from the wavelength, λ, and the angle between the intersecting beams, θ, using equation (6-1).

$$d_f = \frac{\lambda}{2sin\,\frac{\theta}{2}} \tag{6-1}$$

The flow is seeded with a small sample of reflective, neutrally buoyant seeding particles. When a seeding particle passes through the measurement volume, the fringe pattern will be reflected back to the transmitting optics at a much lower intensity, where it is detected by the transmitting optics with a shifted frequency due to the Doppler effect, known as the Doppler frequency, f_d. The detected signal is transmitted via fibre optic cables to a signal processing unit and computer where it is processed to identify individual particle velocities. The component velocity of each particle passing through the measurement volume can be calculated using equation (6-2). A time-averaged velocity measurement is obtained by averaging the velocity measured for a large number of individual particles, the number of which may vary depending on the application and will be optimised for the validation tank as part of this work.

$$u = f_d d_f = f_d \frac{\lambda}{2sin\,\frac{\theta}{2}} \tag{6-2}$$

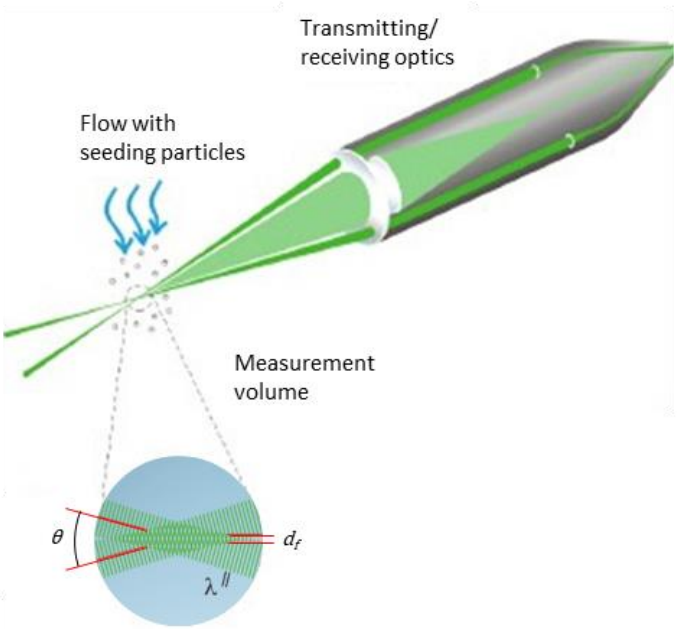

Figure 6-1: Principles of LDV measurements. Adapted from (Dantec Dynamics, n.d.).

For early two-phase models, the definition of the bubble size was typically limited to a single fixed value, or correlations such as the bubble number density, however as computing capability increased, population balance modelling became the preferred option. This provides a distribution of bubble sizes present in the stirred tank, and therefore an additional parameter for which model validation may be performed. The measurement of bubble sizes in stirred tanks has been achieved using a number of invasive and non-invasive techniques as summarised in Table 2-2. In addition, several bubble sizing techniques have been used to approximate the bubble size distribution based upon image processing techniques. These require the user to be able to take clear, well lit images, and are thus largely limited to relatively narrow, clear-walled experimental apparatus with a high level of access to take images. Early implementations of image analysis for bubble sizing required the manual identification and characterisation of individual bubbles such as Zhou et al. (1993), requiring a large amount of time and labour. More recently, computational image processing has been applied to identify bubbles in predominantly backlit flows. For example, Mena et al. (2005) used a threshold method to identify the dark outline and light centre of the in-focus gas bubbles, however there was no distinction made between individual bubbles and bubble clusters, limiting the applicability to relatively low gas fraction applications.

The identification of individual bubbles can be made using shape identification algorithms, which identify the ellipsoidal shape that is typical of rising bubbles (Zaruba et al., 2005; Bröder and Sommerfeld, 2007; Prakash et al., 2012). Shape identification algorithms can also be combined with a breakpoint technique to reconstruct the overlapping sections of clustered ellipsoidal bubbles (Honkanen et al., 2005; Honkanen, 2009), thus predicting the area of a bubble that has been obscured by other bubbles, reducing the risk of under-predicting the bubble size. A further method of bubble sizing through image analysis uses the watershed algorithm proposed by Meyer (1994). This technique identifies the dark regions created by the presence of bubbles as local minima in the light intensity of the image, and applies a catchment basement technique to capture the bubble volumes by ‘filling’ these basins from the bottom up, as shown in Figure 6-2. The bubble is segmented by the boundaries created between the basin regions as shown in Figure 6-2 c). Bubble sizing using watershed algorithms has previously been successfully applied to highly clustered gas-liquid flows (do Amaral et al., 2013; Lau et al., 2013; Karn et al., 2015).

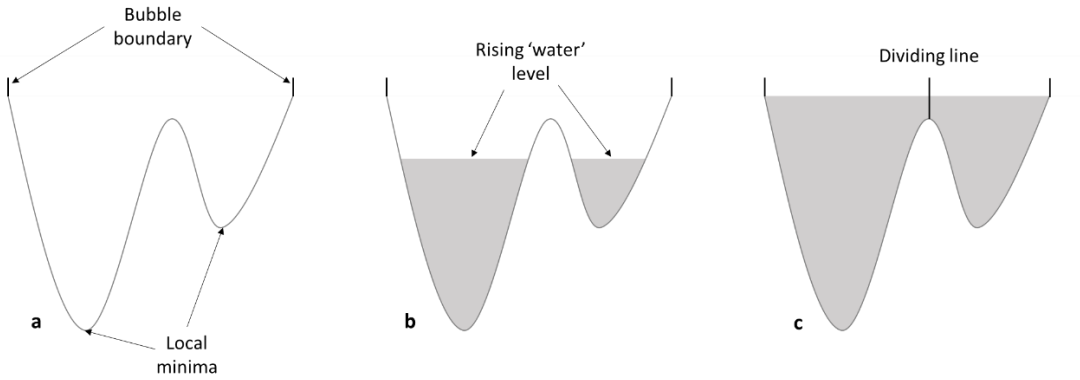

Figure 6-2: Representation of the basin filling technique applied during the watershed algorithm. a) bounded shape, b) partially filled basins, c) segmented basin system.

Some more complex bubble sizing algorithms differentiate between individual and clustered bubbles, applying different analysis techniques to each as appropriate. Ferreira et al. (2012) used the complexity of the shape as a way to classify bubble clusters, but did not attempt to divide the clustered bubbles. Fu and Liu (2016) extended this concept by applying a separate sizing algorithm to the bubble clusters, which uses a complex hybrid of breakpoint analysis, ellipse fitting and watershed segmentation to produce a robust sizing algorithm that is applicable to a wide range of gas fractions. A comparison of the different segmentation abilities of several of these techniques applied to images of overlapping bubbles is also presented by Fu and Liu (2016). The watershed method is noted to accurately identify and maintain the original outline of the bubble, making it a suitable choice for highly deformed bubbles. However, the bubble area obscured by overlapping bubbles is not well captured since the segmentation is achieved by splitting the outline generated by the bubble cluster. Another issue often encountered using the watershed method is oversegmentation of the background image, where background noise is identified as a local minima, and this is often overcome by applying an H-minima criteria so that only minima below a specified depth are accepted (Karn et al., 2015). This may, however, lead to the omission of smaller bubbles from the final analysis.

6.2 Experimental Procedures

Validation experiments are performed in a 9.4 L glass tank, which allows for a high level of access to take measurements and observations of the fluid dynamic behaviour occurring within the tank. The base of the tank is a 228.6 mm × 228.6 mm square, with a filled height of 180 mm to give the same filled volume as a traditional Rushton turbine with a diameter of 228.6 mm. Stirring is provided by a Rushton impeller with a diameter of 76.2 mm, one

third of the tank width, and mounted one impeller diameter from the bottom of the tank. Atmospheric air is sparged into the tank via a variable flow rate pump (H_2O 120) directly below the impeller through a cylindrical sintered metal porous sparger at flow rates of up to 2 $Lmin^{-1}$. The sparger has a length of 10 mm and a diameter of 7 mm, and is mounted horizontally and parallel to the front and rear tank walls.

6.2.1 Laser Doppler Velocimetry (LDV)

Back-scattering LDV is used to measure the liquid-phase flow patterns within the validation tank. The LDV system (TSI Instruments Ltd) uses a 400 mW class 3b argon laser (Melles Griot) to produce a single laser beam, which is split into four distinct beams of 514.5 and 448.0 nm using a Fibrelight beam splitter, and one beam of each wavelength is slightly shifted using a Bragg cell. The split beams are focussed onto fibre optic cables, which transfer the beams to a TSI TR260 transmitting and receiving optics probe, where the beams are projected into the liquid flow to form a measurement volume at the point where they intersect. The returning signals are detected by the receiving optics. The signal is transmitted to a photodetector module (PDM 1000) and signal processor (FSA 3500) which identifies valid data hits and calculates the velocity of each detected particle, which is logged on a computer using the Flowsizer (v1.1.0.0) software.

Prior to starting the measurement, the tank is filled to the desired level with deionised water and seeded with a small amount of neutrally buoyant 32 µm spherical glass beads (Blagden Speciality Chemicals) to seed the flow. The transmitting and receiving optics probe is mounted on a horizontal platform connected to a motor-driven x-y traverse, which is used to move the measurement volume by a known distance within the fluid. By moving the measurement volume in either one or two directions, the LDV apparatus can be used to build up a velocity field as a one-dimensional profile or a two-dimensional plane. A picture of the apparatus used for the LDV measurements is presented in Figure 6-3.

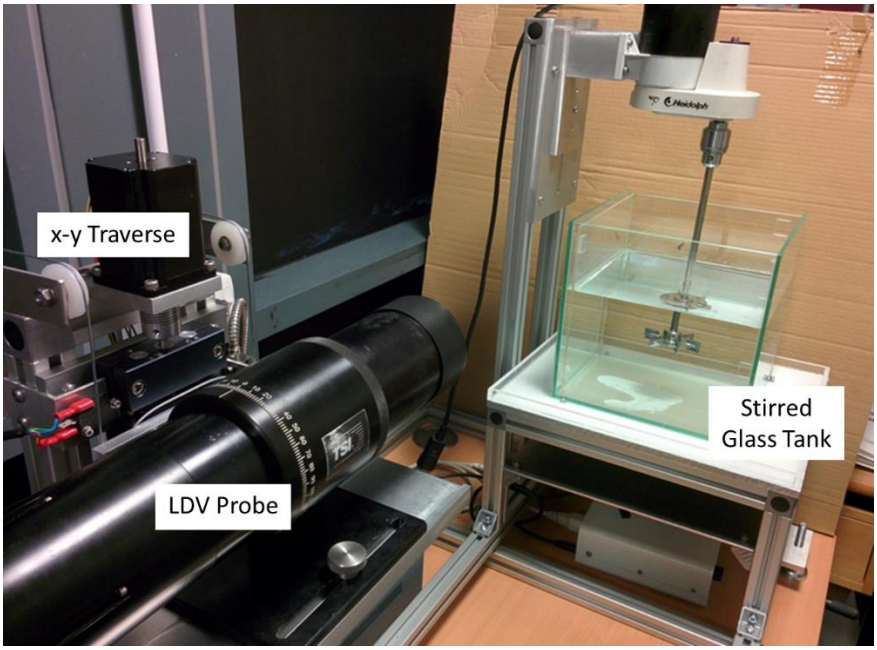

Figure 6-3: Experimental apparatus used for LDV measurements.

At each measurement location within the tank, the measurement procedure is continued until at least 10,000 valid velocity measurements have been made for each velocity component in that location. This sample size has been identified as sufficient by recording the radial and axial velocity components at intervals of 500 data hits and plotting the deviation from the final value. This analysis is presented in Figure 6-4 for both single-phase and two-phase conditions, both in-line with the impeller and in the upper recirculation zone. Between 0 and 4,000 data points, there is a relatively large deviation in the measured mean velocity due to the fluctuating turbulent flow occurring in the stirred tank. Between 4,000 and 7,000 data hits, there is a greater variation for the two-phase measurements than the single-phase measurements, however both still show a significant deviation from the final value, showing that this sample size is not large enough to represent the time-averaged mean velocity. From 7,000 data points onwards, there is very little deviation from the final mean velocity for any velocity component, confirming that the values measured with at least 10,000 data hits is representative of the time-averaged velocity in two-phase systems, both close to the impeller and in the lower-velocity recirculation regions. The similarity between the single-phase and two-phase behaviour suggests that the method is predominantly capturing the liquid-phase velocity in the gas-liquid system.

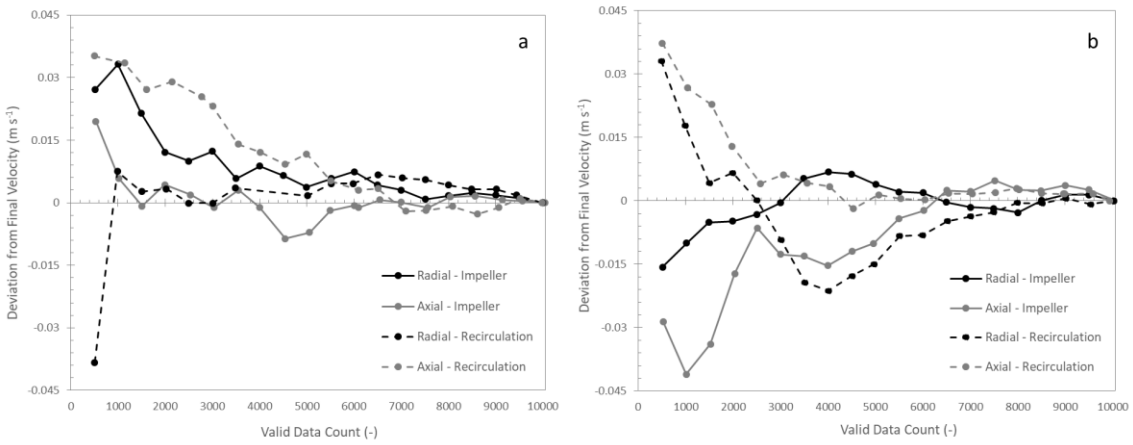

Figure 6-4: Variation of the current mean velocity from the final velocity for increasing data count up to 10,000 data points for the LDV experiments.
a) single phase, b) two phase.

6.2.2 Mass Transfer Experiments

Mass transfer experiments are performed by measuring the dynamic response of the dissolved oxygen concentration within the liquid to a step-change in gassing conditions, in this case switching from nitrogen to air sparging. A similar approach is commonly applied to industrial fermenters, with or without the presence of biomass, known as the dynamic method (Doran, 1995; Garcia-Ochoa et al., 2010). The impeller and gas sparger are set up as previously described in the introduction to Section 6.2. Measurements are taken as a percentage of the saturation concentration using an Oakton DO600 combined galvanic dissolved oxygen and temperature meter, with the temperature of the liquid adjusted to 25°C prior to the experiment using a submerged heating coil as required. The dissolved oxygen meter is fixed horizontally within the fluid flow, between the height of the impeller and the surface of the liquid. The dissolved oxygen is initially reduced to below 10% of saturation by bubbling with nitrogen gas, before the gas feed is switched to air for the measurement phase, which continues until a stable final concentration is achieved.

6.3 Model Setup

The modelled domain is based on the experimental validation tank described in Section 6.2, with the model setup designed to be as similar as possible to the BioMOD model described in Section 5.3 to allow for the most effective comparison of results. This includes using a cubic tank instead of the more traditional cylindrical designs, similar volumetric aeration to the BioMODULE and a range of stirrer speeds that will cover all two-phase flow regimes

seen during the BioMOD modelling. The two-phase model used for the BioMODULE is replicated for the validation work, with the numerical details provided in Chapter 4. The drag force between the gas and liquid phases is modelled using the Ishii-Zuber drag model (Ishii and Zuber, 1979). The setup for the MUSIG model is also kept the same as the optimised model presented in Section 5.5, using 12 size groups between 0 and 9 mm, although it is expected that the bubble size in the validation work will be smaller due to the greater potential for break-up through bubble-impeller interactions and the much smaller liquid volume giving rise to lower bubble residence times.

One of the most significant differences between the two systems is that there are much more significant bubble-impeller interactions in the validation system due to the overhead stirring method used. The model is to be solved across a range of different stirrer speeds from 0 to 400 RPM, meaning that a wide range of different two-phase flow regimes are expected to be encountered, which will cover the range of hydrodynamic conditions expected in the BioMOD reactor. This difference has led to the use of the multiple reference frame (MRF) technique to describe the impeller motion for the validation tank. This is because the immersed solids method applied to the BioMOD tank is unsuitable for use where the gas phase is sparged directly onto the impeller, due to limitations in the way that the solid-gas interactions are implemented (ANSYS Inc., 2016), allowing for the gas phase rising from the sparger to pass through the solid domain.

The validation model is solved as a steady-state solution using the same high-resolution numerical solver scheme and coupled multiphase physics as for the BioMOD model. The model is also solved for identical convergence criteria of 10^{-4} for the RMS residuals of the momentum and turbulence terms, with a maximum permitted imbalance of 0.01 allowed for all parameters including the bubble size.

6.3.1 Domain Definition

The physics and boundary conditions applied are maintained from the BioMOD model, with the exception of the impeller motion model as discussed previously. The free surface of the tank is modelled using the degassing condition, whilst walls are considered no-slip with respect to the liquid phase and free-slip with respect to the gas phase. The impeller blades are assumed to have zero-thickness and zero curvature in order to optimise the meshing process. The entire surface of the cylindrical sparger is assumed to act as an inlet for the

gas phase, with a specified mass flow-rate of 0.01975 g s^{-1}, corresponding to a volumetric aeration rate of 0.21 vvm. A volume fraction of 1 is applied for the gas phase at the inlet, with an initial bubble size of 1.125 mm (size group 2) applied. The flexible tubing used to feed gas to the sparger is not modelled in order to simplify the geometry and allow for a fully structured mesh to be produced. The six-bladed impeller and four corners of the tank allow for a single plane of symmetry to exist within the tank, meaning that only half of the physical domain is modelled, as shown in Figure 6-5 a). A rotational periodicity boundary condition is applied to the two halves of the symmetry plane.

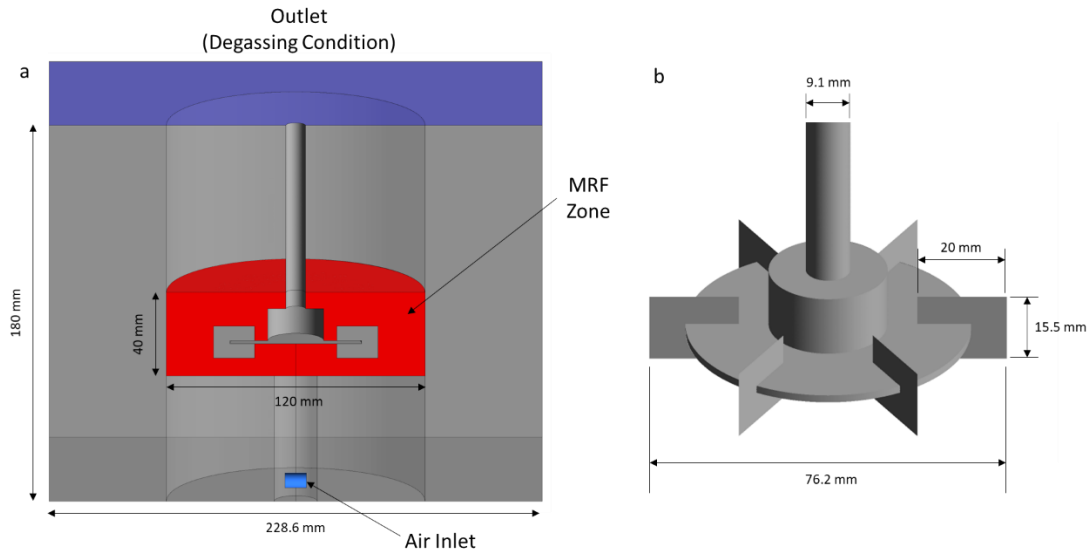

Figure 6-5: Geometry of the tank (a) and impeller (b) used for the validation experiiments.

6.3.2 Meshing

The fluid domain is meshed using a fully structured hexahedral mesh, developed using the ANSYS ICEM software package. The interface between the moving zone (the rotor) and the stationary zone (the stator) is specified with a 1:1 ratio to maximise the robustness of the mesh produced. Four meshes of increasing density are compared for the validation tank, as described in Table 6-1. Each mesh is used to solve the steady-state model at a stirrer speed of 400 RPM and gas flow rate of 2 L min^{-1}, with the volume averaged $k_L a$ calculated using the eddy cell and slip velocity models for each mesh also presented in Table 6-1. From these values it can be concluded that a mesh with density of at least Mesh 3 is required to produce mesh-independent results in respect to mass transfer modelling, although the difference between meshes 2 and 3 is much smaller than the difference between meshes 1 and 2.

Table 6-1: Mesh dependency study for the validation tank at 400 RPM.
Time for solution based on the time taken to reach 1,000 iterations using 16 cores.
[Intel Xeon E5-2670 v2 CPUs, 64 GB RAM].

	Number of Elements			$k_L a$ (hr^{-1}) at 400RPM		Time for Solution (hrs)
	Rotor	**Stator**	**Total**	**Eddy Cell**	**Slip Velocity**	
Mesh 1	45,378	221466	266,844	65.5656	49.6493	3.17
Mesh 2	92,112	459,474	551,586	48.6948	68.8295	7.32
Mesh 3	152,040	701,326	853,366	52.3063	73.0863	10.63
Mesh 4	152,040	1,147,490	1,299,530	52.4342	73.1778	14.98

Profiles for the resultant velocity magnitude and air fraction, plotted against radial distance for a single profile in-line with the centre of the impeller blade, are presented in Figure 6-6 a) and b) respectively. The profiles for both variables presented are very similar for meshes 2 to 4, however Mesh 1 shows a significant deviation from the other meshes in both velocity magnitude and air fraction. This comparative trend is representative of the trends seen for these variables elsewhere in the tank for the different meshes studied. Based on these profiles and the volume-averaged parameters presented in Table 6-1, it can be concluded that Mesh 3 is sufficiently fine to accurately capture the flow characteristics associated with fluid dynamic and mass transfer modelling, and further increases in mesh density do not therefore justify the increased computational expense. All further results in this chapter are therefore generated using Mesh 3.

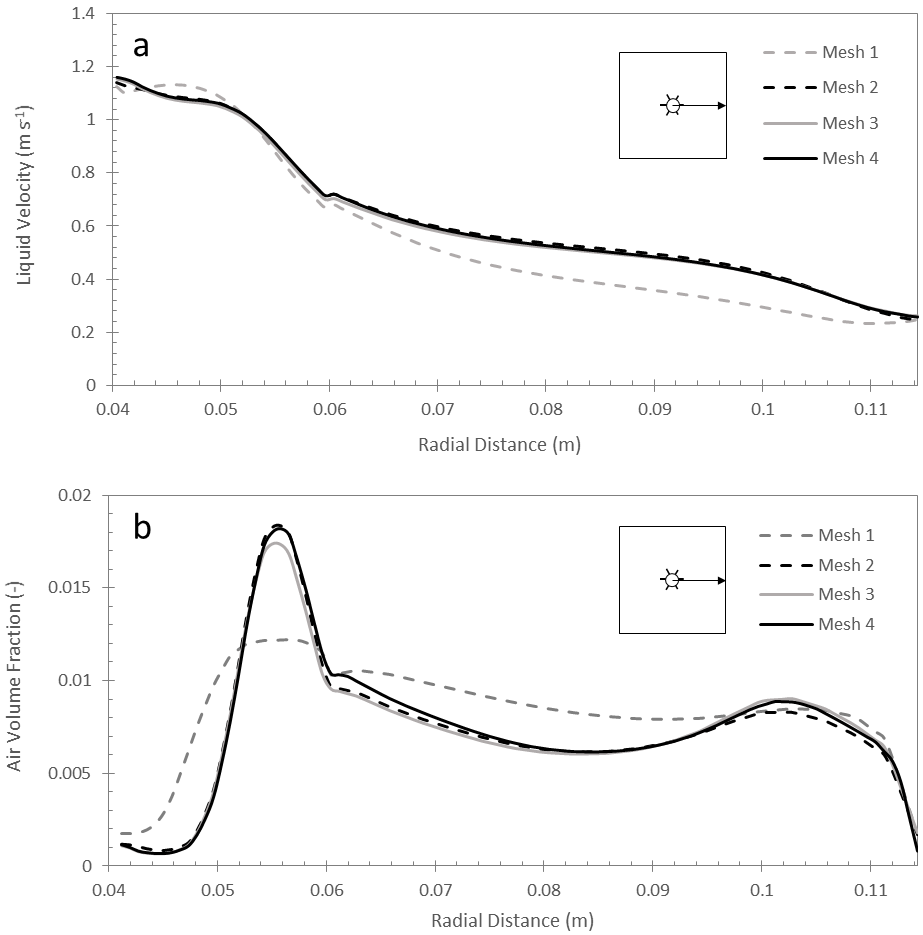

Figure 6-6: Radial profiles for different mesh densities, in-line with the impeller tip. a) Resultant liquid velocity, b) air volime fraction.

The final optimised mesh (Mesh 3) is presented in Figure 6-7 for three different cut-planes. The use of a fully structured mesh means that the mesh density is increased towards the centre of the tank, however O-grid meshing techniques are applied below the impeller to ensure that a convergence to a single node at the centre of the geometry is avoided. The mesh density in-line with the impeller is higher than at the corners of the tank due to the greater velocity gradients existing in this area. Similarly, a fine mesh is applied in-line with the cylindrical gas sparger in order to accurately capture the large velocity gradients occurring in this region due to the gas introduction.

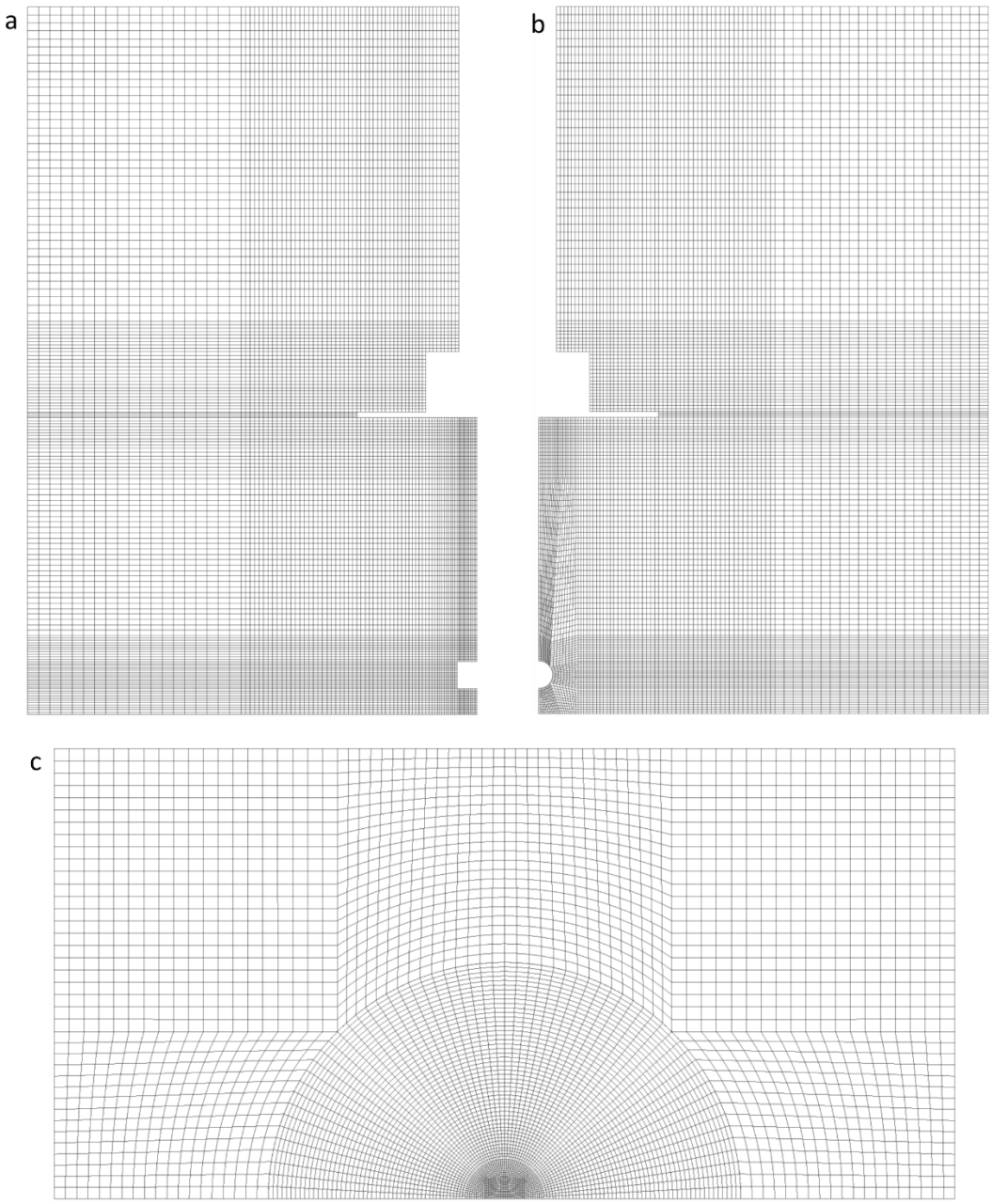

Figure 6-7: Optimised mesh used for the validation stirred tank model.
a) z-y plane – centre of tank, b) z-x plane – centre of tank, c) x-y plane - below impeller

6.4 Flow Patterns Analysis: LDV

Validation of the liquid-phase flow patterns in the laboratory-scale validation tank is performed by comparing the experimental and modelled two-dimensional liquid velocity vector plots at a vertical cut-plane through the centre of the tank. Point measurements in one half of the tank are made using LDV as described in Section 6.2.1 at vertical and radial intervals of 2 cm, and reflected around the central axis of the tank due to symmetry either

side of the impeller. Experimental vector plots are generated from the LDV data using the built-in MATLAB function ‘quiver’. The experimental plots for stirrer speeds of 100 to 400 RPM are compared side-by-side with the modelled vector plot at the equivalent location in Figure 6-8. Each of these plots is normalised to the impeller tip speed at the given conditions, and therefore the difference in velocity magnitude between different stirrer speeds is not represented by these plots.

The qualitative analysis presented in Figure 6-8 shows the transition in the liquid velocity field between buoyancy dominated flow patterns at 100 RPM, driven by the rising gas phase at the centre of the tank, and impeller dominated flow patterns at stirrer speeds of 200 RPM and above. At these higher rotational speeds, the impeller action generates recirculation loops towards the corners of the tank, both above and below the impeller. This is much more similar to the flow patterns seen in single phase stirred tanks (see Joshi et al. (2011a)), showing that the impeller action is the main factor in determining the flow patterns in the different shapes of tank. The most significant change in liquid flow patterns between 200 and 400 RPM is that the velocity profile in-line with the impeller becomes more horizontal, as the increasing radial dispersion of the liquid phase caused by the impeller motion continues to further dominate the buoyancy-driven rise caused by the gas phase present in these regions. This feature can be clearly seen in both the modelled and experimental velocity vector plots. The prominence of the upper recirculation loops also becomes stronger with increasing stirrer speed, however this is more clearly seen in the model than in the experimental vector plots. This may be due to the increased distribution of gas above the impeller causing more fluctuating or unstable flow patterns in this region during LDV measurements, however the choice of a degassing boundary condition may also influence the modelled flow patterns in this area, since no deformation of the free surface is assumed. The lower recirculation loop is in general captured well by both the modelled and experimental vector plots.

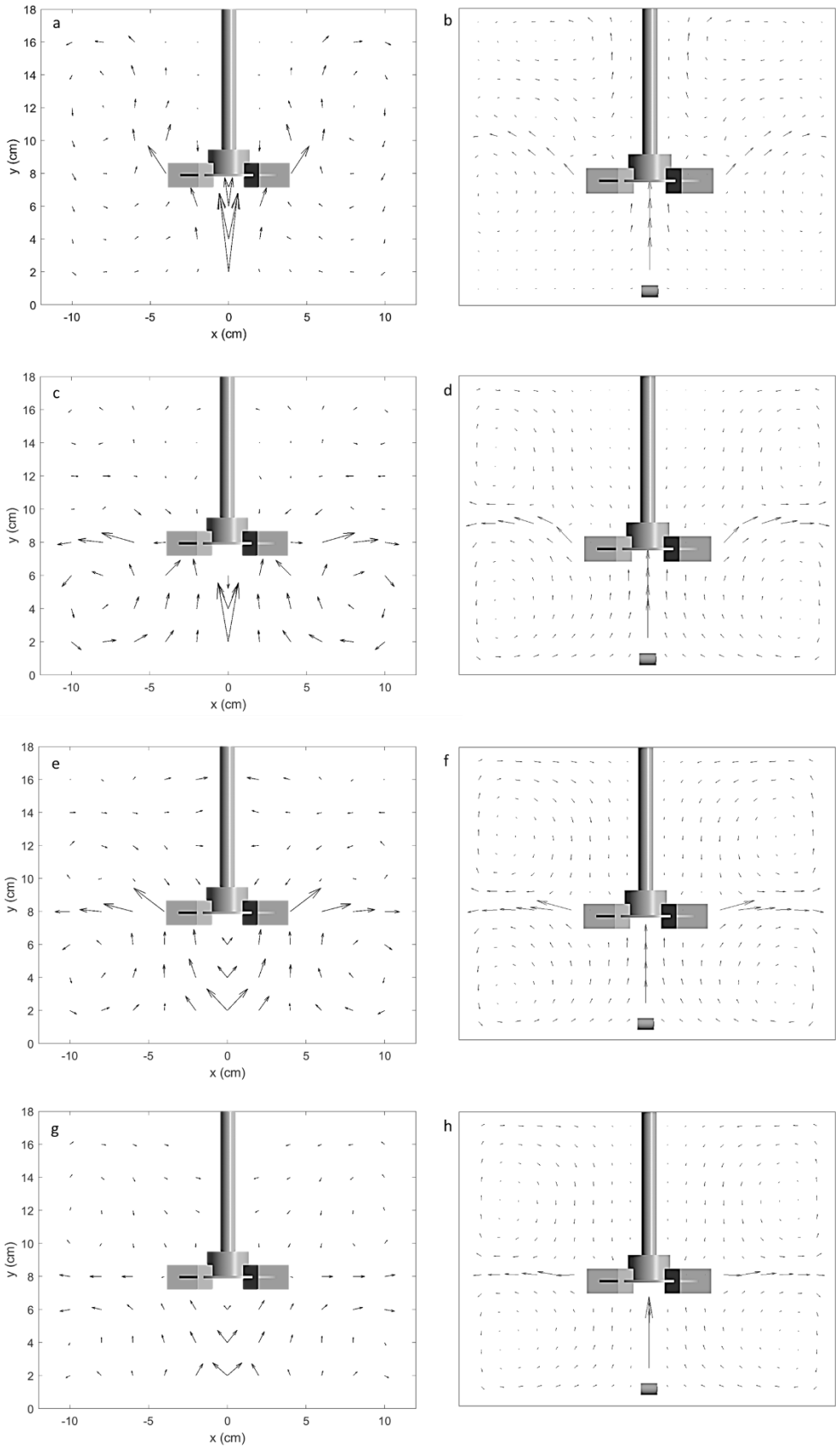

Figure 6-8: A comparison of the experimental (a, c, e, f) and modelled (b, d, f, h) vector plots of liquid velocity at the centre of the validation tank at different impeller rotational speeds.
a-b) 100 RPM, c-d) 200 RPM, e-f) 300 RPM, g-h) 400 RPM.

The quantitative analysis presented in Appendix C-F shows an individual comparison of the radial and axial velocity components at each height and for each stirrer speed measured. In general, a reasonable fit is achieved between the measured and modelled profiles of axial and radial liquid velocity, however there are some very significant differences between the profiles at some locations. Key features such as the change from upward to downward flow are captured well, and the magnitude of the velocity for the modelled and experimental profiles are similar for all of the stirrer speeds analysed. This is particularly significant since the profiles are normalised against the impeller tip speed, meaning that the measured velocity magnitude between different impeller speeds does vary significantly. However, the fit is least good close to the impeller where the greatest degree of turbulent flow is expected. This may be as a result of the experimental time averaging in this region, however this is minimised by using an experimentally optimised number of data point as described by Figure 6-4. The use of a steady state solver may also mean that variations in velocity due to impeller orientation are not captured well in the model, and the use of the k-ε turbulence model is also likely to create the largest discrepancies in highly turbulent regions. The quality of the fit to the quantitative data is similar to that achieved by Wang et al. (2014) using LDV, where the general trends are captured but not the exact profile, and is also significantly worse than the single-phase LDV fits discussed by Joshi et al. (2011a; 2011b). These profiles suggest that the CFD model developed in this thesis is currently unable to perfectly capture the complex hydrodynamic behaviour occurring in gas-liquid stirred tank systems, although the liquid-phase velocity data presented in this thesis can be said to provide a good approximation.

6.5 Gas Distribution

The gas distribution is validated qualitatively by comparing the observed distribution of the gas phase at different stirrer speeds. Imaging is performed for the experimental setup using a Nikon D3200 DSLR camera with backlighting provided by an LED array with a diffuser sheet in between the light source and the back wall of the tank to smooth out the light produced by the individual LEDs. The range of stirrer speeds considered (100 to 400 RPM) covers a wide range of different bubbly flow conditions, with the two-phase flow profiles at low stirrer speeds dominated by the buoyancy of the gas phase, whereas the flow patterns and gas distribution at high stirrer speeds are dominated by the action of the impeller. This transition can be seen in the experimental images shown in Figure 6-9 for increasing stirrer speeds. Each experimental image is accompanied by an equivalent modelled contour plot

of gas distribution for a single cut-plane at the centre of the tank. Each contour plot is presented for the same range of gas fraction values, from 0 to 0.05 as described by the accompanying colour bar. Whilst providing a good basis for comparison of the gas distribution, it is important to note that the experimental images show a three-dimensional representation of the gas distribution, whereas the modelled distribution is presented in only two dimensions.

Increasing the stirrer speed leads to a greater distribution of the gas phase, as smaller bubbles are produced in the turbulent near-impeller flows, which have a lower rise velocity and are therefore more likely to follow the liquid flow patterns. This can be seen in the experimental images for 300 and 400 RPM, where the bubble size is on average much smaller above the impeller than below, whereas there is little observable difference in bubble size above and below the impeller at lower stirrer speeds. At 100 RPM, the gas phase does not extend much beyond the width of the impeller, hitting the impeller disc and rising straight out of the tank with a good comparison between the experimental and modelled distributions. At 200 RPM, there is an increase in the distribution of the gas phase in comparison to 100 RPM, although the experimental image shows a slightly greater distribution than the modelled plot, extending to the upper corners of the tank.

Between 200 and 300 RPM there is a clear change in the flow regime as the action of the impeller becomes more influential. This can be seen in the smaller bubble size presented in the experimental profiles and the lighter blue colours in the modelled contour plot representing a more dispersed gas phase. The experimental and modelled gas distributions compare very well for both 300 and 400 RPM. This suggests that the balance between buoyant and interfacial forces acting on the gas phase is captured accurately by the CFD model. At 300 RPM, the gas phase fills the upper section of the tank, but is not recirculated within the region below the impeller. Furthermore, at 400 RPM the action of the impeller is significant enough to recirculate the gas phase to the bottom of the tank, which is once again captured well by the model. The accumulation of the gas bubbles around the impeller shaft at the surface of the tank is also captured by the model at 400 RPM, despite the use of the degassing boundary condition.

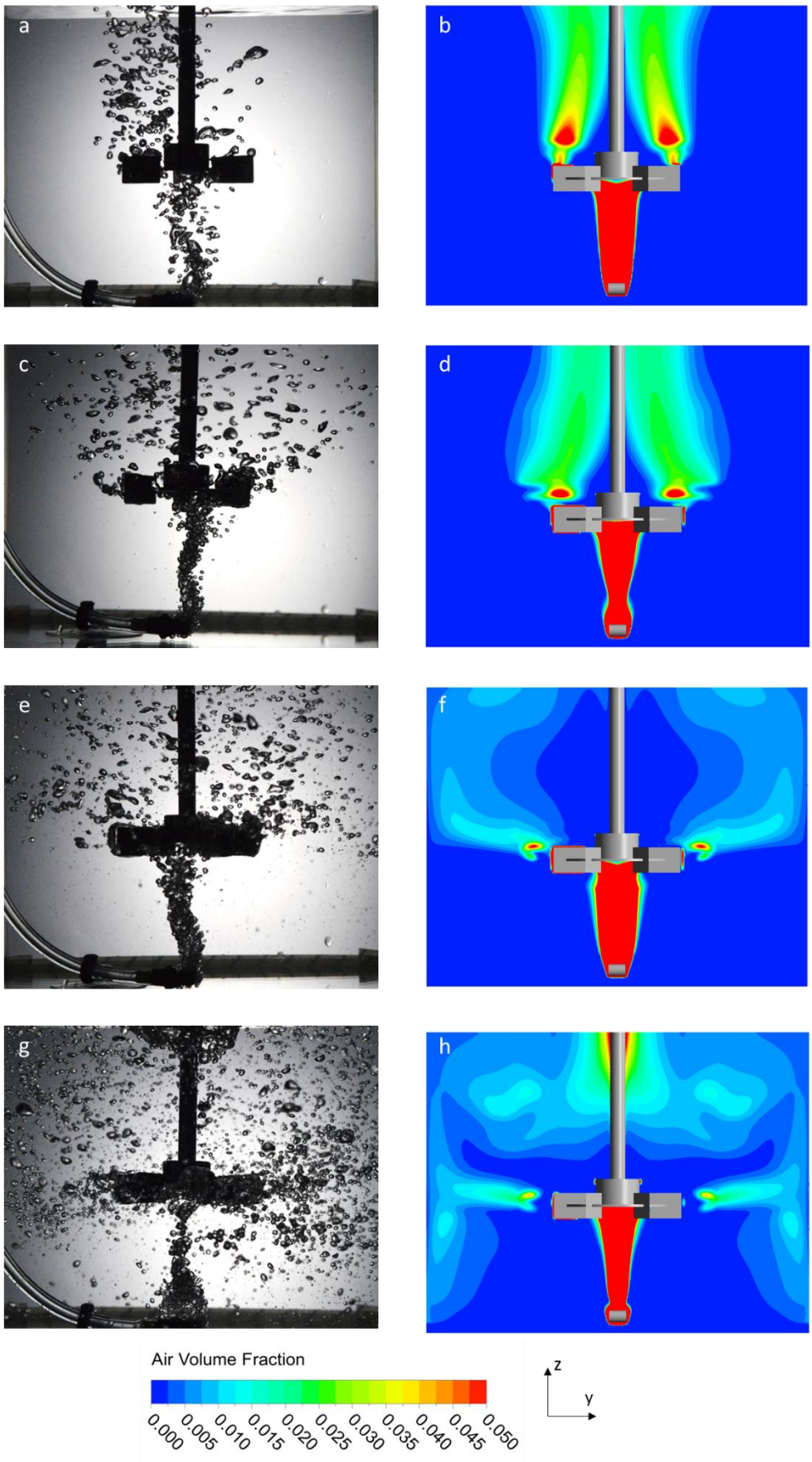

Figure 6-9: Comparison of the experimental and modelled gas dispersion at increasing stirrer speeds. a-b) 100 RPM, c-d) 200 RPM, e-f) 300 RPM, g-h) 400 RPM.

6.6 Bubble Size Distributions

The bubble size distribution within the experimental validation tank is approximated through image analysis using MATLAB and compared to the modelled distribution. The experimental profiles are developed using the analysis of multiple images, of which the images in Figure 6-9 are representative examples, in order to generate a large population size. The bubble size is measured in the specified region using the built-in MATLAB watershed image analysis function as described by Figure 6-2. This allows for irregular shaped, grouped or overlapping bubbles to be identified and their boundaries to be approximated. An approximate bubble size for each identified bubble is then calculated based on the area of a sphere with the same cross-sectional area as the region identified. In order to assign a size to the bubbles, a known dimension is required for comparison, which in this case is the cylindrical section of the impeller located directly above the flat impeller disc, which is located at the centre of the tank and has a known diameter of 25.9 mm. This known dimension is re-measured for each individual image analysed to account for any changes in the camera positioning or the level of zoom applied. A flow-chart describing the implementation of the image analysis procedure within MATLAB is provided in Figure 6-10. Local minima for the light intensity are limited to those with an intensity of less than 70 via the 'imhmin' function (step 4) in order to minimise the number of out-of-focus bubbles captured and prevent oversegmentation of the image through the effects of background noise. A manual side-by-side comparison of each original image and the corresponding processed image is made to ensure that the watershed function provides a reasonable approximation of the bubbles identified. The MATLAB code used for this analysis is included in Appendix B.

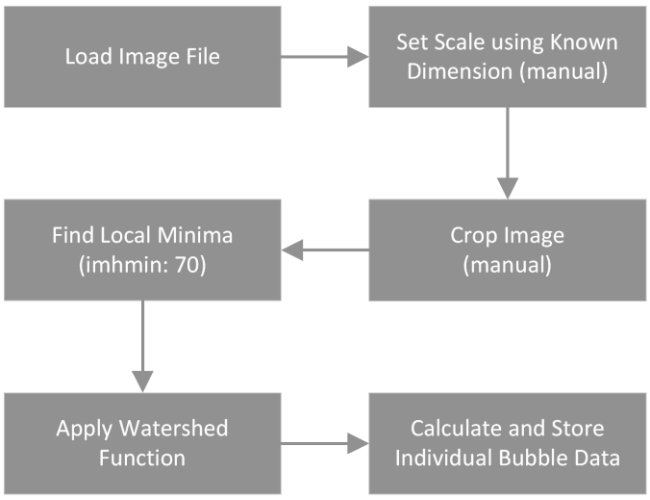

Figure 6-10: Flow chart for the watershed bubble imaging procedure for a single image.

A comparison of the black and white image (Figure 6-11 a) and the watershed outlines (Figure 6-11 b) produced by the MATLAB sizing code for a section of the 300 RPM image (Figure 6-9 e) is presented in Figure 6-11. This analysis shows that the watershed technique can accurately capture the outline of the great majority of individual bubbles, including those with highly distorted shapes such as those identified with a red box. Furthermore, this implementation of the watershed method has also shown a reasonable ability to identify individual bubbles in bubble clusters such as those highlighted in the blue box. The watershed programme is able to approximate the boundary between different bubbles but does not predict the unseen regions of bubbles in the background of the cluster. The programme has also managed to exclude a number of out-of-focus bubbles due to the less well defined border. Bubbles which are outside of the focal plane cannot be measured against a known scale, and should therefore be excluded from the analysis where possible, however there are some significantly out-of-focus bubbles which do feature in the final analysis such as the one highlighted in the yellow box. Finally, there are some very small bubbles within the unfiltered image which are not included in the watershed outline due to their pale interior, which is likely to lead to an over-prediction of the mean bubble size, although many other small bubbles are still included in the final analysis.

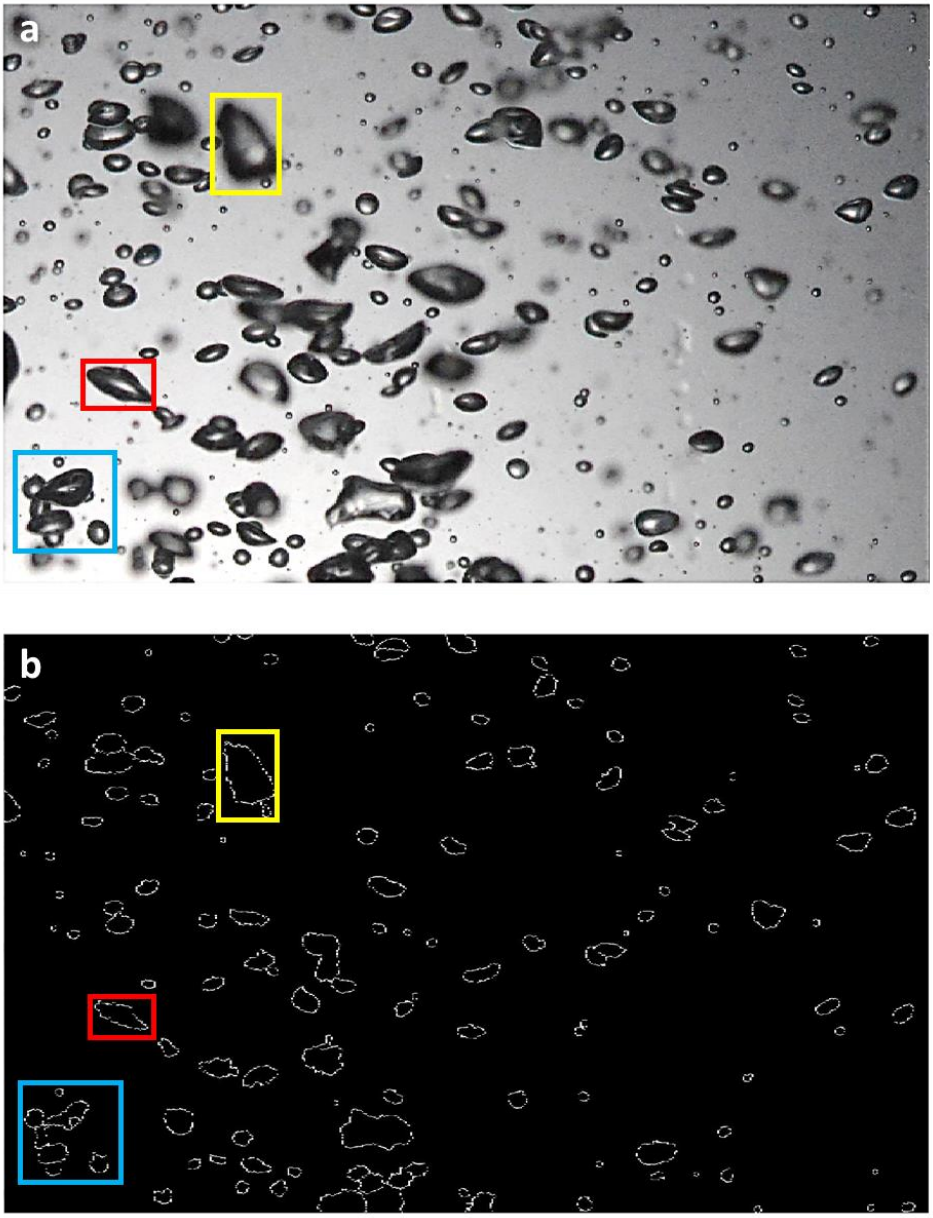

Figure 6-11: A comparison of the original (a) and processed (b) images for the watershed bubble sizing technique for a representative image at 300 RPM.

This analysis is performed only for the region above the impeller disc (76.2 mm from the tank floor). The modelled mean bubble diameter and size distributions are limited to regions of the tank with a gas volume fraction greater than 0.001, thus excluding regions where bubble diameter data is stored but no gas phase is present, however there is no further weighting of the statistics to the gas volume fraction. In contrast, the experimental profiles count individual bubbles, which automatically eliminates regions where no gas is present but may also over-represent regions where there is a higher mean gas volume fraction. However, from studying the experimental images in Figure 6-9 there is no clear variation in the bubble size for different regions of the same image for the different stirrer

speeds, and the effect of this weighting on the final statistics is therefore expected to be minimal.

A comparison of the mean bubble diameter for stirrer speeds of 100 RPM to 400 RPM is included in Table 6-2, along with the population size used to generate the mean diameter and subsequent size distributions. There is a much greater variation in the bubble diameter predicted by the model than has been identified by the experimental sizing, with the greatest difference at 100 RPM where the modelled mean diameter is more than 60% larger than the experimental value. In contrast, the experimental and modelled mean values match very well for rotational speed of 200 and 400 RPM, however the model under-predicts the experimental value at a stirrer speed of 300 RPM.

Table 6-2: Sizing data for the modelled and experimental bubble sizing technique at different stirrer speeds in the region above the impeller.

Stirrer Speed (RPM)	**Population Size (-)**	**Mean Diameter (mm)**	
		Experimental	**Modelled**
100	802	2.81	4.55
200	815	2.39	2.34
300	698	2.13	1.12
400	1104	1.09	0.917

A comparison of the bubble size distributions predicted using the watershed image analysis technique and the modelled size distributions is made in Figure 6-12, with the measured distributions on the left. In order to give the closest possible comparison, the modelled profile is calculated using only locations with a gas phase present, and both analyses only consider bubbles in the region above the impeller. The number and spacing of the bubble sizes in the distribution plots has been selected to represent the setup of the MUSIG model, with 12 equally spaced groups between 0 and 9 mm bubble diameter. All of the experimental profiles give a smooth distribution, suggesting that a large enough sample size is used that a representative distribution can be generated. Both the experimental and modelled distributions show a clear shift towards smaller bubbles with increasing stirrer speed, showing that impeller-induced bubble breakage is a significant factor to be modelled in this system, although the difference in the measured distribution between 200 and 300 RPM is relatively small.

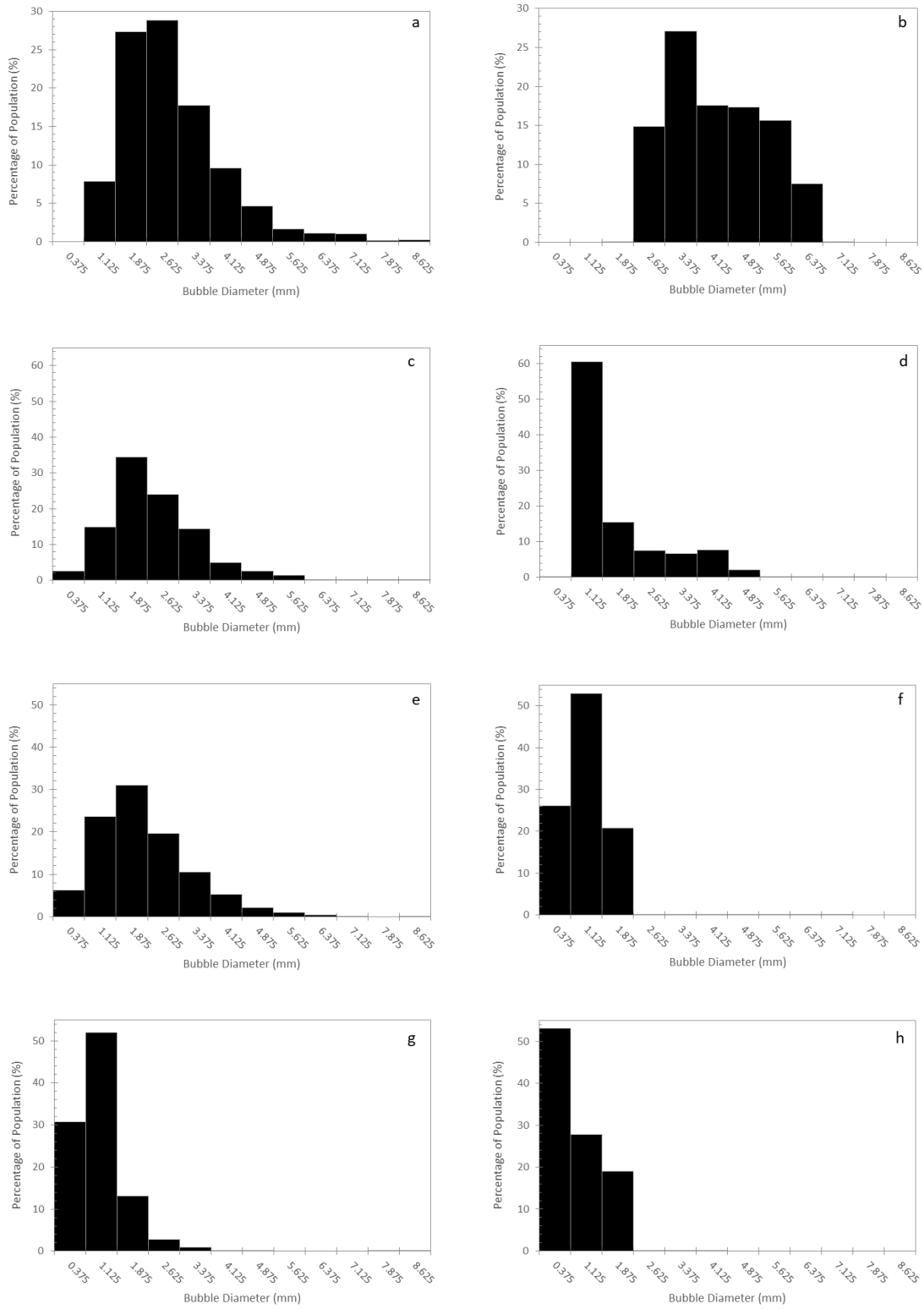

Figure 6-12: Measured and modelled predictions of the bubble size distribution in the region above the impeller for different stirring speeds.

Measured: a) 100 RPM, c) 200 RPM, e) 300 RPM, g) 400 RPM

Modelled: b) 100 RPM, d) 200 RPM, f) 300 RPM, h) 400 RPM

Population size: 100 RPM = 802, 200 RPM = 815, 300 RPM = 698, 400 RPM = 1104.

At 100 RPM, the measured distribution is shifted further towards the larger bubbles than the modelled distribution, however for all other conditions the modelled distribution predicts a smaller bubble size. The width of the distribution also changes with increasing rotational speed for both the modelled and experimental distributions. At 400 RPM, both distributions are very narrow, occupying only three (modelled) and five (measured) of the 12 available size groups. When compared to the broad distributions at 100 RPM, this suggests that the MUSIG parameters may need to be set individually for different flow regimes in order to represent the size distribution with a sufficiently high resolution. Furthermore, at 400 RPM the majority of bubbles in the modelled distribution are in the smallest size group, suggesting very high levels of bubble breakup are occurring.

6.7 Mass Transfer Modelling

Experimental mass transfer profiles for the oxygen transfer from air to water are presented in Figure 6-13 for stirrer speeds of 100 to 400 RPM. They are generated using the dynamic method in an air-water system as described in Section 6.2.2. These curves represent the mean average of three experimental runs, with the error bars generated by calculating the standard deviation from the mean falling within the size of the symbols used for all data points and therefore not included for clarity. This suggests a very high degree of reproducibility for this experimental technique. The curves follow the expected shape for the dynamic method, with the initial gradient of the curves varying depending on the stirrer speed and the curves all approaching the same saturation point. All of the profiles have been normalised to the step-change used for ease of comparison, with the zero point representing the starting concentration (always less than 10% of saturation). The saturation concentration of oxygen at 25°C is used to represent the 100% dissolved oxygen point. There is no significant lag time for any of the curves, which suggests that the liquid-phase may be considered to be well-mixed for all of the conditions and that probe lag is not a factor in the readings.

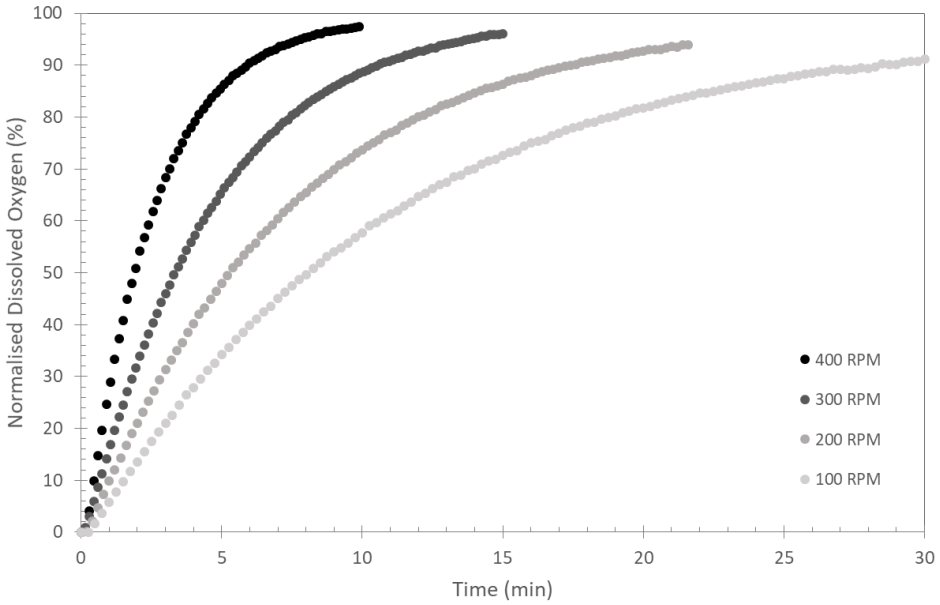

Figure 6-13: Dynamic dissolved oxygen concentration curves for different stirrer speeds.

The profiles presented in Figure 6-13 can be linearised using equation (2-6) in order to obtain a value for the volume-averaged $k_L a$. The measured $k_L a$ for each of the curves presented above is shown in Table 6-3 along with an indication of the quality of the linear fit, represented by the R^2 value. The fit for all of the conditions gives an R^2 of 0.99 or greater, showing that the data fits the standard form of the dynamic model very well. The $k_L a$ increases significantly with increasing stirrer speed, as might be expected from the increased gas distribution and the reduced bubble size identified previously in this chapter for increasing stirrer speed. The increase appears to be non-linear with impeller speed, with the greatest increase in mass transfer achieved between 300 and 400 RPM.

Table 6-3: A comparison of the experimental mass transfer performance at different stirrer speeds.

Stirrer Speed (RPM)	**Air Flow Rate (L min^{-1})**	**vvm (min^{-1})**	**$k_L a$ (hr^{-1})**	**R^2**
100	2.0	0.21	4.82	0.9900
200	2.0	0.21	7.92	0.9993
300	2.0	0.21	12.98	0.9994
400	2.0	0.21	23.19	0.9986

A comparison of the volume-averaged $k_L a$ values for the experimental and modelled systems is presented in Figure 6-14 for the range of 100 to 400 RPM. The modelled profiles are compared for all five of the mass transfer models listed in Section 4.4. As with the BioMOD mass transfer measurements at 400 RPM presented in Figure 5-15, the experimental points fall within the upper and lower limits predicted by the different mass

transfer models, however there is once again a large spread of $k_L a$ values predicted by the different models. The order in which the different models predict the magnitude of the $k_L a$ is also similar between the BioMOD and the validation systems presented in Figure 5-15 and Figure 6-14 respectively. In both instances, the rigid model consistently provides the smallest estimate, followed by the eddy cell and slip velocity models, with the penetration and surface renewal stretch providing the largest predictions of $k_L a$ and changing in order with increasing stirrer speed. This suggests that the CFD models are predicting similar behaviour for the BioMOD and validation cases.

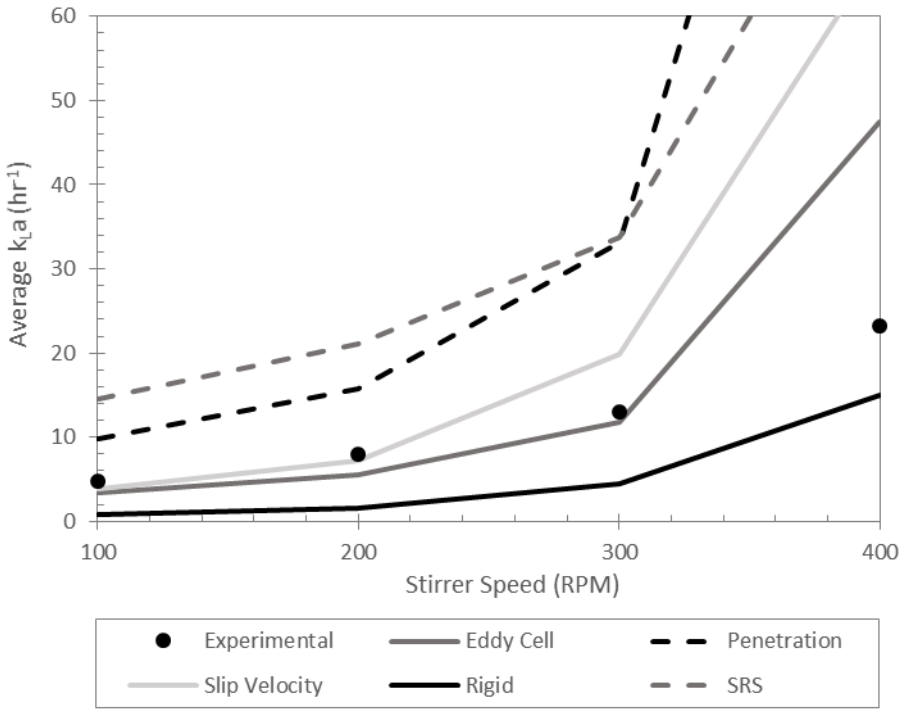

Figure 6-14: A comparison of the experimental and modelled $k_L a$ using five different mass transfer models at stirrer speeds of 100 to 400 RPM.

Between 100 and 300 RPM stirrer speed, the experimental values provide a good fit to both the eddy cell and slip velocity models, with the eddy cell providing a slightly closer match at 300 RPM. The relative similarity between these two models was also observed for the BioMOD system, and is a significant observation since they are calculated from very different liquid and gas-phase variables. However, at 400 RPM the CFD simulation very significantly over-predicts the $k_L a$ for all of the mass transfer models except the rigid model, which provides a poor fit at all other conditions. It is likely that the difference between the modelled and measured profiles occurs as a result of limitations in the computational model rather than limitations in the experimental technique, due to the

very good fit of the dynamic oxygen uptake curves to the linearised dynamic equation (see the R^2 values in Table 6-3) and the high reducibility of the mass transfer curves presented in Figure 6-13.

As previously presented in Figure 5-17 for the BioMOD tank, the variations in k_L and a can be compared individually for different stirrer speeds using the CFD model. The variation in k_L is greater across the range of stirrer speeds modelled for the validation system than the BioMOD reactor, however the most significant influence is on the $k_L a$ of changing the stirrer speed is still provided by the increased interfacial area, as shown in Figure 6-15. There is a greater variation in $k_L a$ for the slip velocity mass transfer model, particularly between 100 and 200 RPM, with very little difference in k_L predicted at higher stirrer speeds. In contrast, the eddy cell model predicts only a gradual increase in k_L across the wide range of stirrer speeds modelled. In contrast, the specific area increases significantly with each increase in stirrer speed. It is therefore likely that the over-prediction of the $k_L a$ seen at 400 RPM is a result of limitations in the modelling of the interfacial area (a), which is dependent upon the modelled gas distribution and the bubble size.

As suggested by Figure 6-12 h), there is a greater proportion of very small bubbles for the modelled distribution, which will lead to a very large interfacial area for these bubbles. The MUSIG model applied for the bubble size distribution in this model may be improved by optimising the bubble size range and number of groups for each stirrer speed modelled, rather than using a relatively wide size range that was calculated for the BioMOD tank. Alternatively, the calibration factors in the coalescence and breakup models (equations (4-41) and (4-44)) may be varied manually to provide a better fit to the experimental results across the range of stirrer speeds. The MUSIG model has been developed and validated largely for test cases based on bubbly flow in pipes such as Krepper et al. (2008), and may therefore not be optimised for the high break-up conditions created by high-speed impellers.

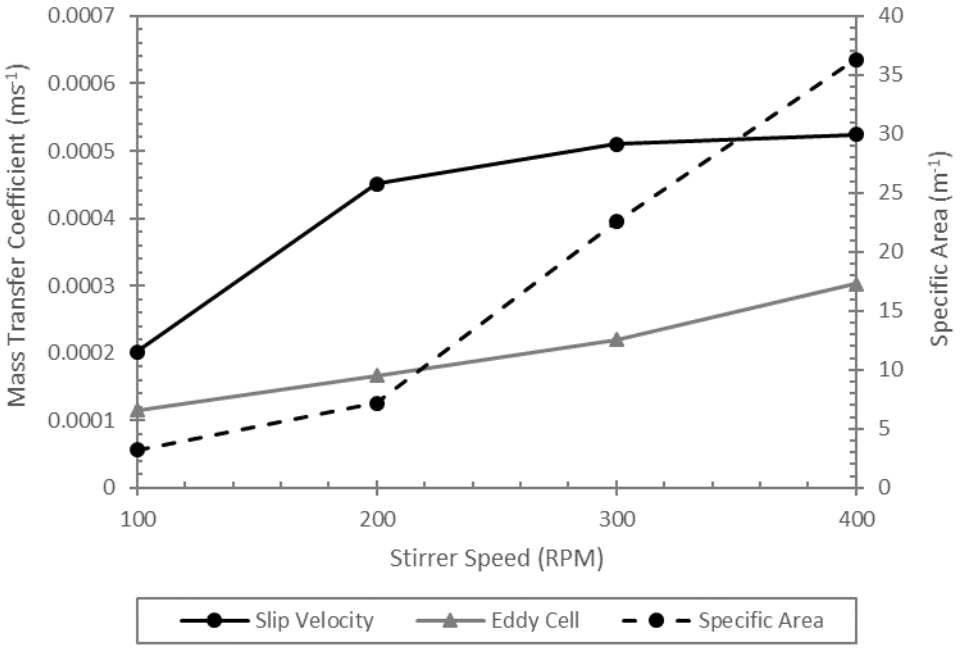

Figure 6-15: Comparison of modelled k_L values in the validation tank for the slip velocity and eddy cell models and the specific interfacial area at stirrer speeds of 100 to 400 RPM.

6.8 Summary

This section has detailed the multi-parameter validation of the CFD model applied to the BioMOD single use technology bioreactor detailed in Chapter 5. The model uses the same computational setup used for the BioMOD model, including the optimised MUSIG parameters and physical models, with the exception if the immersed solids impeller motion model which is considered to be incompatible with the much higher degree of impeller-gas interactions in the validation setup. Experimental measurements and observations are made in a 9.4 L square-bottomed glass tank, with air sparged directly onto a single Rushton impeller mounted one impeller diameter above the tank floor. The gas distribution and bubble size are evaluated by analysing images of the flow at stirrer speeds of 100 to 400 RPM, observed through the clear tank walls. This range covers a wide range of flow regimes, which are influenced by the buoyant gas phase and the mechanical agitation of the impeller. The liquid-phase velocity was measured by using laser Doppler velocimetry (LDV) with a minimum of 10,000 measurements per data point, and the tank-averaged $k_L a$ was calculated from dissolved oxygen measurements using the dynamic method.

The CFD model provides a reasonable fit to all of the experimental parameters at stirrer speeds of 100 to 300 RPM, however the model significantly over-predicts the mass transfer

rate at a stirrer speed of 400 RPM. The qualitative comparison of the gas distribution shows that the changing flow regimes with different stirrer speeds are captured very well, as are the overall liquid-phase flow patterns identified through LDV. This suggests that the interphase forces and impeller motion effects are being captured well by the model. The quantitative analysis of the axial and radial velocity profiles measured at 20 mm height intervals also show a reasonable fit between the experiments and model, with a similar quality of fit to other two-phase stirred tank models published in literature. The predictions of the two-phase flow patterns may be further improved by the use of more complex turbulence modelling, however this is not currently applied in the literature due to the high computational expense.

The experimental bubble size distribution is approximated from experimental images by using a watershed image processing technique, which is shown to capture the outlines of overlapping and highly deformed bubbles with reasonable accuracy. The bubble size for stirrer speeds of 100 to 300 RPM is similar to those predicted for the BioMOD reactor, however the bubble size predicted at 400 RPM is much smaller due to the more dominant impeller-bubble interactions experienced in the validation tank. The distribution at 400 RPM is restricted to only the smallest three size groups for the MUSIG model, which is likely to reduce the accuracy of the bubble size prediction, and therefore affect the mass transfer predictions at high stirrer speeds. The mass transfer, evaluated in terms of $k_L a$, also matches the BioMOD reactor modelling well for stirrer speeds of 100 to 300 RPM, with the order of the magnitude predicted by the different models remaining the same. A very good fit to the experimental data between 100 and 300 RPM is achieved by the eddy cell and slip velocity models, the latter of which also provides a good fit to the BioMOD reactor. The large over-prediction of the $k_L a$ at 400 RPM is linked to the very small bubble size modelled, which is once again shown to have a much bigger variation over the range of stirrer speeds modelled. It is suggested that the MUSIG model for bubble breakup and coalescence may require optimising for use with stirred tank systems at high stirrer speeds, since the MUSIG model is predominantly developed for pipe flow test cases.

7 Microbubbles: Physical and Mass Transfer Properties

One of the most promising methods for improving mass transfer identified during the BioMOD project is the use of smaller bubbles to increase the interfacial area between the gas and liquid phases. The CFD model applied to Chapters 5 and 6 has shown that the interfacial area is by far the most significant factor in improving mass transfer at higher stirrer speeds (see Figure 5-17) rather than flow properties such as the slip velocity or turbulence intensity, which will influence the mass transfer coefficient. However, it is possible to produce a much higher specific area by introducing bubbles in the sub-millimetre range, i.e. microbubbles, to the two-phase system in the place of traditional air sparging and mixing. This chapter will describe the development of a protocol for microbubble sizing and the characterisation of the mass transfer performance of a commercially available microbubble generating pump with an air-water system. The latter is performed in various shapes and volumes of vessel, both with and without the inclusion of mechanical agitation.

7.1 Introduction

Microbubble technology is a fast-developing field of research with a number of potential applications for industrial, scientific and medical purposes as detailed in a number of recent review papers (Khuntia et al., 2012; Temesgen et al., 2017; Agarwal et al., 2011; Parmar and Majumder, 2013). However, the exact classification of a microbubble is not consistent between these sources. For example, Takahashi (2005) defines the upper diameter limit as 50 µm, whereas other sources specify an upper diameter in excess of 100 µm. The identification of microbubbles in this thesis will therefore be based on their characteristics. In addition to microbubbles, even smaller bubbles are classified as nanobubbles, while further classifications such as sub-microbubble or micro-nano-bubble are proposed by some to exist between these two definitions (Temesgen et al., 2017). The potential use of microbubble generation is compared to other available technologies for the supply of CO_2 to microalgae cultures by Zheng et al. (2018), who identified that the main advantage of microbubbles is the gas utilisation, which is considered to be very high in comparison to traditional gas sparging.

Stability

Interest in microbubble technology is high due to a number of interesting physical properties that characterise microbubbles. Firstly, unlike larger bubbles which tend to

undergo coalescence or breakup depending on the local hydrodynamic conditions (see Chapters 5 and 6), microbubbles are very stable in solution. This is concluded to be a result of repulsive forces caused by the high negative surface charge, measured in terms of the zeta potential, ζ, by Takahashi (2005), at neutral and alkaline pH. This high surface charge is also thought to be a key factor in the formation of free radicals from collapsing microbubbles (Takahashi et al., 2007). Microbubbles also have a perfectly spherical shape, making them much easier to characterise than larger bubbles. Microbubbles that exist in an unsaturated solution are widely reported to shrink and disappear within the liquid as opposed to larger bubbles which quickly rise to the surface of the liquid and burst, leading to a high usage of the available gas. Similarly, nanobubbles, with a diameter of less than 200 nm (Agarwal et al., 2011), are reported to follow Brownian motion and may exist within the liquid phase for months due the formation of a thick hydrate film (Khuntia et al., 2012). However, their volume is so small that they will not be considered relevant for mass transfer applications as studied in this thesis.

Rise Velocity

The rise velocity of microbubbles is also very low in comparison to traditional gas-sparged systems, which means that they will have a long residence time in saturated solutions. Takahashi (2005) suggested that the terminal rise velocity of single bubbles in the region of 10 to 100 µm in deionised water is well described by using Stokes law (Stokes, 1851), however Parkinson et al. (2008) suggests that the rise velocity of bubbles of several gases are better described using the Hadamard–Rybczynski equation (Hadamard, 1911; Rybcznski, 1911) in the same size range. The equations used to describe each of these models are presented in equations (7-1) and (7-2) respectively, assuming that the internal viscosity of the bubble is much less than that of the carrier liquid. These models are compared in Figure 7-1 for bubbles of air in water at 25°C up to 200 µm in diameter, with both models predicting a very small rise velocity for microbubbles. Furthermore, due to these low buoyancy effects it is expected that microbubbles will be strongly influenced by any recirculating flow patterns that exist within the liquid, which will further increase their residence time in many typical two-phase applications.

$$U_{T\ (Stokes)} = \frac{2r^2(\rho_L - \rho_G)g}{9\mu_L} \tag{7-1}$$

$$U_{T\ (HR)} = \frac{2r^2(\rho_L - \rho_G)g}{3\mu_L} = \frac{3}{2}U_{T\ (Stokes)} \tag{7-2}$$

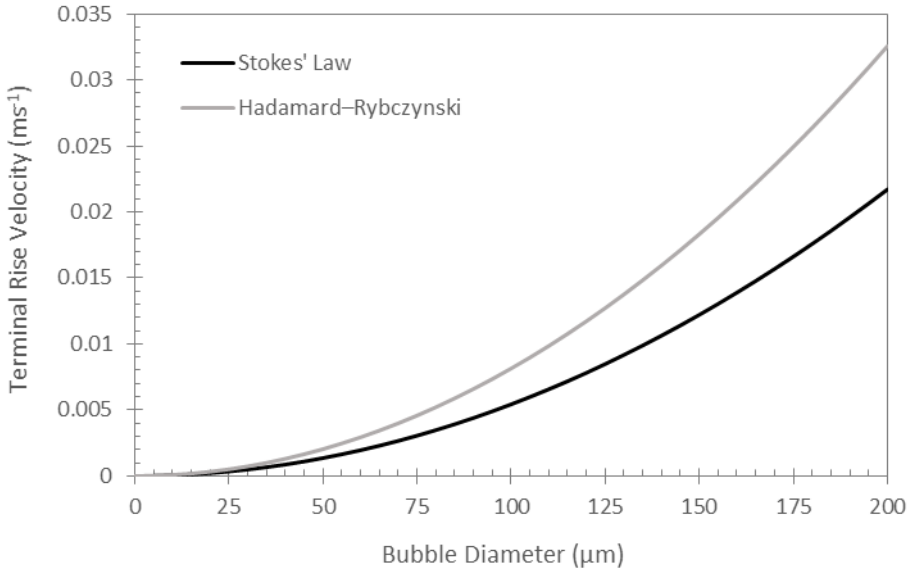

Figure 7-1: Prediction of terminal rise velocity for air bubbles in water in the microbubble range by using Stokes law and the Hadamard–Rybczynski equation.

Generation of Microbubbles

The generation of microbubbles can be achieved through a number of different methods. Microbubble pumps such as the Nikuni pump, described and used later in this chapter, work on a pressurised dissolution principle described by Terasaka et al. (2011) and Khuntia et al. (2012), where the gas and the liquid are mixed under high pressure, usually generated by a pump, followed by a high-pressure settling tank, during which a large proportion of the gas will dissolve into the liquid. The mixture is then rapidly decompressed to produce microbubbles which grow from the dissolved gasses. The size distribution of the bubbles produced can be modified by varying the pressure of the settling tank and the decompression conditions (Terasaka et al., 2011). The characteristics of the microbubbles produced using a pressurised dissolution pump system, such as rise velocity and size distribution, have been reported by Jeon et al. (2018) with respect to various operating conditions, along with a detailed description of the pump design which is similar to the Nikuni pump.

Spiral liquid flow microbubble generators use a rapidly rotating column of liquid to break up larger gas bubbles and produce microbubbles. The rotating flow is generated by

pumping the liquid tangentially into a cylindrical chamber, and introducing air into the spiralling flow centrally at the bottom of the column, as detailed in the European patent application by Ohnari (2000). A similar spiral microbubble device was described by Li and Tsuge (2006a; 2006b), and applied to particle separation through air floatation and the mass transfer of ozone to water. This device was operated with a range of different gas and liquid flow conditions, and with a gas-to-liquid ratio of up to 0.1 making it competitive with microbubble pump technologies. Another method which uses a rotating liquid field is the spinning disc-type microbubble generator (Bredwell and Worden, 1998), in which a rotating disc is immersed in a 5 litre baffled fermenter to generate a very high shear zone in which microbubbles are formed from gas which is continually bubbled into the vessel. However, this application requires a surfactant to stabilise the bubble within a protective shell, which may inhibit the mass transfer potential.

Venturi and ejector-type microbubble generators operate by promoting cavitation and breaking down larger bubbles in a gas-liquid flow through a specially designed constriction within a recirculating flow loop (Terasaka et al., 2011). Several designs have been proposed based upon this concept, with a fresh gas feed typically introduced close to the constriction (Watanabe et al., 2004; Sadatomi et al., 2005; Sadatomi et al., 2012). The effect of the generation and collapse of microbubbles via cavitation through various orifice designs, without the inclusion of a gas inlet stream, has also been extensively studied for food and water treatment applications (Gogate, 2011). Finally, fluidic oscillation is a passive technique that was developed within the Zimmerman group at the University of Sheffield (Zimmerman et al., 2008). It uses a specially shaped gas passage which splits the air between two channels, creating an oscillating gas flow in each channel. Fluidic oscillation has been proposed as a promising technology for several industrial applications including airlift bioreactors (Zimmerman et al., 2009; AL-Mashhadani et al., 2015), floatation separation technologies (Hanotu et al., 2012; Hanotu et al., 2014) and membrane cleaning (Harun and Zimmerman, 2018). However, the formation of microbubbles via fluidic oscillation is highly dependent on the distributor design and materials used (Wesley et al., 2016), and the bubble sizes reported are larger than competing technologies.

A comparative study of several different microbubble generation techniques is provided by Terasaka et al. (2011). The gas volume fraction and mass transfer coefficient were very good for the spiral liquid flow method, especially when low gas flow rates are used. Similar

results were achieved at low gas flow rates using the pressurised dissolution pump, however the other methods all allow for a much greater range of gas flow rates to be used. All of the microbubble generation methods were found to require a high power input to achieve a similar rate of oxygen transfer when compared to typical gas distributors. Ikeura et al. (2011) compared the effectiveness of ozone microbubbles generated by the pressurised dissolution and spiral liquid flow techniques for the removal of residual pesticides from vegetables. The pressurised dissolution method was found to be the most effective method, which was attributed to the smaller bubble size and greater number of bubbles produced.

Mass Transfer

Microbubbles have been investigated as a potential method for intensifying mass transfer in gas-liquid systems in a relatively small number of studies. Bredwell and Worden (1998) investigated the mass transfer of pure oxygen in a bubble column, with microbubbles generated using a disc-type microbubble generator, and stabilised by the surfactant Tween 20 to give a mean diameter of 50-60 μm. The presence of high levels of surfactant used to stabilise the bubbles were observed to reduce the mass transfer rate by up to 75% due to the encapsulation of the bubbles in a charged layer, however the measured $k_L a$ was still significantly higher when compared to conventional gas sparging. However, subsequent computational modelling of a single microbubble in an infinite liquid (Worden and Bredwell, 1998) suggests that non-transferring gases such as nitrogen in air will provide a significant further resistance to mass transfer, and that microbubbles are therefore more suited to use with non-mixture gases. The optimisation of a disc-type microbubble generator is also presented by H.S. Kim et al. (2018) based on $k_L a$ measurements calculated by using the dynamic method as discussed in Section 2.2.4. The mass transfer performance of fluidic oscillation microbubble systems has also been evaluated for the stripping of dissolved CO_2 using Nitrogen microbubbles in an airlift reactor, monitored by pH measurements, showing an improvement in CO_2 removal rates of up to 29% (Al-Mashhadani et al., 2012).

The effect of varying salinity (Kawahara et al., 2009) and surfactant concentrations (Liu et al., 2009) on the $k_L a$ have been investigated, both calculated from measured dissolved oxygen concentration curves. The $k_L a$ has also been investigated in reacting systems, with Li et al. (2016) using a sulphite system to evaluate the mass transfer of oxygen from air

achieved by using a microbubble generating pump recirculating within a standard single-impeller stirred tank. It is suggested that the impeller has little influence on the $k_L a$ in the microbubble system. Khuntia et al. (2013) investigated the mass transfer of ozone, also generated by using a microbubble pump system, for ammonia removal applications at different ozone generation rates in a sealed reactor. Similarly, the mass transfer of ozone into water has been characterised across a wide range of ozone flow rates by Chu et al. (2007; 2008), also using a microbubble pump. This setup is then used to investigate water treatment applications.

In addition to investigating mass transfer, Bredwell and Worden (1998) used microbubbles of syngas during a fermentation of *B. methylotrophicum* using the same spinning disc generation method in an external loop with cell filtration. It is suggested that minimal modifications are required to apply this microbubble technology to existing bioreactor designs, making use of the existing sparging and mixing apparatus. Successful microbubble fermentations have also been reported for the yeast *Saccharomyces cerevisiae* (Kaster et al., 1990; Hensirisak et al., 2002) and the filamentous fungus *Trichoderma reesei* (Weber and Agblevor, 2005), all also using surfactant-stabilised microbubbles generated using the spinning disc technique in an external loop. Microbubbles produced by using a Nikuni pump have been used for aerobic fermentations using the yeast *Rhodoturula mucilaginosa* at the 40 L scale (Ago et al., 2005), using air as the gas phase. This was achieved by running the entire liquid phase through the pump without the separation of cells required for the spinning disc technique described above. It was found that comparable $k_L a$ and cell growth could be achieved using a much smaller gas flow rate using the microbubble pump when compared with traditional air sparging. Finally, bubbles produced by fluidic oscillation have been used in the pilot-scale cultivation of the microalgae *Dunaliella salina* (Zimmerman et al., 2011) using CO_2 gas with a mean bubble diameter of 311 µm and *Saccharomyces cerevisiae* (Hanotu et al., 2016) with a reported mean diameter of approximately 300 µm. Although these diameters fall outside of the normal definitions of microbubbles, the small bubble size is shown to give sufficient mass transfer without the need for stirring.

7.2 Experimental

7.2.1 Generation of Microbubbles

A stable stream of microbubbles is generated within a fixed volume of fluid using a Nikuni KTM20 microbubble pump (Pridham, 2015) supplied by *Aeration and Mixing Ltd*., as shown

in Figure 7-2. A cross-sectional diagram of the pump design is presented in Figure 7-2 a), whereas Figure 7-2 b) shows an operating pump, with the high concentration microbubbles causing the aerated water in the clear tank to appear white. Air is introduced close to the inlet of the pump at 10% v/v, and the pump uses a specially designed centrifugal impeller to pressurise the system and mechanically break down the gas bubble size within the mixed stream. The flow passes through a pressurised settling tank (up to 10 bar) where a large proportion of the gas dissolves into the liquid in accordance with Henry's Law, and any larger bubbles can rise out of solution and are vented via a lift valve at the top of the settling tank. At the outlet of the settling tank, the system is depressurised and a stream of stable microbubbles in solution is generated. This is then released into the bulk liquid where further mass transfer may occur.

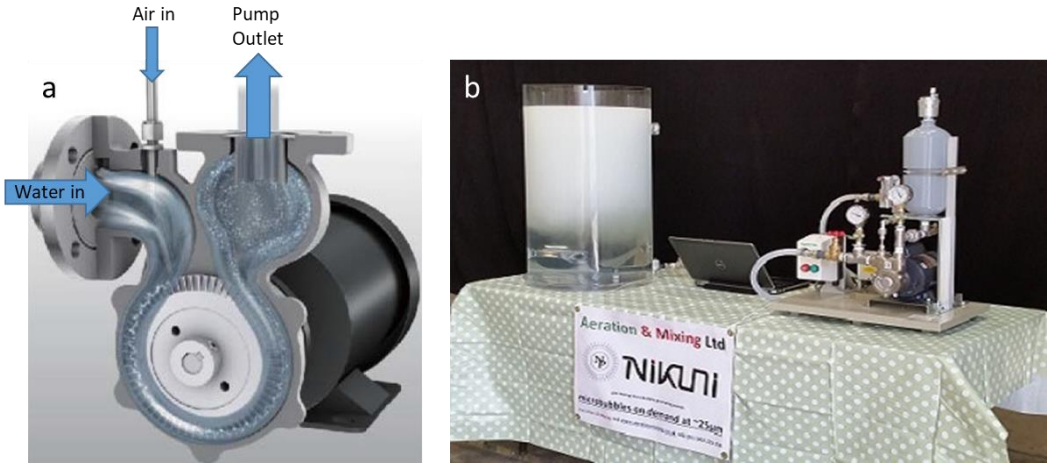

Figure 7-2: Images of the Nikuni KTM20 microbubble pump (Pridham, 2015).
a) cross-section of the pump, b) pump operating with an air-water system.

The properties of the microbubble stream can be modified by varying the upstream and downstream pressures for the pump. Details of the optimised operating conditions for the microbubble pump are provided in the manufacturer supplied documentation (Pridham, 2015). These are summarised in Table 7-1 and are used in all following analysis to produce a stable, reproducible stream of microbubbles in water.

Table 7-1: Microbubble pump operating conditions.

Liquid Flow Rate	16.6 L min^{-1}
Gas Flow Rate	1.6 L min^{-1}
Discharge Pressure	3 to 4 bar(g)
Suction Pressure	-0.2 to -0.3 bar(g)

7.2.2 Measurements of $k_L a$ (Variable Liquid Volume)

The flow rate of liquid and gas through the recirculating loop is determined by the pump capacity at the given operating conditions (Table 7-1), however the volumetric aeration rate for the system may be varied by changing the volume of liquid in the measurement tank. Initially, the water in the measurement tank and recirculating loop is deoxygenated using the microbubble pump, with a feed of pure nitrogen (BOC) used to strip the dissolved oxygen in solution to below 10 % of saturation. The dissolved oxygen concentration and temperature are measured by using a combined galvanic probe (Oakton DO600), which is fully submerged within the measurement tank (15, 70 or 500 L volume) as shown in Figure 7-3. The location of the probe within the tank is not expected to significantly influence the results, and the probe is therefore located so as to minimise interactions with the flow patterns created by the inlet and outlet streams from the pump. However, the probe location is maintained between different runs and conditions in each vessel used to ensure comparable readings.

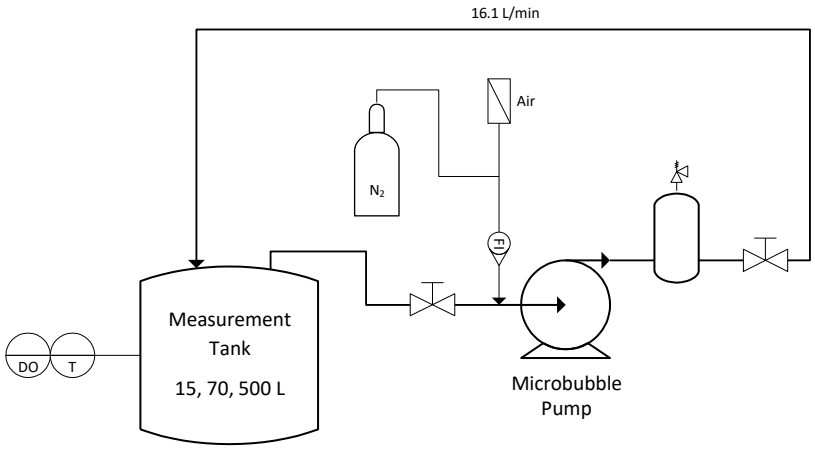

Figure 7-3: Flow diagram for the variable volume $k_L a$ microbubble experiments.

In addition to the liquid volume, different tank sizes and geometries are considered. These consist of a glass culture flask with a maximum filled volume of 15 L, a cylindrical HDPE storage drum with a maximum filled volume of 70 L and a rectangular HDPE storage tank with a maximum filled volume of 500 L. Images of these vessels are presented in Figure 7-4. The use of multiple measurement tanks allows for a wide range of liquid volumes and aspect ratio conditions to be compared for a single microbubble flow rate. Reinforced half-inch tubing is used for the pump inlet and outlet, with the exception of the 500 L rectangular tank which has a built-in drain in one corner which is used to feed the pump and drain the tank. The water temperature at the beginning of the measurement is

adjusted to 25°C, although the heat generated by operating the microbubble pump causes some heating of the liquid by up to 5°C during the course of the measurement process.

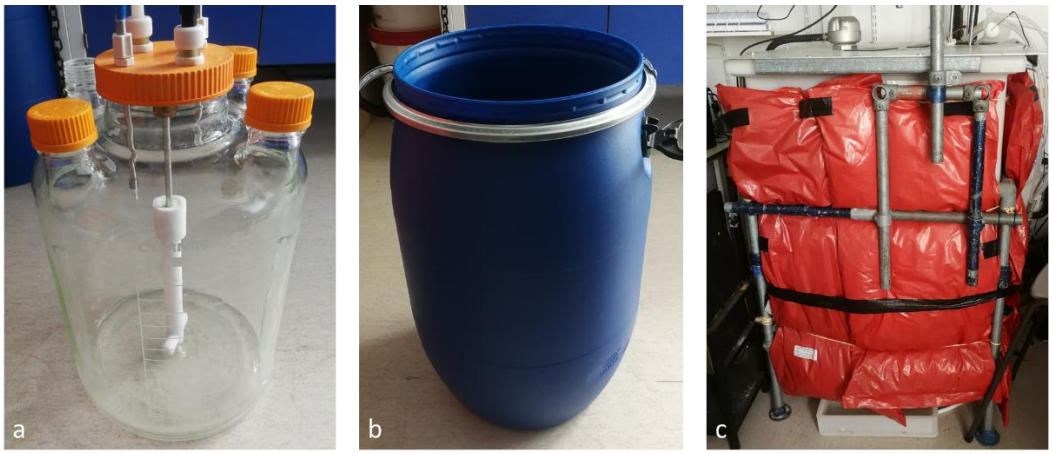

Figure 7-4: Tanks used for the microbubble mass trnasfer experiments.
a) spinner flask - 15 L, b) cylindrical drum - 70 L, c) rectangular tank - 500 L.

7.2.3 Measurements of $k_L a$ (Variable Flow Rate)

In addition to varying tank volume, the effect of different microbubble stream flow-rates are considered for the spinner flask with a fixed liquid volume of 10 L. Since the flow rate of the pumping circuit is fixed, a splitter is required downstream of the settling tank, where a needle valve is used to vary the flow rate into the measurement tank up to a maximum of 2.51 L min^{-1}. As with the variable volume method, a large volume of water is deoxygenated in the previously used 500 L tank using the microbubble pump fed with pure nitrogen, via the dashed circuit in Figure 7-5. Once the oxygen level in the feed tank has fallen below 10% of saturation and the nitrogen bubbles have risen out of solution, the system is configured as shown by the solid lines in Figure 7-5, with the pump outlet stream being split between the 10 L measuring tank and the rest sent to drain. This ensures that there is no pre-mixing of the oxygenated and deoxygenated streams before entering the measurement tank. The feed gas is then switched to air and the set flow rate fed into the measurement tank, where the dissolved oxygen is measured as before. The level of liquid in the measurement tank is kept constant throughout the measurement process by manually controlling a valve on the outlet stream of the measurement tank, which is then also sent to drain.

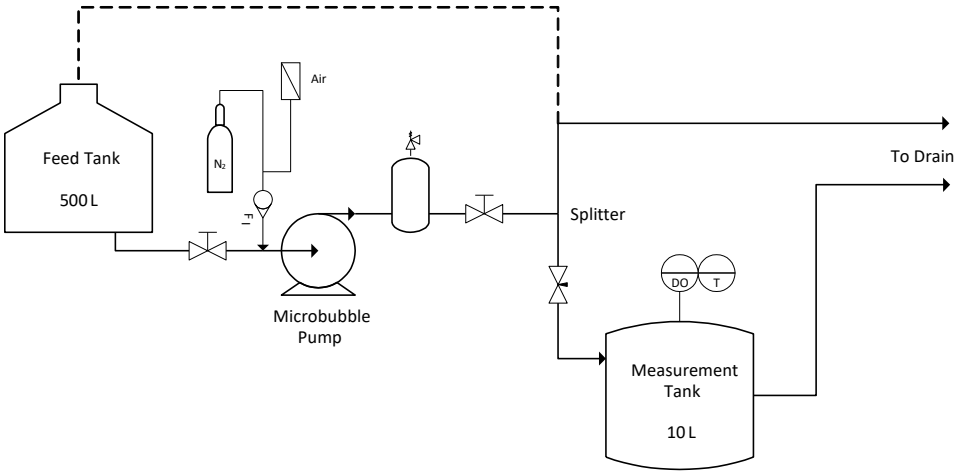

Figure 7-5: Flow diagram for the variable flow rate $k_L a$ microbubble expreiments. The dashed line represents the system during the initial deoxygenation phase.

7.3 Imaging and Sizing of Microbubbles

The sizing of bubbles within a microbubble swarm is achieved by using a custom-built sizing apparatus by applying image processing techniques in MATLAB. To the naked eye, microbubble-containing flows appear as a cloudy solution (see Figure 7-2 a), making it impossible to identify individual bubbles using standard camera imaging in a clear-walled tank. Instead, a high-magnification camera (Thorlabs DCU224M with MVL 6.5× zoom optics) is used to capture individual bubbles within a 10 mm deep polycarbonate slit as shown in Figure 7-6. A continuous feed of microbubbles in water is distributed via a series of 1 mm holes along the bottom of the slit, with excess liquid exiting at the top of the slit which measures 500 mm tall and 110 mm wide. Backlighting is provided via an LED array positioned in-line with the measurement volume, with a translucent diffuser sheet placed between the light source and the measurement slit to smooth out the light from the individual LEDs. The camera is maintained in a fixed location for this analysis, approximately two thirds of the way up the centre of the slit, although it is mounted on a manual x-y-z stage so that the analysis can be repeated in multiple locations in the future. The camera readout is sent to a computer, where a scale with 0.1 mm intervals is imaged at the chosen zoom level to provide a known distance. The position of the camera is adjusted to be equidistant between the front and back walls of the slit.

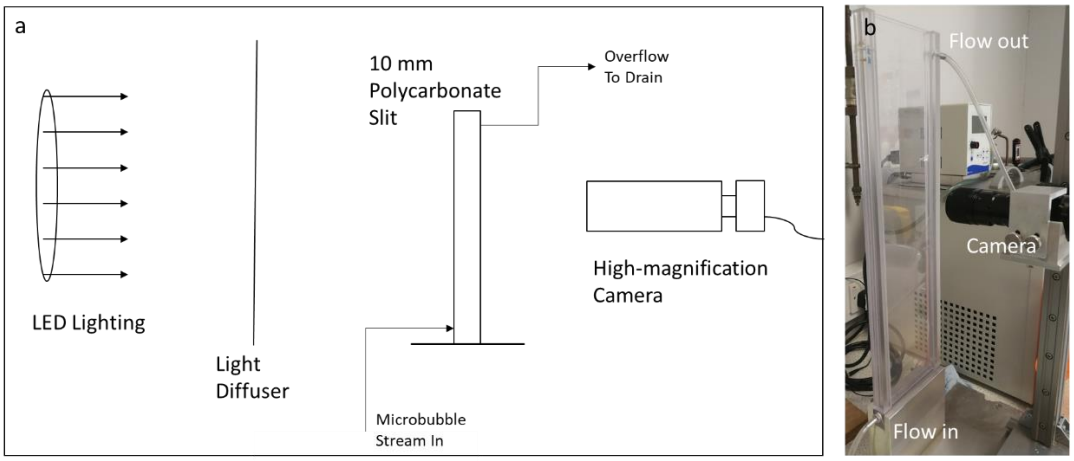

Figure 7-6: Diagram of the experimental setup for the microbubble sizing technique. a) Diagram of the experimetnal setup, b) image of the 10 mm slit used for sizing.

A flowchart of the image processing protocol developed for sizing the microbubbles is shown in Figure 7-7. An alternative image processing technique to the watershed method presented in Section 6.6 is required due to the unique physical properties of microbubbles, which appear as perfectly circular regions in the images. There is also a very strong requirement to remove out-of-focus bubbles from the final analysis due to the high levels of magnification used. Bubble images captured by the high-magnification camera are recorded and loaded into the MATLAB programme in series as .tif files, and analysed using built-in functions. Individual bubbles can be identified as dark circular regions on the images, and a threshold value of light intensity can therefore be used to distinguish between the gas and liquid phases. A manual threshold value is assigned to distinguish between the two phases, the value of which is identified through trial and error for each set of images. This method was judged to identify the interface between the gas and liquid phases better for this case than automatic methods such as Otsu's method (Otsu, 1979). Several filters are then applied to the binary image so that only individual, in-focus bubbles are recorded, as detailed below. This is repeated for several sequential bubble images until a sufficiently large population of bubbles has been captured. The MATLAB code used for this analysis can be found in Appendix G.

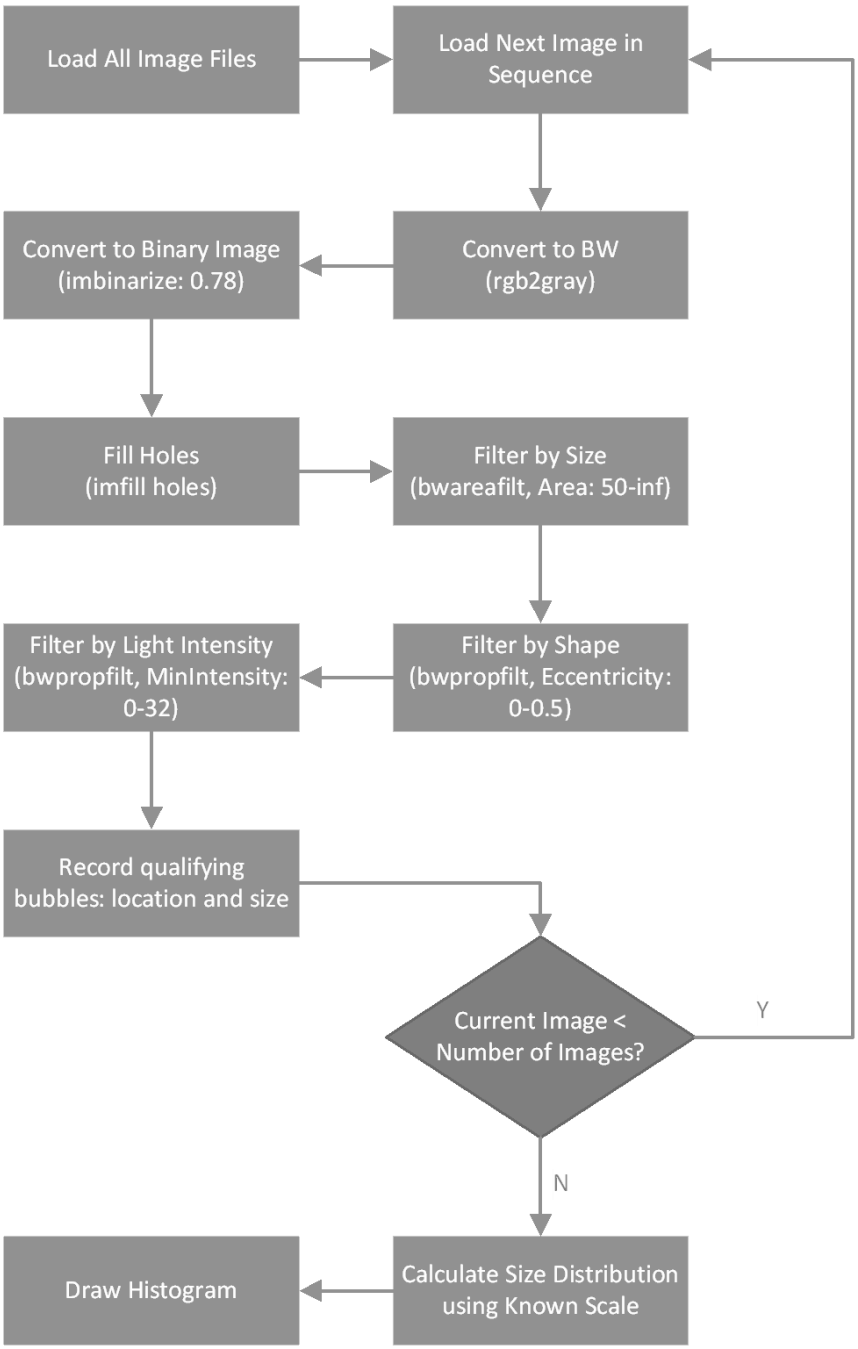

Figure 7-7: Flowchart of the image processing procedure for a series of microbubble images. The names of built-in MATLAB functions used are given in brackets.

The effects that some of the key filters applied during the microbubble image processing have on a typical microbubble image are presented in Figure 7-8, with the scale bar used to provide a known distance shown in Figure e). Figure 7-8 a) shows the captured image converted to black and white, whereas image b) shows the same set of bubbles with a global threshold value of 0.78 applied for the light intensity in order to create a binary image, and the 'imfill' function applied to fill in any completely enclosed holes at the centre

of bubbles. It is clear that there are several shapes in Figure 7-8 b) which are not spherical, and are therefore not representing individual, in-focus bubbles, such as the overlapping pair of bubbles highlighted by the blue box. When compared to the original image, the majority of these can be identified as out-of-focus bubbles, bubbles intersecting the edge of the frame or multiple overlapping bubbles. These are filtered out of image c) according to their shape, based on the eccentricity value, using the 'bwareafilt' function. Only shapes that are sufficiently spherical, with respect to the user defined eccentricity limit, to be regarded as individual bubbles are retained in the final image. The final filtering step described in the flow chart is based on the minimum light intensity in the original greyscale image (Figure 7-8 a). Bubbles with a low light intensity, and which therefore appear darker in image a), are considered to be in focus, whereas out of focus bubbles will have a higher light intensity. This property is used to remove any remaining out-of-focus bubbles from Figure 7-8 c), such as the one highlighted by the red box, leaving Figure 7-8 d) containing only the individual, in-focus bubbles which are used for the sizing statistics. All of the numerical values in this analysis have been set through trial and error, and have therefore been subjected to sensitivity analyses as reported in Section 7.3.1.

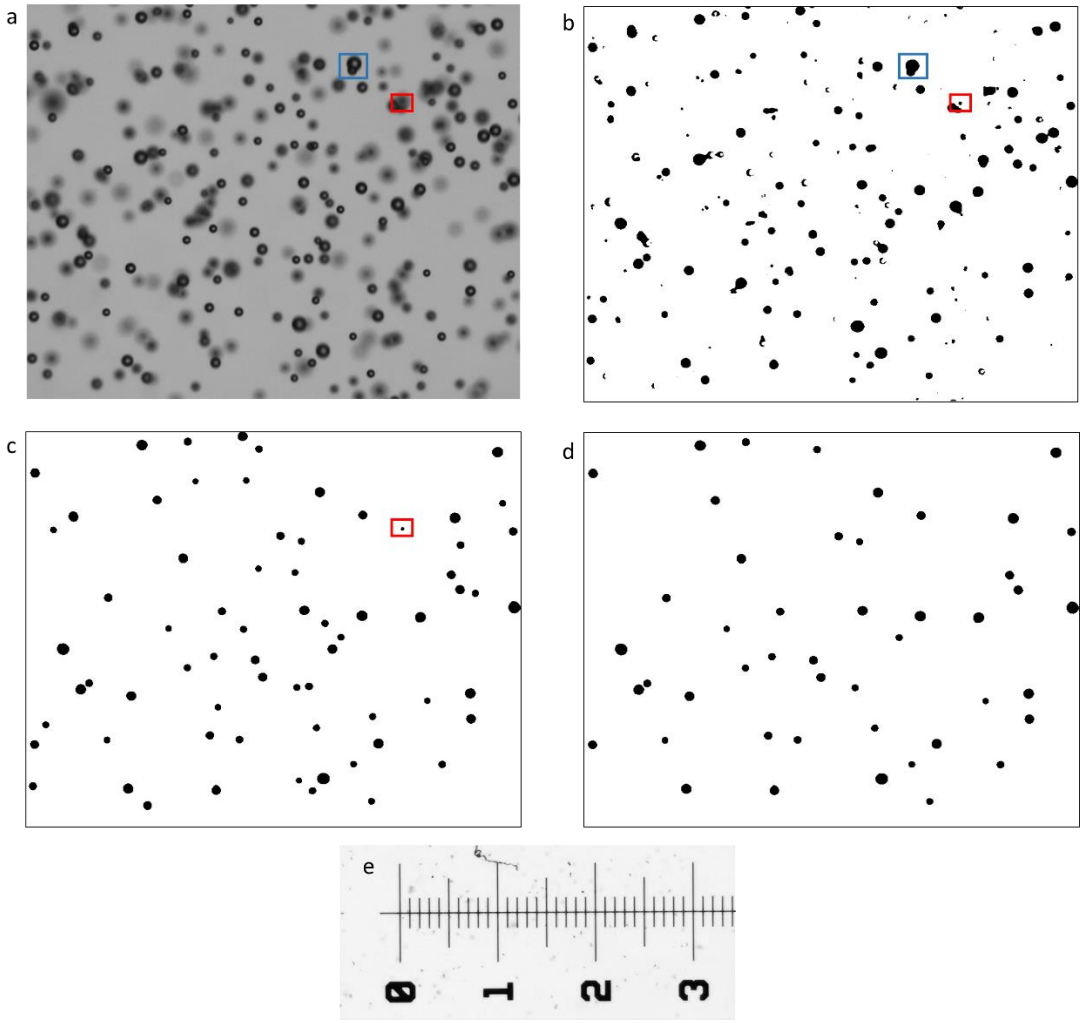

Figure 7-8: Representative microbubble image after various stages of filtering.
a) Black and white image, b) binary image, c) filtered by shape, d) filtered by minimum intensity, e) scale used for sizing (numerical values in mm).

By compiling the analysis of a large number of individual images taken sequentially, using the lowest permitted frame rate to minimise the chance of capturing the same bubble more than once, it is possible to build up a large population of valid bubbles which can be used for statistical analysis. The bubble size distribution presented in Figure 7-9 is developed from 200 individual images, giving a total population size of 4,938 individual bubbles. During the measurement time, the temperature measured in the slit using a digital thermometer did not vary from 25°C by more than ±0.5°C. The size distribution has a smooth shape with maximum population percentage in the 110 µm fraction, which is close to the mean bubble diameter of 101 µm. The distribution covers a large range of bubble sizes, within the limits of 65 to 175 µm diameter. The distribution is slightly steeper for smaller sized bubbles, with a relatively small number of much larger than average bubbles identified.

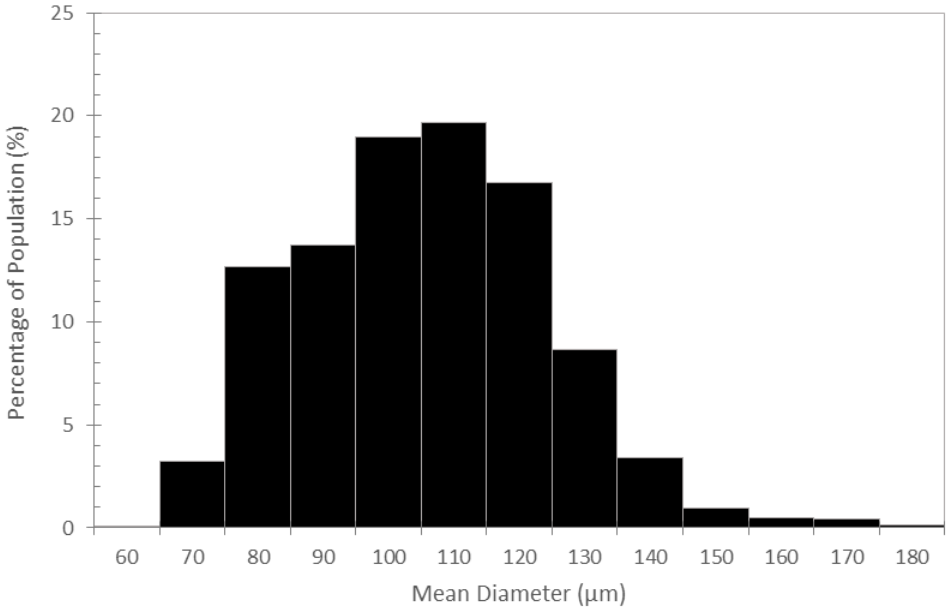

Figure 7-9: Bubble size distribution for microbubles in solution at 25°C.
Pupulation size = 4,938 bubbles from 200 sequential images.

7.3.1 Sensitivity Analysis of the Microbubble Sizing Technique

The first factor that may limit the accuracy of the sizing technique is the population size used. The population size is dependent of the number of images used in the analysis and the level of magnification applied to the lens optics. In order to assess the dependence of the mean bubble diameter on the population size, the series of images used to generate Figure 7-9 is used with an increasing number of images so that the population size is varied. The series always starts with the same image, with additional images being added sequentially to the end of the series to increase the population size, as represented by Figure 7-10 a). Up to a population size of approximately 1,000 bubbles, the calculated mean diameter is shown to be dependent on the population size, however between 1,000 and 2,000 bubbles there is little difference in the mean bubble size recorded. Further increases in population size also yield no significant deviation in mean diameter, showing that a population of at least 1,000 bubbles is required to accurately capture the distribution in bubble size.

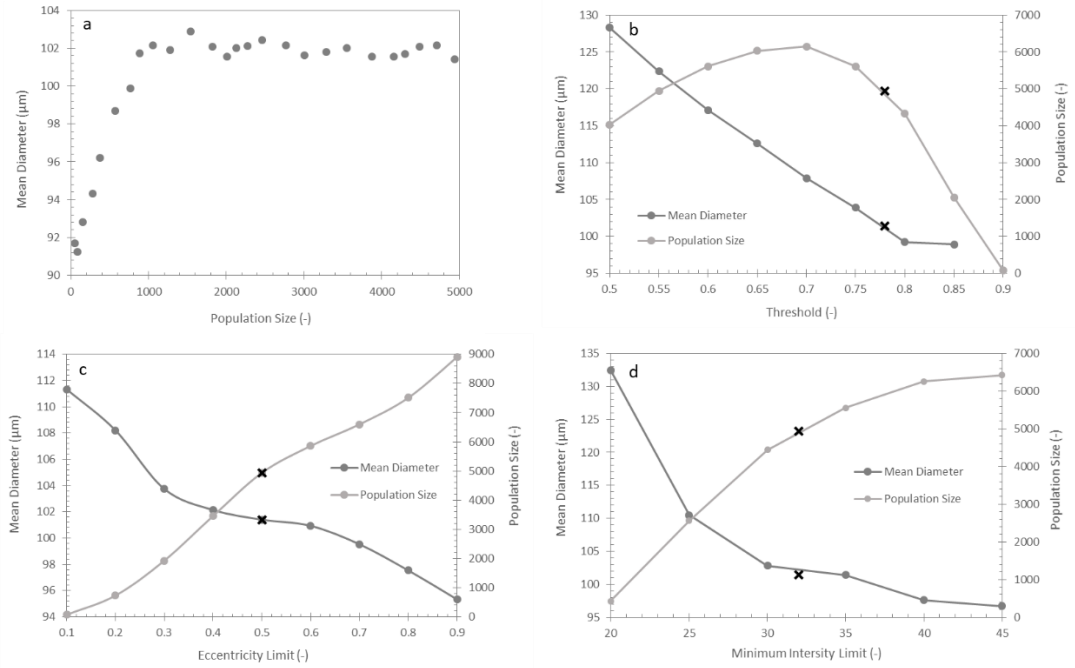

Figure 7-10: Multiple sensitivity analyses for the proposed microbubble sizing technique. a) population size, b) global threshold value, c) eccentricity, d) minimum light intensity.

Further sensitivity analyses were carried out on three additional user-defined parameters in the sizing programme described in Figure 7-7, namely the light intensity threshold for the binary image, the eccentricity of identified shapes and the minimum light intensity value applied for a bubble to be identified as existing in the focal plane. Figure 7-10 b) shows the variation in mean bubble diameter and population size with varying light intensity threshold values, with the selected value of 0.78 represented using the black cross symbol. Reducing the threshold below the selected value causes an increase in bubble size as more of the bubble outline is included for previously identified bubbles, and more out-of-focus bubbles with a larger apparent size and dark appearance are included. The population size is at its largest with a threshold value of approximately 0.7, reducing steeply to zero for a threshold of 0.9 as the majority of bubbles are no longer identified as complete circles. The bubble sizing can therefore be said to be reasonably sensitive to the threshold value used.

The variation in mean bubble diameter and population size with changing shape eccentricity is shown in Figure 7-10 c). Increasing the eccentricity limit increases the number of identified bubbles, as represented by the population size, as more non-circular shapes are considered. However, this also increases the likelihood of capturing objects other than single bubbles, such as overlapping bubbles or bubbles intersecting the edge of the frame. From the value selected, it can be seen that shifting the eccentricity limit in

either direction by a value of 0.1 does not have a large influence on the mean bubble diameter, suggesting that the sizing method is not very sensitive to the eccentricity limit applied in the region selected. Similarly, the variation in mean bubble diameter with the minimum light intensity is shown in Figure 7-10 d). Once again, the variation in mean diameter is fairly small in the region close to the selected value of 32, suggesting that the method is not very sensitive to these parameters, however reducing the applied intensity limit blow 30 causes the mean diameter to increase rapidly and the population size to decrease. This is because only the largest bubbles, which obscure the most light, are captured by this region. In contrast, the population size continues to increase as the minimum intensity limit is increased since more out-of-focus bubbles are included, further decreasing the mean diameter as bubbles with poorly defined boundaries are included in the analysis.

Finally, the experimental image sizing technique used to generate Figure 7-9 is repeated for two further optical magnification levels of 1.8 and 2.2 times the base magnification of the lens. The optimisation of the user-defined parameters outlined in Figure 7-7 is performed individually for each magnification level as previously described. The bubble size distributions generated by using the different magnification levels are compared in Figure 7-11. The three different magnification levels can be said to represent a similar size distribution, although there are some differences in the shape and range of each individual distribution. However, there is no trend between the magnification used and the position of the distribution peak, with the mid-range magnification producing the highest average bubble size. Furthermore, the risk of capturing the same bubble in two consecutive images, thus skewing the results towards smaller bubbles which have a lower rise velocity, does not appear to be a significant factor, since the analysis at magnification levels of 1.25 and 2.2 produce reasonably similar profiles. It is therefore likely that the differences presented in Figure 7-11 occur as a result of the sensitivities in the processing technique discussed previously in this chapter and operating variables such as the flow rate into the slit, and not as a result of the magnification level used.

Examples of this analysis with different threshold values, eccentricity limits and minimum light intensity are presented in Appendix H.

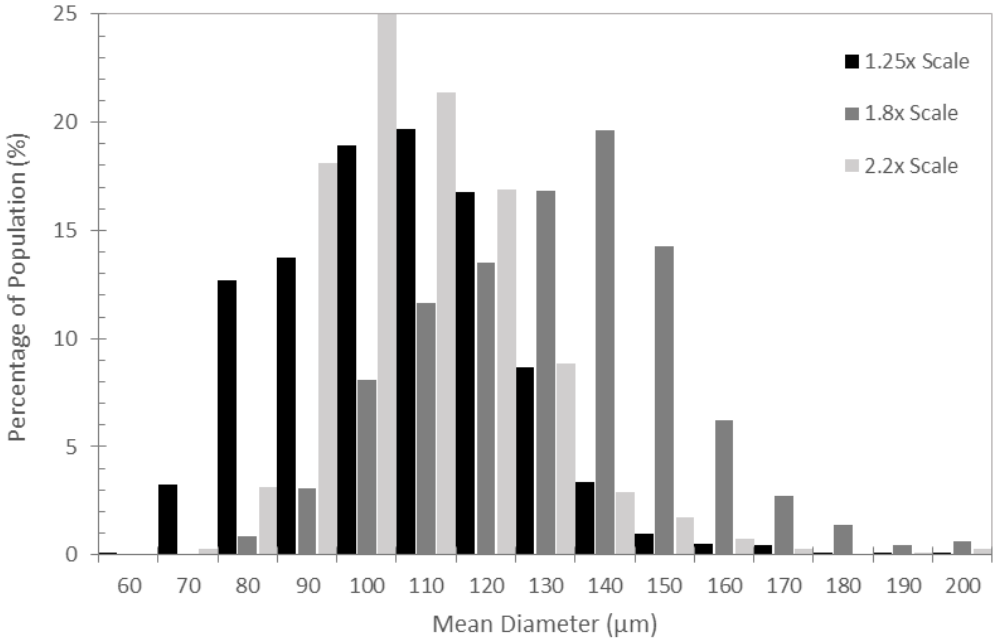

Figure 7-11: A comparison of the bubble size distributions produced using different levels of physical magnification for microbubbles in solution at 25°C.

7.4 Measurement of $k_L a$

Due to the very small size of the microbubbles generated using the Nikuni pump system, they have a great potential for improving mass transfer through a vastly increased interfacial area between the gas bubbles and the liquid phase. Furthermore, the high pressurisation in the recirculation loop which is used to generate the bubbles via the pressurised dissolution mechanism described in Section 7.1 is likely to further increase the mass transfer potential of the pump, particularly in closed systems. This efficient use of the gas phase can be considered in two different ways – an increase in mass transfer performance for the same amount of gas introduced, or the ability to achieve a specified mass transfer performance with significantly less gas usage than traditional sparging. The second of these is particularly beneficial when high-value or hazardous gases are to be used by minimising the amount of gas present within the system at any given time.

The mass transfer performance of the microbubble pump is first evaluated in comparison to the stirred tank experiments detailed in Section 6.7 for the validation of the BioMOD model. Figure 7-12 shows the experimental oxygen uptake profile in comparison to the stirred tank previously studied for the same volumetric aeration rate of 0.21 vvm. The gradient of the microbubble curve shows that the rate of mass transfer when using

microbubbles is far in excess of what can be achieved with traditional air sparging and stirring. Furthermore, the use of the microbubble pump leads to a clear supersaturation of oxygen dissolved within the liquid phase due to pressurisation within the settling tank and the high internal pressure generated within the individual microbubbles, which will be beneficial for interphase mass transfer into the liquid via Henry's law. For Figure 7-12, the dissolved oxygen concentration is normalised against the saturation concentration of oxygen in water at 25°C under atmospheric conditions, as previously presented for the validation tank in Figure 6-13. In order to provide the clearest comparison between the different tanks used in the microbubble experiments, subsequent mass transfer profiles in this chapter have been normalised so that the oxygen concentration measured at the end of each experiment (once a stable reading has been reached) using the DO meter is considered to be the 100% point for each curve. It is assumed that final degree of supersaturation in relation to the atmospheric saturation conditions will be the same for each system studied since the pump operating conditions are maintained at the manufacturer specified values.

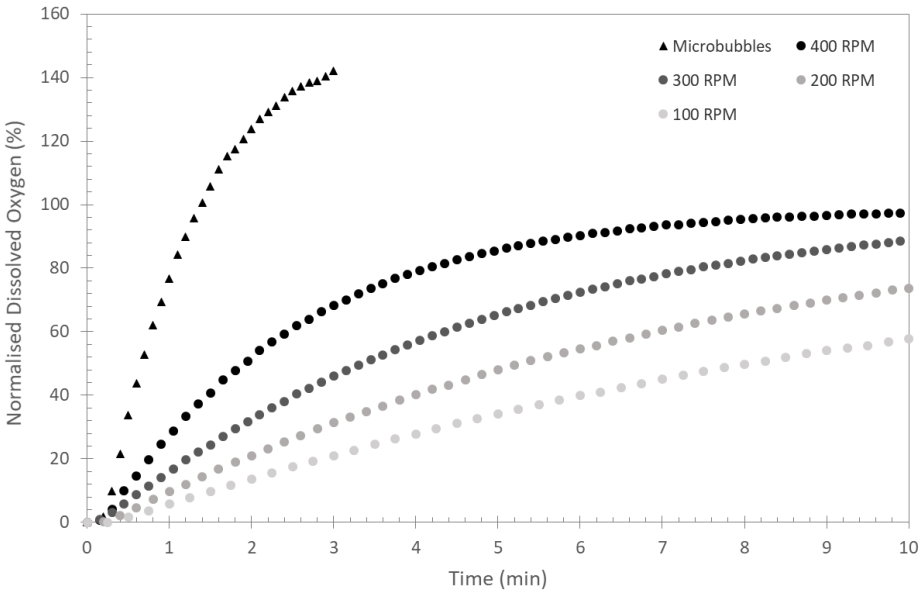

Figure 7-12: Comparison of the microbubble mass transfer performance (including supersaturation) with the sparged stirred tank presented previously in Figure 6-13 for a vvm of 0.21. Normalised against the saturation concentration of dissolved oxygen under atmospheric conditions.

7.4.1 Variable Volume $k_L a$ Measurements

Despite the relatively low volumetric aeration rate used, the volume of liquid used for the microbubble profile in Figure 7-12 (7.62 litres) is very small in relation to the capacity of the pump, leading to a residence time in the measurement tank of just 27.5 seconds. The mass transfer performance of the pump has therefore been evaluated for increasing volumes of water up to a tank volume of 200 L, representing a residence time of 12 minutes. In order to achieve this, three different tanks have been used, as shown in Figure 7-4. Profiles of dissolved oxygen against time are presented in Figure 7-13 for each of the liquid volumes detailed in Table 7-2. Each profile represents the mean of three experiments, with error bars representing the standard deviation from the mean. The error bars are very small for each of the dissolved oxygen profiles, suggesting that the results obtained by using this method are very reproducible. The time required to reach 90% of saturation is also presented in chart d) for each of the profiles included in Figure 7-13 a-c, plotted against the liquid volume. This suggests an approximately linear relationship between the mass transfer performance and the liquid volume, regardless of the geometry of the tank used.

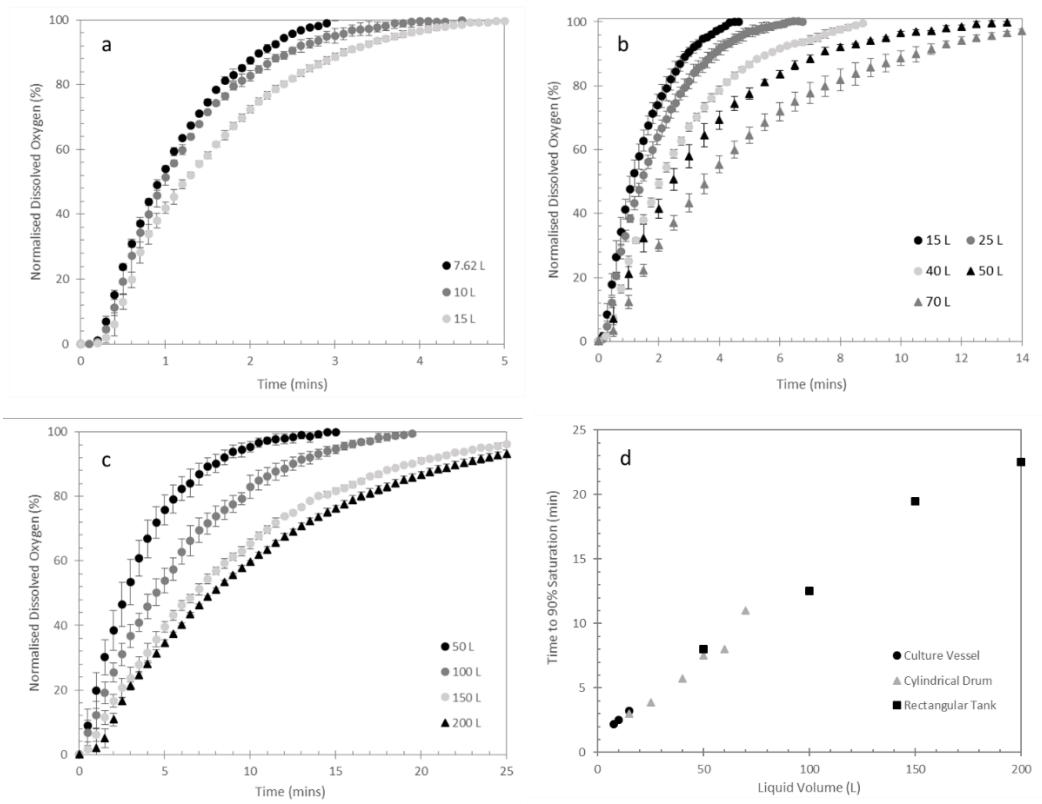

Figure 7-13: Profiles of dissolved oxygen versus time for different tank geometries and liquid volumes by using the Nikuni microbubble pump.
a) culture vessel, b) cylindrical drum, c) rectangular tank, d) time to 90% saturation.
Error bars represent the stanard deviation from three experiments.

In addition to varying the volume of liquid, each of these profiles also represents a different tank geometry or aspect ratio. For example, the rectangular tank with a filled volume of 50 L has a large surface with a shallow level of water. In contrast, the cylindrical drum with the same filled volume will have a relatively small liquid surface area and a large filled height. Despite this, the mass transfer performance of the microbubble pump system has been shown to be independent of the geometry of the measurement tank used, as represented by the overlap in $k_L a$ between different geometries in Figure 7-14. The volume-averaged $k_L a$ values calculated for each of the tank geometries and volumes used – calculated by linearising the curves in Figure 7-13 using equation (2-6) – are shown in Figure 7-14, plotted against tank volume (a) and volumetric aeration rate, vvm (b). The corresponding R^2 values for each of the average $k_L a$ values calculated is presented in Table 7-2, with all values in excess of 0.99 showing a very good fit to the expected trend without the need for any corrections for experimental factors such as probe response time. There is an overlap in liquid volume at 15 L (culture flask and cylindrical drum) and at 50 L (cylindrical drum and rectangular tank). For each of these cases there is no significant variation in the measured $k_L a$ between the two vessels. Furthermore, both of the profiles in Figure 7-14 are smooth and show no immediate variation where there is a crossover between geometries between 50 and 70 L. This is because the microbubbles are distributed evenly between all regions of the tank, with a further large degree of mass transfer expected to occur within the external pump loop. This suggests that the design of the sparging and mixing is much less critical for mass transfer performance when using the microbubble pump than for traditional two-phase contactors, and microbubbles can therefore be used for non-standard applications with a much greater degree of confidence.

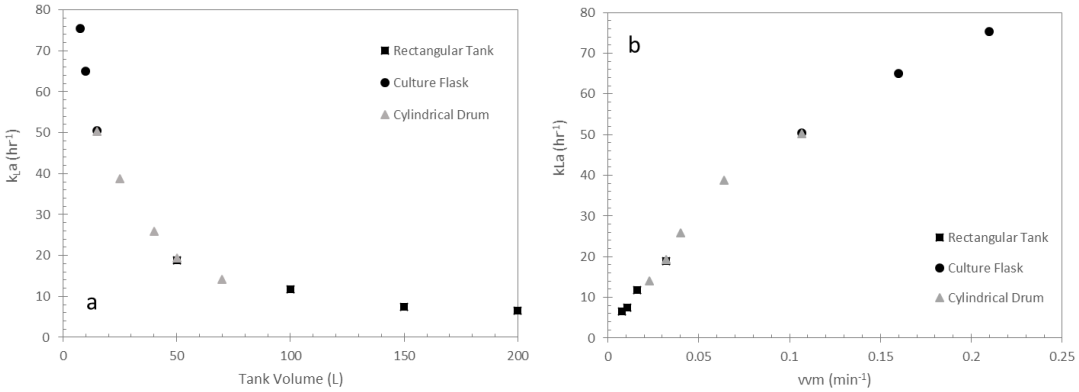

Figure 7-14: The combined change in measured $k_L a$ with a) tank volume and b) vvm using the Nikuni microbubble pump with different tank geometries.

The trend in $k_L a$ with tank volume shows a steep increase towards very small fluid volumes, however it is unfeasible to operate the full pump capacity with such low liquid volumes. However, when the same data is plotted against vvm, there exists a positive, although slightly non-linear trend with increasing vvm. This profile can be used to predict the mass transfer performance of any air-water system in conjunction with the Nikuni microbubble pump, regardless of tank geometry. Furthermore, the supersaturation seen in Figure 7-12 means that the true mass transfer performance in comparison to traditional air sparging will be greater than the numerical value of $k_L a$ presented. Using a vvm of 0.1, as applied for the full-scale BioMOD reactor studied in Chapter 5, gives a $k_L a$ in the region of 50 hr^{-1}, which represents a significant improvement in mass transfer without the need for internal agitation or separate air sparging. However, this vvm could only be achieved at the required scale by using a potentially restrictive pumping capacity of 1,000 L min^{-1} at the specified air-water ratio, whereas the largest single pump manufactured by Nikuni has a capacity of 700 L min^{-1}. In order to confirm this pumping requirement, the performance of larger pumps or multiple pumps in parallel will need to be studied in a similar way to determine the scalability of these curves. Alternatively, using the smaller Nikuni pumps with pure oxygen or oxygen-enriched air could become a more viable option since the gas is present in relatively small volumes and there is therefore no need to over-pressurise the SUT bag.

Table 7-2: Summary of conditions applied for the variable volume microbubble mass transfer experiments.

	Volume (L)	**Air Flow Rate (L min^{-1})**	**vvm (min^{-1})**	**$k_L a$ (hr^{-1})**	**R^2**
Culture Vessel	7.62	1.6	0.210	75.4	0.9864
	10	1.6	0.160	65.1	0.9956
	15	1.6	0.107	50.4	0.9932
Cylindrical Drum	15	1.6	0.107	50.3	0.9896
	25	1.6	0.064	38.8	0.9929
	40	1.6	0.040	25.9	0.9979
	50	1.6	0.032	19.4	0.9952
	70	1.6	0.023	14.1	0.9954
Rectangular Tank	50	1.6	0.032	18.9	0.9967
	100	1.6	0.016	11.8	0.9927
	150	1.6	0.011	7.53	0.9957
	200	1.6	0.008	6.50	0.9964

7.4.2 Effect of Mixing

The modelling work conducted in support of the BioMOD project (Chapters 5 and 6) has shown that for typical two-phase stirred tank systems, the action of the impeller is very important in breaking-up bubbles to improve mass transfer performance through increased interfacial area. However, since the microbubble pump is able to produce a stable stream containing microbubbles, the introduction of mechanical agitation is expected to be less significant in the interphase mass transfer mechanism. In order to evaluate this influence, the six-bladed Rushton impeller detailed in Section 6.3.1 is used to provide stirring within the various measurement tanks at different rotational speeds. A comparison of the mass transfer profiles for the stirred and unstirred conditions is presented in Figure 7-15 for different stirrer speeds in three very different systems; 15 L filled volume in the culture flask, 50 L filled volume in the cylindrical drum and 200 L filled volume in the rectangular tank. In each of the cases, there is very little difference in the dynamic oxygen uptake curves between the stirred and unstirred curves, regardless of the stirring speed applied. This is significant as it suggests that the only stirring required when using microbubbles for fermentation purposes is to keep the solution mixed and any solids in suspension, and which may therefore offset the higher operating power required for the pump when compared to gas sparging in unstirred systems (Terasaka et al., 2011).

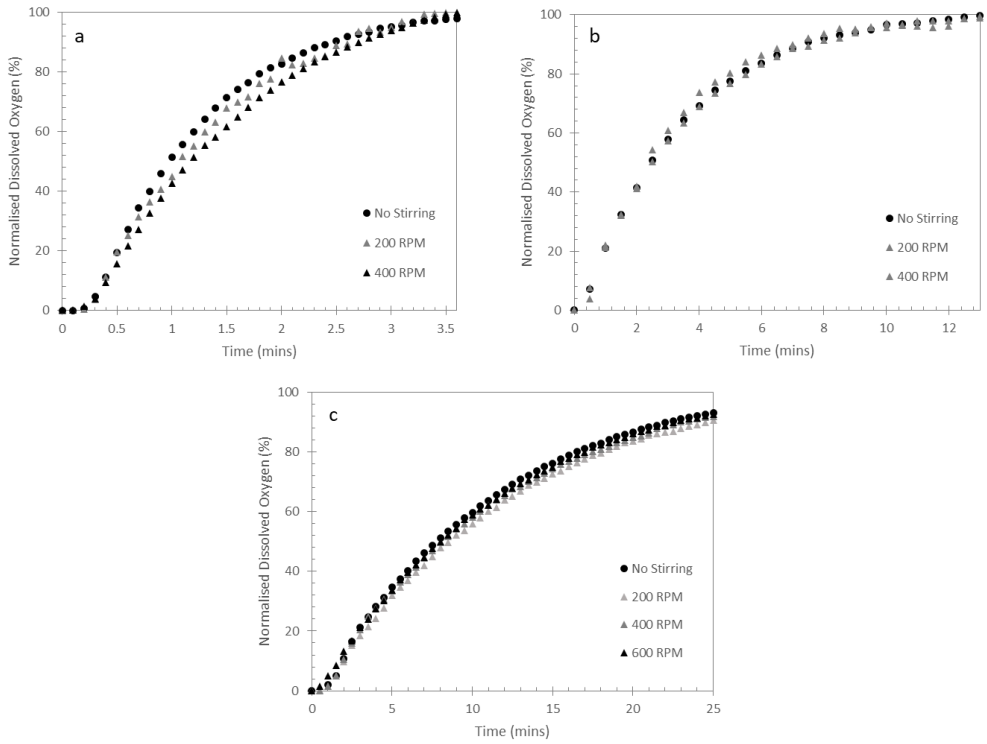

Figure 7-15: Profiles of dissolved oxygen versus time for different stirring speeds in different tank geometries using the Nikuni microbubble pump.
a) culture vessel - 15 L, b) cylindrical drum - 50 L, c) rectangular tank – 200 L.

7.4.3 Variable Flow Rate $k_L a$ Measurements

Whereas the previously presented mass transfer profiles have involved the full 16.1 $Lmin^{-1}$ capacity of the pump being recirculated within a fixed volume of liquid, the microbubble pump can also be used to provide a lower flowrate of microbubbles to a fixed volume using the setup described in Section 7.2.3. This setup represents a continual operation, since the level of liquid in the measurement tank is kept constant, and the system is therefore not left to reach saturation, as shown in Figure 7-16 a) for three different liquid flow rates. The deoxygenated water in the feed tank undergoes only a single pass through the microbubble pump, meaning that contamination of the feed tank is not an issue. The gradient of the profiles in Figure 7-16 b) represents the initial gradient of the same curves compared to the profiles from Figure 7-13 c), with different volume of liquid in the 500 L rectangular tank. This gives a reference for the initial mass transfer performance when the system does not reach saturation via the values presented in Table 7-2.

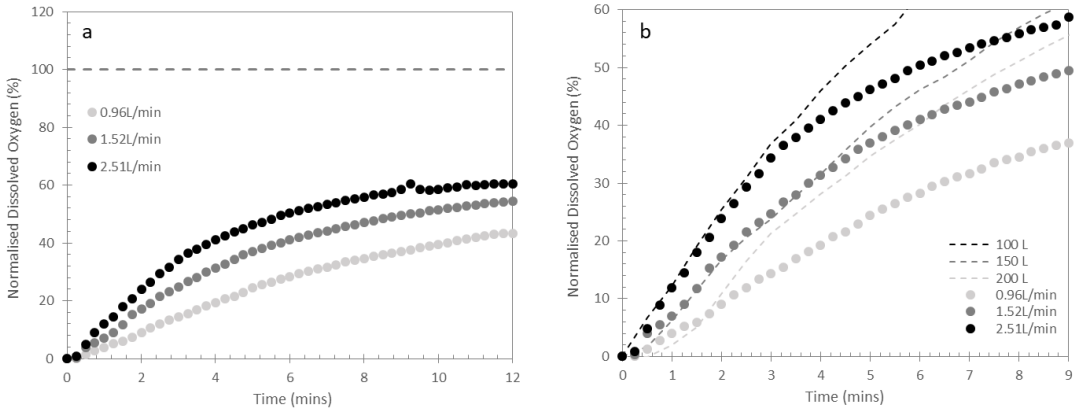

Figure 7-16: Profiles of dissolved oxygen versus time for different microbubble stream flow rates for a fixed 10 L tank volume.
a) compared to the previously measured oxygen saturation using the microbubble pump,
b) compared to the variable liquid volume experiments.

7.5 Summary

This chapter has investigated the use of a commercial microbubble generating pump (Nikuni KTM20) for mass transfer applications, following on from the hypothesis developed in previous chapters that the mass transfer rate in industrial processes is much more dependent on the bubble size than the hydrodynamic conditions. The microbubble pump has been experimentally characterised in terms of size distribution of bubbles produced in pure water by using a newly constructed apparatus consisting of a 10 mm deep transparent slit with backlighting and a high magnification camera. A measurement technique that uses MATLAB image processing functions to identify single, in focus bubbles has been developed, with a smooth distribution identified from a series of 200 images. This distribution has been used to characterise the microbubbles produced as having a mean diameter of 101.4 µm and a range of 65 to 175 µm. The imaging process has been evaluated with a series of sensitivity analyses for parameters such as population size, light intensity, bubble shape and zoom level. The distribution was found to be most sensitive to the threshold light intensity value used to distinguish between the gas and liquid phases, with the other factors deemed to have a minimal impact from small variations from the manually optimised values.

The mass transfer performance of the microbubble pump is characterised with a fixed pump flow rate of 16.1 $Lmin^{-1}$ and a 10% v/v aeration rate in three different vessels at a wide range of operating volumes between 7.62 and 200 litres. The mass transfer

performance, characterised in terms of $k_L a$, is shown to be very reproducible and independent of the geometry of the tank used. The effect of external stirring is also shown to be negligible on the mass transfer performance when using the microbubble pump. This means that a general relationship between the liquid volume and the $k_L a$ can be developed regardless of the tank design. Furthermore, the only stirring required for industrial mass transfer applications such as fermentations would be to keep the solid phase suspended, which could lead to large reductions in energy consumption, especially at large liquid volumes due to the non-linear scaling of impeller power with tank size highlighted for traditional systems in Section 2.1. The microbubble pump is also shown to be applicable to continuous flow conditions, achieving reasonable mass transfer performance through a single pass of the pump.

8 Carbonatation Process Modelling

This chapter details the development of a combined CFD and liquid-phase reaction model, applied entirely within the ANSYS CFX 17 framework, based on a current production-scale sugar cane refining process. The purpose of this modelling work is to better understand the dynamics of the existing process so that process improvement and scale-down to pilot scale may be implemented. The specifications of the existing equipment and process are provided, with CFD models developed incorporating reaction models derived from a reaction scheme previously applied to carbon capture and storage applications. In addition, the reaction model will allow for the better prediction of solids formation and pH under different operating conditions, both of which are critical parameters for downstream processing and filtration.

8.1 Introduction

Carbonatation is a process used to remove impurities during the refinement of cane sugar. Cane sugar refinement is a multi-stage process where impurities and colouring matter are removed from the raw cane sugar, with pure white crystalline sucrose being the major product. This process will involve the melting, treatment and subsequent recrystallization of the raw sugar as described in detail by Baikow (1982). Carbonatation is an intermediate clarification step in the cane sugar refining process, and is used to remove a range of impurities such as phenolics, melanoidins and caramels from a concentrated sugar melt, prior to final decolourisation. Batch carbonatation was performed by the Tate sugar group for many years (Baikow, 1982), prior to the introduction of continuous carbonatation processes such as the one modelled in this chapter. It can provide a competitive alternative to the phosphotation clarification process, in which the melt is treated with a mixture of phosphoric acid (H_3PO_4) and aqueous calcium hydroxide ($Ca(OH)_2$), and other less common clarification processes as also described by Baikow (1982).

During the carbonatation process, a concentrated sucrose solution is pre-mixed with $Ca(OH)_2$ to create an alkaline solution with a pH of around 11, and continually introduced into a large gas-liquid contactor, also referred to as a saturator. Carbon dioxide (CO_2) gas is bubbled through the solution, dissolving into the liquid phase through interphase mass transfer mechanisms analogous to those discussed in Section 4.4. The overall balanced reaction of CO_2 with $Ca(OH)_2$ can be described by equation (8-1), forming solid calcium

carbonate ($CaCO_3$) which rapidly precipitates out of solution and is filtered out directly downstream of the saturator. Impurities become trapped within the carbonate crystal structures and are therefore also removed during the filtration process that immediately follows this treatment. However, there are several intermediate species that exist with this reaction scheme which affect the solution pH and $CaCO_3$ formation as discussed later in this section.

$$Ca(OH)_{2\,(s)} + CO_{2\,(g)} \leftrightharpoons CaCO_{3\,(s)} + H_2O_{(l)} \tag{8-1}$$

Unlike the interphase transfer of oxygen that has been considered in the preceding chapters, the dissolved carbon dioxide in water forms carbonic acid, which is subject to a complex buffering system that changes the distribution of dissolved carbonate species depending on the solution pH. This relationship can be represented graphically by using a Bjerrum plot as shown in Figure 8-1 (Hanrahan, 2012), suggesting that the relative composition of the dissolved carbonate species is likely to change significantly within the pH range between 12 and 8.5 expected during the carbonatation process.

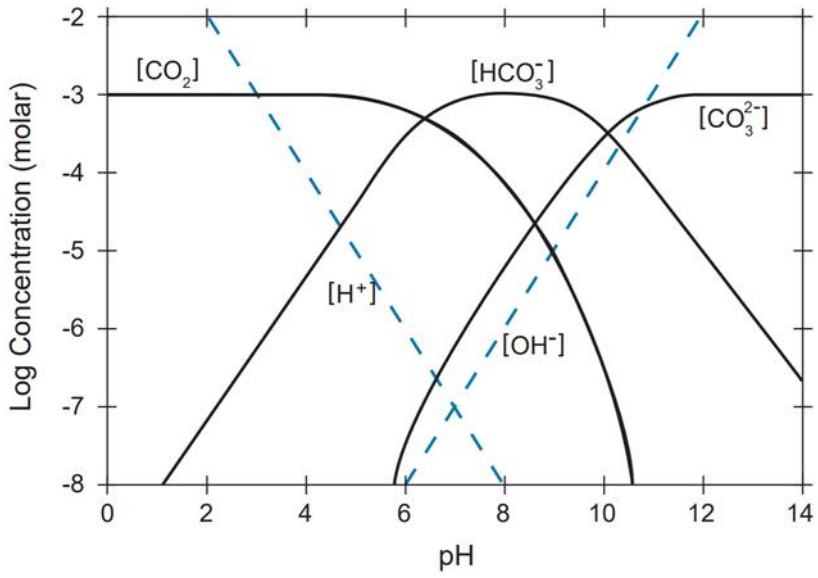

Figure 8-1: Bjerrum plot of the carbonic acid buffering system in water (Hanrahan, 2012).

Whereas there is no published model for the carbonate reaction system described above with respect to sugar refining, the carbonate buffering system in water has been studied in detail in relation to geological systems, where the dissolved carbon concentration and pH are critical factors in the wellbeing of natural watercourses. One such model is the MINTEQA2 software package developed by the Environmental Protection Agency in the

USA during the early 1990s (Allison et al., 1991)**,** which has been used in a number of subsequent studies of environmental aquatic systems. However, the modelling technique used by the MINTEQA2 programme requires an iterative method to calculate the stable equilibrium conditions using tabulated thermodynamic data, and is therefore not appropriate for direct implementation into CFD modelling. However, this model does introduce the concepts of total inorganic carbon and alkalinity, both of which are commonly used to describe the composition of ecological water systems (Stumm and Morgan, 1996). They can therefore be used to develop a closure to the cyclic dependency between solution pH and the relative concentrations of the dissolved carbonate species, as presented in later sections of this chapter.

Another area of research that is relevant to the carbonatation process is a branch of carbon capture and storage (CCS) research that explores the potential for capturing the CO_2 from gas streams such as flue gases as solid $CaCO_3$. Such capture processes may take place either in natural underground systems or in contacting systems with absorbent materials such as monoethanolamine, diethanolamine or calcium hydroxide (Han et al., 2011). The full system of aqueous reactions proceeding from gaseous CO_2 all the way to solid $CaCO_3$ crystals can be described by using a series of reversible kinetic equations, as modelled for a geological CCS system by Mitchell et al. (2010). This model assumes a well-mixed, closed system to which a step-change in the atmospheric concentration of CO_2 gas is introduced. The interphase mass transfer in the published system is therefore described by a kinetically controlled equilibrium between the gas and liquid phases. However, it is considered more appropriate to model the interphase mass transfer during the carbonatation process using film theory as described by equation (2-5), due to the continual bubbling of CO_2 gas used. The subsequent system of liquid-phase equilibrium reactions can then be described by equations (8-2) to (8-6).

$$CO_{2\,(aq)} + H_2O \underset{k_{-2}}{\overset{k_2}{\leftrightharpoons}} H_2CO_3 \tag{8-2}$$

$$H_2CO_3 \underset{k_{-3}}{\overset{k_3}{\leftrightharpoons}} HCO_3^- + H^+ \tag{8-3}$$

$$HCO_3^- \underset{k_{-4}}{\overset{k_4}{\leftrightharpoons}} CO_3^{2-} + H^+ \tag{8-4}$$

$$Ca^{2+} + CO_3^{2-} \underset{k_{-5}}{\overset{k_5}{\leftrightharpoons}} CaCO_{(aq)} \tag{8-5}$$

$$CaCO_{(aq)} \leftrightharpoons CaCO_{(s)} \tag{8-6}$$

The kinetic constants used to model these reactions are presented in Table 8-1, as compiled by Mitchell et al. (2010). This model only considers the main reactions occurring in the specified pH range of 4 < pH < 6, with several other side reactions also reported to occur under different conditions (Han et al., 2011; Segev et al., 2012b). These may also need to be considered when developing a universally applicable model of the reactions involved in the carbonatation process. Despite this, the model of Mitchell et al. (2010) has provided a representative model for the capture of carbon dioxide in natural limestone systems. However, since many of the forward and backward reaction rates summarised in Table 8-1 are very fast, and therefore considered to be much too fast to model directly, a complex series of asymptotic approximations was developed.

Table 8-1: Forward and backward reaction rates for the intermediate reactions of the CCS model presented by Mitchell et al. (2010).

Reaction	Forward	Backward	Source(s)
(8-2)	k_2 = 6 × 10^{-2} s^{-1}	k_{-2} = 2 × 10^{1} s^{-1}	Stumm and Morgan (1996)
(8-3)	k_3 = 1 × 10^{7} s^{-1}	k_{-3} = 5 × 10^{10} $M^{-1}s^{-1}$	Bond et al. (2001), Pocker and Bjorkquist (1977)
(8-4)	k_4 = 3 × 10^{0} s^{-1}	k_{-4} = 5 × 10^{10} $M^{-1}s^{-1}$	Pocker and Bjorkquist (1977)
(8-5)	k_5 = 2 $M^{-1}s^{-1}$	k_{-5} = 1 × 10^{-3} s^{-1}	Warneck (1988)

A further level of complexity when considering the carbonatation process is provided by the continuing dissolution of solid $Ca(OH)_2$ within the saturator vessel. Powdered $Ca(OH)_2$ is typically pre-mixed with the sucrose solution at concentrations far in excess of the saturation level in water (Baikow, 1982). This means that the $Ca(OH)_2$ dissolution proceeds alongside the previously described reactions, providing a continuing source of calcium (Ca^{2+}) ions to prolong the precipitation of solid $CaCO_3$ in the presence of CO_2. This will also affect the pH in the system due to the simultaneous release of free hydroxide (OH^-) ions as described by equation (8-7). This process has been investigated experimentally for several commercially available $Ca(OH)_2$ samples, and a dissolution model developed by Johannsen and Rademacher (1999) as discussed in Section 8.6.2.

$$Ca(OH)_{2\,(s)} \leftrightharpoons {Ca^{2+}}_{(aq)} + 2{OH^-}_{(aq)} \tag{8-7}$$

8.2 Problem Definition

The modelled operating conditions are based on typical operating data supplied by the process operators. In order to limit the number of variable parameters within the model, only the CO_2 flow rate, $Ca(OH)_2$ addition and recycle rates are varied. The operating and modelled conditions are compared in Table 8-2.

Table 8-2: Range of operating conditions specified and modelled for the saturator.

Parameter	**Range Provided**	**Value(s) Used**
Temperature	79 - 85°C	79°C
CO_2 Flow Rate	0.3 - 0.8 t hr^{-1}	0.15, 0.3, 0.5, 0.7, 0.9 t hr^{-1}
Sucrose Feed Flow Rate	125 - 150 t hr^{-1}	125 t hr^{-1}
Recycle Rate	0 - 100 %	0, 50, 100, 150 %
Purity	99 - 99.5 %	99 %
Solids Content	64 - 69 °Bx	65 °Bx
$Ca(OH)_2$ Addition	0.4 - 1.2 wt%	0.4, 0.8 wt%

Under the operating conditions specified above, the physical properties for the sucrose solution required for the hydrodynamic model are presented in Table 8-3, calculated using data sheets provided by the process operators. It is clear that the high viscosity of the liquid phase will cause the hydrodynamic performance to be significantly different from the majority of designs characterised by correlations and models presented in literature, although the surface tension is similar to that of an air-water system for the given temperature.

Table 8-3: Physical properties of the sucrose solution.
79°C, 99% purity, 65°Bx

Density	1282.5 kg m^{-3}
Viscosity	0.009209 Pa s
Surface Tension	0.0721 N m^{-1}

It is assumed that:

- The physical properties are not significantly affected by the changing concentration of dissolved species or the solid particles suspended within the liquid phase.
- The particles of $CaCO_3$ and $Ca(OH)_2$ present are small enough that they exhibit only negligible buoyancy or gravitational effects, and they will therefore follow the liquid flow patterns described by the hydrodynamic model, meaning that they can be considered as components within the liquid phase rather than a discreet solid phase.

- The gas and liquid flows can be decoupled from the chemical reactions, since the majority of the CO_2 gas introduced per pass is assumed to leave the domain at the liquid surface, and will therefore not lead to a significant shrinkage of the bubble size as they rise through the column.

The full model of the reaction kinetics is therefore solved in two stages;

1. The fluid dynamic model is solved with a small timestep until a pseudo-steady state has been reached, represented by a stabilisation of the average fluid flow, turbulence and two-phase parameters with time.
2. The fluid flow fields, turbulence and two-phase parameters from stage 1 are frozen in time, and the interphase mass transfer and reaction model is solved for the liquid-phase components by using a significantly larger timestep.

8.3 Domain Definition

The domain for the saturator vessel used to model the carbonatation process is based on engineering drawings of the existing vessels. These drawings are shown in Figure 8-2 for the saturator vessel (left) and CO_2 distributors (right). The vessel consists of a large cylindrical volume with a 3,800 mm diameter, tapering to a 250 mm diameter outlet at bottom of the vessel. The modelled geometry does not consider internal structures except for the horizontal gas distributors used to introduce CO_2 gas towards the bottom of the vessel. The full three-dimensional geometry is modelled in order to capture the non-symmetrical churning behaviour expected to occur at higher gas flow rates, as predicted in Section 2.1. The freshly limed sucrose feed is introduced above the liquid surface via the inlets labelled N2, and falls through the head space to the liquid surface. This part of the process is not included in the modelled domain due to the computational expense and complexity of modelling the falling liquid using the Euler-Euler reference frame, and the relatively small influence that this process is expected to have on the interphase mass transfer. Similarly, the deformation of the free surface is not considered since the majority of the mass transfer is assumed to occur at the bubble interface. A constant near-atmospheric pressure of CO_2 is maintained in the head space above the liquid surface.

Figure 8-2: CAD geometries of the carbonatation vessel.

Sucrose Outlet

The sucrose outlet at the bottom of the saturator vessel (N1) is modelled as a mass flow outlet, with a specified net mass flow rate out of the domain, set by the required production rate of 125 - 150 t hr^{-1} specified by the process operators.

Liquid Surface

The introduction of fresh feed at the top of the saturator vessel is approximated in the model using an opening boundary condition with a fixed absolute pressure of 1 atmosphere. This allows for the instantaneous flow of both liquid and gas out of the domain, however the net flow of sucrose into the domain will be governed by the mass flow rate specified at the outlet N1. All of the CO_2 gas bubbles leaving the domain across this boundary are assumed to enter the head space, with an incoming sucrose fraction of 1 specified for the opening signifying no entrained gas bubbles. The use of an opening boundary condition could lead to a significant loss of component species (such as Ca^{2+}, $CO_{2\ (aq)}$, $CaCO_3$) within the model, which are not automatically accounted for in the inflowing liquid once they have left the modelled domain across the opening boundary. A

mass balance based on the surface depicted in Figure 8-3 is therefore implemented at the opening to ensure that all component species leaving the domain across the opening are included along with the recirculating and incoming fresh sucrose feed.

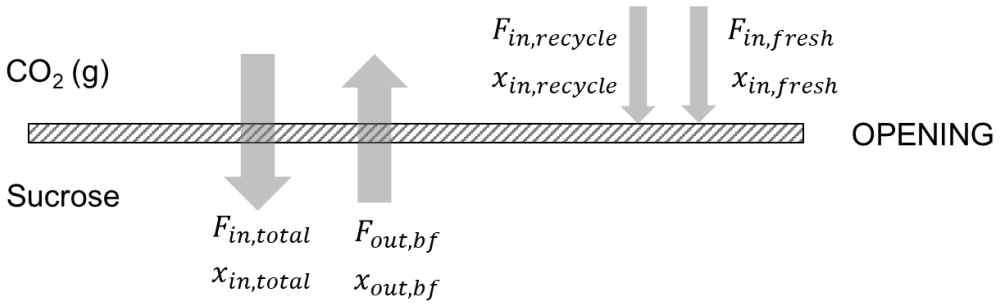

Figure 8-3: Mass balance for a component species at the liquid surface.

The mass flow of the liquid (sucrose) phase exiting the domain across the opening is denoted as the 'backflow', $F_{out,bf}$, with the component mass fraction at the boundary described by $x_{out,bf}$. The incoming fresh feed, at a specified production rate of $F_{in,fresh}$ is also included in this balance. The mass fraction of components in the feed stream is set to match the initial conditions using the term $x_{in,fresh}$, with the fraction all other components not featuring in the inlet stream set to 0. If a recycle stream is present, the component mass fractions in this stream $x_{in,recycle}$ are assumed to be the same as those exiting the domain via the outlet N1, with a specified recycle flow rate of $F_{in,recycle}$. The mass flow rate specified at the outlet N1 is therefore adjusted to include the production rate and the recycle rate. The full balance including recycle for a component species x is presented in equations (8-8) and (8-9).

$$x_{in,total} = \frac{F_{out,bf}x_{out,bf} + F_{in,fresh}x_{in,fresh} + F_{in,recycle}x_{in,recycle}}{F_{in,total}} \tag{8-8}$$

$$F_{in,total} = F_{out,bf} + F_{in,fresh} + F_{in,recycle} \tag{8-9}$$

The physical design of the CO_2 spargers is complex to model, since it uses a 'saw tooth' housing to distribute the gas evenly along the length of the sparger housing. The sparger teeth are spaced 78 mm apart with an internal tooth radius of 3 mm**.** The gas is introduced via a single pipe located at the centre of each housing, as shown in Figure 8-4 (option 1). To model the flow of gas within the sparger housing would require a very fine mesh within the

housing itself, in addition to the additional computational time required to resolve the distribution of gas along the sparger from the centrally-located inlet. Furthermore, the large scale of the saturator design would require the modelling of 896 individual teeth, based on technical drawings provided, each with a high mesh density required to capture the curvature within the tooth. This is clearly not an appropriate method of modelling the CO_2 inlets, and two different simplifications of this design have therefore been compared to the physical design in order to assess the appropriate degree of simplification acceptable when modelling the spargers. These are evaluated in Figure 8-4 for a one meter cubic domain with a single length of sparger at the centre. The two proposed simplifications comprise of modelling the full outline of the sparger housing including teeth, with gas introduced on the underside of the housing between the teeth (option 2), and modelling only the silhouette of the sparger housing – without teeth – with gas introduced on the upper surface of the sparger (option 3).

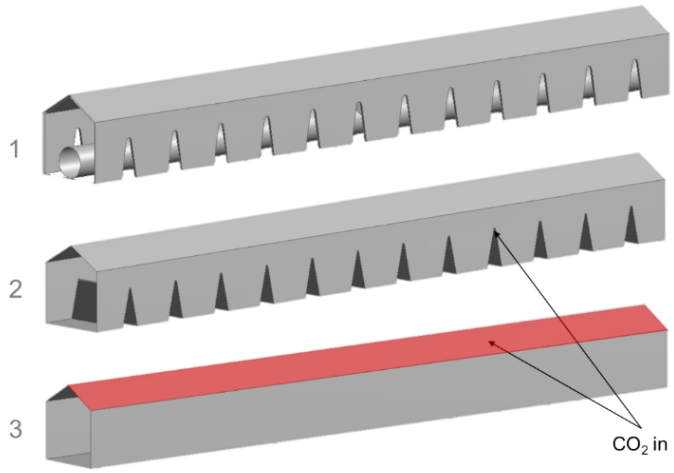

Figure 8-4: Geometry of the actual and proposed simplifications of the modelled CO_2 spargers.
Option 1. Full detail of the sparger, including internal CO_2 pipe.
Option 2. Sparger housing and teeth only, with gas introduced inside the sparger teeth.
Option 3. Silhouette of the sparger housing without teeth, with gas introduced on the upper surface.

The gas distribution produced along the length of the sparger by the three options is compared at 100 mm intervals above the sparger housing for a 1,000 mm cubic domain consisting of a single distributor with symmetry boundary conditions applied to all vertical domain boundaries and opening boundary condition applied to the top and bottom of the domain. The model shows that there is an initial variation between the observed gas fractions in Figure 8-5 a), with the greater degree of simplification leading to a greater over-prediction of the gas fraction directly above the sparger and a less pronounced 'saw-

tooth' pattern. However, the profiles have converged significantly by 200 mm above the sparger housing (Figure 8-5 b-d), and there is a minimal saw-tooth effect from the more detailed designs above this height. This means that the flow can be assumed to be completely independent of the sparger design used after between 5 and 8% of the total filled height above the sparger housing, leading to a minimal impact on the fluid behaviour and mass transfer within the whole domain. The gas inlet for the saturator is therefore modelled based on design option three.

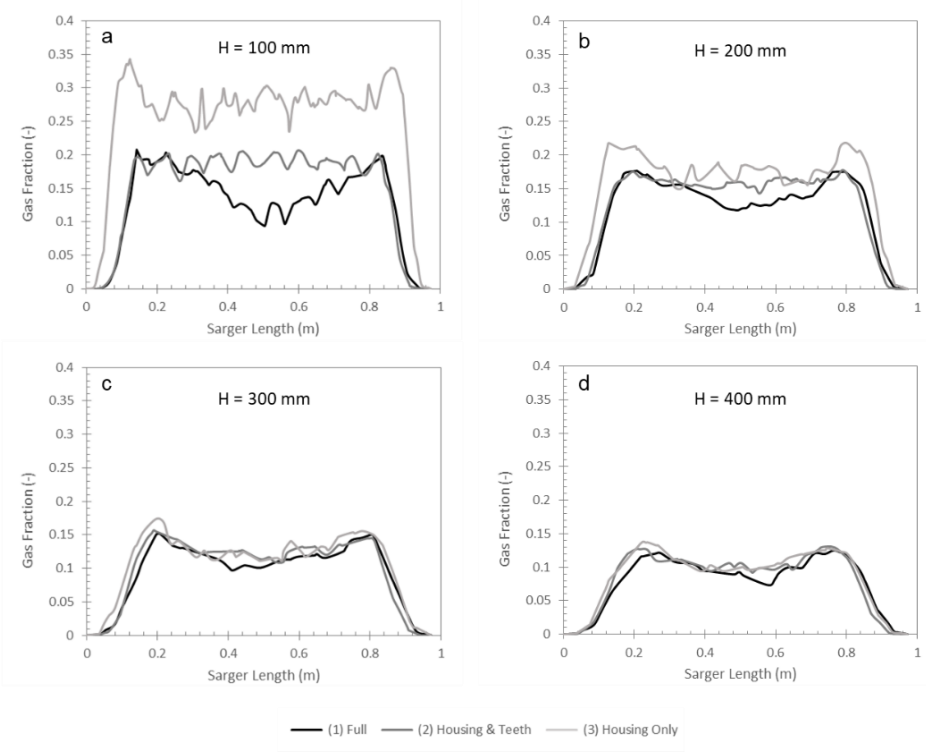

Figure 8-5: CO_2 volume fraction profiles at increasing height (H) above the sparger housing for the different simplifications proposed.
a) 100 mm, b) 200 mm, c) 300 mm, d) 400 mm.

8.4 Meshing

The domain is meshed using a fully unstructured tetrahedral mesh, generated using the ANSYS Meshing software. This approach allows the fine detail required for the complex spargers and vessel exit regions to be meshed in sufficient detail, whereas the bulk of the tank can use a coarser mesh to reduce the overall number of mesh cells, thus optimising the total number of cells required for the large vessel geometry. A mesh dependency study is performed on the domain described above with a CO_2 flow rate of 0.15 t hr^{-1} using five meshes of increasing density. All meshes considered have significant refinement around

the saturator outlet and gas distributors to account for the fine details of the geometry and the large velocity gradients occurring in these regions. Details of the meshes compared are provided in Table 8-4, along with the volume-averaged $k_L a$ values calculated using the slip velocity mass transfer model (equation (2-7)), which was shown to provide a good fit to experimental data at both production and lab-scale processes in Chapters 5 and 6. This analysis shows a variation of $k_L a$ between meshes 1 and 4, whereas meshes 4 and 5 show similar mass transfer values. This suggests that mesh 4 is sufficiently fine to accurately predict the overall mass transfer behaviour of the vessel.

Table 8-4: Mesh dependency study for the carbonatation vessel with a CO_2 flow rate of 0.15 t hr^{-1}. $k_L a$ calculated after 30 seconds simulated time.
Time for solution based on running transient solution to 30 seconds modelled time using 16 cores [2× Intel Xeon E5-2670 v2 CPUs, 126 GB RAM, NVidia Quadro K4000 GPU].

Mesh	Number of Elements	Average $k_L a$ (hr^{-1})	% Difference	Time for Solution (hr)
1	1,082,637	12.225	6.24	18.23
2	1,318,529	12.015	4.41	22.48
3	1,540,836	11.821	2.73	26.08
4	1,872,656	11.660	1.33	31.18
5	2,388,117	11.507	0.00	37.43

In addition to the $k_L a$ values, the axial sucrose velocity profiles are compared at 1 m intervals within the cylindrical section of the carbonatation vessel after 30 seconds of simulation time, as shown in Figure 8-6. Close to the spargers (Figure 8-6 a and b) there is very little difference between the different meshes, with only the coarsest mesh (Mesh 1) showing a deviation from the other profiles. In contrast, towards the liquid surface (Figure 8-6 c and d) there is a significant difference between the predicted velocity profiles generated using the different meshes, primarily towards the walls of the vessel. The coarser meshes show a much flatter velocity profile close to the walls, as they are unable to satisfactorily resolve the steep gradients in this region. However, meshes 4 and 5 show much more similar flow behaviour. It can therefore be concluded that meshes 4 and 5 are sufficiently fine to capture the two-phase hydrodynamic behaviour occurring.

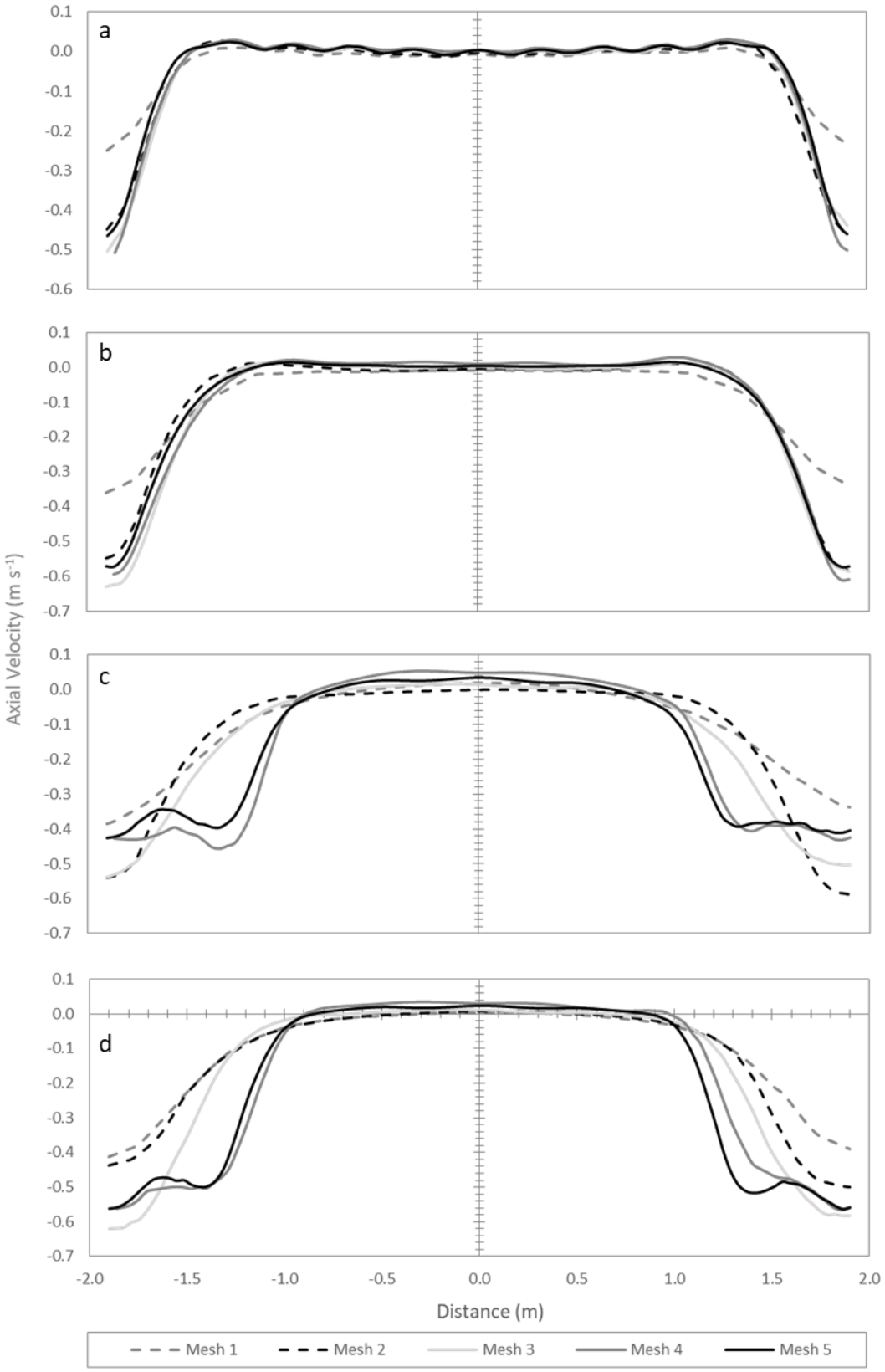

Figure 8-6: Axial velocity profiles for the mesh dependency study at different heights within the cylindrical section of the saturator vessel after 30 seconds simulation time.
a) 1000 mm, b) 2000 mm, c) 3000 mm, d) 4000 mm.

From the above analysis it can be concluded that Mesh 4 is of the required density to give sufficiently mesh-independent results for the flow patterns and mass transfer behaviour, both of which are dependent on the liquid and gas phase behaviours. The selected mesh is compared to the parent geometry in Figure 8-7, showing the mesh refinement applied close to the spargers, walls, free surface and sucrose outlet.

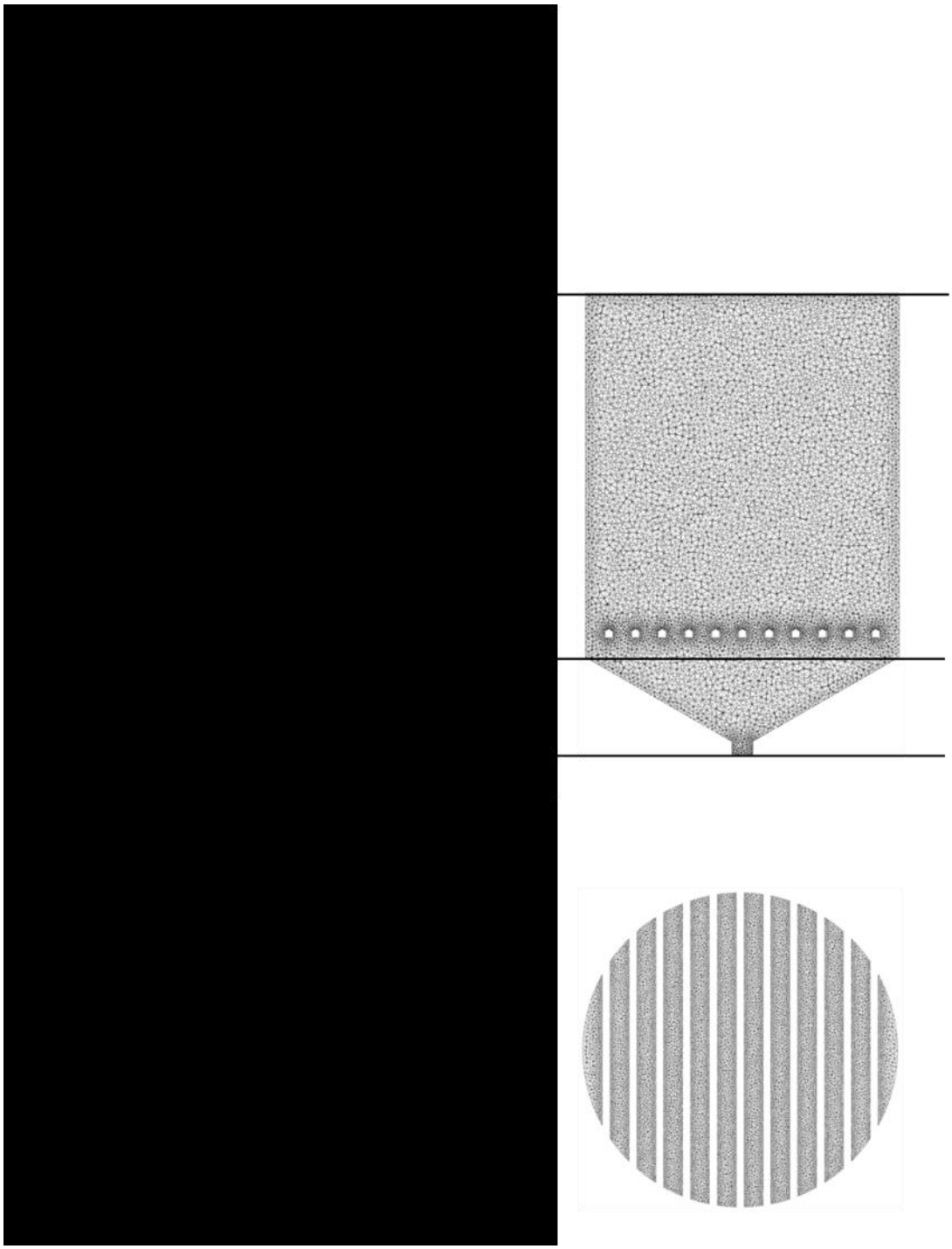

Figure 8-7: Comparison of the CAD geometry and optimised mesh (Mesh 4) for the saturator vessel.

Using the optimised mesh, the bubble size population balance (MUSIG) parameters are optimised at a CO_2 flow rate of 0.15 t hr^{-1}, the most stable hydrodynamic conditions identified in Section 8.5, for the bubble size range and number of divisions. The MUSIG model is initially solved with 12 size groups, with the maximum possible bubble size increased in 3 mm increments from 6 to 15 mm. The minimum permitted size is maintained at 0 mm in all cases. Figure 8-8 shows the bubble size distribution at the liquid surface – where the bubble size is expected to be largest – after 30 seconds solution time for the different size ranges. Each profile shows a narrow distribution with a mean bubble diameter in the region of 6 mm, except for Figure 8-8 a) where the size distribution appears to be constrained by the specified maximum bubble size. The bubble size distribution for this CO_2 flow rate can therefore be said to be unconstrained with a maximum bubble size of 9 mm and above (Figure 8-8 b-d), with larger maximum values at risk of losing resolution of the distribution. The maximum bubble size is therefore set to 12 mm for all of the conditions used, which allows for the presence of larger bubbles caused by increased coalescence at higher CO_2 flow rates. This is confirmed later for higher CO_2 flow rates in Figure 8-13.

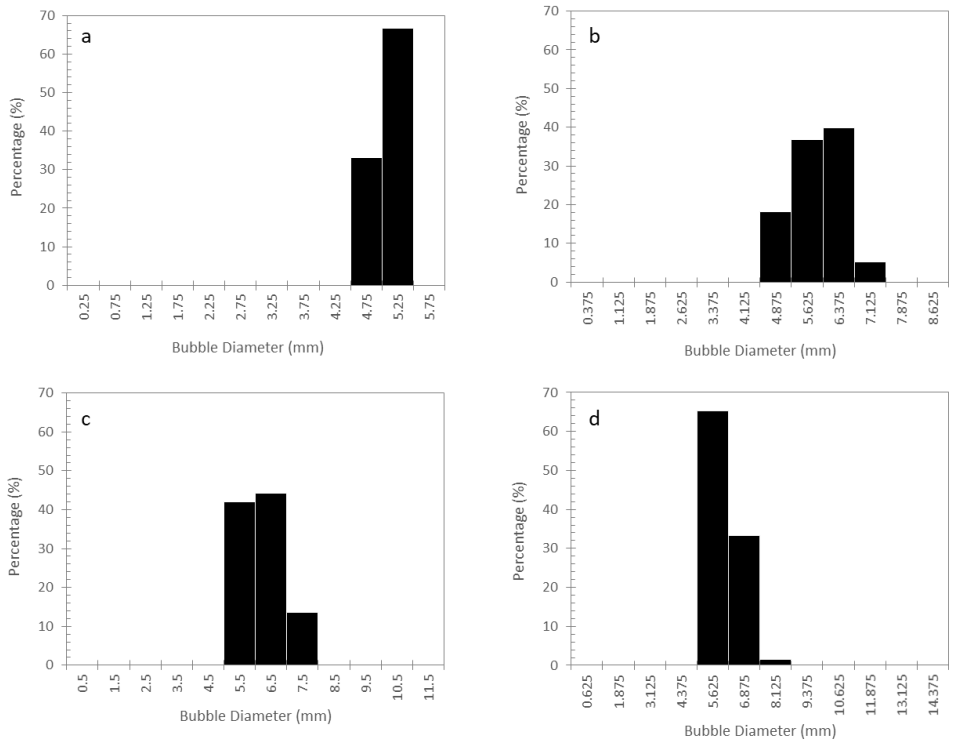

Figure 8-8: Bubble size distributions at the liquid surface of the saturator for different MUSIG ranges. a) 0-6 mm, b) 0-9 mm, c) 0-12 mm, d) 0-15 mm.

Due to the narrow size distributions presented in Figure 8-8, the number of size groups used to discretise the selected diameter range (0-12 mm) is varied between 12 to 24 groups as shown in Table 8-5. The volume averaged $k_L a$ for the entire saturator volume is calculated using the slip velocity model. The difference in mass transfer coefficient between 12 and 18 groups is shown to be much larger than between 18 and 24 groups, suggesting little benefit in terms of solution accuracy in using the highest number of groups. An optimum of 18 size groups will therefore be used for all further simulations, representing a balance between solution accuracy and computational time.

Table 8-5: Volume-averaged $k_L a$ values for different numbers of MUSIG size groups after 30 seconds modelled time (0-12 mm bubble diameter range).
Time for solution based on running transient solution to 30 seconds modelled time using 16 cores [2× Intel Xeon E5-2670 v2 CPUs, 126 GB RAM, NVidia Quadro K4000 GPU].

Number of Groups	Average $k_L a$ (hr^{-1})	% Difference	Time for Solution (hr)
12	11.660	3.34	31.18
18	11.039	1.86	39.55
24	11.248	0.00	49.90

8.5 Fluid Dynamic Behaviour Modelling

The two-phase hydrodynamic model of the saturator vessel has been solved under different operating conditions as outlined in Table 8-2, with a focus on optimising the CO_2 flow rate. The hydrodynamic model for each condition is initialised with zero velocity for both phases and zero gas-fraction conditions. It is solved as a transient simulation with a timestep of 0.1 s until stable mass transfer conditions are achieved. The timestep is selected to give a stable solution and independent results with respect to the timestep chosen. This was achieved by modelling the initial solution stages with increasing timestep size until the limit of solution stability was reached, and checking the solution accuracy against the smallest timestep. For explicit CFD methods often used in older codes, the timestep size is restricted by the Courant number, which is dependent on the local mesh size and the timestep, however the implicit solution method used by ANSYS CFX allows for larger timesteps to be used within the limits of stability and solution accuracy (ANSYS Inc., 2016). Each time step is converged to RMS residuals of 1×10^{-5} and a conservation target of 0.01 using high resolution advection and turbulence numerics and a second order backward Euler transient scheme. The model setup is similar to that applied and validated

in previous chapters, with the Euler-Euler reference frame used in conjunction with the Ishii-Zuber drag model and the k-ε turbulence model.

8.5.1 Flow Patterns and Mass Transfer

The range of CO_2 flow rates used to control the carbonatation process is given as 0.3 to 0.8 t hr^{-1} by the process operators, with the following characterisation applied between 0.15 and 0.9 t hr^{-1} in order to completely capture this range and investigate more extreme values outside of the normal operating window. Due to the strong coupling between the liquid and gas phases through the interphase drag force, this range is expected to give rise to significant variation in the flow patterns and bubble characteristics observed. At 0.15 t hr^{-1}, the lowest CO_2 flow rate modelled, the flow patterns in the saturator vessel can be considered to be structured and stable with time. This is represented by the uniform gas fraction contours presented in Figure 8-9 a) and the recirculating flow patterns seen in Figure 8-9 b) for the liquid phase and c) for the gas phase. However, with the liquid phase being withdrawn at the bottom of the column and the buoyant gas phase exiting the saturator above the liquid surface there is a large difference in the relative velocity profiles, with the dominant gas phase velocity flowing up, whereas the majority of the liquid phase flows downwards within the column. The mean bubble diameter for a horizontal cut plane at heights of 1, 2, 3 and 4 meters within the cylindrical section of the saturator are also presented in Figure 8-9, with the bubble size increasing with height due to coalescence between bubbles. The gas is distributed evenly and at a relatively low volume fraction within the cylindrical region of the saturator as presented in Figure 8-9 a).

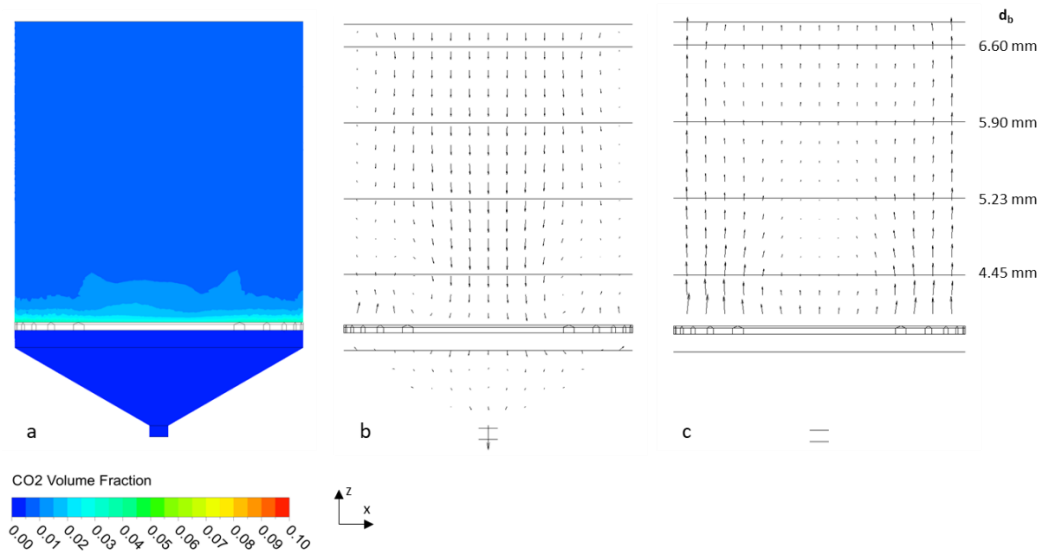

Figure 8-9: Two-phase flow profiles for a CO_2 flow rate of 0.15 t hr^{-1} after 60 seconds modelled time. a) gas volume fraction contours, b) liquid velocity, c) gas velocity and bubble diameter.

In contrast, the instantaneous flow patterns at CO_2 flow rates of 0.3 t hr^{-1} and above show non-symmetrical flow behaviour which is unstable with time, as shown in the liquid and gas phase velocity vector plots in Figure 8-10. This is consistent with the turbulent churn regime identified in Section 2.1 and previously modelled in an air-water system at high gas flow rates by McClure, Aboudha, et al. (2015), also using the k-ε turbulence model. These churning flow profiles can improve the mixing within the liquid phase and reduce the possibility of dead-zones or large concentration gradients developing within the saturator. The intensity of the churning is shown to increase as the gas flow rate increases, with stronger recirculation of both phases identified in Figure 8-10. Furthermore, the distribution of bubble sizes within the tank also changes significantly with increasing CO_2 flow rate. At 0.3 t hr^{-1} (Figures d-f) there is still a significant coalescence of bubbles identified when moving upwards within the column, similar to the 0.15 t hr^{-1} case, however at flow rates of 0.5 t hr^{-1} (Figures g-i) and above there is much less difference in the mean diameter with height due to the increased levels of turbulence. The flow patterns between the two phases are much more similar in the turbulent churn regime, with both phases appearing to follow similar instantaneous recirculation patterns. The distribution of the gas phase can also be strongly linked to the flow patterns, with regions of high and low gas fraction following the velocity vectors as the gas bubbles are entrained in the churning flow patterns. The overall gas fraction within the majority of the saturator can also be seen to increase with the gas flow rate, as can be identified from the colour bar in Figure 8-10.

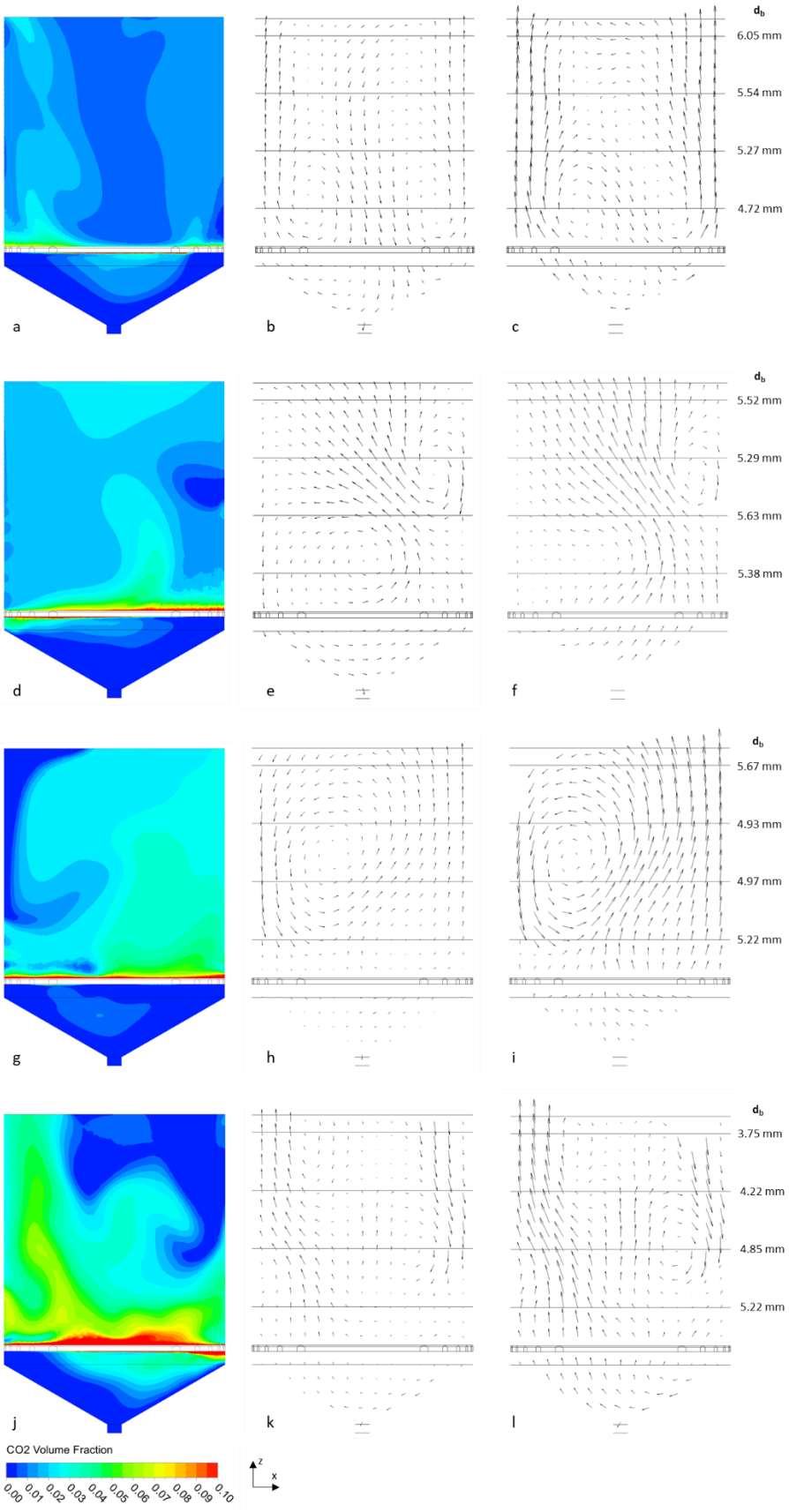

Figure 8-10: Instantaneous two-phase flow profiles for CO_2 flow rate of 0.3 t hr^{-1} (a-c), 0.5 t hr^{-1} (d-f), 0.7 t hr^{-1} (g-i) and 0.9 t hr^{-1} (j-l) after 60 seconds modelled time.
a, d, g, j) gas fraction contours, b, e, h, k) liquid velocity, c, f, i, l) gas velocity and bubble diameter.

As discussed in Chapters 5 and 6, the interphase mass transfer rate, quantified in terms of $k_L a$, is dependent on several parameters including the gas volume fraction, bubble size and the liquid flow conditions. It can therefore be expected that the flow characteristics identified in Figure 8-10 will lead to an increase in mass transfer across this range of CO_2 flow rates due to the higher volume fraction of gas and more intense mixing. The volume averaged $k_L a$ for the saturator can be predicted using the same interphase mass transfer models as applied to the BioMOD reactor in Section 5.7.2. The slip velocity model (equation (2-11)) is chosen as the most suitable model for use in this chapter. This is based on the ability to model k_L with reasonable accuracy for both the validation and full-scale BioMOD models in previous chapters, which suggests that it is applicable at multiple length scales and two-phase flow regimes. It is applied to the three-dimensional saturator model using the physical parameters listed in Table 8-3 for the sucrose solution. The mass diffusivity of carbon dioxide in the sucrose is assumed to be the same as in water, with a fixed value of 1.92×10^{-9} m^2 s^{-1} applied throughout this section (Cussler, 1997).

The trend in the $k_L a$ values, volume-averaged across the entire saturator, are presented in Figure 8-11 for the first 60 seconds after initiating the gas flow for CO_2 flow rates of 0.15, 0.3, 0.5, 0.7 and 0.9 t hr^{-1}. This range covers the typical operating range of 0.3 to 0.8 t hr^{-1}. The average $k_L a$ at the end of this period increases with increasing CO_2 gassing rate, due to the greater amount of CO_2 entering the system and the improved mixing conditions, however the model is observed to have reached a pseudo-steady after 30 seconds once the average $k_L a$ values have plateaued and the flow regime has become fully developed. In addition, the stability of the average $k_L a$ values with time decreases as the CO_2 flow rate increases, as signified by the saw-tooth profiles at 0.7 and 0.9 t hr^{-1}. This is as a result of the time-dependent churning flow patterns presented in Figure 8-10, with the fluctuating local hydrodynamic conditions leading to unstable local $k_L a$ values.

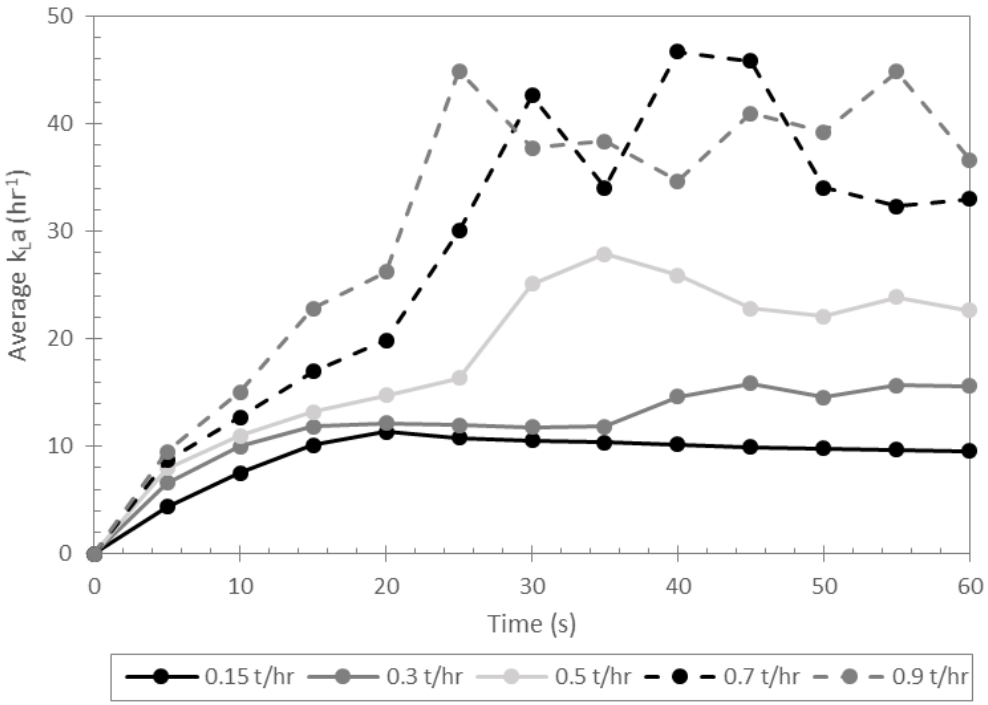

Figure 8-11: Volume-averaged $k_L a$ profiles during the first 60 seconds of operation for increasing CO_2 flow rates.

In order to better represent some of the key flow parameters, Figure 8-12 presents a set of volume-averaged and time-averaged parameters over the period of 30 to 60 seconds for different CO_2 flow rates, during which time it assumed that a pseudo-steady state has been established as suggested by Figure 8-11. Combining these two averaging techniques gives a representative value of the temporal mean of the following parameters. The typical operating range of CO_2 flow rates is represented by the grey box in Figure 8-12.

CO_2 Volume Fraction: The volume fraction of gas in the system increases with the gas flow rate as shown in Figure 8-12 a), however this increase with the volume of gas introduced is not linear as the increased CO_2 volume fraction causes a faster and non-uniform bubble rise as seen in the flow profiles in Figure 8-10. The rate of increase in gas fraction appears to decrease at flow rates close to the typical operating maximum of 0.8 t hr^{-1}. This parameter provides an important check that the hydrodynamic model is responding to inputs in a physically valid manner.

Average $k_L a$: Figure 8-12 b) represents the temporal mean of the profiles presented in Figure 8-11 from 30 to 60 s. The average $k_L a$ increases steeply between 0.15 and 0.7 t hr^{-1} CO_2, suggesting that varying the CO_2 flow rate within the range currently used will result

in significantly different levels of dissolved carbonates within the liquid phase, and therefore will affect the reactions leading to the formation of solid $CaCO_3$ and associated impurities removal. Furthermore, the average $k_L a$ does not increase significantly between 0.7 and 0.9 t hr^{-1}, suggesting that the increasing the CO_2 flow rate above the currently used range will offer little change in the mass transfer performance. The average $k_L a$ values are expected to be influenced by the bubble diameter and the two-phase flow conditions.

Turbulent Kinetic Energy (TKE): Figure 8-12 c) gives a representation of the levels of turbulence generated in the system, which for the carbonatation vessel is generated predominantly through bubble-induced turbulence due to the absence of external mechanical agitation. The turbulence at 0.15 t hr^{-1} is very low, consistent with the stable flow patterns discussed previously, and increases steeply with increasing CO_2 flow rate up to 0.7 t hr^{-1}. Above this value there is a decrease in the TKE, which may represent the onset of gas channelling within the saturator. The very low levels of turbulence seen at 0.15 t hr^{-1} are consistent with the idea that this condition operates within or close to the homogeneous bubbly flow regime, whereas the other flow rates studied are expected to operate in the turbulent churning regime, as suggested by the higher turbulence levels modelled.

Mean Bubble Diameter: The mean bubble diameter depends upon a balance between the break-up and coalescence mechanisms described in Section 4.3. Increasing the CO_2 flow rate significantly increases the turbulence within the saturator vessel, as seen in Figure 8-12 c), which will promote bubble breakup. However, there will also be an increase in the probability that two bubbles will collide due to the increased gas fraction present, especially with the gas being introduced at a single height, which will in turn promote bubble coalescence. These competing factors mean that there is no consistent trend in average bubble size with CO_2 flow rate, as seen in Figure 8-12 d). The largest bubble size is seen at 0.3 t hr^{-1}, where the turbulent flow is not as developed as higher flow rates, with the smallest average bubble size seen at 0.7 and 0.9 t hr^{-1}. However the overall variation in bubble size is fairly small, which means that this is unlikely to be the main factor influencing the changes in mass transfer performance with increasing CO_2 flow rate. The magnitude of the average bubble sizes predicted by the model are consistent with the constant bubble diameter values applied in literature, as summarised for similar bubble column systems by Table 2-5.

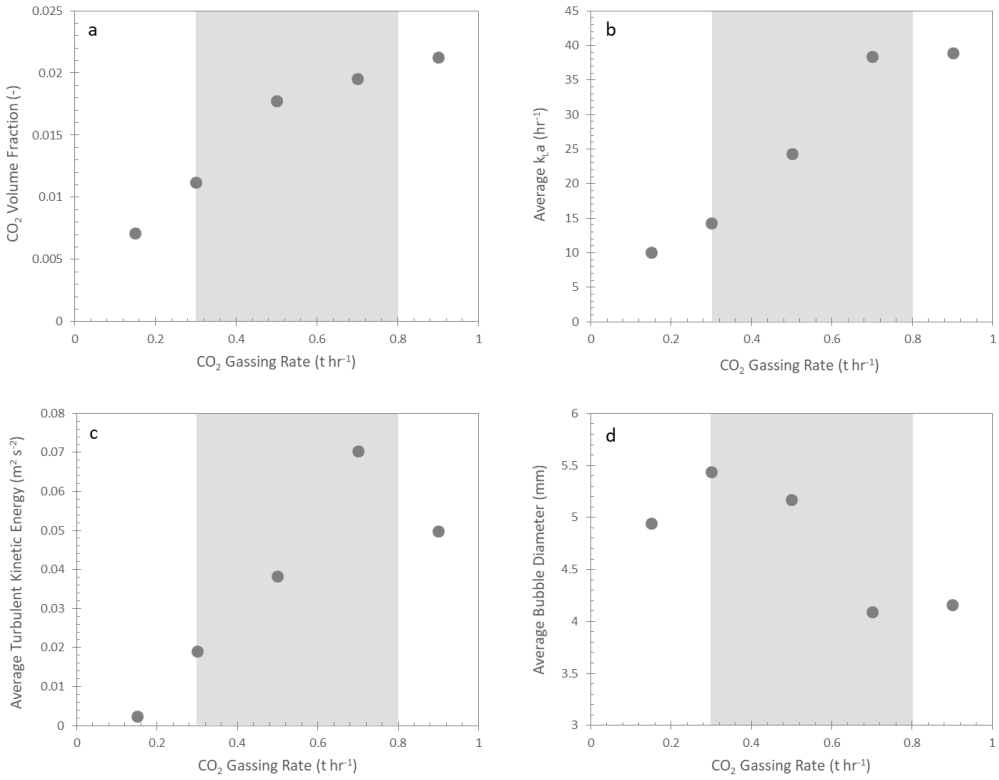

Figure 8-12: Volume and time-averaged profiles for the saturator under different CO_2 flow rates for the period of 30 to 60 seconds.
a) CO_2 volume fraction, b) $k_L a$, c) turbulent kinetic energy, d) bubble diameter.

In addition to the volume and time averaged bubble diameter presented in Figure 8-12 d), the distribution of bubble sizes at the liquid surface is presented in Figure 8-13 for each CO_2 flow rate modelled. The profiles have a much smoother profile than those presented in Figure 8-8 owing to the higher number of size groups modelled. The narrowest size distribution is shown for a CO_2 flow rate of 0.15 t hr^{-1}, which is consistent with the description of the homogeneous bubbly flow regime provided by Shah et al. (1982) and the low levels of turbulence identified in Figure 8-12 c). For the profiles generated at higher CO_2 flow rates, in particular 0.7 and 0.9 t hr^{-1}, the entire distribution is shifted towards the smaller bubbles, as the turbulence-driven bubble break-up mechanism becomes more significant. The majority of bubbles at the liquid surface are larger than the inlet size (group 5, 3 mm), with only 0.7 and 0.9 t hr^{-1} showing any bubbles smaller than the inlet size, suggesting that bubble coalescence is still the dominant mechanism occurring in the saturator. The profiles presented in this figure have a good resolution between groups – with no group containing more than 30% of the total – and include bubble sizes across the permitted range. However, the distribution does not appear to be constrained by the

MUSIG model specification, suggesting that the optimisation of the MUSIG model presented previously is appropriate at all conditions modelled.

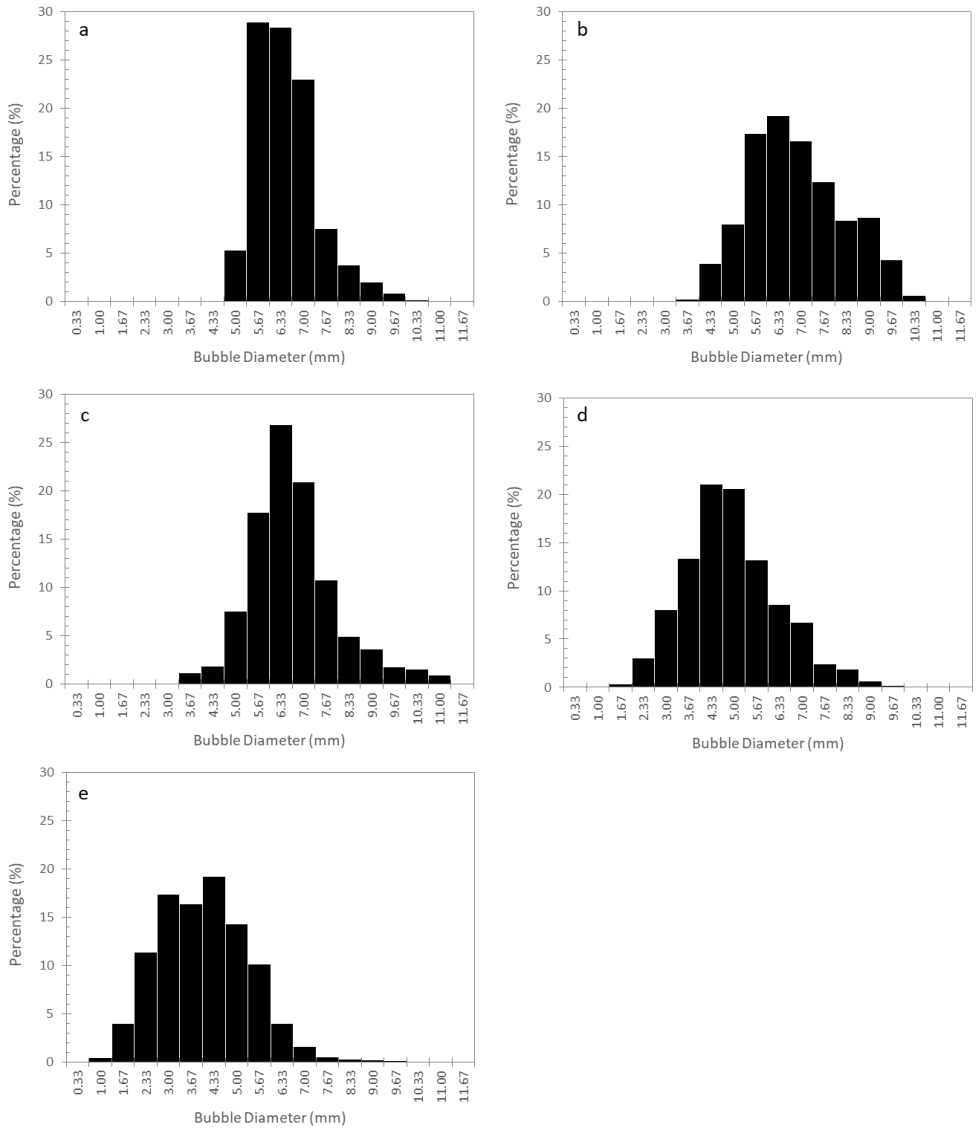

Figure 8-13: Bubble size distributions at the liquid surface for different CO_2 gas flow rates. a) 0.15 t hr^{-1}, b) 0.3 t hr^{-1}, c) 0.5 t hr^{-1}, d) 0.7 t hr^{-1}, e) 0.9 t hr^{-1}.

8.5.2 Shear Stress

Shear stress is an important parameter for the saturator design, as high shear environments can promote the break-up of $CaCO_3$ agglomerates into smaller fragments which are more difficult to filter and have a greater chance of dissolving back into the liquid phase. The resultant magnitude of the total shear stress, τ, can be calculated by using

equation (8-10) from the individual shear stress tensors for a Cartesian coordinate system, which are obtained from the velocity gradients (equations (8-11) to (8-13)).

$$\tau = \sqrt{{\tau_x}^2 + {\tau_y}^2 + {\tau_z}^2} \tag{8-10}$$

where

$$\tau_x = \mu \sqrt{\left(\frac{du}{dx}\right)^2 + \left(\frac{dv}{dx}\right)^2 + \left(\frac{dw}{dx}\right)^2} \tag{8-11}$$

$$\tau_y = \mu \sqrt{\left(\frac{du}{dy}\right)^2 + \left(\frac{dv}{dy}\right)^2 + \left(\frac{dw}{dy}\right)^2} \tag{8-12}$$

$$\tau_z = \mu \sqrt{\left(\frac{du}{dz}\right)^2 + \left(\frac{dv}{dz}\right)^2 + \left(\frac{dw}{dz}\right)^2} \tag{8-13}$$

and u, v, w are the velocity components.

Shear stress contour plots for the different CO_2 flow rates are presented in Figure 8-14. Each plot is scaled based upon the same range of shear stress from 0 to 0.1 Pa, as described by the colour scale bar provided. Although this level of shear is well below the stress required to break a single $CaCO_3$ crystal, higher shear stress may cause the break-up of solid agglomerates into finer particles, which are harder to filter out of the treated solution and may promote increased rates of re-dissolution. From all of the contour plots presented, there are two main regions where the shear stress is highest: close to the spargers and at the bottom outlet of the vessel. These are regions where the area available for flow is reduced, with the introduction of the gas phase at the spargers causing a further disruption to the flow in this region. Both areas of high shear are relatively close to the saturator exit, and therefore increase the likelihood of small particles entering the product stream. Further regions of high shear can be seen in the fluid contacting region above the spargers at higher CO_2 flow rates, where there are large gradients in the velocity field due to the churning flow patterns. The shear stress in this region is seen to increase in magnitude and distribution as the CO_2 flow rate is increased.

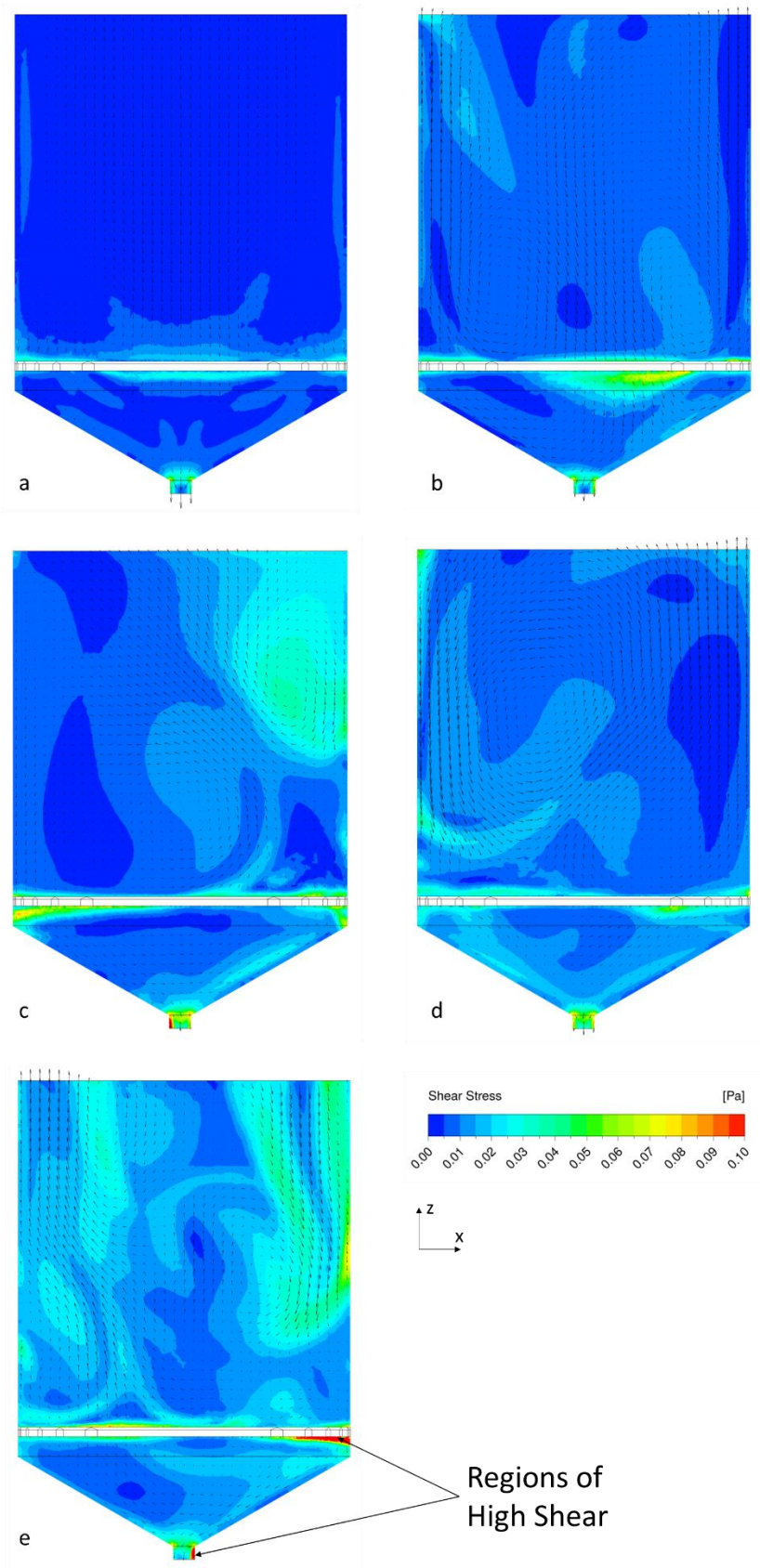

Figure 8-14: Contour plots of resultant shear stress for a vertical cut-plane at the centre of the saturator after 60 seconds modelled time.
Vector arrows represent the liquid-phase velocity.
a) 0.15 t hr^{-1}, b) 0.3 t hr^{-1}, c) 0.5 t hr^{-1}, d) 0.7 t hr^{-1}, e) 0.9 t hr^{-1}.

The time averaged shear stress between 30 and 60 seconds is presented in Figure 8-15 for the volume averaged (a) and maximum value (b) profiles at different CO_2 flow rates. Both profiles show a significant rise in shear stress across the range of CO_2 flow rates modelled, including the typical operating range highlighted by the grey box. Furthermore, the maximum shear stress is consistently greater than one order of magnitude larger than the volume average, suggesting that the solid agglomerates are exposed to much higher stresses at the high-shear locations identified above than in the rest of the saturator. For both curves, the steepest increase occurs between 0.15 and 0.3 t hr^{-1}, which has been identified as the transitional region between stable and churning flow regimes. The shear then increases further as the churning flow patterns become more pronounced, suggesting that an optimal CO_2 flow rate with regards to shear stresses will be lower than the maximum value currently used, with the average profiles in Figure 8-15 b) appearing to plateau around 0.5 t hr^{-1}.

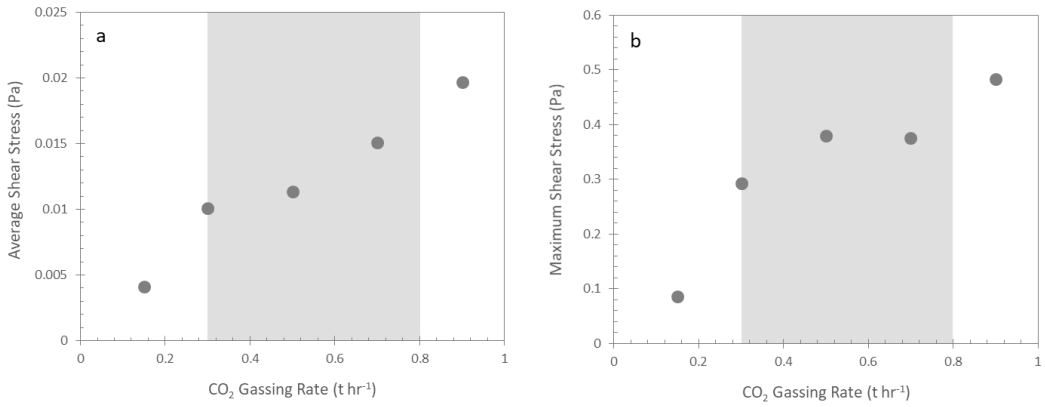

Figure 8-15: Shear stress profiles under differnent CO_2 flow rates.
a) volume averaged, b) maximum.

8.5.3 Interphase Mass Transfer

In addition to calculating the volume-averaged $k_L a$ values, the interphase mass transfer model can be used to compare the profiles of dissolved carbon dioxide concentration $[CO_2]$ with time at the different gassing rates, as described by equation (8-14). This equation is modelled within the CFD framework as a mass fraction source term for a component in the liquid phase, within a sub-domain covering the entire modelled geometry. This approach assumes that there are no further reactions in the aqueous phase, and no solids formed. Therefore, the term $[CO_2]$ in this instance represents all of the dissolved carbonate species, since there is no consideration of the solution pH at this level

of modelling, and therefore no knowledge of the distribution of the different carbonate species described in Figure 8-1.

$$\frac{d[CO_2]}{dt} = k_L a([C^*] - [CO_2]) \quad (8\text{-}14)$$

The saturation concentration of CO_2 $[C^*]$ is calculated to be 9.88 mol m^{-3} using Henry's law, adjusted for the reaction temperature of 79°C using the Van't Hoff equation as described by Sander (2015).

The profiles presented in Figure 8-16 show the dissolved CO_2 profiles at the bottom outlet of the saturator for a total production rate of 125 t hr^{-1}, assuming that no further reactions take place as described above. The model assumes initial conditions of zero dissolved CO_2 and a fully developed two-phase flow field, frozen after 60 seconds of the hydrodynamic model presented in Figure 8-11. Freezing the hydrodynamic conditions (liquid and gas velocities, turbulence, gas volume fraction and bubble size) in time allows for only the reaction model to be solved, significantly reducing the number of calculations required. Furthermore, the rate at which the reactions are occurring (of the order of minutes to hours) is not compatible with the short sub-second timesteps required to model the hydrodynamic behaviour. The mass transfer rates at the time that the hydrodynamic conditions are frozen are shown to be representative of the mean values (see Figure 8-11). However, using the instantaneous flow patterns may risk unrepresentative concentration profiles developing within the saturator. Since the reactions are being decoupled from the flow profiles, it is necessary to assume that the reactions do not significantly change the hydrodynamics of the system, for example by shrinking the bubble size due to the interphase mass transfer of CO_2.

Each profile in Figure 8-16 reaches a steady state concentration within the first 30 minutes of operation, however in all cases this is below the saturation concentration for CO_2 at the operating temperature due to the continual addition of fresh sucrose at the liquid surface. Between 0.15 and 0.7 t hr^{-1}, the profiles become increasingly steep in the initial phase and reach a higher equilibrium value as the mass transfer performance improves. However, between 0.7 and 0.9 t hr^{-1} there is very little difference in the profiles, as predicted by the volume averaged values presented in Figure 8-11. Despite the churning flow profiles at

higher aeration rates, all of the profiles presented are smooth, possibly as a result of freezing the hydrodynamic conditions at the outlet with time. This analysis is useful for representing the effect that the CO_2 flow rate has on the interphase mass transfer, and confirming the appropriate implementation of the mass balance at the liquid surface. However, it is clearly an over-simplification of the complex reaction scheme occurring during the carbonatation process and gives no indication of important operating parameters such as pH and $CaCO_3$ formation.

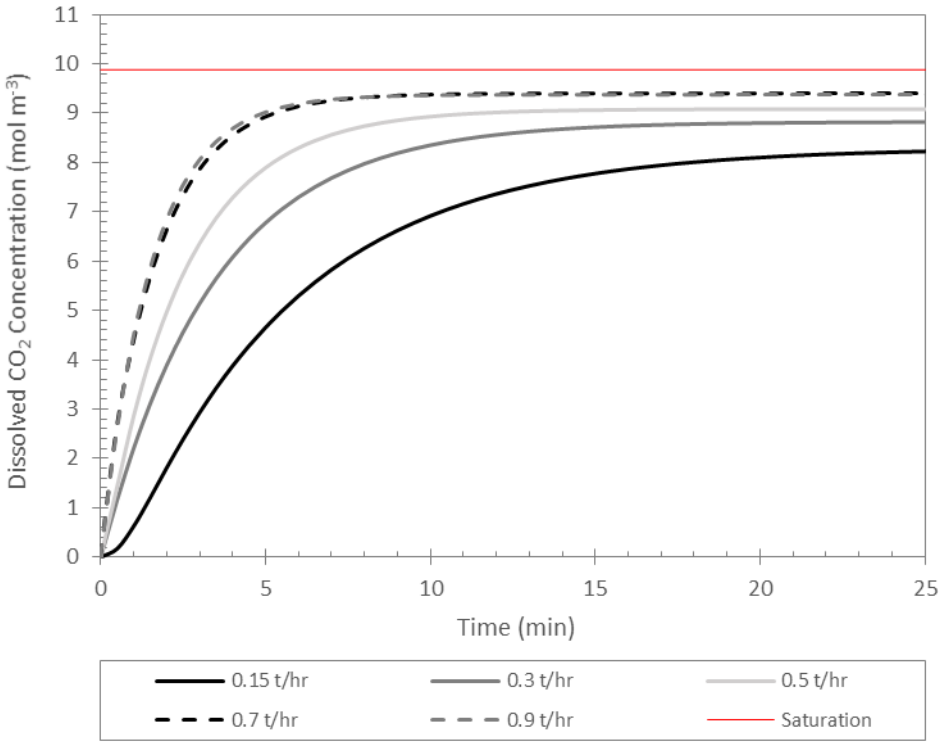

Figure 8-16: Dissolved CO_2 profiles at the saturator outlet, assuming no further reactions, for different CO_2 gas flow rates.

The above profiles take an average of 6.54×10^5 core seconds (11.36 hours using 16 cores) to reach 30 minutes simulated time, with a conversion target of 1×10^{-5} for the CO_2 mass fraction residuals, in comparison to the full hydrodynamic model which requires 2.58×10^6 core seconds (44.83 hours using 16 cores) to model the first minute of operation. This represents an improvement of 118.4 times for solving just the mass transfer in comparison to just the hydrodynamic equations, and highlights the significant and necessary time savings that can be achieved by decoupling the two-phase flow fields from the reactions. Furthermore, the profiles presented are smooth and respond to the changing CO_2 flow rate in a physically expected manner. This suggests that the necessary assumption that gas

bubbles do not shrink due to interphase transport is not significantly detrimental as to result in a physically non-valid model.

Contour plots representing the dissolved CO_2 concentration at a central vertical cut-plane of the saturator are presented for each CO_2 flow rate in Figure 8-17. Each plot is presented alongside its own colour bar due to the significantly different saturation concentrations reached under each condition. The variation in the local concentration, as represented by the upper and lower limits of the colour bar, is much larger for 0.15 t hr^{-1} than the other conditions. This is due to the low levels of turbulent mixing, which can also be seen in the uniform contours and flow patterns at 0.15 t hr^{-1}. The lowest CO_2 concentration is seen at the top of the saturator, where the fresh sucrose feed mixes with the recirculating liquid in accordance with the mass balance presented in Figure 8-3. This is less pronounced for the other conditions, where the turbulent churning flow causes the mixing of the fresh feed into the bulk fluid to be improved. The mixing appears to be most intense in the large two-phase contacting region above the spargers, where the majority of the gas-liquid interactions are occurring, with the largest concentration gradients found in this region. In all of the cases presented, the contour plots show a strong resemblance to the flow patterns, as the dissolved CO_2 component is transported based upon the frozen liquid velocity field.

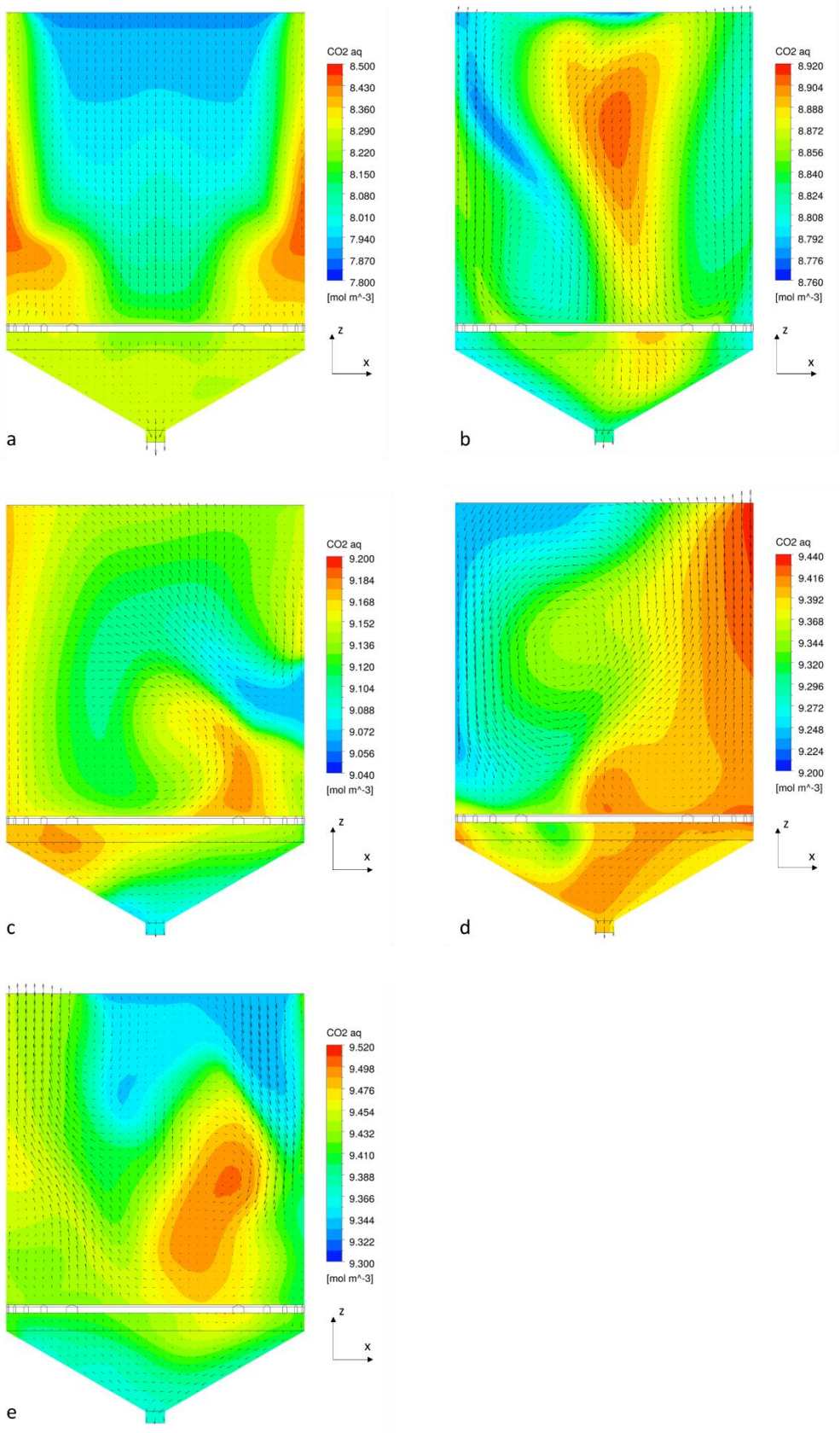

Figure 8-17: Contour plots of dissolved CO_2 concentration for a vertical cut-plane at the centre of the saturator after 30 minutes modelled time, assuming no further reactions occur.
Vector arrows represent the liquid-phase velocity.
a) 0.15 t hr^{-1}, b) 0.3 t hr^{-1}, c) 0.5 t hr^{-1}, d) 0.7 t hr^{-1}, e) 0.9 t hr^{-1}.

8.6 Reaction Modelling

The set of reactions involved in the carbonatation process represents a complex series of equilibria, which have not previously been reported to be implemented in the context of CFD modelling. The time required for the carbonatation reactions to develop is not compatible with being solved alongside the hydrodynamics, with the reactions occurring over several minutes to hours and the hydrodynamic model requiring sub-second timesteps in order to capture the flow complexity. The reactions are therefore solved with the flow patterns, turbulence and two-phase fields frozen in time after 60 seconds, when the instantaneous flow patterns are assumed to be representative of the pseudo steady-state flow patterns within the saturator as suggested by Figure 8-11. This means that the modelling of the reactions has been decoupled from the flow patterns, with the necessary assumptions that the outcomes of the reactions occurring – the precipitation and dissolution of solids and the consumption of gaseous CO_2 – do not significantly influence the hydrodynamic behaviour within the saturator. The solid species are also assumed to be neutrally buoyant and follow the liquid flow patterns, and are therefore modelled along with the dissolved species as components in the liquid phase.

It is not feasible to solve the whole reaction scheme using the forward and backward reactions proposed by Mitchell et al. (2010) due to the very fast reaction rates between the dissolved carbonate species presented in Table 8-1. A comparison of three different proposed simplifications of the reaction scheme is presented alongside the validation work for the carbonatation reactions in Section 9.3. The proposed methods of modelling the series of reversible reactions are investigated and compared with experimental pH and dissolved carbonate data in a laboratory-scale validation setup in the absence of $Ca(OH)_2$. An iterative equilibrium method of solving the carbonate equilibrium equations is identified as the most appropriate model based on the ability to capture the buffering mechanism of the system and the relatively large timestep under which the model remains stable. This forms the basis of the reaction modelling applied in this section for the full-scale carbonatation vessel, as well as the further validation for a water and $Ca(OH)_2$ system described in Section 9.4. The validation work presented is able to represent the behaviour of the system with reasonable accuracy under different operating conditions in water, which is shown to undergo similar fundamental behaviour when sucrose is present. The validation of the full reaction model is discussed in more detail in Chapter 9.

8.6.1 Aqueous Reactions in the Absence of Calcium Hydroxide

Under the selected method, the aqueous reaction system is simplified with the introduction of the term C_T, which represents the total aqueous carbon species present in the system, as described by equation (8-15). These species represent the molar concentrations of the dissolved species in equations (8-2) to (8-5).

$$[C_T] = \left[CO_{2(aq)}\right] + [H_2CO_3] + [HCO_3{}^-] + \left[CO_3{}^{2-}\right] \tag{8-15}$$

All CO_2 of the entering the aqueous phase is assumed to immediately enter the C_T component, with the assumption that equilibrium has been reached between the different aqueous carbon species at each timestep. Whereas this is known to be true for the ionic species (H_2CO_3, $HCO_3{}^-$ and $CO_3{}^{2-}$), it is not necessarily true for the conversion of $CO_{2\,(aq)}$ to H_2CO_3, which is a rate-determined reaction (Segev et al., 2012b). However, due to the very fast reaction in relation to the interphase mass transfer processes, it has been assumed that all carbonate species are at instantaneous equilibrium at each time step, an assumption also applied by Segev et al. (2012a).

The equilibrium concentrations of each of the species involved in the equilibrium reactions can be related to the concentration of aqueous CO_2 using the equilibrium constants and the pH via the concentration of free protons (H^+), as shown in equations (8-16) to (8-18). The equilibrium constant is calculated by dividing the forward reaction rate by the backward reaction rate for each of the reactions in Table 8-1, and have been adjusted for the reaction temperature of 79°C via the Van't Hoff equation using tabulated enthalpy of formation data (Green and Perry, 2008). The corrected equilibrium constants used in this chapter are presented in Table 8-6.

$$[H_2CO_3] = K_2\left[CO_{2(aq)}\right] \tag{8-16}$$

$$[HCO_3{}^-] = \frac{K_2K_3\left[CO_{2(aq)}\right]}{[H^+]} \tag{8-17}$$

$$\left[{CO_3}^{2-}\right] = \frac{K_2 K_3 K_4 \left[CO_{2(aq)}\right]}{[H^+]^2} \tag{8-18}$$

Table 8-6: A comparison of equilibrium constants at 25°C and 79°C.

Equilibrium Constant	25°C	79°C
K_2	0.003	0.00135
K_3	0.0002 M	0.00032 M
K_4	6×10^{-11} M	1.51×10^{-10} M

Combining these expressions with equation (8-15) and rearranging gives an expression for C_T in terms of the CO_2 and H^+ concentrations (equation (8-19)). This allows for the distribution of dissolved carbonate species for a given pH to be calculated.

$$[C_T] = \left[CO_{2(aq)}\right]\left(1 + K_2 + \frac{K_2 K_3}{[H^+]} + \frac{K_2 K_3 K_4}{[H^+]^2}\right) \tag{8-19}$$

This model requires an iterative method to step the solution forward with time, due to the circular dependency between the pH and the concentration of dissolved CO_2. This is achieved by calculating the carbonate species concentrations at the current timestep (t) based upon the H^+ component from the previous timestep ($t-1$). The resulting instantaneous concentrations are described by equations (8-20) to (8-23).

$$\left[CO_{2(aq)}\right]_t = \frac{[C_T]_t}{\left(1 + K_2 + \frac{K_2 K_3}{[H^+]_{t-1}} + \frac{K_2 K_3 K_4}{{[H^+]_{t-1}}^2}\right)} \tag{8-20}$$

$$[H_2CO_3]_t = K_2\left[CO_{2(aq)}\right]_t \tag{8-21}$$

$$[{HCO_3}^-]_t = \frac{K_2 K_3 \left[CO_{2(aq)}\right]_t}{[H^+]_{t-1}} \tag{8-22}$$

$$\left[{CO_3}^{2-}\right]_t = \frac{K_2 K_3 K_4 \left[CO_{2(aq)}\right]_t}{{[H^+]_{t-1}}^2} \tag{8-23}$$

The change in C_T and H^+ for each time step is described by a pair of coupled differential equations ((8-24) and (8-25)), which are applied as mass fraction source terms in a in a sub-domain covering the entire modelled geometry. The change in H^+ is calculated based upon the change in C_T multiplied by the fractions of ${HCO_3}^-$ and ${CO_3}^{2-}$, which are the species involved in the generation and consumption of H^+ ions via equations (8-3) and (8-4). This will give the net consumption or generation of H^+ via the carbonic acid buffering system for the current timestep.

$$\frac{d[C_T]_t}{dt} = k_L a(C^* - [C_T]_{t-1}) \tag{8-24}$$

$$\frac{d[H^+]_t}{dt} = \frac{d[C_T]_t}{dt}\left(\frac{[{HCO_3}^-]_t + 2[{CO_3}^{2-}]_t}{[C_T]_t}\right) \tag{8-25}$$

8.6.2 Aqueous Reactions in the Presence of Calcium Hydroxide

In addition to the aqueous reactions detailed in section 8.6.1, the carbonatation process has the additional complexities of undissolved $Ca(OH)_2$ solids in the reacting mixture and the generation of solid $CaCO_3$ crystals. These processes involve the generation or consumption of solid species and are both directly dependent upon the buffering system described above.

The additional reactions modelled in this section are described by equations (8-26) to (8-28). The reversible dissolution of $Ca(OH)_2$ is described by equation (8-26). The formation of solid $CaCO_3$ is modelled by equation (8-27), and is a simplification based upon combining equations (8-5) and (8-6), with the assumption that the majority of $CaCO_3$ will exist in the solid form at any time. The re-dissolution of $CaCO_3$ in the presence of gaseous CO_2 is assumed to form the stable aqueous species calcium bicarbonate ($Ca(HCO_3)_2$) via equation (8-28). This is consistent with the observations of Ahn et al. (1996) (in Korean) and Montes-Hernandez et al. (2008), both as reported by Han et al. (2011). It is assumed that equation (8-28) is irreversible, and replaces the backwards reaction described by Mitchell et al. (2010) using the rate constant k_{-5}. This is a reasonable assumption since the dissolved concentration of $Ca(HCO_3)_2$ is expected to be present in concentrations well below the saturation value. Furthermore, the total dissolved concentrations of carbonate

species measured during the validation experiments in Section 9.4 are significantly above the saturation concentration of CO_2, supporting the hypothesis that a stable bicarbonate species is formed through continued CO_2 bubbling. There is also a clear dissolution of the solid $CaCO_3$ with continued gas bubbling measured during the validation experiments once the excess $Ca(OH)_2$ has been consumed.

$$Ca(OH)_{2\,(s)} \underset{k_b}{\overset{k_f}{\leftrightharpoons}} Ca^{2+} + 2OH^- \tag{8-26}$$

$$Ca^{2+} + {CO_3}^{2-} \overset{k_5}{\rightarrow} CaCO_{3\,(s)} \tag{8-27}$$

$$CaCO_{3\,(s)} + {HCO_3}^- + H^+ \overset{k_{-5}}{\longrightarrow} Ca(HCO_3)_2 \tag{8-28}$$

The dissolution of solid $Ca(OH)_2$ is simulated based on the model of Johannsen and Rademacher (1999), presented in equation (8-29), which was developed from experimental data using several commercially available $Ca(OH)_2$ samples.

$$\frac{d[Ca(OH)_2]}{dt} = A_p\left(k_f - k_b[Ca^{2+}][OH^-]_1{}^2\right) \tag{8-29}$$

The forward and backward rate constants used in the dissolution model are also based upon the data compiled by Johannsen and Rademacher (1999), however unlike the original paper the backward reaction constant k_b is assumed to be independent of the $Ca(OH)_2$ loading. The trend suggested by Johannsen and Rademacher provides a very poor fit to the experimental data (R^2 = 0.43), and is virtually indistinguishable in trend to the forward reaction rate, which was considered by the same authors to be constant. Furthermore, extrapolating this trend into the higher $Ca(OH)_2$ concentrations used in this study leads to a poor prediction of the dissolution rate.

The dissolution rate of $Ca(OH)_2$ is dependent on the solid particle size, which is introduced through the surface area of $Ca(OH)_2$ particles per unit volume, A_p. This is related to the local concentration of $Ca(OH)_2$ using equations (8-30) to (8-32) (Johannsen and Rademacher, 1999), meaning that the dissolution rate predicted by equation (8-29) is also dependent on the local $Ca(OH)_2$ concentration.

$$A_p = N_p \, 4\pi \left(\frac{d_p}{2}\right)^2 \tag{8-30}$$

$$d_p = 2\left(\frac{3}{4}\frac{[Ca(OH)_2]_t \, M_{Ca(OH)_2}}{N_p \, \rho_{Ca(OH)_2}}\right) \tag{8-31}$$

$$N_p = \frac{[Ca(OH)_2]_0 \, M_{Ca(OH)_2}}{\rho_{Ca(OH)_2} \, V_{p,0}} \tag{8-32}$$

where N_p is the number of $Ca(OH)_2$ particles, d_p is the particle diameter, $M_{Ca(OH)_2}$ is the molar mass of $Ca(OH)_2$ and $V_{p,0}$ is the initial volume of a $Ca(OH)_2$ particle.

The dissolution of $Ca(OH)_2$ is modelled as occurring in response to the increase in H^+ concentration during the interphase mass transfer of CO_2. This is due to the dependence of the $Ca(OH)_2$ dissolution reaction on the concentration of OH^- in solution. The first step of the reaction scheme is therefore to calculate the change in the concentration of C_T in response to the interphase mass transfer and the formation of $CaCO_3$ (equation (8-33)). For this step, Ca^{2+} and H^+, which is used to calculate ${CO_3}^{2-}$, are brought forward from the previous timestep in an iterative method similar to that used in section 8.6.1.

$$\frac{d[C_T]_t}{dt} = k_L a(C^* - [C_T]_{t-1}) - k_5[Ca^{2+}]_{t-1}\left[{CO_3}^{2-}\right]_{t-1} - k_{-5}[CaCO_3]_{t-1} \tag{8-33}$$

In addition to the distribution of C_T, the formation of solid $CaCO_3$ and the subsequent formation of $Ca(HCO_3)_2$, based on equations (8-27) and (8-28) respectively, are modelled at this stage. They are implemented into the ANSYS CFX framework as mass fraction source terms as described by equations (8-34) and (8-35).

$$\frac{d[CaCO_3]_t}{dt} = k_5[Ca^{2+}]_{t-1}\left[{CO_3}^{2-}\right]_{t-1} - k_{-5}[CaCO_3]_{t-1} \tag{8-34}$$

$$\frac{d[Ca(HCO_2)_2]_t}{dt} = k_{-5}[CaCO_3]_{t-1} \quad (8\text{-}35)$$

There is an additional consumption of free hydrogen ions after this first reaction stage due to the formation of aqueous $Ca(HCO_3)_2$ via equation (8-28). This concentration is denoted as $[H^+]_1$, signifying the concentration of H^+ after the first stage of the reaction scheme, and is calculated as shown in equation (8-36).

$$[H^+]_1 = [H^+]_{t-1} - ([Ca(HCO_3)_2]_t - [Ca(HCO_3)_2]_{t-1}) \quad (8\text{-}36)$$

When solid $Ca(OH)_2$ is present, the second stage of this reaction scheme is to model the dissolution of $Ca(OH)_2$ using equation (8-29). The concentration of OH^- ions after the first step (during which the concentration of hydrogen ions will change due to the carbonic acid buffering system described previously) can be calculated using the electro-neutrality assumption as applied by Johannsen and Rademacher (1999), whereby it is assumed that the combined charge of all charged species within the aqueous phase will be approximately equal to zero. A balance of the charged species present in solution after stage one is presented in equation (8-37), giving an approximation of the present free hydroxide concentration, $[OH^-]_1$.

$$[OH^-]_1 = 2[Ca^{2+}]_{t-1} + [H^+]_1 - 2\left[{CO_3}^{2-}\right]_t - [{HCO_3}^-]_t \quad (8\text{-}37)$$

The next stage of the reaction scheme is to model the dissolution of $Ca(OH)_2$ using equation (8-29) as a mass source term, with the hydroxide ion concentration $[OH^-]_1$. The source term for Ca^{2+} ions is also calculated during this stage as described by equation (8-38).

$$\frac{d[Ca^{2+}]_t}{dt} = -\frac{d[Ca(OH)_2]_t}{dt} - k_5[Ca^{2+}]_{t-1}\left[{CO_3}^{2-}\right]_t \quad (8\text{-}38)$$

The pH of the solution following the dissolution of $Ca(OH)_2$ can be calculated using the concentration of free H^+ ions in solution. For each mole of $Ca(OH)_2$ dissolved, two moles of free OH^- ions will be generated according to equation (8-26), giving the new concentration $[OH^-]_2$ after the second phase of the reaction scheme as described by equation (8-39). This is converted to a concentration of free hydrogen ions, named $[H^+]_2$

referring to the second step in the reaction scheme, using the dissociation constant of water as described by equation (8-40). This is assumed to hold a typical value of 1×10^{-14} M^2 that is regularly applied for pure water.

$$[OH^-]_2 = [OH^-]_1 - 2([Ca(OH)_2]_t - [Ca(OH)_2]_{t-1}) \tag{8-39}$$

$$[H^+]_2 = \frac{K_w}{[OH^-]_2} \tag{8-40}$$

The overall change in $[H^+]$ for the timestep is calculated from the difference in free hydrogen ions between the previous timestep (t_{-1}) and the final concentration for the current timestep (t), calculated using equation (8-40). As with the other component species within the liquid phase, this is implemented as a mass fraction source term using equation (8-41).

$$\frac{d[H^+]}{dt} = \frac{[H^+]_2 - [H^+]_{t-1}}{t - t_{-1}} \tag{8-41}$$

In the absence of solid $Ca(OH)_2$, the second step of this reaction scheme is not required and the model for $[H^+]$ can be simplified to follow the reaction course outlined by equation (8-25), since the opposing influence on the solution pH due to the generation of OH^- ions is no longer present. This will be the case at any location within the saturator where the $Ca(OH)_2$ concentration is completely depleted, and is implemented as such in the model. The solution procedure for a single timestep in both cases is summarised in a flow chart presented in Figure 8-18.

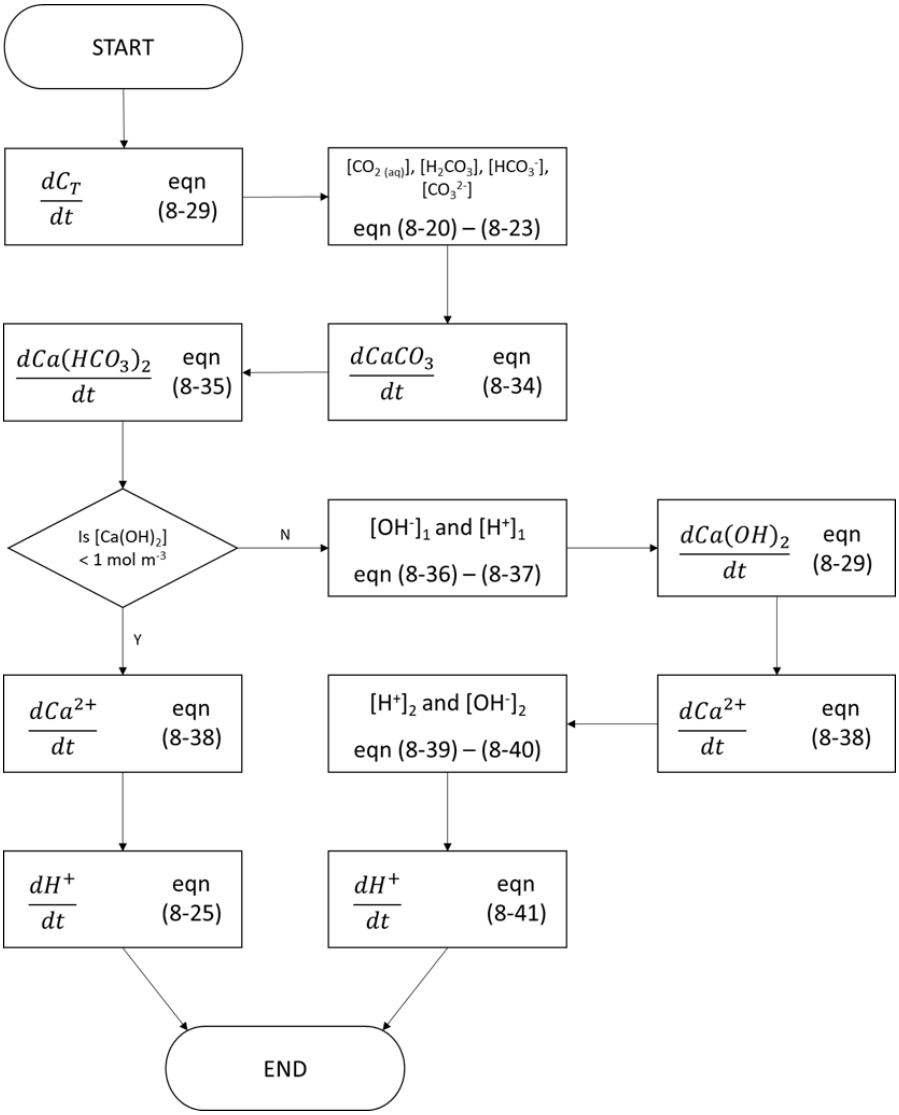

Figure 8-18: Flowchart of the solution procedure used for the carbonatation reaction scheme, applied for a single timestep.

8.6.3 Reaction Modelling Results

The series of reactions represented by equations (8-15) to (8-41), which describe the liquid-phase reactions occurring both in the presence and absence of $Ca(OH)_2$, are solved for the saturator with a typical operating CO_2 flow rate of 0.5 t hr^{-1}. For this, the hydrodynamic conditions reported in Section 8.5 – including the flow patterns, gas distribution, bubble size and turbulence – are frozen in time after 60 seconds, where the flow patterns have previously been judged to achieve a pseudo-steady state. This means that the modelled reactive species profiles will be dependent on the instantaneous flow patterns at the time they were frozen, however it is assumed that the frozen conditions are representative of the average flow conditions during the course of the reaction. The reaction model is

initialised with a starting $Ca(OH)_2$ concentration of 0.4 wt% throughout the entire saturator vessel and in the fresh feed introduced at the liquid surface via the mass balance described in Figure 8-3. Similarly, the initial and inlet pH is set to be 12.2 based on the model of Johannsen and Rademacher (1999) in the absence of gaseous CO_2. All other operating conditions are set based on the values specified in Table 8-2.

Evaluation of the reaction model is based on profiles calculated at the liquid outlet at the bottom of the saturator vessel and analysis of the pH and concentration profiles for a vertical cut plane at the centre of the saturator. The reaction model is run for 150 minutes of modelled time in order for the component species to have reached steady state at the outlet. The profiles presented in Figure 8-19 show that there are two clear phases of operation following start-up. During the first phase (up to 30 minutes), the solid $Ca(OH)_2$ that remains in the vessel is being consumed as the liquid-phase reactions progress, maintaining a constant pH (Figure 8-19 a) and Ca^{2+} concentration (Figure 8-19 c) in the liquid phase. In contrast, the concentration of $CaCO_3$ and $Ca(HCO_3)_2$ (Figure 8-19 d) increase rapidly during this phase as the $Ca(OH)_2$ being dissolved is converted to solid $CaCO_3$ via the reaction scheme described previously. During this initial phase the total dissolved carbonate species (C_T) reaches a steady state which is far below the saturation concentration, as shown in Figure 8-19 b), as is it rapidly consumed by the liquid-phase reactions. During the second phase of operation, which occurs after 30 minutes under these conditions, the solid $Ca(OH)_2$ in the majority of the vessel has been consumed, leaving only the fresh $Ca(OH)_2$ in the incoming sucrose feed to be converted into fresh $CaCO_3$. Inevitably, this leads to a steep drop in $CaCO_3$ and $Ca(HCO_3)_2$ from the previous values.

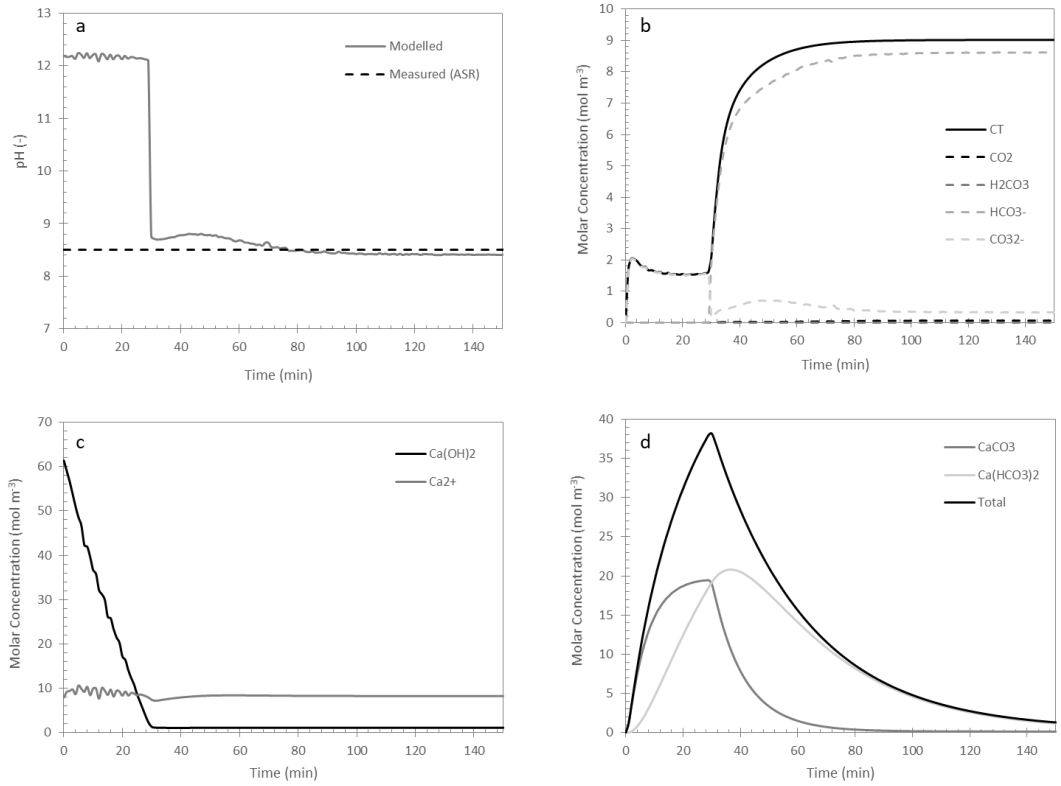

Figure 8-19: pH and concentration profiles at the saturator outlet with a CO_2 flow rate of 0.5 t hr^{-1}. a) pH, b) C_T, c) $Ca(OH)_2$ and Ca^{2+}, d) $CaCO_3$ and $Ca(HCO_3)_2$.

The pH modelled at the saturator outlet for a CO_2 flow rate of 0.5 t hr^{-1} matches very well with the typical operating value of 8.5, once the $Ca(OH)_2$ in the system has been consumed, and remains close to this value until the end of the 150 minute modelled time. The step-change in pH observed in Figure 8-19 a) is very similar to the step-change observed for the closed hydroxide-in-water system used by Han et al. (2011) and in the validation experiments detailed in Section 9.4, however the final pH value achieved for the continuous system modelled here is significantly higher than the published and validation experiments. This can be attributed to the continual addition of solid $Ca(OH)_2$ in the incoming sucrose stream, which introduces a fresh source of OH^- ions to oppose the carbonate buffering system described previously. The total inorganic carbon described in Figure 8-19 b) reaches two different steady state values depending on the presence of $Ca(OH)_2$ as described above, however the distribution of carbonate species is very different between the two phases of the reaction. During the initial stage, where the pH is high, the majority of C_T is of the form ${CO_3}^{2-}$, which further promotes the formation of solid $CaCO_3$. In contrast, the major component during the second phase, where the pH is much lower, is shown to be H_2CO_3, meaning that there is much less ${CO_3}^{2-}$ available for the formation of solid $CaCO_3$. This matches well with the predictions of the Bjerrum plot

presented in Figure 8-1, suggesting that the carbonate buffering system in the liquid phase is being modelled in a realistic way.

The distribution of the calcium carbonate formed between $CaCO_3$ and $Ca(HCO_3)_2$ can be seen in Figure 8-19 d). Initially, the majority of the calcium carbonate remains in the form $CaCO_3$, however as the total concentration increases, the relative concentration of $Ca(HCO_3)_2$ also increases. From observations made in Section 9.5, where the validation experiments are re-run in sucrose solutions of increasing concentration, it is expected that the presence of dissolved sucrose will hinder the re-dissolution of $CaCO_3$. The true concentrations of solids is therefore likely to lie in between the $CaCO_3$ value predicted by the model described above and the sum of the modelled $CaCO_3$ and $Ca(HCO_3)_2$ concentrations in Figure 8-19 d).

The distribution of the pH and various liquid-phase component species within the saturator vessel after 90 minutes simulated time are presented in Figure 8-20 for a vertical cut-plane through the centre of the vessel. The component flow patterns all show a significant resemblance to the liquid-phase flow patterns presented in Figure 8-9 and Figure 8-10. Furthermore, the concentration profiles for the three liquid-phase component species (b-d) show a relatively small variation in the concentration within the saturator, suggesting that the churning flow patterns are creating a well-mixed liquid phase, which is captured by the model despite the use of the frozen flow field. This means that the outlet values used to generate plots b) to d) in Figure 8-19 are representative of the bulk liquid phase. However, the range of pH values presented in Figure 8-20 a) is much greater, with the pH at the outlet appearing to be higher than the majority of the saturator. The volume-averaged pH in the saturator is calculated to be 6.48, which is lower than the value suggested at the outlet and therefore also lower than the typical operating value of 8.5.

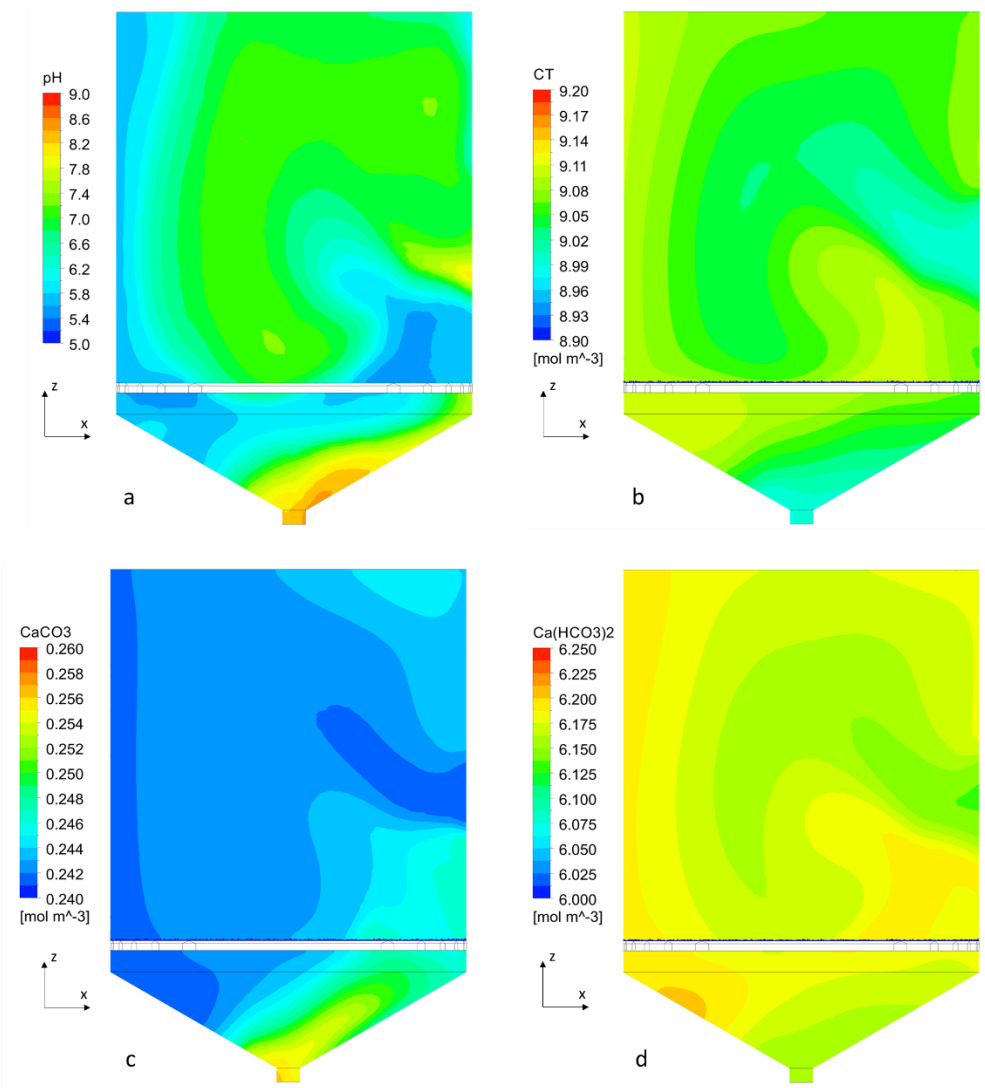

Figure 8-20: pH and molar concentration contour plots for a vertical cut plane at the centre of the saturator with a CO_2 gas flow rate of 0.5 t hr^{-1}.
a) pH, b) C_T, c) $CaCO_3$, d) $Ca(HCO_3)_2$.

8.6.4 Effect of Varying Carbon Dioxide Flow Rate

The inlet flow rate of CO_2 gas is varied between 0.15 and 0.9 t hr^{-1} using the values included in Table 8-2, and previously modelled with regards to hydrodynamic conditions. Profiles for the pH and various component species concentrations at the bottom saturator outlet are presented in Figure 8-21 for the different CO_2 gas flow rates modelled. The time taken for the $Ca(OH)_2$ present in the saturator at the beginning of the simulation to be consumed decreases as the flow rate of CO_2 increases, as can be seen in Figure 8-21 b) and from the step change in pH shown in Figure 8-21 a). This is due to the greater amount of dissolved carbonate species entering the liquid phase, with the dissolution rate clearly coupled to the interphase mass transfer previously presented in terms of $k_L a$. Similarly, the

$CaCO_3$ concentration increases more steeply during the initial stage of the process when a higher CO_2 flow rate is applied, however there is much less variation between the different gassing conditions at the end of the 90 minutes modelled time as the supply of fresh $Ca(OH)_2$ becomes limiting. The concentration of C_T during the initial phase, where there is a high consumption of ${CO_3}^{2-}$ ions, also increases in accordance with the volume-averaged mass transfer coefficient, however all values predicted during this phase are much lower than the saturation concentration. In contrast, the C_T profiles observed once the initial $Ca(OH)_2$ has been consumed appear to closely match the profiles where only mass transfer is modelled, presented in Figure 8-16, in terms of shape and steady-state concentration.

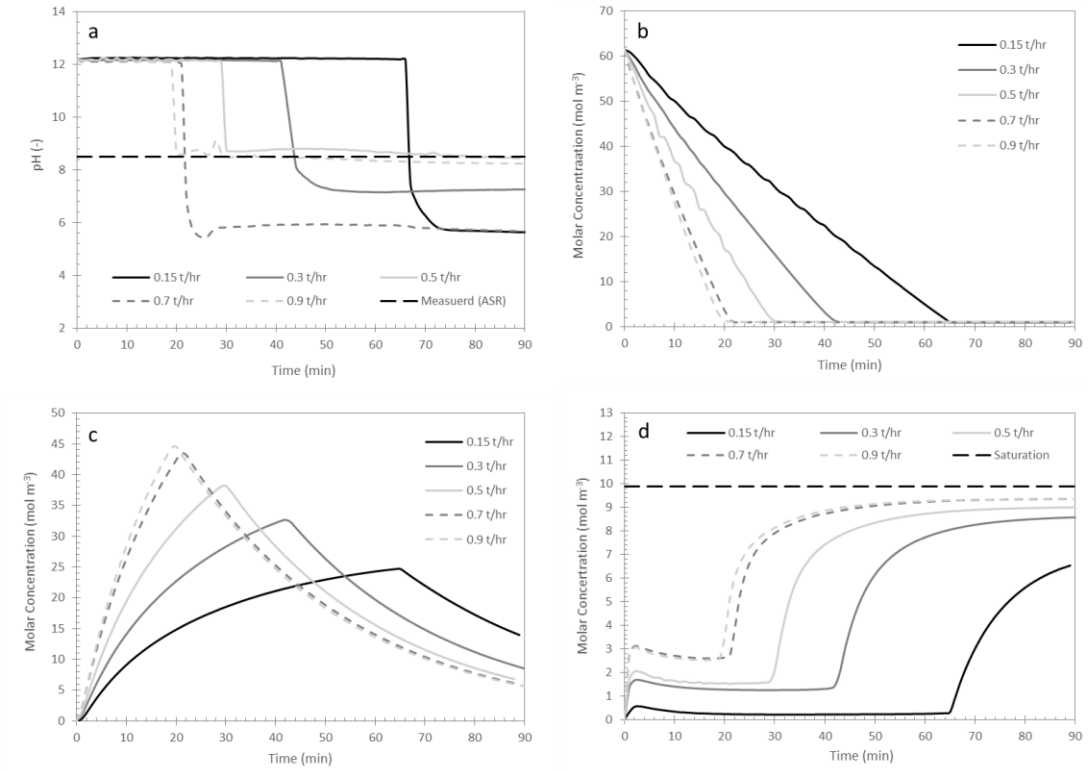

Figure 8-21: pH and concentration profiles at the saturator outlet for varying CO_2 flow rates. a) pH, b) $Ca(OH)_2$, c) $CaCO_3$ and $Ca(HCO_3)_2$ (combined), d) C_T.

The range of pH values predicted within the saturator is similar between the different CO_2 flow rates modelled, with the five contour plots presented in Figure 8-22 using the same colour bar representing the pH range of 5 to 9. This matches reasonably well with the typical operating pH value of 8.5 currently seen. The strong dependence of the modelled pH on the flow patterns can be clearly seen by comparing Figure 8-9 and Figure 8-10 with Figure 8-22. For a CO_2 flow rate of 0.15 t hr^{-1}, there is a much greater difference in the

modelled pH throughout the saturator when compared to the other conditions, as the structured flow patterns create a gradient between the fresh feed entering at the top with a higher pH and the treated sucrose with a lower pH at the outlet. For the other flow rates, which are operating in an unsteady churning regime, the pH varies within the range identified and is dependent on the mixing flow patterns. This also explains the apparent lack of trend in the final value of the outlet pH presented in Figure 8-21 a), since the outlet pH is dependent on the flow patterns at the time which the hydrodynamic parameters have been frozen. The maximum variation in volume-averaged pH from the 0.5 wt% value of 6.48 is ±0.16, showing that there is in fact no dependence of the pH on the CO_2 flow rate predicted by the model.

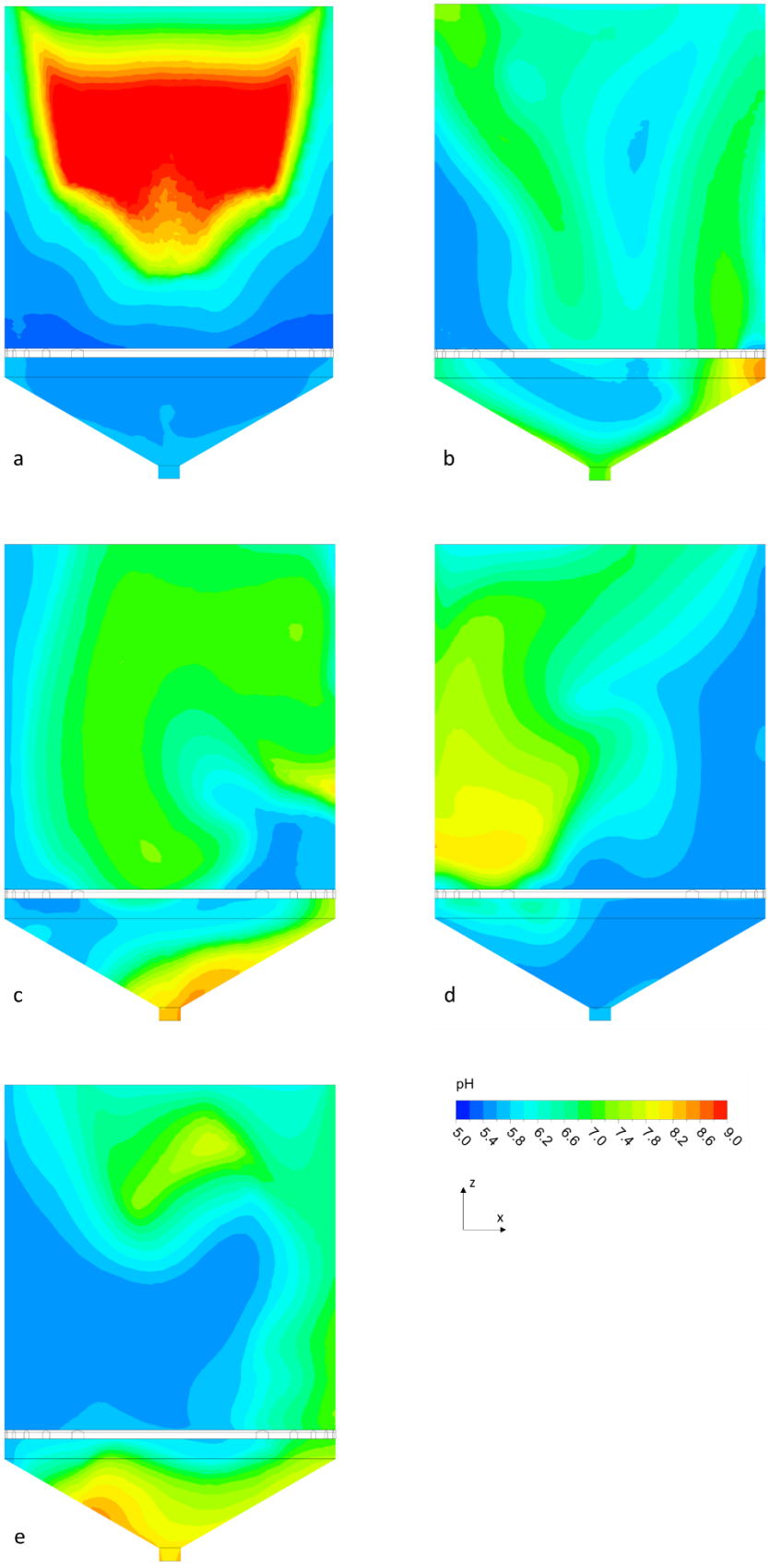

Figure 8-22: pH contour plots for a vertical cut plane at the centre of the saturator with varying CO_2 gas flow rates.
a) 0.15 t hr^{-1}, b) 0.3 t hr^{-1}, c) 0.5 t hr^{-1}, d) 0.7 t hr^{-1}, e) 0.9 t hr^{-1}.

8.6.5 Effect of Varying Calcium Hydroxide Concentration

The reaction model detailed above is repeated for the same set of CO_2 flow rates using a higher $Ca(OH)_2$ concentration of 0.8 wt% in the initial conditions and the fresh sucrose feed. These simulations use the same frozen hydrodynamic conditions applied in Section 8.6.4, since the changing solids and liquid-phase concentrations have been assumed not to significantly influence the flow patterns. With the increased initial concentration, the time for the start-up concentration to be consumed increases with the $Ca(OH)_2$ concentration increase, with the two lowest CO_2 flow rates not reaching full consumption within the 90 minutes simulated time, as represented by Figure 8-23 b). The overall trends in the outlet concentration profiles for $CaCO_3$ and $Ca(HCO_3)_2$ (plot c) and C_T (plot d) do not significantly change from the lower hydroxide concentration, other than the longer initial phase as the $Ca(OH)_2$ is consumed. However, the magnitude of the concentration of $CaCO_3$ produced increases in line with the increase in feed concentration.

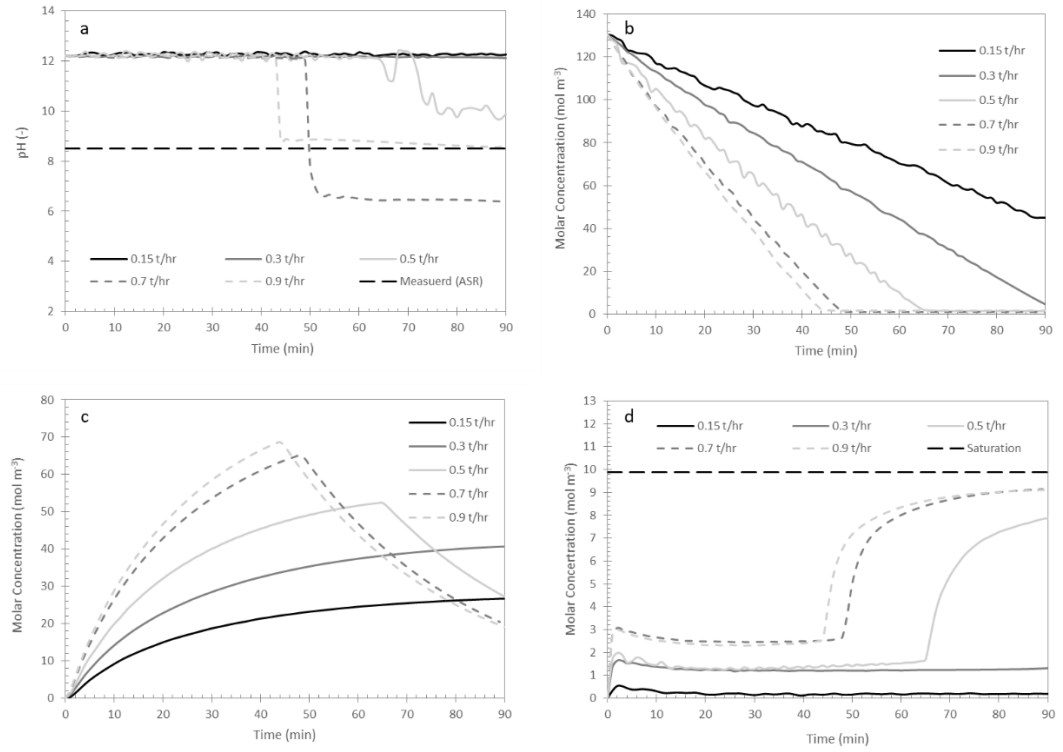

Figure 8-23: pH and concentration profiles at the saturator outlet for varying $Ca(OH)_2$ concentration.
a) pH, b) $Ca(OH)_2$, c) $CaCO_3$ and $Ca(HCO_3)_2$ (combined), d) C_T.

Once again, the modelled pH distributions within the saturator, and therefore also at the saturator outlet, are highly dependent on the flow patterns at the time that the hydrodynamic conditions are frozen, as represented by the varying outlet pH presented in

Figure 8-23 a). However, there is once again little variation in the volume-averaged values between the different CO_2 flow rates for which the starting $Ca(OH)_2$ has been consumed within the simulated time. The pH in the saturator remains at the starting value for 0.15 and 0.3 t hr^{-1} flow rates due to the unreacted hydroxide present. The volume-averaged pH values modelled at different gas flow rates are presented in Figure 8-24, alongside the corresponding values at 0.4 wt% $Ca(OH)_2$ addition. This shows that increasing the amount of $Ca(OH)_2$ in the feed stream results in an increase in the pH in the saturator under normal operating conditions, and can therefore be used to control the pH. However, the modelled pH is still significantly lower than the typical operating pH, suggesting that although the model responds to varying conditions in a plausible manner, the assumptions or model constants used to predict the dissolved species reactions may require some further development. The main consequences of increasing the $Ca(OH)_2$ concentration can therefore be said to be a longer start-up period before the operating pH is established, with a greater carbonate production and higher pH achieved during normal operation.

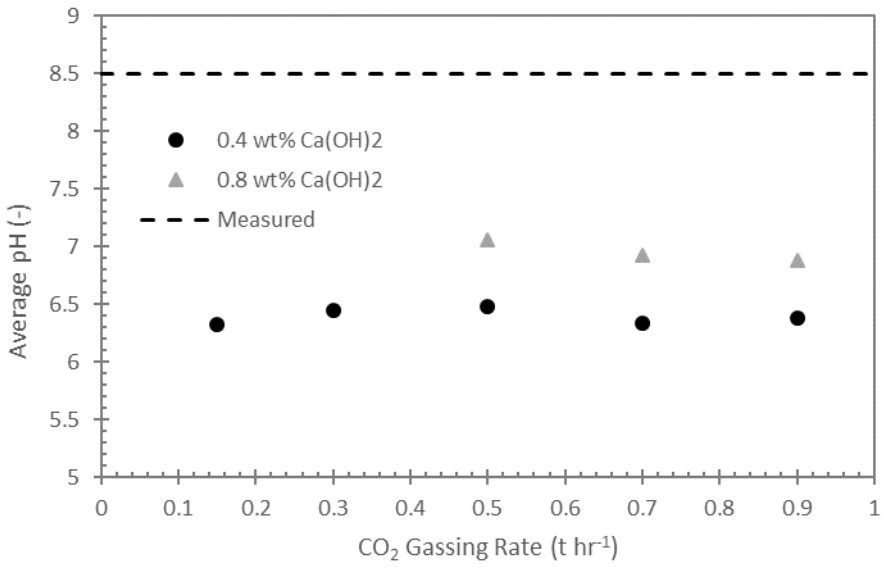

Figure 8-24: Volume-averaged pH values for different CO_2 flow rates and $Ca(OH)_2$ loading.

8.7 Influence of Including a Liquid-Phase Recycle

One method that has been considered by the operators to improve the current carbonatation performance is to introduce a liquid-phase recycle to the saturator. This is achieved in the model by maintaining the same production rate for the overall process but

increasing the flow of sucrose at the saturator outlet and recycling a fraction of this stream with the fresh feed, thus requiring new hydrodynamic simulations to be performed. A pre-defined fraction of the outlet flow is recycled into the bulk liquid via the mass balance at the liquid surface presented in Figure 8-3. For example, a 100% liquid recycle will have a total flow rate of 250 t hr^{-1} at the saturator outlet in order to maintain the specified 125 t hr^{-1} production rate for the unit.

The influence of including a liquid-phase recycle on the equilibrium reaction scheme and hydrodynamics described above has been investigated using the CFD model developed in previous chapters. This is applied for a 0.5 t hr^{-1} CO_2 flow rate with recycle rates of 50, 100 and 150% of the incoming sucrose feed and 0.4 wt% $Ca(OH)_2$. Due to the increased flow rate at the bottom outlet of the saturator, the hydrodynamic model has been solved for 60 seconds for each of the new recycle conditions. The transient volume-averaged $k_L a$ profiles for the different recycle conditions are presented in Figure 8-25, which is analogous to the profiles presented for varying CO_2 flow rates in Figure 8-11. The profiles of volume-averaged $k_L a$ between the different recycle rates are very similar, with the only significant deviation from the trend occurring after 60 seconds for the highest recycle rate of 150%. This means that introducing a sucrose recycle should not significantly affect the average two-phase hydrodynamic conditions.

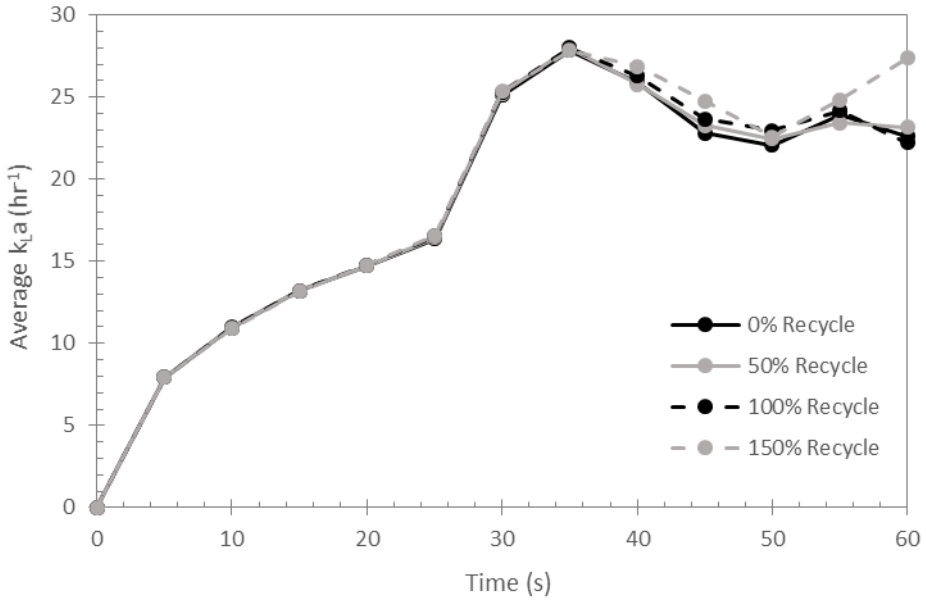

Figure 8-25: Volume-averaged $k_L a$ profiles during the first 60 seconds of operation for varying liquid-phase recycle rates.

The reaction model has been solved for the selected recycle rates using the flow patterns frozen after 60 seconds of the hydrodynamic model, as previously described. The reaction profiles for the modelled components are presented in Figure 8-26. Comparing these profiles shows that introducing a recycle of up to 100% has very little influence on the performance of the process, with very similar concentration profiles seen for all of the dissolved species. In contrast, and despite the slightly higher volume-averaged $k_L a$ identified in Figure 8-25, the 150% recycle shows much worse performance in terms of the conversion of CO_2 to $CaCO_3$ and $Ca(CaOH)_2$ consumption. It is proposed that this reduction in performance may be due to the dilution of the fresh feed by non-reacting dissolved species within the vessel, particularly at the liquid surface where the fresh feed is introduced.

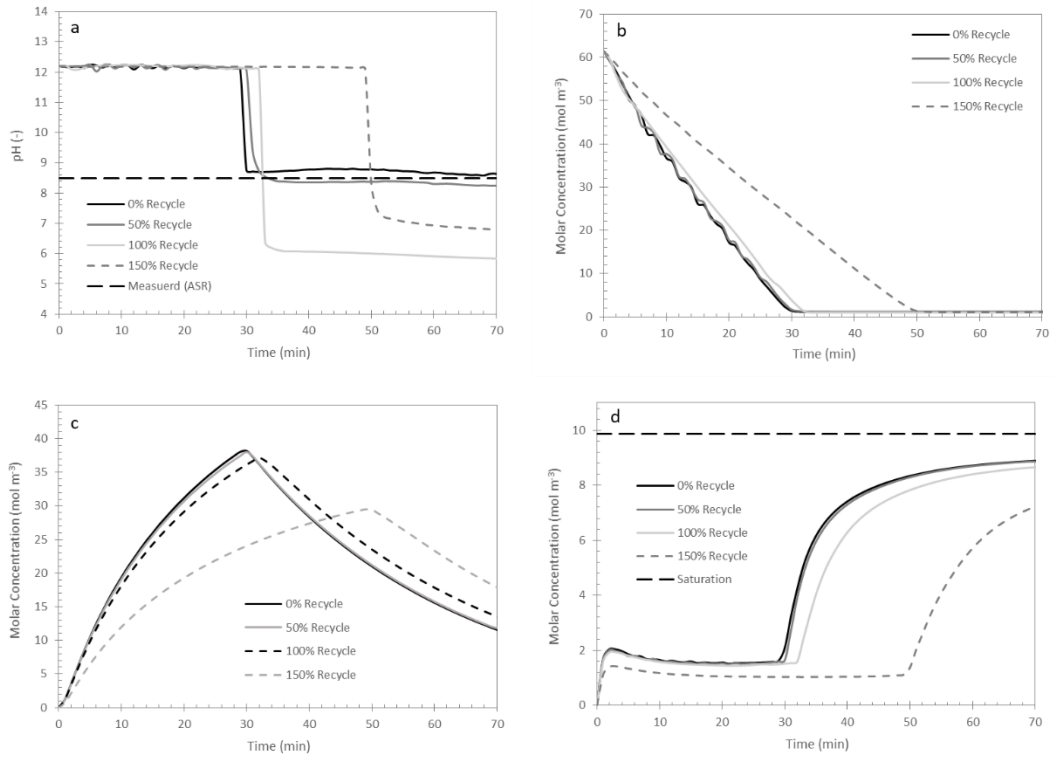

Figure 8-26: pH and concentration profiles at the saturator outlet for varying recycle rates. a) pH, b) $Ca(OH)_2$, c) $CaCO_3$ and $Ca(HCO_3)_2$ (combined), d) C_T.

A comparison of the pH contours for a vertical cut plane, combined with the liquid-phase velocity vectors, is presented in Figure 8-27. Although there are some differences in the flow patterns and distribution of the pH, the distributions do not appear to show any significant trends in pH with varying recycle rate. This is supported by the volume-averaged pH values, which are calculated to be 6.40, 6.10 and 6.14 for recycle rates of 50, 100 and

150% respectively. As with previously presented profiles, the pH has a relatively wide range of different values present in the vessel, which are strongly coupled with the flow patterns. From these models and previous analysis it can be concluded that there is no benefit to be gained from including a liquid recycle since the turbulent churning flow patterns that develop within the column provide sufficient mixing of the liquid-phase components. Furthermore, very high recycle rates may reduce the performance of the column and should therefore be avoided.

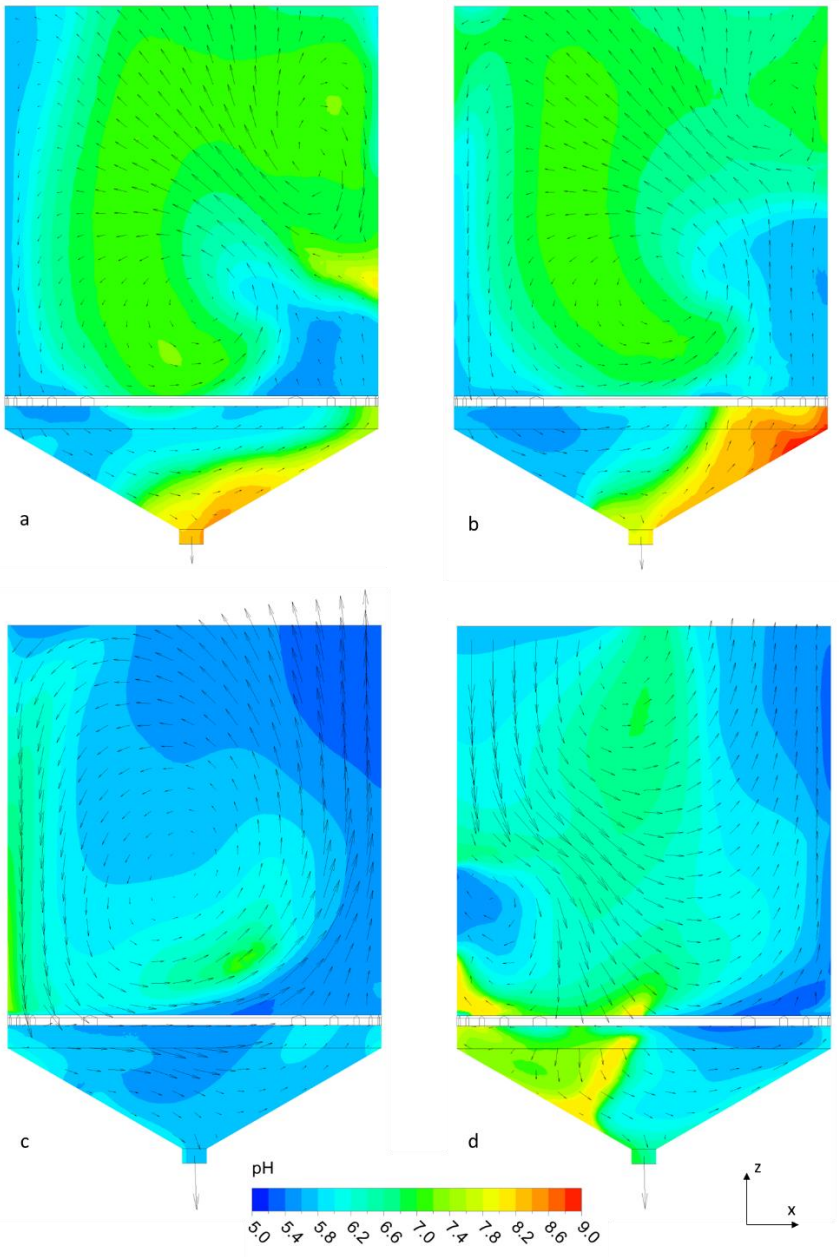

Figure 8-27: pH contour plots and liquid-phase velocity vectors for a vertical cut plane at the centre of the saturator with varying recycle rate.
a) 0% recycle, b) 50% recycle, c) 100% recycle, d) 150% recycle.

8.8 Summary

This chapter has detailed the successful development of a CFD model for an industrial-scale continuous carbonatation vessel currently operated during the refining of cane sugar. Carbon dioxide gas is bubbled through a concentrated solution of sucrose and calcium hydroxide, with solid calcium carbonate being precipitated and trapping impurities within the solids, which are filtered out immediately downstream. Computational analysis of the hydrodynamics has been performed over a wide range of CO_2 gas flow rates, and show that the saturator is operating in the turbulent churning bubbling regime under normal operating conditions. Increasing the flow rate of CO_2 within the operating range leads to an increase in the mass transfer performance, quantified in terms of the parameter $k_L a$, however further increases above the current operating range do not show any significant improvement. The shear stress is another important parameter in the saturator operation since high shear can break up $CaCO_3$ agglomerates, making them harder to filter downstream. The shear stress is shown to significantly increase at higher CO_2 flow rates, as the turbulent mixing becomes more intense, with the highest shear stress experienced close to the gas spargers and the liquid outlet. Optimising the hydrodynamics therefore represents a trade-off between achieving good interphase mass transfer performance and minimising shear stress, both of which can be controlled within the current operating range of conditions.

A model of the complex chemical reactions occurring in the liquid phase and the formation of solid $CaCO_3$ crystals has been developed and applied in the context of CFD modelling for the first time. The reaction model has been applied to the three-dimensional domain using frozen hydrodynamic conditions in order to overcome the different timescales at which the reaction and hydrodynamic processes occur. The complex liquid-phase carbonate reactions are modelled using an iterative equilibrium model due to the impracticality of modelling the very fast forward and backward reactions explicitly. The turbulent mixing within the vessel under typical operating conditions means that there are no significant gradients in dissolved species developing, however the pH profiles show a significant variation in local values, which is likely to be a consequence of using the frozen hydrodynamic conditions. Reducing the CO_2 flow rate below typical operating conditions results in more stable flow patterns developing, for which a pH gradient does develop within the vessel. However, the volume-averaged pH is shown not to change with different CO_2 flow rates, but can be controlled by varying the amount of $Ca(OH)_2$ added. Furthermore, it is shown that there is

no benefit from introducing a liquid-phase recycle since the mixing in the vessel is already good under operating conditions due to the turbulent flow patterns. The reaction model responds to all conditions applied in a physically feasible manner, however the modelled pH is below the typical operating value provided by the process operators, suggesting that further model refinement may be required, especially for the dissolved carbonate reactions. Further validation of the reaction model in a closed water-CO_2 system with $Ca(OH)_2$ addition is presented in Chapter 9.

The following key recommendations can therefore be made for the operation of the carbonatation process:

- A CO_2 flow rate in excess of 0.15 t hr^{-1} is required to achieve churn-turbulent flow, which is necessary to produce well-mixed conditions.
- The current range of operating conditions is sufficient for controlling the interphase mass transfer rate (CO_2 flow rate of 0.3 – 0.8 t hr^{-1}).
- There is a large increase in shear stress identified across the operating range of CO_2 flow rates at all locations within the vessel. An optimum CO_2 flow rate of 0.5 t hr^{-1} is therefore proposed as a compromise between mass transfer and shear stress.
- The pH can only be controlled by varying the inlet $Ca(OH)_2$ concentration.
- There is no benefit from introducing a liquid-phase recycle for either mass transfer or mixing, since there are only very small gradients in aqueous-phase components under normal operating conditions.

9 Validation of the Carbonatation Model

Due to the limited availability of experimental data from the full-scale carbonatation process described in Chapter 8, a series of laboratory-scale experiments have been developed in an attempt to validate the reaction scheme applied to the carbonatation model. The hydrodynamic conditions are assumed to be sufficiently similar to the BioMOD setup so that the validation work presented in Chapter 6 applies for the two-phase hydrodynamic and mass transfer phenomena. The process used for the validation experiments is simplified from the production-scale process by creating a closed system with regards to the liquid phase, eliminating the need to model the inflow and outflow of component species and allowing the system to reach saturation.

9.1 Experimental Procedure

A model solution is formed by adding pure calcium hydroxide powder (Scientific Laboratory Supplies Ltd) to deionised water at 25°C, using the cylindrical glass spinner flask previously described for the microbubble experiments (see Figure 7-4 a) with a filled liquid volume of 10 L. The water is initially heated to the required temperature using a submerged heating coil, following which the temperature in the vessel is maintained by gentle external heating. The pH and temperature are continually monitored using a pH probe and meter (Oakton pH700) and a separate temperature probe (Testo 905 T1). The solution is magnetically stirred in the absence of gas until the pH has stabilised, signifying a saturation of calcium hydroxide within the liquid phase. Pure carbon dioxide gas (BOC) is then bubbled through the mixture at flow rates of up to 7 L min^{-1} through a ring sparger with a diameter of 84 mm and six evenly spaced 1.5 mm diameter holes on the upper surface, suspended at a height of 36 mm from the base of the tank. Stirring in not applied during the reaction phase since it is assumed that the rising gas bubbles create sufficient mixing within the liquid phase to prevent the build-up of significant concentration gradients or solids settling within the vessel. The head space is maintained with an unpressurised atmosphere of carbon dioxide. A diagram of the experimental setup used is presented in Figure 9-1.

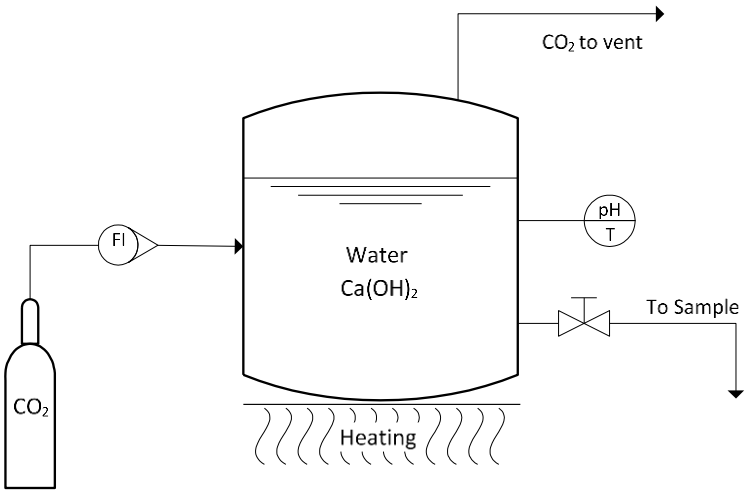

Figure 9-1: Diagram of the carbonatation validation experimental setup

The pH of the reacting mixture is continually monitored using the submerged pH probe. A 50 mL sample of the liquid phase is taken via syringe at five minute intervals throughout the reaction. These are each split into two 25 mL samples, with one of the samples filtered using a 45 µm syringe filter disc (Fisher Scientific) to remove all of the solids. Both samples are then buffered to a pH of 4.8 to 5.2 using 10% v/v of CO_2 buffer solution (Thermo Scientific Orion 950210) so that all carbonate species (both dissolved and solids) are converted to aqueous carbon dioxide. The buffer solution also provides a constant background ionic strength of the solution for more accurate measurement. The buffered solutions are analysed using a carbon dioxide ion specific electrode (Thermo Scientific Orion 9502BNWP), with the electrode potential measured using a bench-top meter with mV readout (Thermo Fisher Scientific Orion Star A111). This analysis is performed immediately upon taking the sample to minimise the potential for CO_2 transfer with the atmosphere and heat loss to the surroundings.

The mV readings recorded by the meter are converted to a concentration in mol m^{-3} using the two-point calibration method outlined in the electrode documentation (Thermo Fisher Scientific Inc., 2008). The lower concentration standard consists of a 1000 ppm solution of $CaCO_3$ (Thermo Scientific Orion 950207) and the higher concentration standard consists of 0.1 M $NaHCO_3$ (Thermo Scientific Orion 950206). The calibration plot used to generate the experimental carbonate profiles in this chapter is shown in Figure 9-2, with the error bars representing the standard deviation from four repeats conducted across several week of measurements. The small error associated with these points suggests that the probe is operating correctly for the duration of the experiments presented, with minimal electrode

drift experienced. The plot is known to be linear in the range of concentrations covered by this analysis (Thermo Fisher Scientific Inc., 2008), meaning that a more detailed calibration plot is not required.

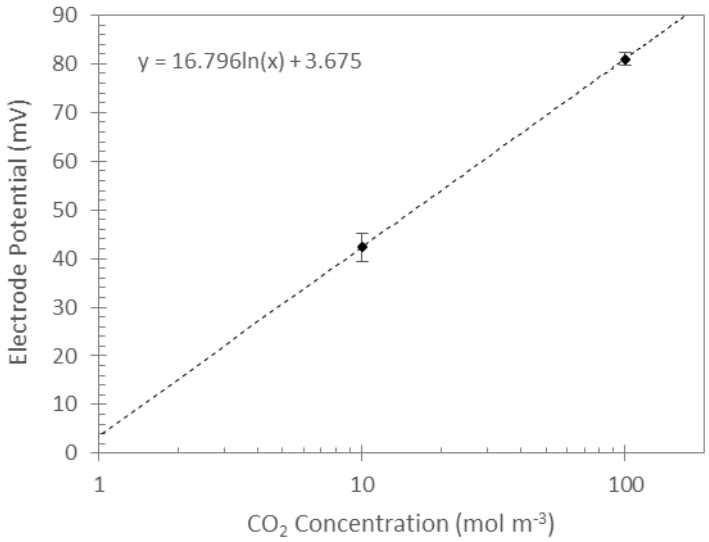

Figure 9-2: Calibration curve for the carbon dioxide electrode.
The error bars represent the standard deviation of four repeats across several weeks.

9.2 Model Setup

The fluid domain for the validation experiments can be divided into 60° sections in the radial direction due to the symmetry provided by the ring sparger and cylindrical flask, with only one of these segments being modelled. The CO_2 gas is introduced via a mass source point at an angle of 30° from the edge of the segment, as described by the red sphere in Figure 9-3. This means that the solid components of the ring sparger are not included in the modelled domain due to their minimal influence on the flow behaviour, which allows for a greatly simplified structured mesh to be applied. The fluid interfaces between segments are defined as symmetry planes, as they are located equidistant between the gas source points, with the upper liquid surface modelled as an outlet using the degassing boundary condition. All other physical boundaries are modelled as walls, with no-slip condition for the liquid phase and free-slip condition for the gas phase. This means that, unlike the full-scale carbonatation model, there is no flow of liquid component into or out of the domain and the reactions will therefore continue to saturation values with the continual supply of CO_2 gas.

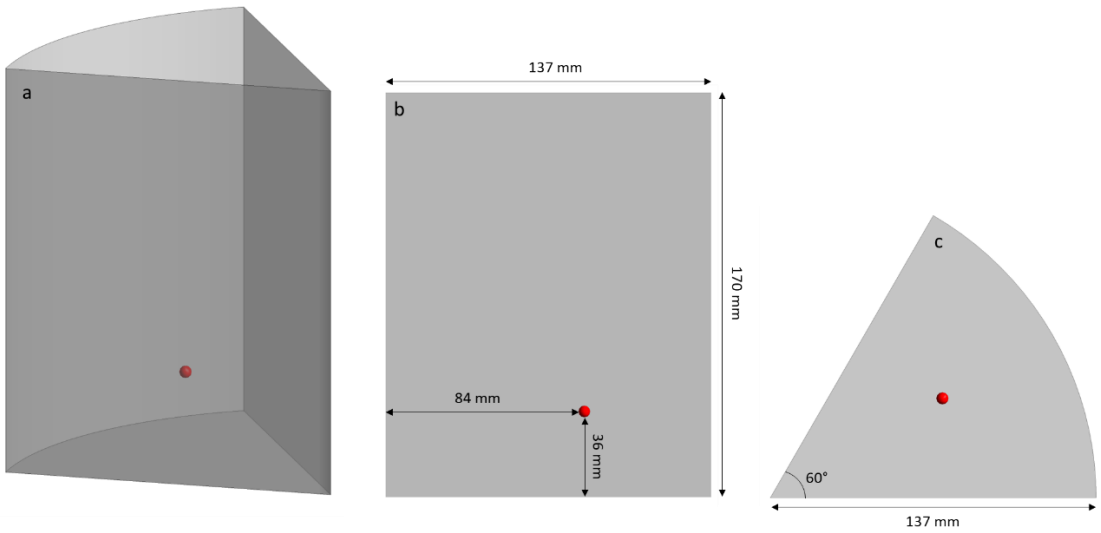

Figure 9-3: Geometry used for the carbonatation validation model.
a) 3D geometry b) vertical cut plane, c) horizontal cut plane.

The hydrodynamic equations modelled are consistent with the model described in Chapter 8, with the exception that the liquid phase properties are modelled on pure water at 25°C rather than sucrose solutions (density = 997 kg m^{-3}, dynamic viscosity = 0.000890 Pa s, surface tension = 0.072 N m^{-1}). As with the reaction model applied to the full-scale carbonatation process in Chapter 8, the flow patterns are assumed to be independent of the reactions occurring, meaning that they can be solved separately based on different timescales. This requires the assumption that the majority of the gas entering the domain exits at the liquid surface. The setup of the MUSIG parameters for the carbonatation validation model is defined using the same parameters as the BioMODULE validation work detailed in Section 6.3, due to the similarities in hydrodynamic conditions and physical scale between the two experimental setups, with both using water as the continuous phase. The gas phase is therefore modelled using 12 size groups between limits of 0 and 9 mm. The inlet diameter is assumed to be in size group 3 (diameter = 1.875 mm), which provides a good fit to the size of the holes in the ring sparger.

The hydrodynamic model is solved using a steady state solver due to the greater stability of the flow patterns in the validation system. The model is solved with a timestep of 0.01 seconds, until convergence criteria of 10^{-4} are reached for the RMS residuals of momentum and turbulence parameters, and a maximum imbalance of 0.01 is identified for all parameters including bubble size. The model is solved using high-resolution advection and turbulence numerics, giving second-order accurate results.

The domain is meshed using the ANSYS ICEM 17.0 software package. Four structured meshes of increasing density have been compared for the purposes of a mesh dependence study, as described by Table 9-1. By increasing the number of vertical, horizontal and radial divisions as shown, the density of the mesh is increased and the corresponding volume-averaged $k_L a$ calculated using the slip velocity model for a CO_2 flow rate of 4 L min^{-1}. The $k_L a$ decreases rapidly with increasing mesh density for meshes 1 to 3, however there is little difference in the $k_L a$ between meshes 3 and 4 despite the increased computational load. It can therefore be concluded that mesh 3 is the optimal mesh for use with the carbonatation validation model.

Table 9-1: Mesh dependency study for the carbonatation validation system.
Time for solution based on 16 cores run to the stated steady-state convergence criteria.
[2× Intel Xeon E5-2670 v2 CPUs, 126 GB RAM, NVidia Quadro K4000 GPU].

Mesh	**Number of Divisions**			**Number of Elements**	$k_L a$ **(hr^{-1})**	**Time for Solution (hrs)**
	Vertical	**Horizontal**	**Radial**			
1	50	30	20	28,420	15.48	0.23
2	75	45	30	97,680	9.279	0.54
3	90	54	45	212,265	4.360	3.98
4	100	60	60	350,460	4.438	6.03

The two-phase hydrodynamics of the validation system is presented in Figure 9-4 for a CO_2 4 L min^{-1}. This shows that the gas phase introduced via the ring sparger rises directly out of the domain and is not recirculated. The liquid phase flow patterns are driven by the rising gas bubbles, with recirculation either side of the gas inlet causing mixing within the entire vertical cut-plane. This upwards velocity is assumed to be strong enough to keep the solid species ($Ca(OH)_2$ and $CaCO_3$) suspended in the liquid. This is supported by the fact that there was minimal settling observed during the 45 minute experimental time under all CO_2 flow rates. The bubble size in the tank increases with height due to coalescence of bubbles in the rising plume, as has been seen in the full-scale carbonatation vessel.

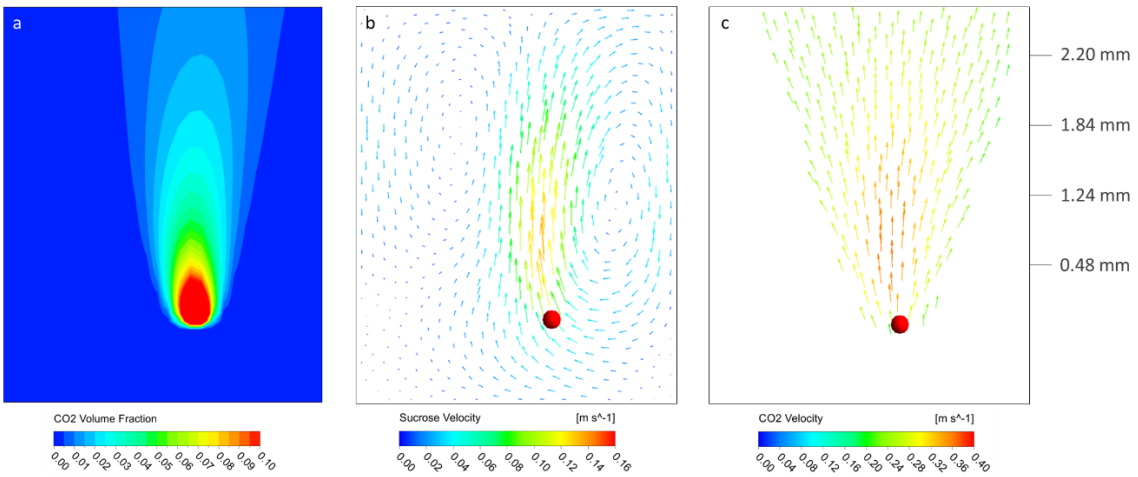

Figure 9-4: Gas fraction and two-phase flow patterns for a vertical cut-plane in-line with the sparger hole for a CO_2 flow rate of 4 Lmin^{-1}.
a) CO_2 volume fraction, b) liquid velocity vectors, c) gas velocity vectors with mean bubble diameter.

9.3 Aqueous Reactions

The validation model is initially solved in the absence of calcium hydroxide in order to evaluate the transfer of carbon dioxide from the gas to the liquid phase and the carbonate buffering system that that exists for the dissolved species. As described in Section 8.6, the full series of forward and backward reactions described by Mitchell et al. (2010) cannot be reasonably implemented into a CFD framework due to the very fast forward and backward reactions occurring, as signified by the reaction rates presented in Table 8-1. Different methods for modelling this equilibrium system are therefore compared for the validation model with three different simplifications. The pH is used to evaluate the effectiveness of the different models, since H^+ is generated during the reactions.

The first simplification option is to only solve the forward reactions, since the constant supply of CO_2 gas may be considered as driving the reactions in the forward direction, whereas the reaction series presented by Mitchell et al. (2010) describes an equilibrium system responding to a single step-change in CO_2 concentration. The dissolved carbonate model with only the forward reactions is described by equations (9-1) to (9-4).

$$CO_{2\,(g)} \rightarrow CO_{2\,(aq)} \tag{9-1}$$

$$CO_{2\,(aq)} + H_2O \overset{k_2}{\rightarrow} H_2CO_3 \tag{9-2}$$

$$H_2CO_3 \overset{k_3}{\rightarrow} HCO_3^- + H^+ \tag{9-3}$$

$$HCO_3^- \overset{k_4}{\rightarrow} CO_3^{2-} + H^+ \tag{9-4}$$

The second proposed simplification is to base this series of reactions on the slowest reaction, which is assumed to be rate-limiting. Han et al. (2011) identifies that equation (8-2) can become the rate-limiting step, as unlike the others it is not an instantaneous ionic reaction. The buffering system under this simplification is therefore described by a single reversible reaction as defined by equation (9-5).

$$CO_{2\,(aq)} + H_2O \underset{k_{-2}}{\overset{k_2}{\leftrightharpoons}} CO_3^{2-} + 2H^+ \tag{9-5}$$

Finally, the series of reactions is solved using an iterative equilibrium method as described in Section 8.6.1. The carbonate buffering system is described by equations (8-19) to (8-23), using the total dissolved carbon species, C_T, and assuming that all of the reactions involved in the buffering system create an instantaneous equilibrium at each time step. This is compared to the other proposed simplifications and the experimental pH profile in Figure 9-5 for a CO_2 flow rate of 4 L min^{-1}. Equilibrium constants for the dissolved carbonate reactions are applied for a temperature of 25°C as described in Table 8-6.

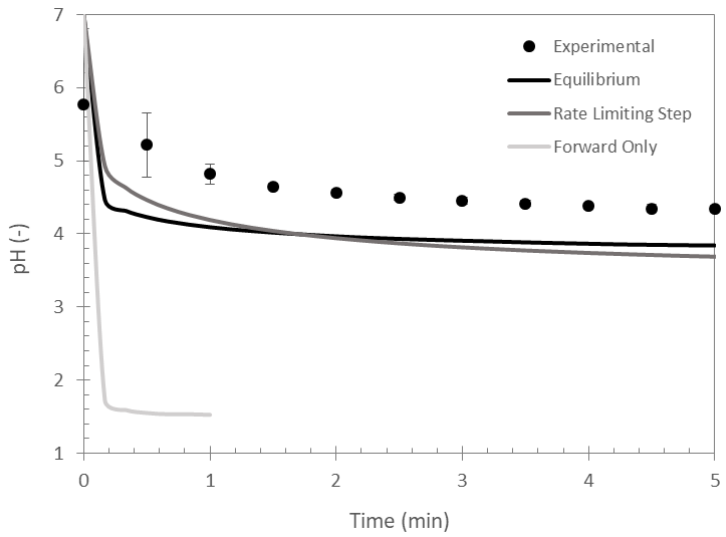

Figure 9-5: pH profiles for a water-CO_2 system for different aqueous reaction simplifications.

The pH profiles for the equilibrium and rate-limiting step techniques are very similar, suggesting that the assumption of the rate limiting step in this scheme is reasonable for the pH range experienced under these conditions. Both models provide a reasonable match to the measured pH, although they both under-predict the final value by a similar amount. In contrast, the forward-only reaction scheme vastly under-predicts the pH, in addition to requiring a much smaller timestep to solve it, which is compared to the other proposed simplifications in Table 9-2. The equilibrium simplification gives stable results with a timestep of 1 second, compared to 0.01 for the rate limiting step simplification, meaning that it can be solved approximately 100 times faster. The equilibrium method is therefore applied to all further modelled conditions, implemented as described in Sections 8.6.1 and 8.6.2 in the absence and presence of solid $Ca(OH)_2$ respectively.

Table 9-2: Timestep required to model each reaction simplification proposed.

Simplification	Time Step Required
Equilibrium	1 s
Rate Limiting Step	0.01 s
Forward Only	0.0001 s

The selected equilibrium method for describing the dissolved carbonate species has been applied to the validation system in the absence of $Ca(OH)_2$ for CO_2 gas flow rates of 2, 4 and 7 L min^{-1}. The profiles of dissolved carbonate species and pH during a 45 minute reaction are presented in Figure 9-6 for each flow rate. The saturation concentration of C_T applied in the model is based on the experimental value of 47.0 mol m^{-3}, which is the mean

value from the 9 experiments that are used to generate Figure 9-6 a), c) and e). The error bars represent the standard deviation from the mean of three experiments performed for each condition.

In the absence of $Ca(OH)_2$, the parameter C_T is assumed to consist of $CO_{2\ (aq)}$, H_2CO_3, HCO_3^- and CO_3^{2-} only. From Figure 8-1 it can be assumed that the majority of the carbonate species at the pH measured exists in the form of $CO_{2\ (aq)}$. For both the experimental and modelled profiles of C_T, the initial gradient of the profile increases and the time taken to reach equilibrium decreases with increasing CO_2 flow rate as the interphase mass transfer rate becomes greater. However, the modelled value is consistently higher than the experimental value until saturation has been reached for all three profiles. This suggests that the modelled mass transfer rate is too high, and further optimisation of the hydrodynamic model or the mass transfer model used may be required. In contrast, the pH profiles between the different conditions are very similar, with an almost instantaneous drop in pH from the initial neutral pH to a final value of 4.18, averaged between all of the experimental profiles. This final value is consistently higher than the modelled value of 3.67, although the model can still be said to provide a reasonable fit to the experimental profiles of C_T and pH in the absence of $Ca(OH)_2$. This analysis provides a further justification for using the equilibrium model to describe the dissolved carbonate system, since the change in pH is shown to occur very quickly in comparison to the interphase mass transfer.

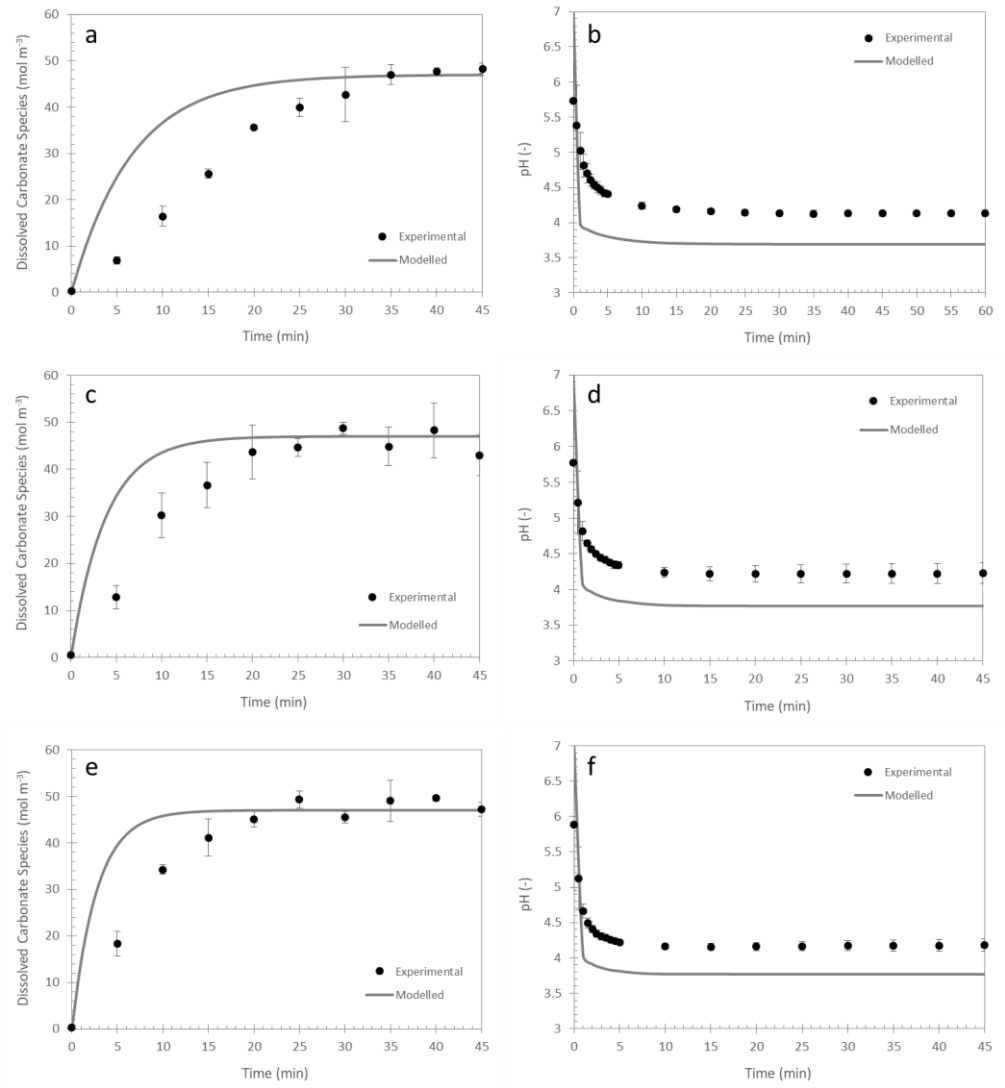

Figure 9-6: Profiles of dissolved carbonate species (a,c,e) and pH (b,d,f) for different CO_2 flow rates in the absence of $Ca(OH)_2$.
a-b) 2 L min^{-1}, c-d) 4 L min^{-1}, e-f) 7 L min^{-1}.

9.4 Carbonate Formation

The formation of solid $CaCO_3$, driven by the interphase mass transfer of CO_2 gas into the liquid phase, is modelled using the reaction scheme described in Section 8.6 and compared to experimental data. A 'base case' scenario of 0.5 wt% $Ca(OH)_2$ addition and 4 L min^{-1} CO_2 gas flow rate is initially considered, as presented in Figure 9-7. Experimental measurements are made using the process described in Section 9.1. Analysis of the filtered sample presented in Figure 9-7 a) is assumed to represent the sum of all of the aqueous carbonate species identified within in the system, namely $CO_{2\ (aq)}$, H_2CO_3, HCO_3^-, CO_3^{2-} and $Ca(HCO_3)_2$. Similarly, the unfiltered sample is assumed to represent the same species with the addition of solid $CaCO_3$, as shown in Figure 9-7 c). The difference between the

two measurements gives the concentration of solid calcium carbonate present, as presented in Figure 9-7 b). Finally, the pH during the course of the reaction is presented in Figure 9-7 d). As previously, the error bars represent the standard deviation from the mean of three experiments.

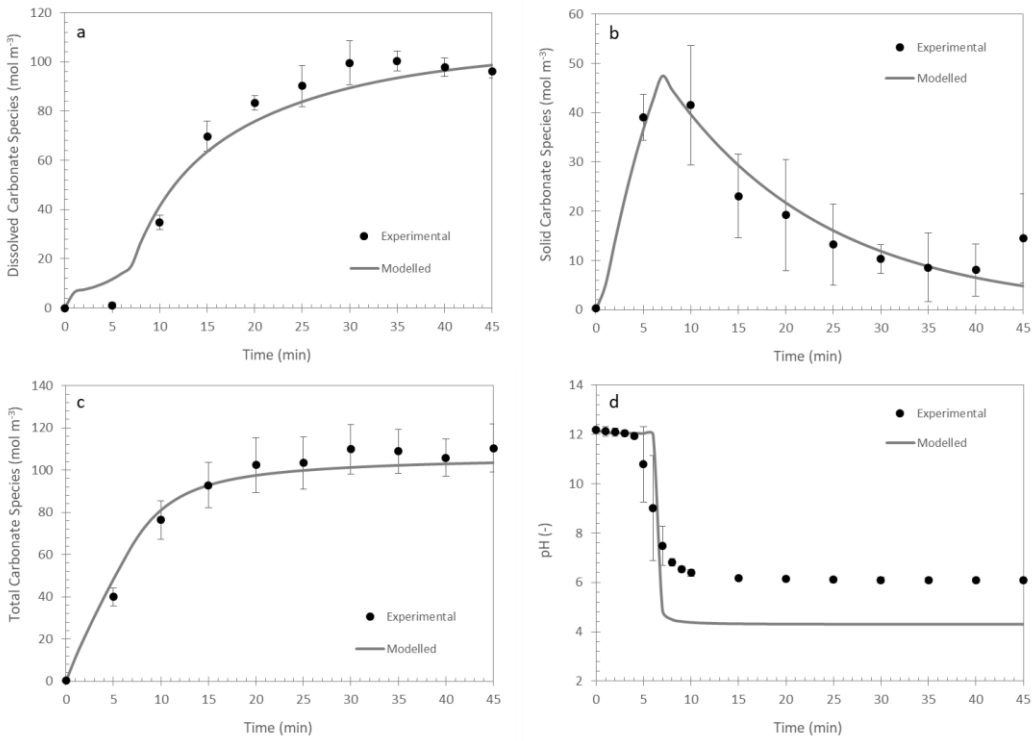

Figure 9-7: Experimental and modelled profiles of solid and dissolved carbonate species and pH for a CO_2 flow rate of 4 Lmin^{-1} and 0.5 wt% $Ca(OH)_2$ loading.
a) dissolved carbonate species, b) solid carbonate species, c) total carbonate species, d) pH.

The model provides a very good fit to the measured concentrations of both dissolved and undissolved carbonate species under the base case conditions, with the majority of points in Figure 9-7 a) to c) falling within the error bars. The total carbonate species increases to a maximum concentration in the region of 100 mol m^{-3}, which is significantly higher than the saturation concentration of 47 mol m^{-3} measured in the absence of $Ca(OH)_2$. The plot of pH against time (Figure 9-7 d) shows an initially constant pH as the suspended $Ca(OH)_2$ particles initially present in solution are consumed, followed by a steep decrease in pH once the available $Ca(OH)_2$ has been consumed. During the initial period, the concentration of solid $CaCO_3$ increases rapidly as the forward reactions progress quickly due to the abundance of CO_3^- ions in solution at high pH. Consequently, the levels of dissolved carbonate species during this phase are very low in relation to the total carbonate species, although the dissolved levels predicted by the model after 5 minutes are

higher than the measured value, which is still very close to zero. In contrast, once the available $Ca(OH)_2$ has been consumed there is a drop in the amount of solid $CaCO_3$ measured, which is assumed by the model to dissolve irreversibly into the stable aqueous form of $Ca(HCO_3)_2$. The initial pH (calculated based on the model of Johannsen and Rademacher (1999)) and the timing of the $Ca(OH)_2$ depletion is captured very well by the model, however the final pH is significantly lower in the model than the experiments. The final measured pH is also much higher than had been measured without the addition of $Ca(OH)_2$.

This analysis has been repeated for a higher $Ca(OH)_2$ concentration of 1 wt%, using the same hydrodynamic model with a CO_2 gas flow rate of 4 L min^{-1}. The modelled profiles do not fit the experimental data as well as the 0.5 wt% case, as shown in Figure 9-8. The major difference between the experimental and modelled profiles is the length of the initial phase of the reaction, where the solid $Ca(OH)_2$ is being consumed, which is significantly over-predicted by the model. This is signified by the delay in the sharp pH decrease shown in Figure 9-8 d). For both profiles, this pH drop occurs after a longer time than the 0.5 wt% base case due to the greater concentration of suspended $Ca(OH)_2$ solids present. For a constant rate of dissolution, it may be expected that the $Ca(OH)_2$ depletion will occur after twice the time of the base case model. Whereas the modelled profile does not reach depletion until slightly after two times that of the 0.5 wt% case, the experimental pH drops to the final value after only three additional minutes of CO_2 sparging. This suggests that the dissolution of $Ca(OH)_2$ may not be complete at the time that the drop in pH occurs, most likely due to suppression of the dissolution mechanism by the higher concentration of $CaCO_3$ solids present. This would also support the lower carbonate species measured in Figure 9-8 a) and c), since there is less solid $CaCO_3$ available to dissolve back into solution. The final pH is under-predicted by the model by a similar amount as base case.

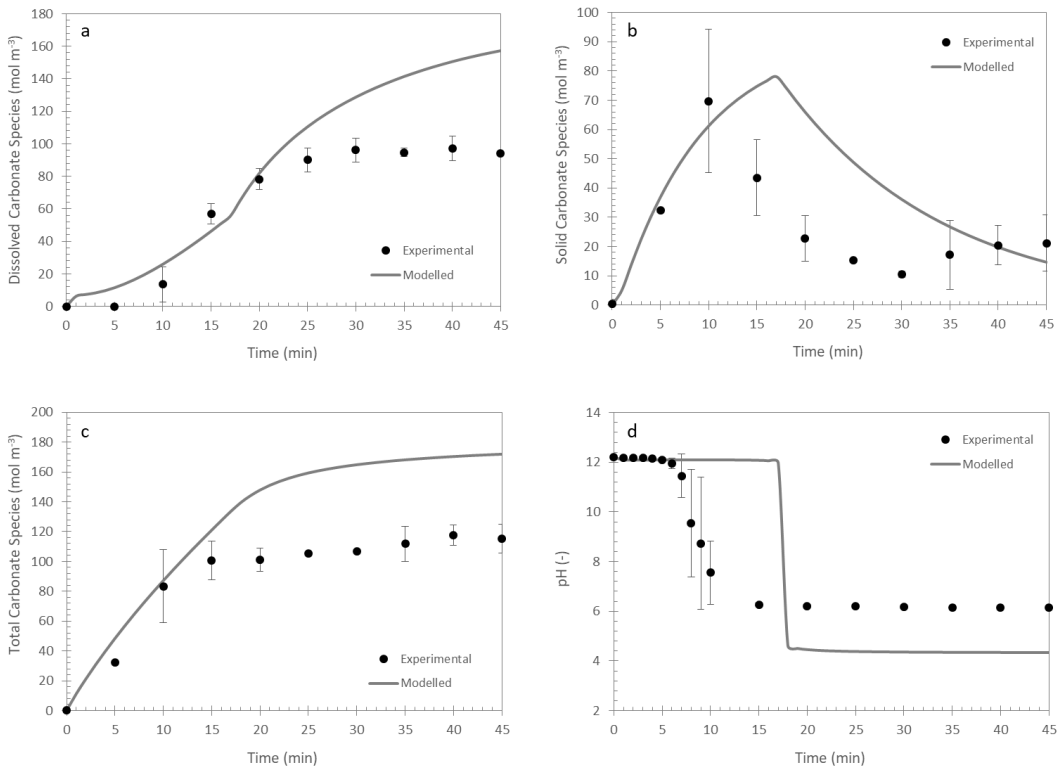

Figure 9-8: Experimental and modelled profiles of solid and dissolved carbonate species and pH for a CO_2 flow rate of 4 Lmin^{-1} and 1 wt% $Ca(OH)_2$ loading.
a) dissolved carbonate species, b) solid carbonate species, c) total carbonate species, d) pH.

In addition to changing the $Ca(OH)_2$ loading, one of the main methods employed to control the reactions occurring in the saturator is to vary the CO_2 flow rate. The hydrodynamic model has been solved in Section 9.3 for CO_2 flow rates of 2 and 7 L min^{-1}, in addition to the base case of 4 L min^{-1}. The full reaction scheme is therefore solved for these conditions using the frozen flow profiles with an initial $Ca(OH)_2$ concentration of 0.5 wt%. The profiles of carbonate species concentrations and pH are presented for the lower flow rate of 2 L min^{-1} in Figure 9-9. The profiles of dissolved and total carbonate concentration (a and c) match well between the experimental and modelled profiles, and the time taken for the $Ca(OH)_2$ to become depleted is captured well by the model, as represented by the pH profiles in Figure 9-9 d). This takes longer than for the base case due to the lower mass transfer rate achieved by using a lower gas flow rate. The biggest difference between the experimental and modelled profiles is the solid $CaCO_3$ concentration presented in Figure 9-9 c), which is under-predicted by the model for the majority of measured data points. This parameter is subject to the greatest experimental error due to its dependence on two measured values, however it is likely that the re-dissolution of $Ca(OH)_2$ is captured less

well by the model under lower CO_2 since the modelled profiles falls well outside of the error identified from three experimental runs.

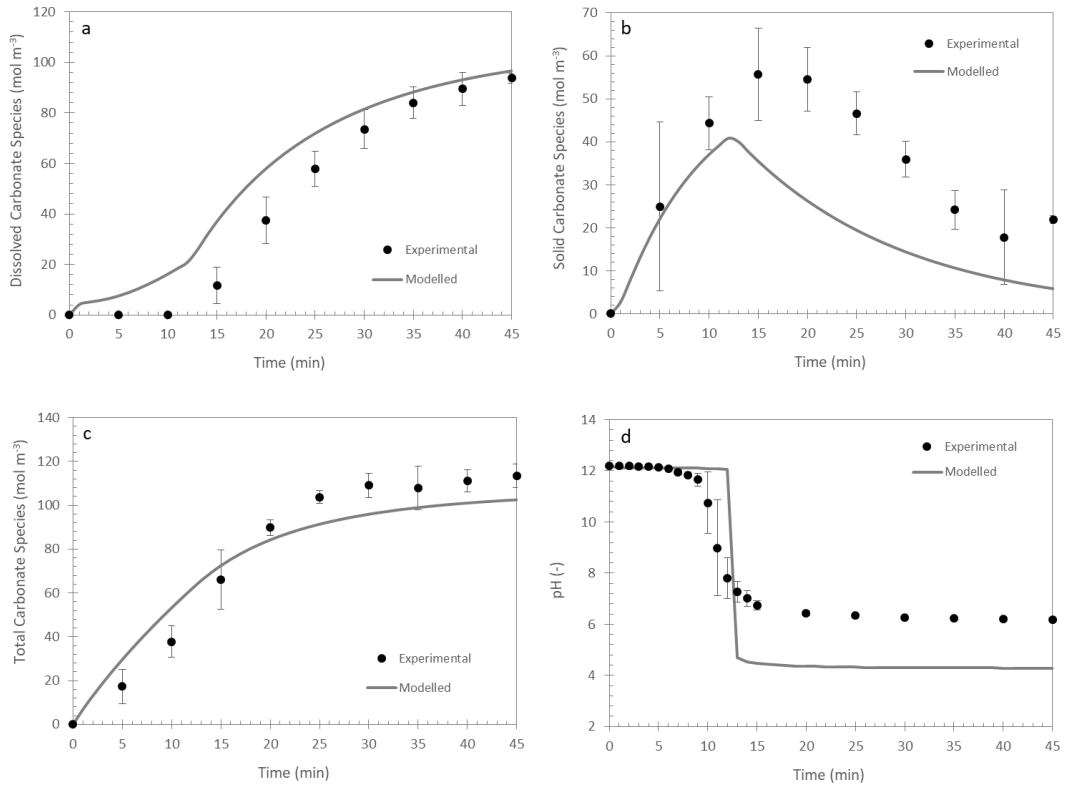

Figure 9-9: Experimental and modelled profiles of solid and dissolved carbonate species and pH for a CO_2 flow rate of 2 Lmin^{-1} and 0.5 wt% $Ca(OH)_2$ loading.
a) dissolved carbonate species, b) solid carbonate species, c) total carbonate species, d) pH.

The same set of experimental and modelled profiles are presented for a CO_2 flow rate of 7 L min^{-1} in Figure 9-10, and provide a similarly good fit between the modelled and experimental profiles as the base case (4 L min^{-1}). The main difference between the two flow rates is the time taken for the solid $Ca(OH)_2$ to be used up, which is identified by the drop in pH as presented in Figure 9-10 d). The modelled profiles of dissolved and solid carbonate species follow the experimental profiles very well, showing the same behaviour as in Figure 9-7, albeit with a faster interphase mass transfer rate.

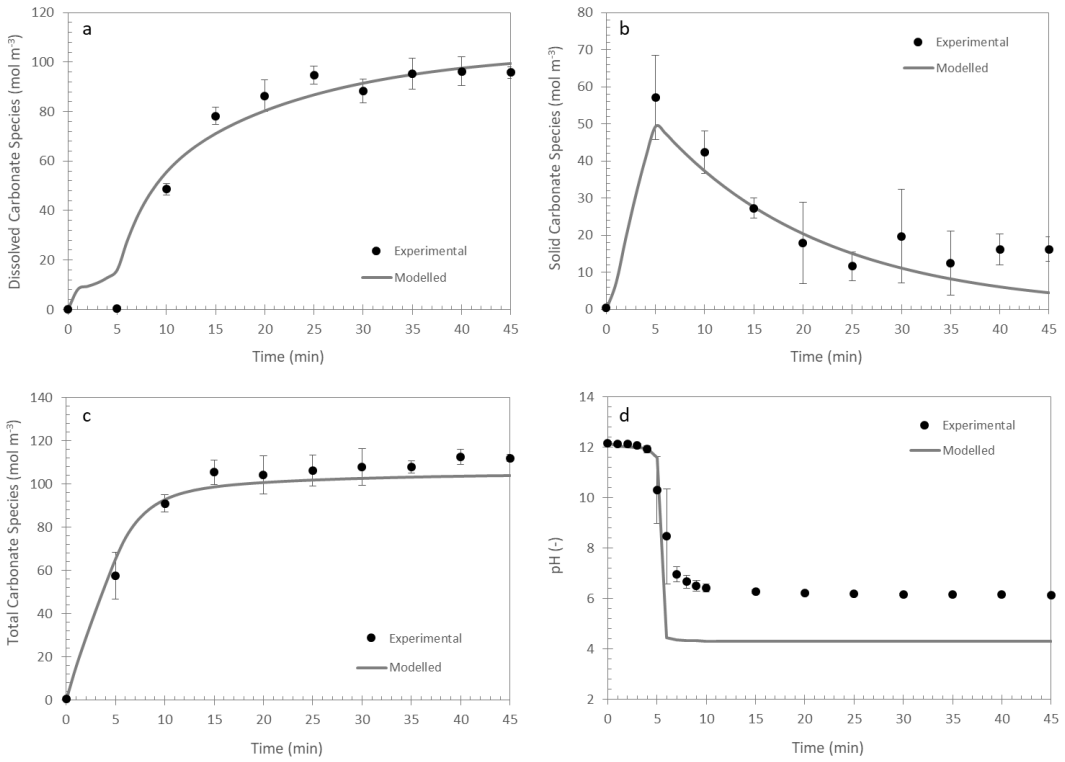

Figure 9-10: Experimental and modelled profiles of solid and dissolved carbonate species and pH for a CO_2 flow rate of 7 Lmin^{-1} and 0.5 wt% $Ca(OH)_2$ loading.
a) dissolved carbonate species, b) solid carbonate species, c) total carbonate species, d) pH.

9.5 Reaction in Sucrose

The 'base case' scenario of 4 L min^{-1} CO_2 flow rate and 0.5 wt% $Ca(OH)_2$ has been repeated with the addition of 10 and 20 wt% sucrose (Scientific Laboratory Supplies Ltd). The sucrose is completely dissolved in the heated water before the calcium hydroxide addition. This will give an indication of the influence that increasing sucrose concentration will have on the reaction scheme detailed above, which is developed from reactions in uncontaminated water. The hydroxide-saturated sucrose solution is a much darker brown colour at the start of the reaction than has been observed for the pure water case, as shown in Figure 9-11 a) for a 10 wt% sucrose solution before the carbon dioxide feed has been initiated. In contrast, Figure 9-11 b) shows the same sucrose solution after 15 minutes of CO_2 sparging, where the pH has dropped to a value of 5.84. Once the initial $Ca(OH)_2$ has been consumed, the solution possesses a much brighter white colour as a result of the $CaCO_3$ solids that have been generated during the reaction process.

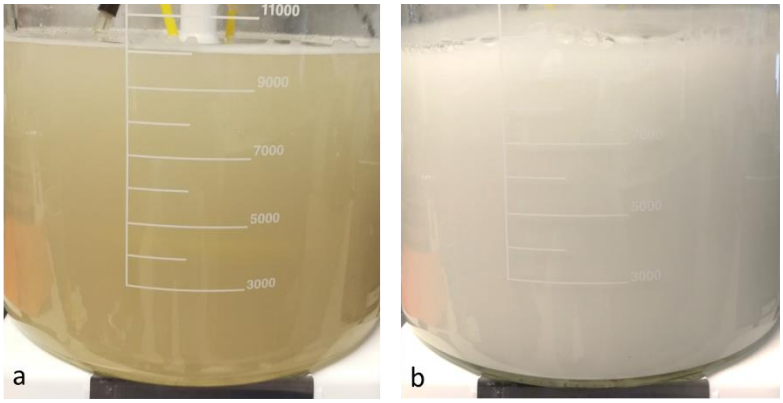

Figure 9-11: A comparison of the reacting system with 10 wt% sucrose for a 4 L min^{-1} CO_2 flow rate. a) initial, b) after 15 minutes.

A comparison of the curves for a 4 L min^{-1} CO_2 flow rate in water (solid lines) and sucrose (points) is made in Figure 9-12. The total concentration of carbonate species, both solid and dissolved, does not change significantly in comparison to the pure water curves, as shown by Figure 9-12 c). The majority of the values for the total carbonate species on the sucrose curves fall within the predicted margin of error, showing that interphase mass transfer has not been affected by the presence of sucrose at these concentrations. However, the distribution of carbonate species between the solid and aqueous phases is different when sucrose is added to the liquid phase, as shown in Figure 9-12 a) and b). The concentration of solid carbonate species is consistently higher when sucrose is present, however there is no clear trend identified between 10 and 20 wt% sucrose. This could be explained by an inhibition of the calcium carbonate dissolution mechanism, however since there is no further change between 10 and 20 wt% sucrose addition it is not clear that this phenomena would become more pronounced at higher sucrose concentrations. Finally, the pH of the bulk solution is compared for the different sucrose concentrations in Figure 9-12 d). Once again, there is a clear shift in the point where the undissolved calcium hydroxide becomes depleted between the 0 wt% and 10 wt% sucrose solution, however there is little further shift when the sugar concentration is doubled to 20 wt%. There is also more of a drift in pH from the starting value before this depletion point is reached. This analysis suggests that although there are differences identified in the system with the addition of the sucrose, the profiles are sufficiently similar to show that the reaction scheme developed will be applicable for the application to sucrose solutions.

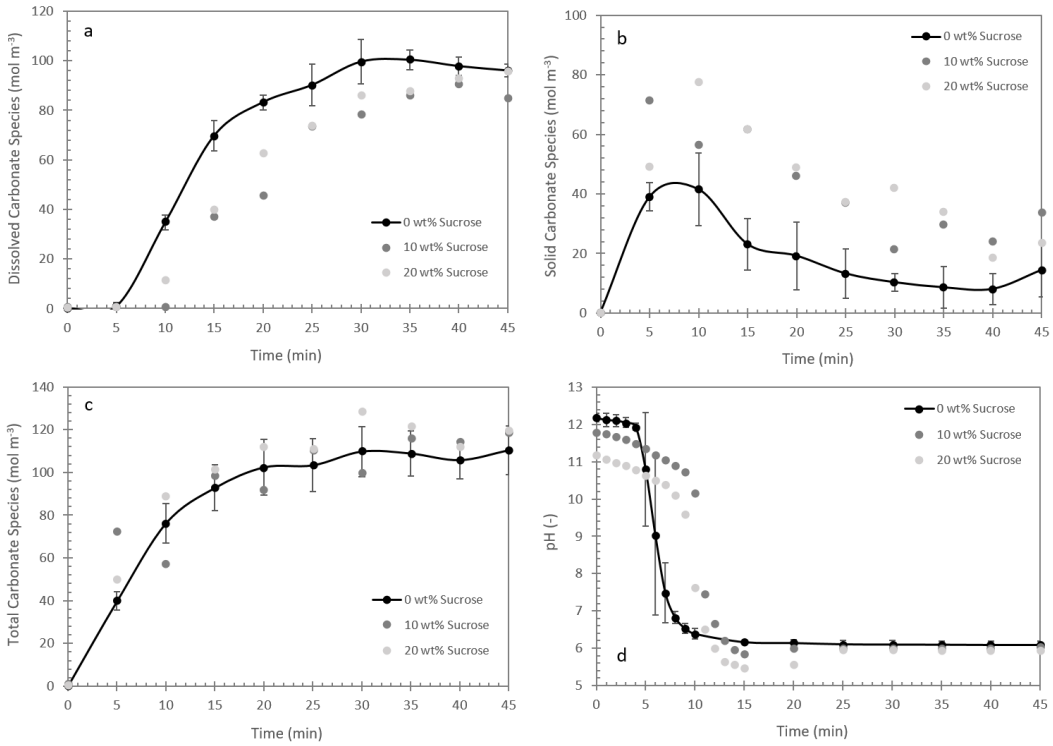

Figure 9-12: Comparison of the experimental carbonate species and pH profiles for pure water and sucrose solutions for a CO_2 flow rate of 4 Lmin^{-1} and 0.5 wt% $Ca(OH)_2$.
a) dissolved carbonate species, b) solid carbonate species, c) total carbonate species, d) pH.

9.6 Summary

This chapter has detailed the development of a series of experiments designed to validate the reaction scheme previously applied to the full-scale carbonatation system operated in industry, as described in Section 8.6. A model system is produced by bubbling CO_2 gas within a 10 litre vessel containing a mixture of water and solid $Ca(OH)_2$. The concentration of the solid and dissolved carbonate species and the pH are measured and compared to a CFD model of the system under the same set of conditions. Three potential simplifications for the aqueous carbonate reactions have been evaluated in the absence of $Ca(OH)_2$ due to the very fast speed of the forward and backward reactions, which makes their direct implementation incompatible with CFD modelling. A simplification that assumes equilibrium between carbonate species at each timestep is selected as the most appropriate, providing a good fit to the measured pH and allowing the system to be modelled with a large time step of up to 1 second. This model has been solved in the absence of $Ca(OH)_2$ for CO_2 flow rates of 2, 4 and 7 L min^{-1}, with the model over-predicting the mass transfer rate, but still providing a reasonable fit to the dissolved carbonate species concentration and pH.

The validation system has also been evaluated with $Ca(OH)_2$ addition of 0.5 wt% at three different CO_2 gas flow rates. The model provides a very good fit to the experimental measurements of the dissolved and solid carbonate species under all three CO_2 flow rates. A significant proportion of the solid $CaCO_3$ is shown to dissolve back into solution once the $Ca(OH)_2$ present in the system at the start of the reaction has been consumed, whilst the total carbonate species in the system increases to a maximum within the reaction time. The model also captures the point at which the pH in the system drops rapidly from the starting value to the final value, which is assumed to signify the point at which the solid $Ca(OH)_2$ present at the start of the reaction has been used up. However the model is shown to significantly under-predict the final pH for all CO_2 flow rates tested, suggesting that some further refinement of the carbonate species model or the reaction constants used for it may be required. The model provides a less good fit to the experimental data for a $Ca(OH)_2$ addition of 1 wt%, with the difference in the time taken for the pH to drop between different concentrations suggesting that there may be unreacted $Ca(OH)_2$ present in the system at the higher concentration. Finally, the experimental analysis has been repeated using two different concentrations of sucrose. This has suggested no significant difference in the overall system of reactions taking place, however the re-dissolution of solid $CaCO_3$ may be hindered by the sucrose, with a significantly higher concentration of solids identified at both sucrose concentrations. The model developed can therefore be applied to the full-scale carbonatation with a good degree of confidence that the physical and chemical processes occurring are being modelled in a reasonable manner.

10 Conclusions

A comprehensive review of the published literature relating to the computational fluid dynamic (CFD) modelling of gas-liquid stirred tank reactors has been conducted as part of this thesis. This has helped to identify the current consensus on several modelling options relating to industrial-scale two-phase flow modelling. The following specification was identified as the basis of the CFD modelling presented in this thesis: Euler-Euler reference frame, k-ε turbulence model and a population modelling to describe the bubble size. Other modelling decisions such as the interphase drag model and mass transfer model appear to have no clear consensus in the literature, and are therefore evaluated as part of this modelling work.

The first industrial application of the CFD model studied is a single-use-technology (SUT) bioreactor, which has been developed as part of a collaborative industrial project known as BioMOD. The two-phase CFD model has been used to evaluate the performance and characteristics of the system under a range of different operating conditions. It has been found that there is a change in the dominant flow characteristic between impeller speeds of 200 and 300 RPM. The flow patterns are dominated by the rising gas bubbles at low stirrer speeds, whereas the force introduced by the impeller is high enough to achieve recirculating liquid flow patterns and a good dispersion of the gas phase at higher stirrer speeds. This also causes a significant reduction in the bubble size despite the impeller being floor-mounted and significantly smaller in diameter in comparison to the tank size than typical stirrer tank designs. The average $k_L a$ values predicted by five mass transfer models have been compared to experimentally derived values for a 'base case' operating condition. There is a wide spread of different values predicted by the models, with the experimental values falling within the predicted range. The best fit to the experimental value was found to be achieved by the slip velocity, surface renewal stretch and penetration models. The CFD model predicts that increasing the air flow rate above current operating levels could be used as a method of increasing the $k_L a$, however this would require modifications to the current sparger system.

The results of the CFD model have also been validated at the laboratory scale within a 9.4 L stirred glass tank, due to the limited access to take measurements within the industrial-scale bioreactor. The parameters chosen for validation are the gas distribution (qualitative) and the liquid-phase velocity, bubble size distribution and mass transfer coefficient

(quantitative). The distribution of the gas phase within the validation tank at various stirrer speeds is captured well by the CFD model, whereas the liquid-phase velocity vectors are also captured reasonably well. However, differences between the experimental and modelled profiles have been identified, in particular close to the impeller blades. It is likely that the fit may be improved using more complex turbulence modelling techniques such as those often applied to single-phase stirred tank models, however these will result in very high computational loads, making the model too time consuming for industrial-scale applications. Validation of the bubble size distribution and mass transfer performance, quantified in terms of $k_L a$, show that the model captures the volume-averaged mass transfer well for stirrer speeds of 100 to 300 RPM when using the eddy cell and slip velocity models. The slip velocity model also provides a good fit to the measured $k_L a$ for the full-scale BioMOD tank, and is therefore recommended as the most suitable of the studied models for use with CFD modelling. However, this model considerably over-predicts the $k_L a$ for a stirrer speed of 400 RPM, which is thought to occur as a result of the very small bubble size predicted at this speed, which the model is not optimised to capture. It is therefore concluded that the CFD model is sufficiently accurate to realistically describe the fluid dynamic and mass transfer behaviour under the range of conditions experienced within the BioMOD system, however the model is not universally applicable without application-specific optimisation of the population balance parameters to describe the bubble size.

A further conclusion that can be made from the BioMOD project is that specific interfacial area, which is dependent on the bubble size and gas fraction, is the most influential factor in the increase in mass transfer performance with increasing stirrer speed. This can be seen in both the full-scale and validation systems, which show relatively small variations in the liquid-phase mass transfer coefficient modelled despite the very different flow regimes identified across each stirrer speed range. This means that the mass transfer performance of gas-liquid systems may be significantly improved by using microbubbles (gas bubbles in the micron size range) in the place of traditional gas sparging. This has been investigated in Chapter 7 by using a commercially available microbubble generating pump. By measuring the dynamic changes in dissolved oxygen concentration in three different vessels with various volumes of water from 7.62 to 200 L, it can be concluded that the mass transfer performance is independent of the tank geometry used, and is therefore a function of liquid volume only when pump operating conditions are maintained. Similarly, the

influence of mechanical agitation on the mass transfer rate has been found to be negligible, meaning that the only agitation required when using the pump would be to maintain mixing and the suspension of any additional phase. The microbubble pump was found to achieve a much greater mass transfer rate for a specified volume of gas than traditional air sparging, however its applicability to biological applications is complicated by the large pressure drop across the pump and the necessity for sterile operation, which is likely to require the additional complexity of a filtration step before the pump. Furthermore, the high liquid pumping capacity required to achieve high mass transfer rates means that very large pumps would be needed for industrial-scale applications such as the BioMOD tank. Therefore, although microbubbles have been shown to have a great potential for intensifying mass transfer processes, especially for systems with non-typical geometry, the Nikuni pump studied is concluded not to be a suitable solution for the BioMOD project.

The previously described work has focussed only on mass transfer between the gas and liquid phases, however industrial two-phase systems often involve complex aqueous or three-phase reactions such as those involved in the carbonatation process, an intermediate step during the refining of cane sugar. A hydrodynamic model has been applied to an industrial-scale carbonatation vessel, based upon the finding of the BioMOD modelling work with adjusted physical properties for the viscous sucrose solution and carbon dioxide gas. The model has been solved for a for a range of typical operating gas flow rates, which has shown that the column is operating within the churn-turbulent regime during normal operating conditions, and as such there is a good degree of mixing of the liquid phase. Modelling of the mass transfer using the slip velocity model shows that changing the gas flow rate within the currently used range allows for the interphase mass transfer rate to be controlled, however further increases above 0.7 t hr^{-1} show little improvement in mass transfer. Furthermore, higher gas flow rates also result in higher local and average shear stress, which may break up solid agglomerate particles, and therefore an optimum flow rate exists within the current operating range at approximately 0.5 t hr^{-1}.

In addition to the hydrodynamic model, the interphase mass transfer and chemical reactions occurring within the carbonatation process have been modelled directly within the CFD framework using hydrodynamic conditions that are frozen in time. Since the system of forward and backward reactions involved in the carbonate equilibrium is too fast to be solved explicitly, an iterative system whereby the species are assumed to be in

equilibrium with the pH from the previous timestep has been developed and evaluated. The predicted outlet pH under typical operating conditions is close to the pH measured in the production-scale process, however further validation was performed at the laboratory scale due to the limited access to take measurements for the full-scale process. A 10 L model system was developed to represent the key reactions taking place, consisting of a closed system of water and calcium hydroxide, with carbon dioxide gas continually bubbled through. Experimental measurements of the pH and the concentration of both dissolved and solid carbonate species are compared to a CFD-based model of the same system. The carbonate concentrations were captured very well by the model across the three gas flow rates used, showing that the modelled system is representative of the aqueous-phase reactions occurring. However, the model provides a less good fit when the starting calcium hydroxide concentration is increased. Furthermore, the modelled pH is consistently lower than the measured value, which suggests that the model could be improved by refining the kinetic constants used and exploring the role of side reactions in the aqueous reaction scheme. Finally, it has been shown that the series of reactions responds in a similar way when sucrose is present in the model system, suggesting that the model will remain representative of the industrial-scale carbonatation process, however the re-dissolution of calcium carbonate with the continued was noted to be slowed by the presence of sucrose.

11 Future Work

The work detailed in this thesis can be broadly divided into three areas of interest: modelling and validation of the BioMOD reactor, microbubble characterisation and mass transfer experiments and the modelling and validation of the carbonatation process. Whereas the objectives of the project have been largely met for each of these areas, there is still scope for further development of the experimental and modelling work described, and further opportunities to adapt the techniques developed for other applications, as detailed in this chapter.

11.1 BioMOD Project

The BioMOD project and accompanying validation work has provided a high level of detail relating to the performance of a newly developed single-use-technology bioreactor. The analysis has been performed for an idealised air-water system, however the rheology of real fermentation broths can be very different. This may include an increase in the liquid viscosity as the cell concentration increases and the development of non-Newtonian rheology, especially for high concentrations of filamentous organisms such as algae. A further factor affecting the two-phase properties is the presence of antifoaming agents, which alter the shape and size of the air bubbles and will therefore have an impact on the predictions of the interphase mass transfer models. This would also need to be accounted for in the interphase drag and population balance models. In addition to the changing rheological properties, it would be possible to couple the results of the CFD mass transfer model with a Monod-style kinetic cell growth model such as those described by Garcia-Ochoa et al. (2010). This has the potential to provide a fully predictive model of cell growth when combined with cell kinetics data from small-scale scoping experiments. However, creating such a model would require a novel approach to modelling the dynamic rheological behaviour since biological processes tend to occur over timescales of several days, which is incompatible with the timescales of both fluid dynamic (sub-second) and mass transfer (minutes) processes.

The validation experiments included in this report may be further strengthened by applying the existing techniques to a wider range of physical applications, such as different tank geometries, air flow rates and impeller types. Furthermore, the experimental techniques applied in this section can also be applied to the validation of models with the addition of antifoaming surfactants, high viscosity and non-Newtonian fluids. This would require using

appropriate transparent surfactants or viscosity modifiers such as carboxymethylcellulose (CMC) or xanthan gum as model systems. The present validation process may also be advanced by upgrading to more sophisticated experimental techniques such as three-dimensional LDV, phase-Doppler anemometry (PDA) or PIV to measure the velocity and bubble size distribution, albeit with considerable additional equipment costs. Further developments of the CFD model may be investigated, starting with optimising the MUSIG model parameters for a stirrer speed of 400 RPM and investigating the effects of varying the calibration factors in the breakup and coalescence models. The accuracy of the model may also be improved by investigating more advanced modelling options such as the LES turbulence model and sliding mesh technique for impeller motion, however these would need to be assessed for their simulation time with respect to the industrial-scale process. The current model setup may also be revised as new models become available and available computing power increases.

11.2 Microbubble Mass Transfer

The microbubble analysis has established a protocol for sizing microbubbles, and this may be expanded to include an analysis of the bubble rise velocity by modifying the MATLAB code to identify and track individual bubbles and increasing the frame rate used for the camera. This will give a greater understanding of the behaviour of microbubbles in a swarm, and provide a comparison to the single-microbubble rise velocity experiments found in literature. The characterisation experiments may be performed at a range of different liquid temperatures, surfactant concentrations or with viscosity modifiers in order to identify the changes in the properties of the bubbles generated. The operating conditions of the microbubble pump, such as upstream and downstream pressure and the gas flow rate may also be varied experimentally in order to evaluate the manufacturer recommended conditions and identify the operating window for microbubble generation. The microbubble characterisation technique may be used as the basis for the CFD modelling of microbubble flows, with the measured size distribution used as an initial condition for the bubble size distribution in the model.

The microbubble mass transfer experiments may be also be expanded to include the use of surfactants and viscosity modifiers as discussed above, however it may also be used with reacting or biological systems, where there is a consumption of the transferred species within the liquid phase. This may be achieved by integrating the microbubble generator

with a laboratory-scale bioreactor system and comparing the mass transfer and cell growth performance to traditional sparging and stirring protocols. This will also allow for the influence that the presence of microbubbles and the impacts that bubble bursting may have on living cells to be investigated. Finally, the microbubble mass transfer experiments may be repeated with pure soluble gasses in the place of air, in order to investigate the effect that the presence of inert gases may be having on the mass transfer performance, and to investigate other potential mass transfer applications for the Nikuni pump.

11.3 Carbonatation

The chapters of this thesis relating to the carbonatation process have described the development and validation of a model for the hydrodynamic conditions, interphase mass transfer and the chemical reactions occurring during the carbonatation process. This model can now be used to assess any proposed design variations for the full-scale process, or scale-down to pilot scale processes for research and development activities. It has been assumed in this work that the three-phase system may be modelled as a pseudo two-phase system, with the solid particles acting as additional components in the liquid phase. Future work could include modelling the process as a full three-phase system, with discreet solid particles within the fluid. Any future three-phase model would have to include the growth and shrinkage of the solids depending on the local concentration and pH conditions, however this may prove to be unreasonably expensive computationally when considered at the full production scale. The coupling of the flow patterns between the solid and the liquid phases would also have to be considered in this model, including interphase drag and particle settling phenomena.

The validation for the carbonatation project may be extended to include a wider range of temperatures, hydroxide concentrations and sucrose concentrations in order to give a greater variety of data for the model to be validated against. In particular, a greater knowledge of the effect that high sucrose concentrations may have on the reactions would improve confidence in the reaction model applied to the full-scale carbonatation process. The existing reaction model has been shown to consistently under-predict the pH in the validation system, which suggests that further refinement is required with respect to modelling the carbonate buffering system, of which the pH is a crucial component. This will require a more thorough analysis of the equilibrium constants applied to this section of the model. Similarly, the reaction model may be enhanced by investigating the influence that

side reactions which have been claimed to occur at different pH conditions may have on the concentration profiles modelled. This also extends to the re-dissolution of solid calcium carbonate particles resulting from the continued bubbling of carbon dioxide gas, which has been assumed to form a single stable compound in this work, and has been shown to be affected by the presence of sucrose in the liquid phase.

References

Agarwal, A., Ng, W.J. and Liu, Y., 2011. Principle and applications of microbubble and nanobubble technology for water treatment. *Chemosphere*, 84(9), pp.1175–1180.

Ago, K.I., Nagasawa, K., Takita, J., Itano, R., Morii, N., Matsuda, K. and Takahashi, K., 2005. Development of an aerobic cultivation system by using a microbubble aeration technology. *Journal of Chemical Engineering of Japan*, 38, pp.757–762.

Ahmed, S.U., Ranganathan, P., Pandey, A. and Sivaraman, S., 2010. Computational fluid dynamics modeling of gas dispersion in multi impeller bioreactor. *Journal of Bioscience and Bioengineering*, 109(6), pp.588–597.

Ahn, J.W., Park, C.H., Kim, J.H., Lee, J.K. and Kim, H., 1996. Synthesis of ultrafine calcium carbonate powders from high concentrated calcium hydroxide solution. *Journal of the Korean Crystal Growth and Crystal Technology*, 6(4), pp.509–520.

Akita, K. and Yoshida, F., 1973. Gas holdup and volumetric mass transfer coefficient in bubble columns. Effects of liquid properties. *Industrial & Engineering Chemistry Process Design and Development*, 12(1), pp.76–80.

Al-Mashhadani, M.K.H., Bandulasena, H.C.H. and Zimmerman, W.B., 2012. CO2 mass transfer induced through an airlift loop by a microbubble cloud generated by fluidic oscillation. *Industrial & Engineering Chemistry Research*, 51(4), pp.1864–1877.

AL-Mashhadani, M.K.H., Wilkinson, S.J. and Zimmerman, W.B., 2015. Airlift bioreactor for biological applications with microbubble mediated transport processes. *Chemical Engineering Science*, 137, pp.243–253.

Allison, J.D., Brown, D.S. and Novo-Gradac, K.J., 1991. MINTEQA2: A geochemical assessment model for environmental systems. Athens, Georgia: EPA.

Altaras, G.M., Eklund, C., Ranucci, C. and Maheshwari, G., 2007. Quantitation of interaction of lipids with polymer surfaces in cell culture. *Biotechnology and Bioengineering*, 96(5), pp.999–1007.

Alves, S.S., Maia, C.I. and Vasconcelos, J.M.T., 2002. Experimental and modelling study of gas dispersion in a double turbine stirred tank. *Chemical Engineering Science*, 57(3), pp.487–496.

Alves, S.S., Maia, C.I. and Vasconcelos, J.M.T., 2004. Gas-liquid mass transfer coefficient in stirred tanks interpreted through bubble contamination kinetics. *Chemical Engineering and Processing: Process Intensification*, 43(7), pp.823–830.

Alves, S.S., Maia, C.I., Vasconcelos, J.M.T. and Serralheiro, A.J., 2002. Bubble size in aerated stirred tanks. *Chemical Engineering Journal*, 89(1–3), pp.109–117.

do Amaral, C.E.F., Alves, R.F., Da Silva, M.J., Arruda, L.V.R., Dorini, L., Morales, R.E.M. and Pipa, D.R., 2013. Image processing techniques for high-speed videometry in horizontal two-phase slug flows. *Flow Measurement and Instrumentation*, 33, pp.257–264.

Andersson, B., Andersson, R., Mortensen, M., Sudiyo, R. and Wachem, B. Van, 2011. *Computational Fluid Dynamics for Engineers*. Cambridge: Cambridge University Press.

ANSYS Inc., 2016. ANSYS CFX-Solver Theory Guide. Canonsburg.

Appa, H., Deglon, D.A. and Meyer, C.J., 2014. Numerical modelling of mass transfer in an autoclave. *Hydrometallurgy*, 147–148, pp.234–240.

Arlov, D., Revstedt, J. and Fuchs, L., 2008. Numerical simulation of a gas–liquid Rushton stirred reactor – LES and LPT. *Computers & Fluids*, 37(7), pp.793–801.

Azbel, D., 1981. *Two-phase flows in chemical engineering*. Cambridge: Cambridge University Press.

Bach, C., Yang, J., Larsson, H., Stocks, S.M., Gernaey, K. V., Albaek, M.O. and Krühne, U., 2017. Evaluation of mixing and mass transfer in a stirred pilot scale bioreactor utilizing CFD. *Chemical Engineering Science*, 171, pp.19–26.

Baikow, V.E., 1982. *Manufacture and Refining of Raw Cane Sugar*. 2nd ed. Amsterdam: Elsevier Scientific Publishing Company.

Bakker, A. and Van den Akker, H.E.A., 1994. A computational model for the gas-liquid flow in stirred reactors. *Chemical Engineering Research & Design, Transactions of the Institute of Chemical Engineers, Part A*, 72(A4), pp.594–606.

Bao, Y., Yang, J., Wang, B. and Gao, Z., 2015. Influence of impeller diameter on local gas dispersion properties in a sparged multi-impeller stirred tank. *Chinese Journal of Chemical Engineering*, 23(4), pp.615–622.

Barigou, M. and Greaves, M., 1991. A capillary suction probe for bubble size measurement.

Measurement Science and Technology, 2(4), pp.318–326.
Basavarajappa, M. and Miskovic, S., 2016. Investigation of gas dispersion characteristics in stirred tank and flotation cell using a corrected CFD-PBM quadrature-based moment method approach. *Minerals Engineering*, 95, pp.161–184.
Bertrand, J. and Couderc, J.P., 1985. Evaluation of the power consumption in agitation of viscous newtonion or pseudoplastic liquids by two-bladed, anchor or gate agitators. *Chemical Engineering Research and Design*, 63(4), pp.259–263.
Besagni, G., Inzoli, F. and Ziegenhein, T., 2018. Two-phase bubble columns: A comprehensive review. *ChemEngineering*, 2, 13, pp.1–79.
Bond, G.M., Stringer, J., Brandvold, D.K., Simsek, F.A., Medina, M.-G. and Egeland, G., 2001. Development of integrated system for biomimetic CO2 sequestration using the enzyme carbonic anhydrase. *Energy & Fuels*, 15(2), pp.309–316.
BPSA, 2007a. Guide to disposal of single-use bioprocess systems. *Bioprocess International*, pp.22–28.
BPSA, 2007b. Recommendations for extractables and leachables testing. *BioPharm International*, 5(11), pp.36–49.
Brecht, R., 2009. Disposable bioreactors: Maturation into pharmaceutical glycoprotein manufacturing. In: R. Eibl and D. Eibl, eds. *Disopsable Bioreactors*. Heidelberg: Springer, pp.1–32.
Bredwell, M.D. and Worden, R.M., 1998. Mass-transfer properties of microbubbles. 1. experimental studies. *Biotechnology Progress*, 14(1), pp.31–38.
Bröder, D. and Sommerfeld, M., 2007. Planar shadow image velocimetry for the analysis of the hydrodynamics in bubbly flows. *Measurement Science and Technology*, 18(8), pp.2513–2528.
Brucato, A., Ciofalo, M., Grisafi, F. and Micale, G., 1994. Complete numerical simulation of flow fields in baffled stirred vessels: the inner-outer approach. *IChemE Symposium Series*, 136, pp.155–162.
Brucato, A., Grisafi, F. and Montante, G., 1998. Particle drag coefficients in turbulent fluids. *Chemical Engineering Science*, 53(18), pp.3295–3314.
Buffo, A., Vanni, M. and Marchisio, D.L., 2012. Multidimensional population balance model for the simulation of turbulent gas-liquid systems in stirred tank reactors. *Chemical Engineering Science*, 70, pp.31–44.
Burns, A.D., Frank, T., Hamill, I. and Shi, J.M., 2004. The Favre averaged drag model for turbulent dispersion in Eulerian multi-phase flows. *5th International Conference on Multiphase Flow*, (392), pp.1–17.
Catapano, G., Czermak, P., Eibl, R., Eibl, D. and Pörtner, R., 2009. Bioreactor Design and Scale-Up. *Cell and Tissue Reaction Engineering*. Berlin, Heidelberg: Springer, pp.173–259.
Chen, M., Wang, J., Zhao, S., Xu, C. and Feng, L., 2016. Optimization of dual-impeller configurations in a gas-liquid stirred tank based on computational fluid dynamics and multiobjective evolutionary algorithm. *Industrial and Engineering Chemistry Research*, 55(33), pp.9054–9063.
Chu, L.B., Xing, X.H., Yu, A.F., Sun, X.L. and Jurcik, B., 2008. Enhanced treatment of practical textile wastewater by microbubble ozonation. *Process Safety and Environmental Protection*, 86(5), pp.389–393.
Chu, L.B., Xing, X.H., Yu, A.F., Zhou, Y.N., Sun, X.L. and Jurcik, B., 2007. Enhanced ozonation of simulated dyestuff wastewater by microbubbles. *Chemosphere*, 68(10), pp.1854–1860.
Clift, R., Grace, J.R. and Weber, M.E., 1978. Bubbles, drops, and particles. *Drying Technology*, 11, pp.263–264.
Cockx, A., Do-Quang, Z., Audic, J.M., Liné, A. and Roustan, M., 2001. Global and local mass transfer coefficients in waste water treatment process by computational fluid dynamics. *Chemical Engineering and Processing: Process Intensification*, 40(2), pp.187–194.
Coulson, J.M., Richardson, J.F., Backhurst, J.R. and Harker, J.H., 1999. *Coulson and Richardson's Chemical Engineering Volume 1 - Fluid Flow, Heat Transfer and Mass Transfer*. 6th ed. Amsterdam: Elsevier.
Cussler, E.L., 1997. *Diffusion: Mass Transfer in Fluid Systems*. Cambridge Series in Chemical Engineering. Cambridge: Cambridge University Press.
Danckwerts, P. V., 1951. Significance of liquid-film coefficients in gas absorption. *Industrial & Engineering Chemistry*, 43(6), pp.1460–1467.
Danckwerts, P. V., 1970. *Gas-Liquid Reactions*. New York: McGraw-Hill Inc.
Dantec Dynamics, n.d. *Measurement principles of LDA* [Online]. Available from:

http://www.dantecdynamics.com/measurement-principles-of-lda [Accessed 1 May 2015].
Deen, N.G. and Solberg, T., 2000. Comparison of PIV and LDA measurement methods applied to the gas-liquid flow in a bubble column. *10th International Symposium on Appllications of Laser Techniques to Fluid Mechanics*, pp.1–12.
Deen, N.G., Solberg, T. and Hjertager, B.H., 2002. Flow generated by an aerated rushton impeller: Two-phase PIV experiments and numerical simulations. *The Canadian Journal of Chemical Engineering*, 80(4), pp.1–15.
Derksen, J. and Van den Akker, H.E. a., 1999. Large eddy simulations on the flow driven by a Rushton turbine. *AIChE Journal*, 45(2), pp.209–221.
Dhanasekharan, K.M., Sanyal, J., Jain, A. and Haidari, A., 2005. A generalized approach to model oxygen transfer in bioreactors using population balances and computational fluid dynamics. *Chemical Engineering Science*, 60(1), pp.213–218.
Dhotre, M.T., Niceno, B. and Smith, B.L., 2008. Large eddy simulation of a bubble column using dynamic sub-grid scale model. *Chemical Engineering Journal*, 136(2–3), pp.337–348.
Doran, P.M., 1995. *Bioprocess Engineering Principles*. London: Elsevier.
Dreher, T., Husemann, U., Zahnow, C., De Wilde, D., Adams, T. and Greller, G., 2013. High cell density escherichia coli cultivation in different single-use bioreactor systems. *Chemie-Ingenieur-Technik*, 85(1–2), pp.162–171.
Dreher, T., Walcarius, B., Husemann, U., Klingenberg, F., Zahnow, C., Adams, T., de Wilde, D., Casteels, P. and Greller, G., 2014. Microbial ighh cell density fermentations in a stirred single-use bioreactor. In: D. Eibl and R. Eibl, eds. *Disposable Bioreactors II*. Berlin, Heidelberg: Springer Berlin Heidelberg, pp.127–147.
Eggels, J.G.M., 1996. Direct and large-eddy simulation of turbulent fluid flow using the lattice-Boltzmann scheme. *International Journal of Heat and Fluid Flow*, 17(3), pp.307–323.
Eibl, R., Kaiser, S., Lombriser, R. and Eibl, D., 2010. Disposable bioreactors: The current state-of-the-art and recommended applications in biotechnology. *Applied Microbiology and Biotechnology*, 86(1), pp.41–49.
Ekambara, K. and Dhotre, M.T., 2010. CFD simulation of bubble column. *Nuclear Engineering and Design*, 240(5), pp.963–969.
Elqotbi, M., Vlaev, S.D., Montastruc, L. and Nikov, I., 2013. CFD modelling of two-phase stirred bioreaction systems by segregated solution of the Euler–Euler model. *Computers & Chemical Engineering*, 48, pp.113–120.
Falch, F.A. and Heden, C.-G., 1963. Disposable shaker flasks. *Biotechnology and Bioengineering*, 5, pp.211–220.
Fan, R., Marchisio, D.L. and Fox, R.O., 2004. Application of the direct quadrature method of moments to polydisperse gas–solid fluidized beds. *Powder Technology*, 139(1), pp.7–20.
Ferreira, A., Pereira, G., Teixeira, J.A. and Rocha, F., 2012. Statistical tool combined with image analysis to characterize hydrodynamics and mass transfer in a bubble column. *Chemical Engineering Journal*, 180, pp.216–228.
Fletcher, D.F., McClure, D.D., Kavanagh, J.M. and Barton, G.W., 2017. CFD simulation of industrial bubble columns: Numerical challenges and model validation successes. *Applied Mathematical Modelling*, 44, pp.25–42.
Frössling, N., 1938. Über die verdunstung fallender tropfen. *Gerlands Beiträge zur Geophysik*, 52, pp.170–216.
Fu, Y. and Liu, Y., 2016. Development of a robust image processing technique for bubbly flow measurement in a narrow rectangular channel. *International Journal of Multiphase Flow*, 84, pp.217–228.
Galliher, P.M., Hodge, G., Guertin, P., Chew, L. and Deloggio, T., 2011. Single-Use Bioreactor Platform for Microbial Fermentation. *Single-Use Technology in Biopharmaceutical Manufacture*. Hoboken, NJ, USA: John Wiley & Sons, Inc., pp.241–250.
Garcia-Ochoa, F., Gomez, E., Santos, V.E. and Merchuk, J.C., 2010. Oxygen uptake rate in microbial processes: An overview. *Biochemical Engineering Journal*, 49(3), pp.289–307.
GE Healthcare, 2013. Microbial fermentation in single-use Xcellerex ™ XDR-50 MO fermentor system.
Gelves, R., Dietrich, a. and Takors, R., 2014. Modeling of gas-liquid mass transfer in a stirred tank bioreactor agitated by a Rushton turbine or a new pitched blade impeller. *Bioprocess and Biosystems Engineering*, 37(3), pp.365–375.

Ghadge, R.S., Ekambara, K. and Joshi, J.B., 2005. Role of hydrodynamic flow parameters in lipase deactivation in bubble column reactor. *Chemical Engineering Science*, 60(22), pp.6320–6335.
Gimbun, J., Liew, S.Y., Nagy, Z.K. and Rielly, C.D., 2016. Three-way coupling simulation of a gas-liquid stirred tank using a multi-compartment population balance model. *Chemical Product and Process Modeling*, 11, pp.205–216.
Gimbun, J., Rielly, C.D. and Nagy, Z.K., 2009. Modelling of mass transfer in gas-liquid stirred tanks agitated by Rushton turbine and CD-6 impeller: A scale-up study. *Chemical Engineering Research and Design*, 87(4), pp.437–451.
Gogate, P.R., 2011. Hydrodynamic cavitation for food and water processing. *Food and Bioprocess Technology*, 4(6), pp.996–1011.
Gosman, A.D., Lekakou, C., Politis, S., Issa, R.I. and Looney, M.K., 1992. Multidimensional modeling of turbulent two-phase flows in stirred vessels. *AIChE Journal*, 38(12), pp.1946–1956.
Green, D.W. and Perry, R.H., 2008. *Perry's Chemical Engineers' Handbook*. 8th ed. New York: McGraw-Hill.
Hadamard, J.S., 1911. Mouvement permanent lent d'une sphere liquide et visqueuse dans un liquide visqueux. *Comptes rendus de l'Académie des Sciences*, 152, pp.1735–1738.
Hagesaether, L., Jakobsen, H.A., Hjarbo, K. and Svendsen, H.F., 2000. A coalescence and breakup module for implementation in CFD-codes. *Computer Aided Chemical Engineering*, 8, pp.367–372.
Han, S.J., Yoo, M., Kim, D.W. and Wee, J.H., 2011. Carbon dioxide capture using calcium hydroxide aqueous solution as the absorbent. *Energy & Fuels*, 25(8), pp.3825–3834.
Hanotu, J., Bandulasena, H.C.H. and Zimmerman, W.B., 2012. Microflotation performance for algal separation. *Biotechnology and Bioengineering*, 109(7), pp.1663–1673.
Hanotu, J., Karunakaran, E., Bandulasena, H., Biggs, C. and Zimmerman, W.B., 2014. Harvesting and dewatering yeast by microflotation. *Biochemical Engineering Journal*, 82, pp.174–182.
Hanotu, J., Kong, D. and Zimmerman, W.B., 2016. Intensification of yeast production with microbubbles. *Food and Bioproducts Processing*, 100, pp.424–431.
Hanrahan, G., 2012. Aqueous Chemistry. *Key Concepts in Environmental Chemistry*. Elsevier, pp.73–106.
Harun, M.H.C. and Zimmerman, W.B., 2018. Membrane defouling using microbubbles generated by fluidic oscillation. *Water Supply*, 19(1), pp.97–106.
Harvey, P.S. and Greaves, M., 1982a. Turbulent flow in an agitated vessel. Part I: A predictive model. *Trans IChemE*, 60, pp.195–200.
Harvey, P.S. and Greaves, M., 1982b. Turbulent flow in an agitated vessel. Part II: Numerical solution and model predictions. *Trans IChemE*, 60, pp.201–210.
Hensirisak, P., Parasukulsatid, P., Agblevor, F.A., Cundiff, J.S. and Velander, W.H., 2002. Scale-up of microbubble dispersion generator for aerobic fermentation. *Applied Biochemistry and Biotechnology*, 101(3), pp.211–227.
Hewitt, G.F. and Roberts, D.N., 1969. *Studies of two-phase flow patterns by simultaneous x-ray and flash photography*. Atomic Energy Research Establishment, Harwell.
Higbie, R., 1935. The rate of absorbtion of a pure gas into a still liquid during short periods of exposure. *Transactions of the American Institute of Chemical Engineers*, 31, pp.365–389.
Hinze, J.O., 1955. Fundamentals of the hydrodynamic mechanism of splitting in dispersion processes. *AIChE Journal*, 1(3), pp.289–295.
Honkanen, M., 2009. Reconstruction of a three-dimensional bubble surface from high-speed orthogonal imaging of dilute bubbly flow. *WIT Transactions on Engineering Sciences*, 63, pp.469–480.
Honkanen, M., Saarenrinne, P., Stoor, T. and Niinimäki, J., 2005. Recognition of highly overlapping ellipse-like bubble images. *Measurement Science and Technology*, 16(9), pp.1760–1770.
Huang, Q., Yang, C., Yu, G. and Mao, Z.-S., 2010. CFD simulation of hydrodynamics and mass transfer in an internal airlift loop reactor using a steady two-fluid model. *Chemical Engineering Science*, 65(20), pp.5527–5536.
Hughmark, G.A., 1980. Power requirements and interfacial area in gas-liquid turbine agitated systems. *Industrial & Engineering Chemistry Process Design and Development*, 19(4), pp.638–641.
Ikeura, H., Kobayashi, F. and Tamaki, M., 2011. Removal of residual pesticide, fenitrothion, in vegetables by using ozone microbubbles generated by different methods. *Journal of Food*

Engineering, 103(3), pp.345–349.
Iranzo, A., Barbero, R., Domingo, J., Cuadra, D., Costa, J., Martín, J.F., Ullán, R. V and Barredo, J.L., 2011. Numerical investigation of the effect of impeller design parameters on the performance of a multiphase baffle-stirred reactor. *Chemical Engineering & Technology*, 34(8), pp.1271–1280.
Ishii, M., 1975. *Thermo-Fluid Dynamic Theory of Two-Phase Flow*. Paris: Eyerolles.
Ishii, M. and Zuber, N., 1979. Drag coefficient and relative velocity in bubbly, droplet or particulate flows. *AIChE Journal*, 25(5), pp.843–855.
Jahoda, M., Tomášková, L. and Moštěk, M., 2009. CFD prediction of liquid homogenisation in a gas–liquid stirred tank. *Chemical Engineering Research and Design*, 87(4), pp.460–467.
Jajuee, B., Margaritis, A., Karamanev, D. and Bergougnou, M. a., 2006. Application of surface-renewal-stretch model for interface mass transfer. *Chemical Engineering Science*, 61(12), pp.3917–3929.
Jeon, S.Y., Yoon, J.Y. and Jang, C.M., 2018. Bubble size and bubble concentration of a microbubble pump with respect to operating conditions. *Energies*, 11, 1864, pp.1–13.
Johannsen, K. and Rademacher, S., 1999. Modelling the kinetics of calcium hydroxide dissolution in water. *Acta Hydrochimica et Hydrobiologica*, 27(2), pp.72–78.
Jones, N., 2015. Single-use processing for microbial fermentations. *BioProcess International*, 13(4).
Joshi, J.B., Nere, N.K., Rane, C. V., Murthy, B.N., Mathpati, C.S., Patwardhan, A.W. and Ranade, V. V., 2011a. CFD simulation of stirred tanks: Comparison of turbulence models. Part I: Radial flow impellers. *The Canadian Journal of Chemical Engineering*, 89(1), pp.23–82.
Joshi, J.B., Nere, N.K., Rane, C. V., Murthy, B.N., Mathpati, C.S., Patwardhan, A.W. and Ranade, V. V., 2011b. CFD simulation of stirred tanks: Comparison of turbulence models (Part II: Axial flow impellers, multiple impellers and multiphase dispersions). *The Canadian Journal of Chemical Engineering*, 89(4), pp.754–816.
Joshi, J.B., Pandit, A.B. and Sharma, M.M., 1982. Mechanically agitated gas-liquid reactors. *Chemical Engineering Science*, 37(6), pp.813–844.
Junne, S. and Neubauer, P., 2018. How scalable and suitable are single-use bioreactors? *Current Opinion in Biotechnology*, 53, pp.240–247.
Kaiser, S.C., Eibl, R. and Eibl, D., 2011. Engineering characteristics of a single-use stirred bioreactor at bench-scale: The Mobius CellReady 3L bioreactor as a case study. *Engineering in Life Sciences*, 11(4), pp.359–368.
Kálal, Z., Jahoda, M. and Fořt, I., 2014. CFD prediction of gas-liquid flow in an aerated stirred vessel using the population balance model. *Chemical and Process Engineering*, 35(1), pp.55–73.
Kapp, T., Boehm, J., Chase, J., Craig, J., Davis, K., Gupta, V., Montgomery, S.A. and Ott, K., 2010. Road map to implementation of single-use systems. *BioProcess International*, 8(4), pp.10–19.
Karn, A., Ellis, C., Arndt, R. and Hong, J., 2015. An integrative image measurement technique for dense bubbly flows with a wide size distribution. *Chemical Engineering Science*, 122, pp.240–249.
Kaster, J.A., Michelsen, D.L. and Velander, W.H., 1990. Increased oxygen transfer in a yeast fermentation using a microbubble dispersion. *Applied Biochemistry and Biotechnology*, 24(1), pp.469–484.
Kawahara, A., Sadatomi, M., Matsuyama, F., Matsuura, H., Tominaga, M. and Noguchi, M., 2009. Prediction of micro-bubble dissolution characteristics in water and seawater. *Experimental Thermal and Fluid Science*, 33(5), pp.883–894.
Kawase, Y., Halard, B. and Moo-Young, M., 1992. Liquid-phase mass transfer coefficients in bioreactors. *Biotechnology and Bioengineering*, 39, pp.1133–1140.
Kerdouss, F., Bannari, A. and Proulx, P., 2006. CFD modeling of gas dispersion and bubble size in a double turbine stirred tank. *Chemical Engineering Science*, 61(10), pp.3313–3322.
Kerdouss, F., Bannari, A., Proulx, P., Bannari, R., Skrga, M. and Labrecque, Y., 2008. Two-phase mass transfer coefficient prediction in stirred vessel with a CFD model. *Computers & Chemical Engineering*, 32(8), pp.1943–1955.
Khopkar, A.R., Aubin, J., Xuereb, C., Le Sauze, N., Bertrand, J. and Ranade, V. V, 2003. Gas-liquid flow generated by a pitched-blade turbine: Particle image velocimetry measurements and computational fluid dynamics simulations. *Industrial & Engineering Chemistry Research*, 42(21), pp.5318–5332.
Khopkar, A.R., Rammohan, A.R., Ranade, V.V. and Dudukovic, M.P., 2005. Gas–liquid flow generated

by a Rushton turbine in stirred vessel: CARPT/CT measurements and CFD simulations. *Chemical Engineering Science*, 60(8–9), pp.2215–2229.
Khopkar, A.R. and Ranade, V. V, 2006. CFD simulation of gas–liquid stirred vessel: VC, S33, and L33 flow regimes. *AIChE Journal*, 52(5), pp.1654–1672.
Khopkar, A.R. and Tanguy, P.A., 2008. CFD simulation of gas–liquid flows in stirred vessel equipped with dual rushton turbines: influence of parallel, merging and diverging flow configurations. *Chemical Engineering Science*, 63(14), pp.3810–3820.
Khuntia, S., Majumder, S. and Ghosh, P., 2012. Microbubble-aided water and wastewater purification: A review. *Reviews in Chemical Engineering*, 28, pp.191–221.
Khuntia, S., Majumder, S.K. and Ghosh, P., 2013. Removal of ammonia from water by ozone microbubbles. *Industrial & Engineering Chemistry Research*, 52(1), pp.318–326.
Kim, H.S., Lim, J.Y., Park, S.Y. and Kim, J.H., 2018. Effects of distance of breaker disk on performance of ejector type microbubble generator. *KSCE Journal of Civil Engineering*, 22(4), pp.1096–1100.
Kim, M., Na, J., Park, S., Park, J.H. and Han, C., 2018. Modeling and validation of a pilot-scale aqueous mineral carbonation reactor for carbon capture using computational fluid dynamics. *Chemical Engineering Science*, 177, pp.301–312.
Knazek, R.A., Gullino, P.M., Kohler, P.O. and Dedrick, R.L., 1972. Cell culture on artificial capillaries: An approach to tissue growth in vitro. *Science*, 178, pp.65–67.
Krepper, E., Lucas, D., Frank, T., Prasser, H.M. and Zwart, P.J., 2008. The inhomogeneous MUSIG model for the simulation of polydispersed flows. *Nuclear Engineering and Design*, 238(7), pp.1690–1702.
Krishna, R. and Van Baten, J.M., 2003. Mass transfer in bubble columns. *Catalysis Today*, 79–80, pp.67–75.
Kulkarni, A.A., 2007. Mass transfer in bubble column reactors: effect of bubble size distribution. *Industrial & Engineering Chemistry Research*, 46(7), pp.2205–2211.
Kumar, S. and Ramkrishna, D., 1996. On the solution of population balance equations by discretization—I. A fixed pivot technique. *Chemical Engineering Science*, 51(8), pp.1311–1332.
Laakkonen, M., Alopaeus, V. and Aittamaa, J., 2006. Validation of bubble breakage, coalescence and mass transfer models for gas–liquid dispersion in agitated vessel. *Chemical Engineering Science*, 61(1), pp.218–228.
Laakkonen, M., Moilanen, P., Alopaeus, V. and Aittamaa, J., 2007. Modelling local bubble size distributions in agitated vessels. *Chemical Engineering Science*, 62(3), pp.721–740.
Lamont, J.C. and Scott, D.S., 1970. An eddy cell model of mass transfer into the surface of a turbulent liquid. *AIChE Journal*, 16(4), pp.513–519.
Lane, G.L., Schwarz, M.P. and Evans, G.M., 2002. Predicting gas–liquid flow in a mechanically stirred tank. *Applied Mathematical Modelling*, 26(2), pp.223–235.
Lane, G.L., Schwarz, M.P. and Evans, G.M., 2005. Numerical modelling of gas–liquid flow in stirred tanks. *Chemical Engineering Science*, 60(8), pp.2203–2214.
Lau, Y.M., Deen, N.G. and Kuipers, J.A.M., 2013. Development of an image measurement technique for size distribution in dense bubbly flows. *Chemical Engineering Science*, 94, pp.20–29.
Li, P. and Tsuge, H., 2006a. Ozone transfer in a new gas-induced contactor with microbubbles. *Journal of Chemical Engineering of Japan*, 39, pp.1213–1220.
Li, P. and Tsuge, H., 2006b. Water treatment by induced air flotation using microbubbles. *Journal of Chemical Engineering of Japan*, 39, pp.896–903.
Li, X., Li, P., Zu, L. and Yang, C., 2016. Gas-liquid mass transfer characteristics with microbubble aeration – I. Standard stirred tank. *Chemical Engineering & Technology*, 39(5), pp.945–952.
Linek, V., Kordač, M., Fujasová, M. and Moucha, T., 2004. Gas-liquid mass transfer coefficient in stirred tanks interpreted through models of idealized eddy structure of turbulence in the bubble vicinity. *Chemical Engineering and Processing: Process Intensification*, 43(12), pp.1511–1517.
Linek, V., Moucha, T. and Kordač, M., 2005. Mechanism of mass transfer from bubbles in dispersions Part I. Danckwerts' plot method with sulphite solutions in the presence of viscosity and surface tension changing agents. *Chemical Engineering and Processing: Process Intensification*, 44(3), pp.353–361.
Liu, C., Zhang, L., Yang, J., Guo, J. and Li, Z., 2009. Effects of surfactants on oxygen transfer in microbubble aeration. *2009 International Conference on Energy and Environment Technology*. pp.531–534.

Liu, Y.-J., Li, W., Han, L.-C., Cao, Y., Luo, H., Al-Dahhan, M. and Dudukovic, M.P., 2011. γ-CT measurement and CFD simulation of cross section gas holdup distribution in a gas–liquid stirred standard Rushton tank. *Chemical Engineering Science*, 66(17), pp.3721–3731.

Löffelholz, C., Kaiser, S.C., Kraume, M., Eibl, R. and Eibl, D., 2014. Dynamic Ssngle-use bioreactors used in modern liter- and m3- scale biotechnological processes: Engineering characteristics and scaling up. In: D. Eibl and R. Eibl, eds. *Disposable Bioreactors II*. Berlin, Heidelberg: Springer Berlin Heidelberg, pp.1–44.

Lopes, A.G., 2015. Single-use in the biopharmaceutical industry: A review of current technology impact, challenges and limitations. *Food and Bioproducts Processing*, 93, pp.98–114.

Lu, W.-M. and Ju, S.-J., 1987. Local gas holdup, mean liquid velocity and turbulence in an aerated stirred tank using hot-film anemometry. *The Chemical Engineering Journal*, 35(1), pp.9–17.

Luo, H. and Svendsen, H.F., 1996. Theoretical model for drop and bubble breakup in turbulent dispersions. *AIChE Journal*, 42(5), pp.1225–1233.

Luo, J.Y., Gosman, A.D., Issa, R., Middleton, J.C. and Fitzgerald, M.K., 1993. Full flow field computation of mixing in baffled stirred vessels. *Chemical Engineering Research and Design*, 71, pp.342–344.

Maltby, R., Tian, S. and Chew, Y.M.J., 2018. Computational studies of a novel magnetically driven single-use-technology bioreactor: A comparison of mass transfer models. *Chemical Engineering Science*, 187, pp.157–173.

Marchisio, D.L. and Fox, R.O., 2005. Solution of population balance equations using the direct quadrature method of moments. *Journal of Aerosol Science*, 36(1), pp.43–73.

Mavros, P., 2001. Flow visualization in stirred vessels. *Chemical Engineering Research and Design*, 79(2), pp.113–127.

McClure, D.D., Aboudha, N., Kavanagh, J.M., Fletcher, D.F. and Barton, G.W., 2015. Mixing in bubble column reactors: Experimental study and CFD modeling. *Chemical Engineering Journal*, 264, pp.291–301.

Mcclure, D.D., Kavanagh, J.M., Fletcher, D.F. and Barton, G.W., 2014. Development of a CFD model of bubble column bioreactors: Part two - comparison of experimental data and CFD predictions. *Chemical Engineering and Technology*, 37(1), pp.131–140.

McClure, D.D., Kavanagh, J.M., Fletcher, D.F. and Barton, G.W., 2015. Oxygen transfer in bubble columns at industrially relevant superficial velocities: Experimental work and CFD modelling. *Chemical Engineering Journal*, 280, pp.138–146.

McClure, D.D., Kavanagh, J.M., Fletcher, D.F. and Barton, G.W., 2016. Characterizing bubble column bioreactor performance using computational fluid dynamics. *Chemical Engineering Science*, 144, pp.58–74.

McClure, D.D., Liu, Z., Barton, G.W., Fletcher, D.F. and Kavanagh, J.M., 2018. Oxygen transfer in pilot-scale contactors: An experimental and computational investigation into the effect of contactor design. *Chemical Engineering Journal*, 344, pp.173–183.

McGraw, R., 1997. Description of aerosol dynamics by the quadrature method of moments. *Aerosol Science and Technology*, 27(2), pp.255–265.

Mena, P.C., Pons, M.N., Teixeira, J.A. and Rocha, F.A., 2005. Using image analysis in the study of multiphase gas absorption. *Chemical Engineering Science*, 60(18), pp.5144–5150.

Meyer, F., 1994. Topographic distance and watershed lines. *Signal Processing*, 38(1), pp.113–125.

Mitchell, M.J., Jensen, O.E., Cliffe, K.A. and Maroto-Valer, M.M., 2010. A model of carbon dioxide dissolution and mineral carbonation kinetics. *Proceedings of the Royal Society A: Mathematical, Physical and Engineering Sciences*, 466(2117), pp.1265–1290.

Moilanen, P., Laakkonen, M., Visuri, O., Alopaeus, V. and Aittamaa, J., 2008. Modelling mass transfer in an aerated 0.2 m3 vessel agitated by Rushton, Phasejet and Combijet impellers. *Chemical Engineering Journal*, 142(1), pp.95–108.

Montante, G., Horn, D. and Paglianti, A., 2008. Gas–liquid flow and bubble size distribution in stirred tanks. *Chemical Engineering Science*, 63(8), pp.2107–2118.

Montante, G., Paglianti, A. and Magelli, F., 2007. Experimental analysis and computational modelling of gas–liquid stirred vessels. *Chemical Engineering Research and Design*, 85(5), pp.647–653.

Montes-Hernandez, G., Fernández-Martínez, A., Charlet, L., Tisserand, D. and Renard, F., 2008. Textural properties of synthetic nano-calcite produced by hydrothermal carbonation of calcium hydroxide. *Journal of Crystal Growth*, 310(11), pp.2946–2953.

Morchain, J., Gabelle, J.-C. and Cockx, A., 2014. A coupled population balance model and CFD

approach for the simulation of mixing issues in lab-scale and industrial bioreactors. *AIChE Journal*, 60(1), pp.27–40.
Morud, K.E. and Hjertager, B.H., 1996. LDA measurements and CFD modelling of gas-liquid flow in a stirred vessel. *Chemical Engineering Science*, 51(2), pp.233–249.
Mudde, R.F., Groen, J.S. and Van Den Akker, H.E.A., 1998. Application of LDA to bubbly flows. *Nuclear Engineering and Design*, 184(2–3), pp.329–338.
Mudde, R.F. and Simonin, O., 1999. Two- and three-dimensional simulations of a bubble plume using a two-fluid model. *Chemical Engineering Science*, 54(21), pp.5061–5069.
Murthy, B.N., Deshmukh, N.A., Patwardhan, A.W. and Joshi, J.B., 2007. Hollow self-inducing impellers: Flow visualization and CFD simulation. *Chemical Engineering Science*, 62(14), pp.3839–3848.
Murthy, J.Y., Mathur, S.R. and Choudhury, D., 1994. CFD simulation of flows in stirred tank reactors using a sliding mesh technique. *IChemE Symposium Series*, 136, pp.341–348.
Ndiaye, M., Gadoin, E. and Gentric, C., 2018. CO2 gas–liquid mass transfer and kLa estimation: Numerical investigation in the context of airlift photobioreactor scale-up. *Chemical Engineering Research and Design*, 133, pp.90–102.
Ohnari, H., 2000. *Swing type fine air bubble generating device*. European Patent Application EP1112773A1.
Otsu, N., 1979. A threshold selection method from gray-level histograms. *IEEE Transactions on Systems, Man, and Cybernetics*, 9(1), pp.62–66.
Parkinson, L., Sedev, R., Fornasiero, D. and Ralston, J., 2008. The terminal rise velocity of 10–100 µm diameter bubbles in water. *Journal of Colloid and Interface Science*, 322(1), pp.168–172.
Parmar, R. and Majumder, S.K., 2013. Microbubble generation and microbubble-aided transport process intensification—A state-of-the-art report. *Chemical Engineering and Processing: Process Intensification*, 64, pp.79–97.
Pericleous, K. and Patel, M., 1987. The modelling of tangential and axial agitators in chemical reactors. *PCH Physicochemical Hydodynamics*, 8(2), pp.105–123.
Petitti, M., Nasuti, A., Marchisio, D.L., Vanni, M., Baldi, G., Mancini, N. and Podenzani, F., 2010. Bubble size distribution modeling in stirred gas–liquid reactors with QMOM augmented by a new correction algorithm. *AIChE Journal*, 56(1), pp.36–53.
Petitti, M., Vanni, M., Marchisio, D.L., Buffo, A. and Podenzani, F., 2013. Simulation of coalescence, break-up and mass transfer in a gas–liquid stirred tank with CQMOM. *Chemical Engineering Journal*, 228, pp.1182–1194.
Pietrzykowski, M., Flanagan, W., Pizzi, V., Brown, A., Sinclair, A. and Monge, M., 2013. An environmental life cycle assessment comparison of single-use and conventional process technology for the production of monoclonal antibodies. *Journal of Cleaner Production*, 41, pp.150–162.
Pocker, Y. and Bjorkquist, D.W., 1977. Stopped-flow studies of carbon dioxide hydration and bicarbonate dehydration in water and water-d2. Acid-base and metal ion catalysis. *Journal of the American Chemical Society*, 99(20), pp.6537–6543.
Pollard, D. and Kistler, C., 2017. Disposable Bioreactors. In: C. Larroche, M.Á. Sanromán, G. Du and A. Pandey, eds. *Current Developments in Biotechnology and Bioengineering*. Amsterdam: Elsevier, pp.353–379.
Pora, H. and Rawlings, B., 2009. A user's checklist for introducing single-use components into process systems. *BioProcess International*, 7(4), pp.9–16.
Prakash, V.N., Tagawa, Y., Calzavarini, E., Mercado, J.M., Toschi, F., Lohse, D. and Sun, C., 2012. How gravity and size affect the acceleration statistics of bubbles in turbulence. *New Journal of Physics*, 14(10), p.105017.
Prasher, B.D. and Wills, G.B., 1973. Mass transfer in an agitated vessel. *Industrial and Engineering Chemistry: Process Design and Development*, 12(3), pp.351–354.
Pridham, P.W., 2015. Nikuni Co. KTM Series Pumps. Aeration and Mixing Ltd.
Prince, M.J. and Blanch, H.W., 1990. Bubble coalescence and break-up in air-sparged bubble columns. *AIChE Journal*, 36(10), pp.1485–1499.
Ranade, V. and Dommeti, S.M.S., 1996. Computational snapshot of flow generated by axial impellers in baffled stirred vessels. *Chemical Engineering Research and Design*, 74, pp.476–484.
Ranade, V. V. and Deshpande, V.R., 1999. Gas–liquid flow in stirred reactors: Trailing vortices and gas accumulation behind impeller blades. *Chemical Engineering Science*, 54(13–14), pp.2305–

2315.
Ranade, V.V. and Van den Akker, H.E.A., 1994. A computational snapshot of gas—liquid flow in baffled stirred reactors. *Chemical Engineering Science*, 49(24), pp.5175–5192.
Ranade, V.V., Perrard, M., Xuereb, C., Le Sauze, N. and Bertrand, J., 2001. Influence of gas flow rate on the structure of trailing vortices of a Rushton turbine: PIV measurements and CFD simulations. *Chemical Engineering Research and Design*, 79(8), pp.957–964.
Ranganathan, P. and Sivaraman, S., 2011. Investigations on hydrodynamics and mass transfer in gas-liquid stirred reactor using computational fluid dynamics. *Chemical Engineering Science*, 66(14), pp.3108–3124.
Ravise, A., Cameau, E., De Abreu, G. and Pralong, A., 2009. Hybrid and disposable facilities for manufacturing of biopharmaceuticals: Pros and cons. In: R. Eibl and D. Eibl, eds. *Disposable Bioreactors*. Heidelberg: Springer, pp.185–220.
Rawlings, B. and Pora, H., 2009. Environmental impact of single-use and reusable bioprocess systems. *BioProcess International*, 7(2), pp.18–25.
Rybcznski, W., 1911. Über die fortschreitende Bewegung einer flüssigen Kugel in einem zähen Medium. *Bulletin international de l'Académie des sciences de Cracovie, A*, pp.40–46.
Sadatomi, M., Kawahara, A., Kano, K. and Ohtomo, A., 2005. Performance of a new micro-bubble generator with a spherical body in a flowing water tube. *Experimental Thermal and Fluid Science*, 29(5), pp.615–623.
Sadatomi, M., Kawahara, A., Matsuura, H. and Shikatani, S., 2012. Micro-bubble generation rate and bubble dissolution rate into water by a simple multi-fluid mixer with orifice and porous tube. *Experimental Thermal and Fluid Science*, 41, pp.23–30.
Saffman, P.G. and Turner, J.S., 1956. On the collision of drops in turbulent clouds. *Journal of Fluid Mechanics*, 1(1), pp.16–30.
Sander, R., 2015. Compilation of Henry's law constants (version 4.0) for water as solvent. *Atmospheric Chemistry and Physics*, 15(8), pp.4399–4981.
Sato, Y. and Sekoguchi, K., 1975. Liquid velocity distribution in two-phase bubble flow. *International Journal of Multiphase Flow*, 2(1), pp.79–95.
Scargiali, F., D'Orazio, A., Grisafi, F. and Brucato, A., 2007. Modelling and simulation of gas–liquid hydrodynamics in mechanically stirred tanks. *Chemical Engineering Research and Design*, 85(5), pp.637–646.
Segev, R., Hasson, D. and Semiat, R., 2012a. Rigorous modeling of the kinetics of calcium carbonate deposit formation. *AIChE Journal*, 58(4), pp.1222–1229.
Segev, R., Hasson, D. and Semiat, R., 2012b. Rigorous modeling of the kinetics of calcium carbonate deposit formation - CO2 effect. *AIChE Journal*, 58(7), pp.2286–2289.
Selma, B., Bannari, R. and Proulx, P., 2010. Simulation of bubbly flows: Comparison between direct quadrature method of moments (DQMOM) and method of classes (CM). *Chemical Engineering Science*, 65(6), pp.1925–1941.
Shah, Y.T., Kelkar, B.G., Godbole, S.P. and Deckwer, W.-D., 1982. Design parameters estimations for bubble column reactors. *AIChE Journal*, 28(3), pp.353–379.
Shukla, A. a. and Gottschalk, U., 2013. Single-use disposable technologies for biopharmaceutical manufacturing. *Trends in Biotechnology*, 31(3), pp.147–154.
Singh, V., 1999. Disposable bioreactor for cell culture using wave-induced agitation. *Cytotechnology*, 30(1), pp.149–158.
Sommerfeld, M., 2001. Validation of a stochastic Lagrangian modelling approach for inter-particle collisions in homogeneous isotropic turbulence. *International Journal of Multiphase Flow*, 27(10), pp.1829–1858.
Stokes, G.G., 1851. On the effect of the internal friction of fluids on the motion of pendulums. *Transactions of the Cambridge Philosophical Society*, 9, p.8.
Stumm, W. and Morgan, J.J., 1996. *Aquatic chemistry: chemical equilibria and rates in natural waters*. New York: John Wiley.
Sungkorn, R., Derksen, J.J. and Khinast, J.G., 2012. Euler–Lagrange modeling of a gas–liquid stirred reactor with consideration of bubble breakage and coalescence. *AIChE Journal*, 58(5), pp.1356–1370.
Szekely, J., J. Wang, H. and M. Kiser, K., 1976. Flow pattern velocity and turbulence energy measurements and predictions in a water model of an argon-stirred ladle. *Metallurgical Transactions B*, 7, pp.287–295.

Tabib, M. V., Roy, S.A. and Joshi, J.B., 2008. CFD simulation of bubble column—An analysis of interphase forces and turbulence models. *Chemical Engineering Journal*, 139(3), pp.589–614.
Taghavi, M., Zadghaffari, R., Moghaddas, J. and Moghaddas, Y., 2011. Experimental and CFD investigation of power consumption in a dual Rushton turbine stirred tank. *Chemical Engineering Research and Design*, 89(3), pp.280–290.
Takahashi, M., 2005. ζ Potential of microbubbles in aqueous solutions: Electrical properties of the gas - Water interface. *Journal of Physical Chemistry B*, 109(46), pp.21858–21864.
Takahashi, M., Chiba, K. and Li, P., 2007. Free-radical generation from collapsing microbubbles in the absence of a dynamic stimulus. *The Journal of Physical Chemistry B*, 111(6), pp.1343–1347.
Talvy, S., Cockx, A. and Liné, A., 2007. Modeling of oxygen mass transfer in a gas–liquid airlift reactor. *AIChE Journal*, 53(2), pp.316–326.
Temesgen, T., Bui, T.T., Han, M., Kim, T. and Park, H., 2017. Micro and nanobubble technologies as a new horizon for water-treatment techniques: A review. *Advances in Colloid and Interface Science*, 246, pp.40–51.
Terasaka, K., Hirabayashi, A., Nishino, T., Fujioka, S. and Kobayashi, D., 2011. Development of microbubble aerator for waste water treatment using aerobic activated sludge. *Chemical Engineering Science*, 66(14), pp.3172–3179.
Thermo Fisher Scientific Inc., 2008. *Carbon Dioxide Ion Selective Electrode User Guide* [Online]. Available from: https://assets.thermofisher.com/TFS-Assets/LSG/manuals/D15856~.pdf [Accessed 17 April 2019].
Tomiyama, A., 1998. Struggle with computational bubble dynamics. *Multiphase Science and Technology*, 10, pp.369–405.
Tzounakos, A., Karamanev, D.G., Margaritis, A. and Bergougnou, M.A., 2004. Effect of the surfactant concentration on the rise of gas bubbles in power-law non-Newtonian liquids. *Industrial & Engineering Chemistry Research*, 43(18), pp.5790–5795.
Van't Riet, K., 1979. Review of measuring methods and results in nonviscous gas-liquid mass transfer in stirred vessels. *Industrial & Engineering Chemistry Process Design and Development*, 18(3), pp.357–364.
Van't Riet, K. and Smith, J.M., 1973. The behaviour of gas-liquid mixtures near Rushton turbine blades. *Chemical Engineering Science*, 28(4), pp.1031–1037.
Vlaev, S.D., Tsibranska, I. and Dzhonova-Atanasova, D., 2018. Hydrodynamic characterization of dual-impeller submerged membrane bioreactor relevant to single-use bioreactor options. *Chemical Engineering Research and Design*, 132, pp.930–941.
Wang, H., Jia, X., Wang, X., Zhou, Z., Wen, J. and Zhang, J., 2014. CFD modeling of hydrodynamic characteristics of a gas-liquid two-phase stirred tank. *Applied Mathematical Modelling*, 38(1), pp.63–92.
Wang, T. and Wang, J., 2007. Numerical simulations of gas-liquid mass transfer in bubble columns with a CFD-PBM coupled model. *Chemical Engineering Science*, 62(24), pp.7107–7118.
Wang, W. and Mao, Z., 2002. Numerical simulation of gas-liquid flow in a stirred tank with a Rushton impeller. *Chinese Journal of Chemical Engineering*, 10(4), pp.385–395.
Wang, W., Mao, Z. and Yang, C., 2006. Experimental and numerical investigation on gas holdup and flooding in an aerated stirred tank with Rushton impeller. *Industrial & Engineering Chemistry Research*, 45(3), pp.1141–1151.
Warneck, P., 1988. *Chemistry of the Natural Atmosphere*. San Diego: Academic Press Inc.
Watanabe, K., Fujiwara, A., Takagi, S. and Matsumoto, Y., 2004. The experimental study of micro-bubble generator by venturi tube. *Proceedings of the Annual Meeting of the Japaneese Society of Multiphase Flow*, pp.185–186.
Weber, J. and Agblevor, F.A., 2005. Microbubble fermentation of Trichoderma reesei for cellulase production. *Process Biochemistry*, 40(2), pp.669–676.
Wesley, D.J., Smith, R.M., Zimmerman, W.B. and Howse, J.R., 2016. Influence of surface wettability on microbubble formation. *Langmuir*, 32(5), pp.1269–1278.
Witz, C., Treffer, D., Hardiman, T. and Khinast, J., 2016. Local gas holdup simulation and validation of industrial-scale aerated bioreactors. *Chemical Engineering Science*, 152, pp.636–648.
Wolf, D. and Manning, F.S., 1966. Impact tube measurement of flow patterns, velocity profiles and pumping capacities in mixing vessels. *The Canadian Journal of Chemical Engineering*, 44(3), pp.137–142.

Worden, R.M. and Bredwell, M.D., 1998. Mass-transfer properties of microbubbles. 2. Analysis using a dynamic model. *Biotechnology Progress*, 14(1), pp.39–46.

Wutz, J., Lapin, A., Siebler, F., Schäfer, J.E., Wucherpfennig, T., Berger, M. and Takors, R., 2016. Predictability of kLa in stirred tank reactors under multiple operating conditions using an Euler-Lagrange approach. *Engineering in Life Sciences*, 16(7), pp.633–642.

Xu, P., Clark, C., Ryder, T., Sparks, C., Zhou, J., Wang, M., Russell, R. and Scott, C., 2017. Characterization of TAP Ambr 250 disposable bioreactors, as a reliable scale-down model for biologics process development. *Biotechnology Progress*, 33(2), pp.478–489.

Yang, F., Zhou, S. and An, X., 2015. Gas–liquid hydrodynamics in a vessel stirred by dual dislocated-blade Rushton impellers. *Chinese Journal of Chemical Engineering*, 23(11), pp.1746–1754.

Yang, J., Bao, Y., Lin, M., Zhu, S. and Gao, Z., 2013. Experimental study and numerical simulation of local void fraction in cold-gassed and hot-sparged stirred reactors. *Chemical Engineering Science*, 100, pp.83–90.

Yeoh, S.L., Papadakis, G. and Yianneskis, M., 2004. Numerical simulation of turbulent flow characteristics in a stirred vessel using the LES and RANS approaches with the sliding/deforming mesh methodology. *Chemical Engineering Research and Design*, 82(7), pp.834–848.

Zamankhan, P., 2010. Large eddy simulation and PIV experiments of air–water mixing tanks. *Communications in Nonlinear Science and Numerical Simulation*, 15(6), pp.1511–1525.

Zaruba, A., Krepper, E., Prasser, H.-M. and Schleicher, E., 2005. Measurement of bubble velocity profiles and turbulent diffusion coefficients of the gaseous phase in rectangular bubble column using image processing. *Experimental Thermal and Fluid Science*, 29(7), pp.851–860.

Zhang, H., Zhang, K. and Fan, S., 2009. CFD simulation coupled with population balance equations for aerated stirred bioreactors. *Engineering in Life Sciences*, 9(6), pp.421–430.

Zhang, Y., Yang, C. and Mao, Z., 2008. Large eddy simulation of the gas–liquid flow in a stirred tank. *AIChE Journal*, 54(8), pp.1963–1974.

Zheng, Q., Xu, X., Martin, G.J.O. and Kentish, S.E., 2018. Critical review of strategies for CO2 delivery to large-scale microalgae cultures. *Chinese Journal of Chemical Engineering*, 26(11), pp.2219–2228.

Zhou, Z.A., Egiebor, N.O. and Plitt, L.R., 1993. Frother effects on bubble size estimation in a flotation column. *Minerals Engineering*, 6(1), pp.55–67.

Zimmerman, W.B., Hewakandamby, B.N., Tesař, V., Bandulasena, H.C.H. and Omotowa, O.A., 2009. On the design and simulation of an airlift loop bioreactor with microbubble generation by fluidic oscillation. *Food and Bioproducts Processing*, 87(3), pp.215–227.

Zimmerman, W.B., Tesa, V., Butler, S. and Bandulasena, H.C.H., 2008. Microbubble generation. *Recent Patents on Engineering*, 2, pp.1–8.

Zimmerman, W.B., Zandi, M., Hemaka Bandulasena, H.C., Tesař, V., James Gilmour, D. and Ying, K., 2011. Design of an airlift loop bioreactor and pilot scales studies with fluidic oscillator induced microbubbles for growth of a microalgae Dunaliella salina. *Applied Energy*, 88(10), pp.3357–3369.

Appendix A: Comparison of the k-ε and LES Turbulence Models: Single Phase

The large eddy simulation is a transient-only turbulence model, which uses a filter to distinguish between small and large sized eddies in turbulent flow. Large eddies are modelled directly using the Navier-Stokes equations, whereas small eddies – which are considered to have a much less significant influence on the overall flow patterns (Andersson et al., 2011) – are approximated using a much less computationally demanded subgrid-scale closure model. A generalised filter function (G) for an example parameter Φ can be expressed as:

$$\bar{\Phi}(\boldsymbol{x}) = \int \Phi(\boldsymbol{x}')\, G(\boldsymbol{x}; \boldsymbol{x}') d\boldsymbol{x}',$$

The filtered variable is denoted by an overbar, whereas the unresolved part of the variable is denoted by an inverted comma, and can be defined as:

$$\Phi' = \Phi - \bar{\Phi}$$

The filtered form of the momentum equation can therefore be expressed as follows. The need for a closure model arises from the term $\overline{u_\iota u_j}$ in the residual stress tensor, τ_{ij}.

$$\frac{\partial \bar{u}_\iota}{\partial t} + \rho \frac{\partial \bar{u}_\iota \bar{u}_j}{\partial x_j} = \frac{\partial \bar{\bar{P}}}{\partial x_j} + \mu \frac{\partial^2 \bar{u}_\iota}{\partial x_j \partial x_j} - \frac{\partial \tau_{ij}}{\partial x_j}, \quad \tau_{ij} = \overline{u_\iota u_j} - \bar{u}_\iota \bar{u}_j$$

This work uses the Smagorinsky model as a closure to the subgrid scale model. The residual stress tensor, τ_{ij}, and subgrid viscosity, μ_{sgs}, are calculated as follows:

$$\tau_{ij} = \frac{1}{3}\delta_{ij}\tau_{kk} + 2\mu_{sgs}\bar{S}_{ij}, \quad \bar{S}_{ij} = \frac{1}{2}\left(\frac{\partial \bar{u}_i}{\partial x_j} + \frac{\partial \bar{u}_j}{\partial x_i}\right)$$

$$\mu_{sgs} = \rho(C_S \Delta)^2 \sqrt{2\bar{S}_{ij}\bar{S}_{ij}}$$

where τ_{kk} is the isotropic part of the subgrid stresses, $\overline{S}_{ij}$ is the large-scale strain rate tensor and C_S is the Smagorinsky constant, which is not a universal constant, with a value of 0.1 used in this work.

The instantaneous velocity fields shown in Figure A1 are very different for the k-ε and LES turbulence models for a Rushton impeller in water at a stirrer speed of 100 RPM. The k-ε model (a) is showing the time-averaged profiles produced by the RANS approximations, with a smooth distribution of velocity throughout the tank. In contrast, the LES model (b) depicts the motion of individual eddies which are produced by the action of the impeller. These create a much more chaotic appearance to the distribution of velocity within the tank, and do not remain constant with time. It is apparent that the two profiles are describing the same flow features, such as a large radial velocity close to the impeller and recirculation in the upper and lower corners of the tank, however the detail of the turbulent flow is much greater for the LES model.

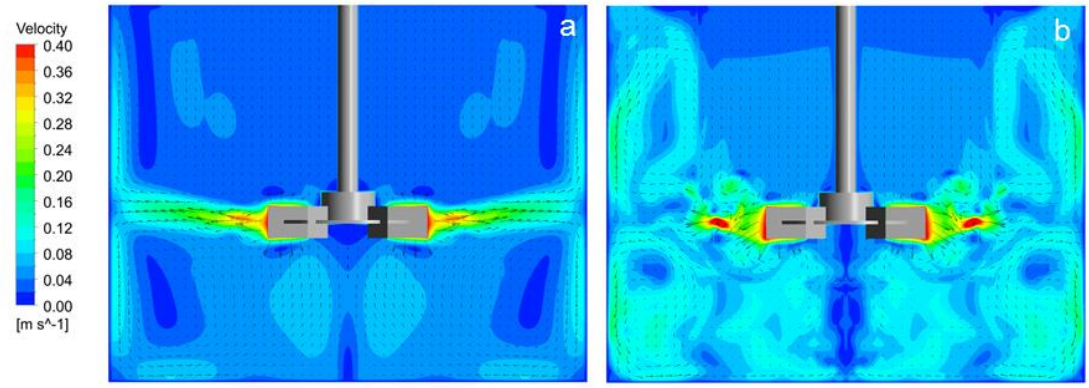

Figure A1: A comparison of the instantaneous single-phase flow patterns for the k-ε (a) and LES (b) turbulence models.

In order to compare to the time-averaged profiles for the LES and k-ε models, the instantaneous velocity fields generated using the LES model have been averaged over the final ten impeller revolutions modelled. These are comparable to experimental LDV profiles and provide a more useful reference for evaluating the flow behaviour within stirred tanks than the instantaneous patterns. For the Rushton impeller shown in Figure A2, the LES model provides a better prediction of the velocity profile close to the impeller, where the greatest levels of turbulence are present, however the prediction towards the tank wall shows little difference between the models.

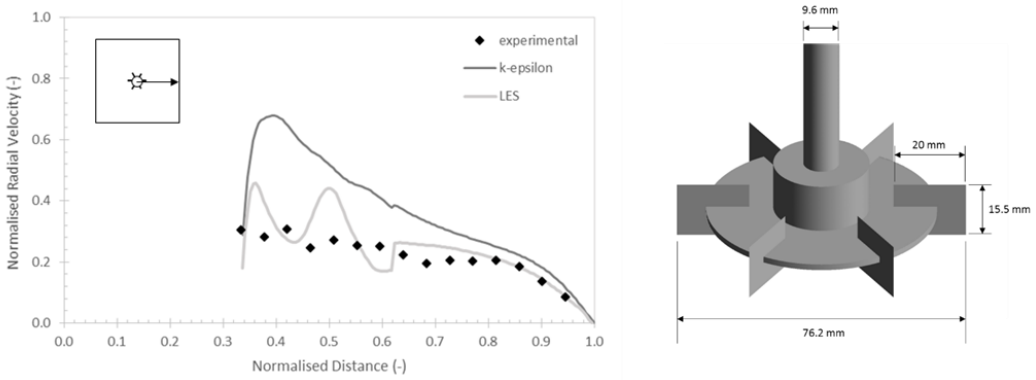

Figure A2: A comparison of the experimental and modelled time-averaged single-phase velocity profiles in-line with a Rushton impeller.

The prediction of the flow patterns is also well captured by the k-ε model throughout the rest of the tank, as shown by the comparison of the modelled flow patterns with LDV measurements presented in Figure A3. The key flow features are captured well by the k-ε model, suggesting little value in using the more advanced but more computationally expensive LES turbulence model to represent time-averaged flow patterns.

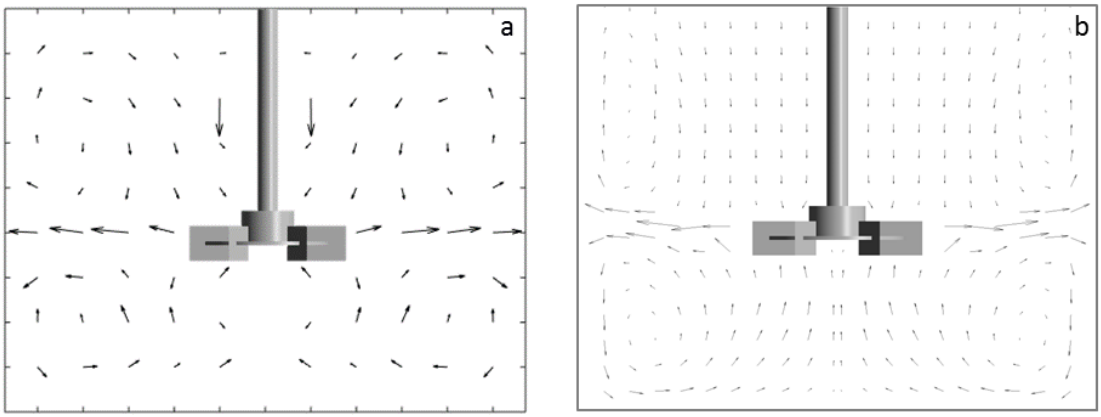

Figure A3: A comparison of the experimental (a) and modelled (b) single-phase velocity vector plots for a Rushton impeller at 100 RPM, using the k-ε turbulence model.

Figure A4 shows that neither of the turbulence models provides a very good fit to the velocity profile in-line with a four-bladed radial impeller, however there is no benefit identified for using one model over the other in terms of solution accuracy for this case.

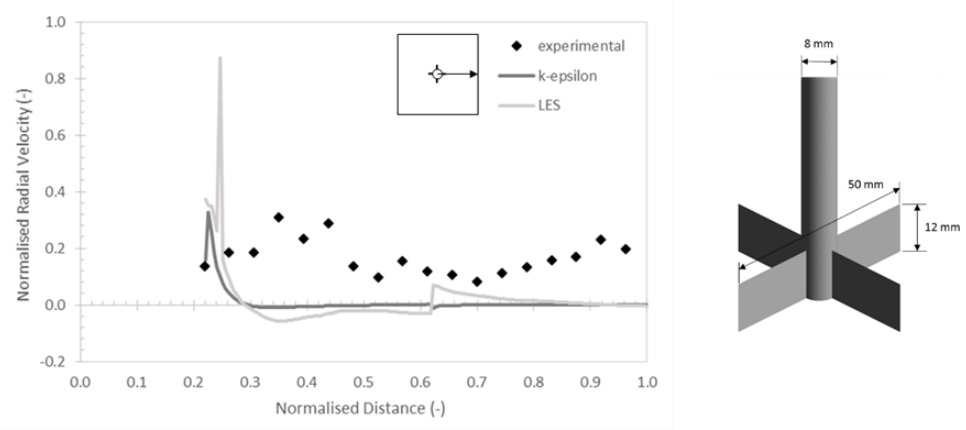

Figure A4: A comparison of the experimental and modelled time-averaged single-phase velocity profiles in-line with a four-bladed radial flow impeller.

Finally, the time-averaged horizontal velocity profiles at a location below an axial impeller are compared for the two turbulence models in Figure A5. This shows that for a location further away from the impeller, both models are able to provide a very good fit to the experimental profile. Once again, this comparison shows that there is no benefit from using the LES turbulence model when the instantaneous velocity field is not of particular interest, and the significant additional computational expense required to run the more complex LES model as a transient solution is not justified for the single-phase cases presented.

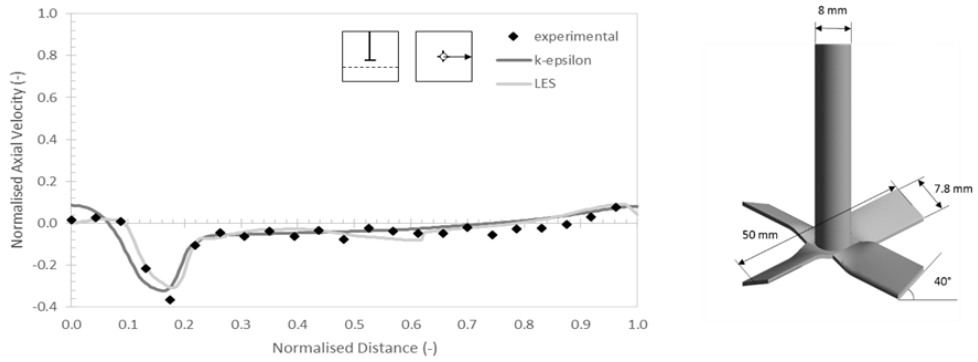

Figure A5: A comparison of the experimental and modelled time-averaged single-phase velocity profiles below a four-bladed axial flow impeller.

Appendix B: MATLAB Code for the Watershed Bubble Sizing Technique

```
clear
close all

[selectName, selectPath] = uigetfile('*.jpg');
filename = fullfile(selectPath,selectName)

I = imread(filename);
imshow(I)

imdistline

prompt = 'Scale from Image: ';
pixels = input(prompt);

close

Scale = pixels/25.908;

Icrop = imcrop(I);
close

BW = rgb2gray(Icrop);
I2 = imhmin(imcomplement(BW),70);
L = watershed(I2);

figure; imshowpair(Icrop,L==0,'montage')

stats =
regionprops('table',L,'Centroid','MajorAxisLength','MinorAxisLength'
,'EquivDiameter');

centers2 = stats.Centroid;
diameters2 = mean([stats.MajorAxisLength stats.MinorAxisLength],2);
radii2 = diameters2/2;

figure; imshow(Icrop)
hold on
viscircles(centers2,radii2,'Color','b');
hold off

prompt = 'Histogram - Minimum Bubble Diameter: ';
dbmin = input(prompt);
prompt = 'Histogram - Maximum Bubble Diameter: ';
dbmax = input(prompt);
prompt = 'Histogram - Number of Bins: ';
numbin = input(prompt);

Diameter = stats.EquivDiameter/Scale;
figure;
histogram(Diameter,numbin,'BinLimits',[dbmin,dbmax],'Normalization',
'probability')
yticklabels(yticks*100)
ylabel('Percentage (%)')
xlabel('Bubble Diameter (mm)')

disp(' ')
fprintf('Bubble data is held in the variable "Diameter"')
disp(' ')
```

Appendix C: Qualitative Comparison of the Experimental and Modelled Liquid-Phase Velocity Profiles at Increasing Tank Height: 100 RPM

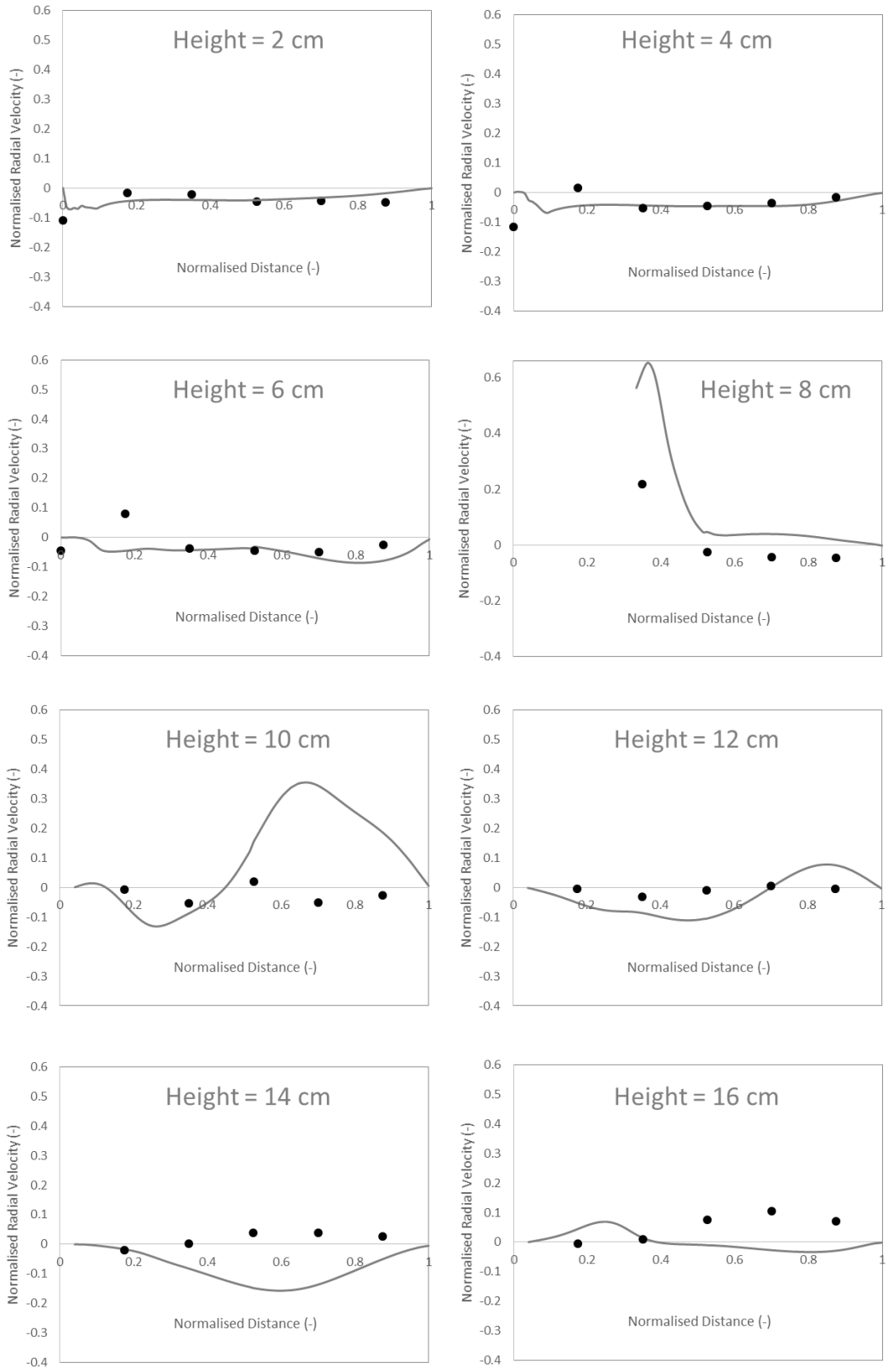

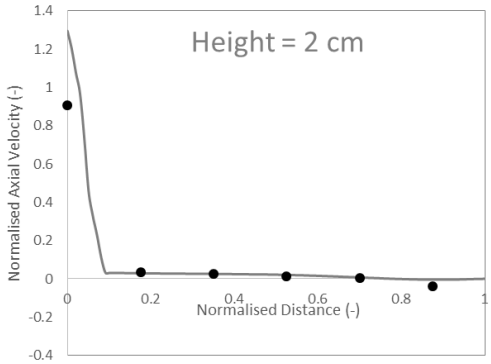
Height = 2 cm
Normalised Axial Velocity (-)
Normalised Distance (-)

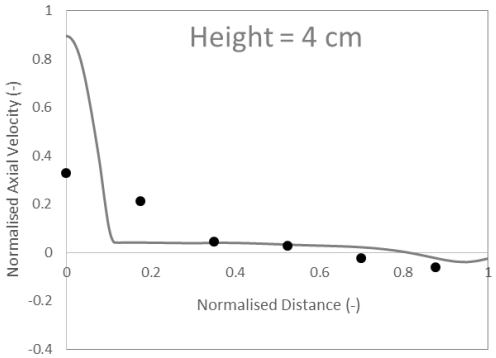
Height = 4 cm
Normalised Axial Velocity (-)
Normalised Distance (-)

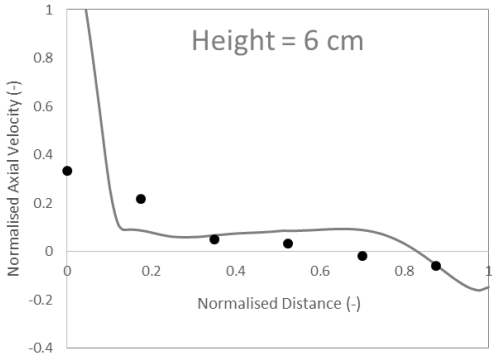
Height = 6 cm
Normalised Axial Velocity (-)
Normalised Distance (-)

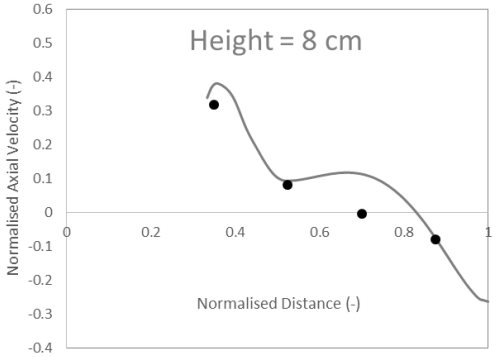
Height = 8 cm
Normalised Axial Velocity (-)
Normalised Distance (-)

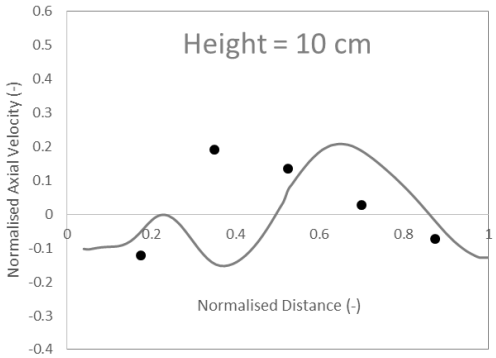
Height = 10 cm
Normalised Axial Velocity (-)
Normalised Distance (-)

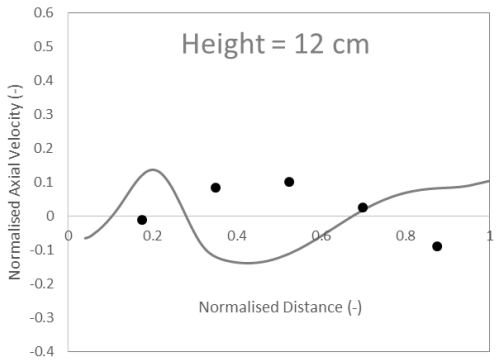
Height = 12 cm
Normalised Axial Velocity (-)
Normalised Distance (-)

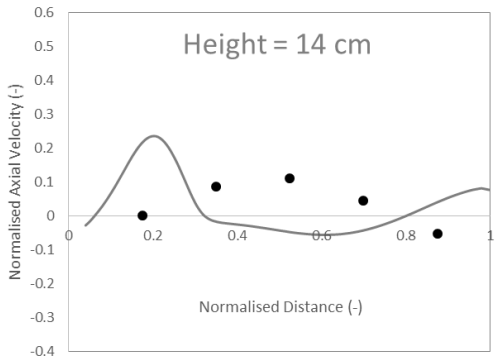
Height = 14 cm
Normalised Axial Velocity (-)
Normalised Distance (-)

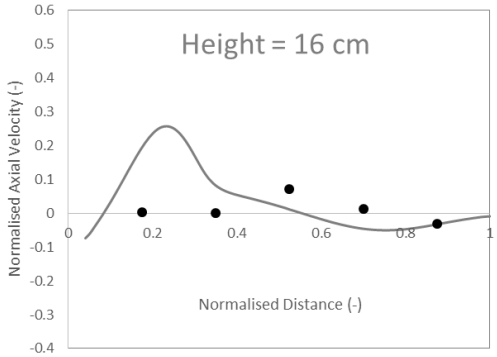
Height = 16 cm
Normalised Axial Velocity (-)
Normalised Distance (-)

Appendix D: Qualitative Comparison of the Experimental and Modelled Liquid-Phase Velocity Profiles at Increasing Tank Height: 200 RPM

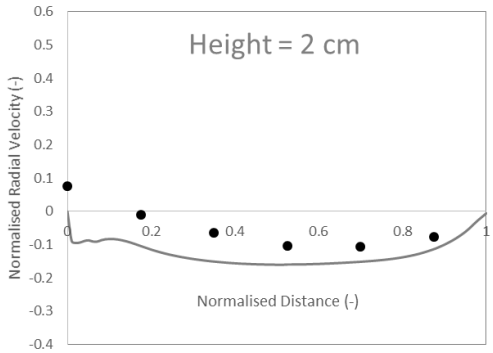

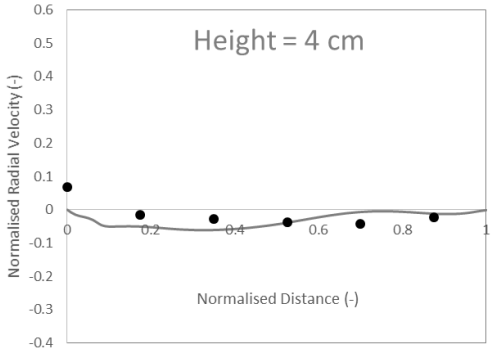

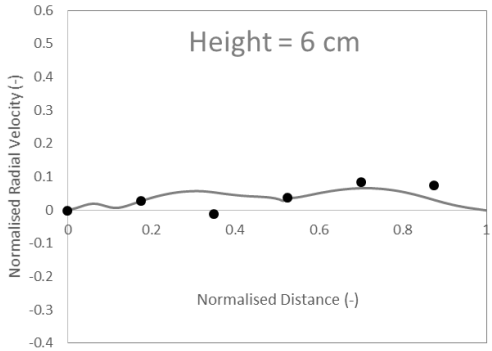

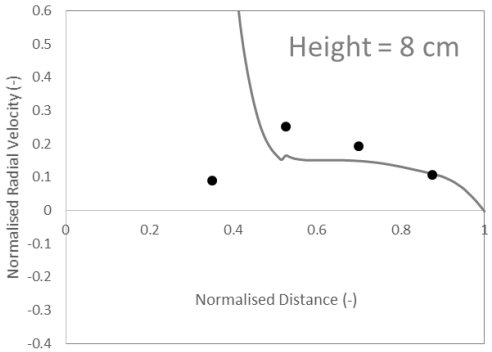

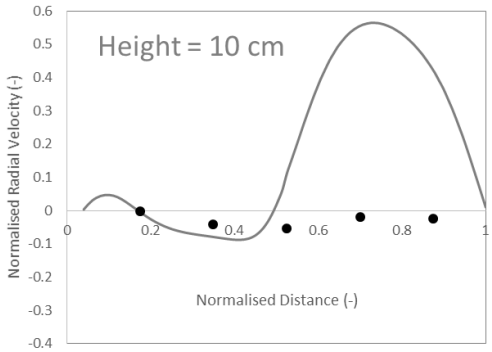

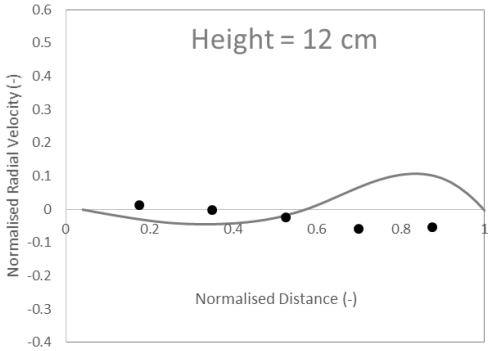

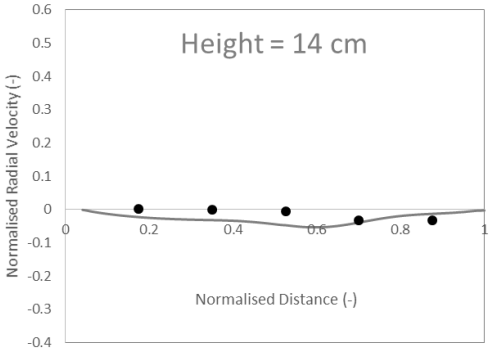

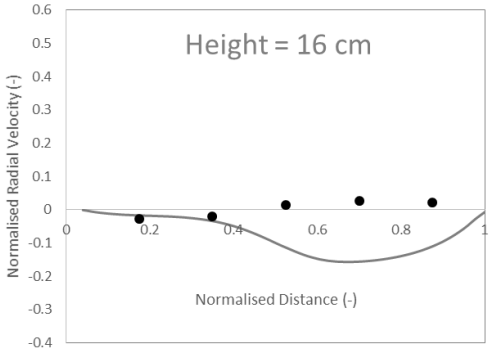

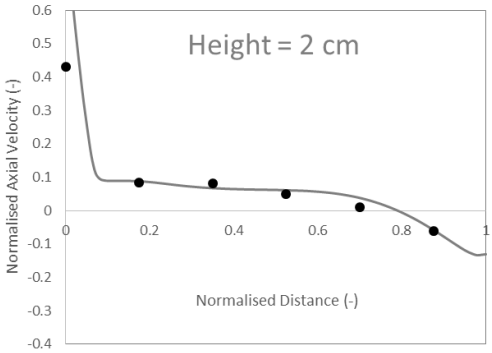
Height = 2 cm
Normalised Axial Velocity (-)
Normalised Distance (-)

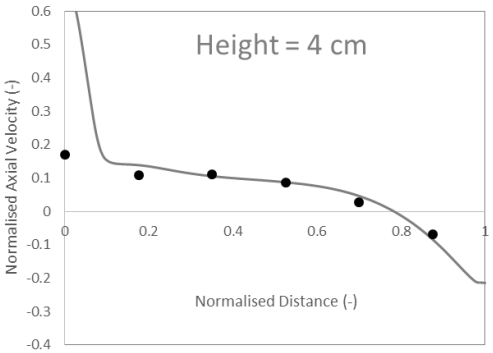
Height = 4 cm
Normalised Axial Velocity (-)
Normalised Distance (-)

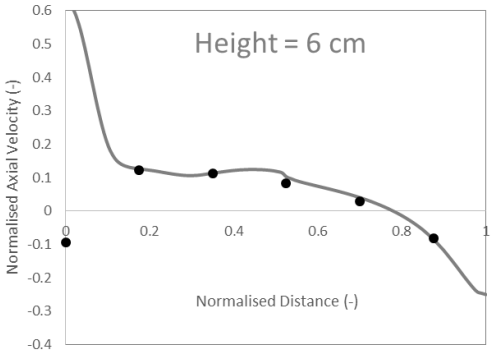
Height = 6 cm
Normalised Axial Velocity (-)
Normalised Distance (-)

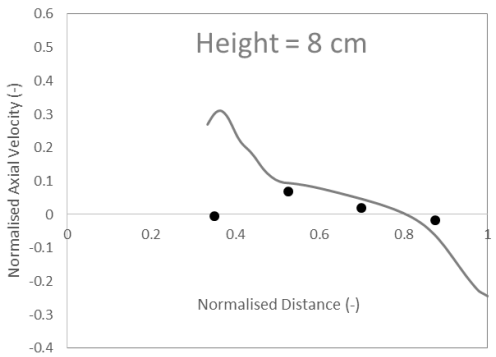
Height = 8 cm
Normalised Axial Velocity (-)
Normalised Distance (-)

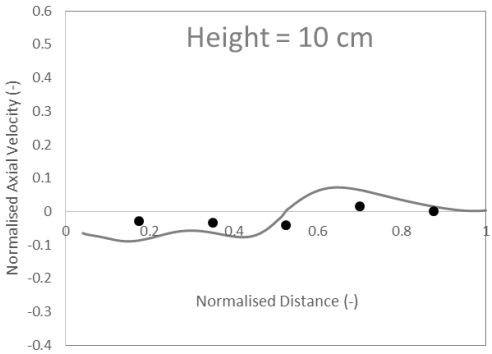
Height = 10 cm
Normalised Axial Velocity (-)
Normalised Distance (-)

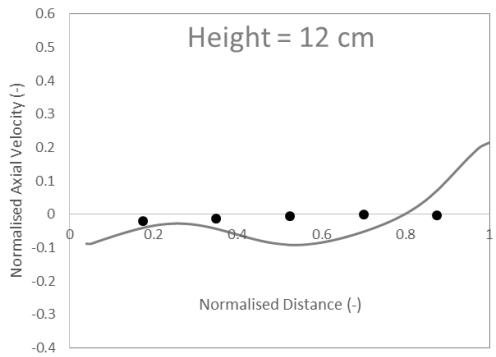
Height = 12 cm
Normalised Axial Velocity (-)
Normalised Distance (-)

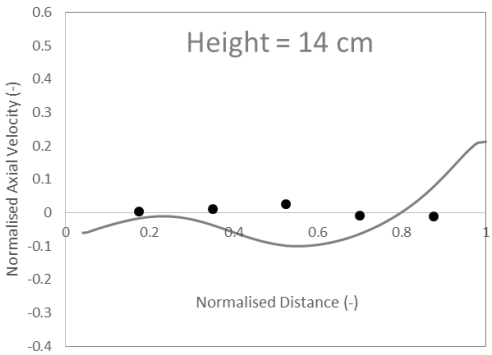
Height = 14 cm
Normalised Axial Velocity (-)
Normalised Distance (-)

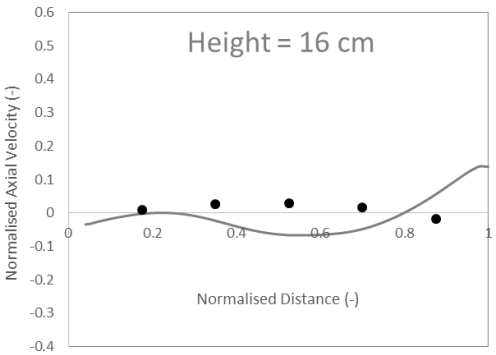
Height = 16 cm
Normalised Axial Velocity (-)
Normalised Distance (-)

Appendix E: Qualitative Comparison of the Experimental and Modelled Liquid-Phase Velocity Profiles at Increasing Tank Height: 300 RPM

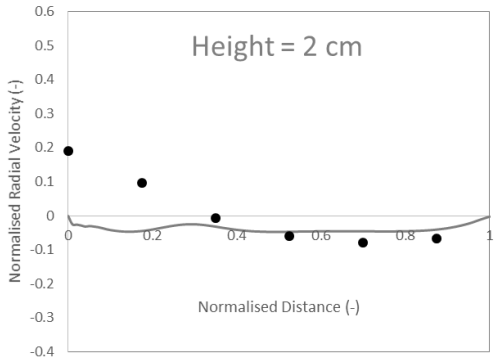

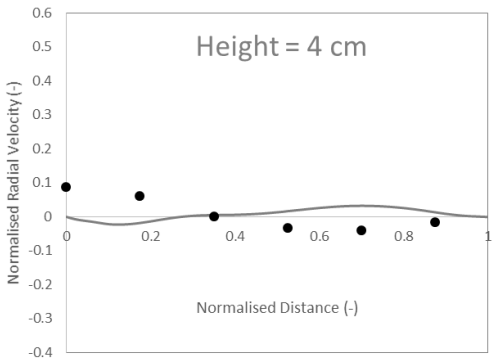

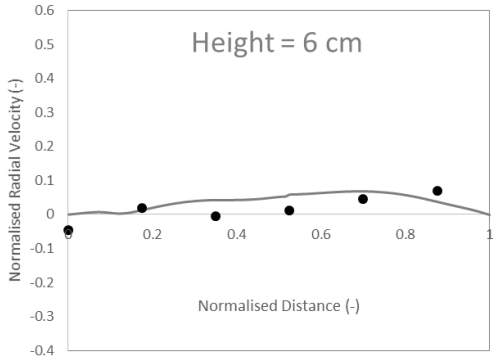

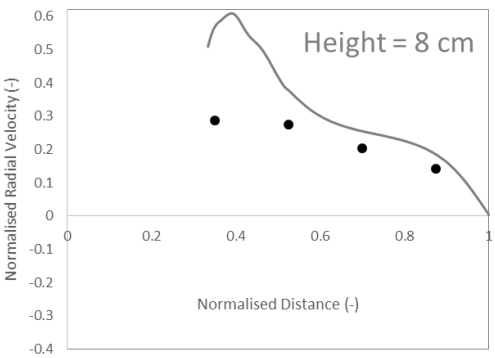

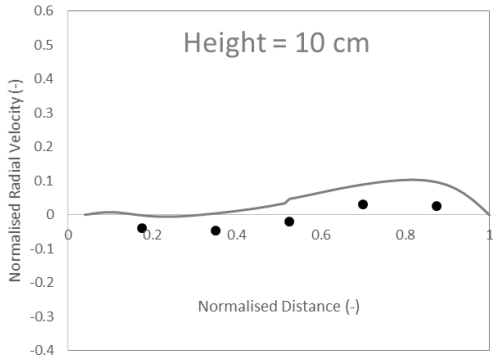

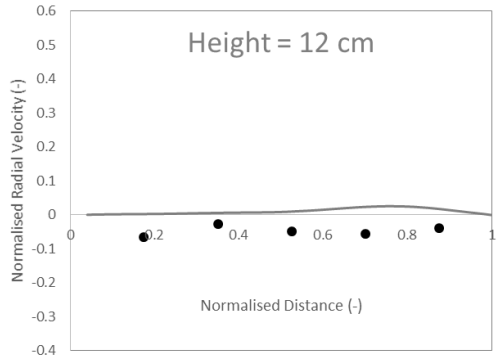

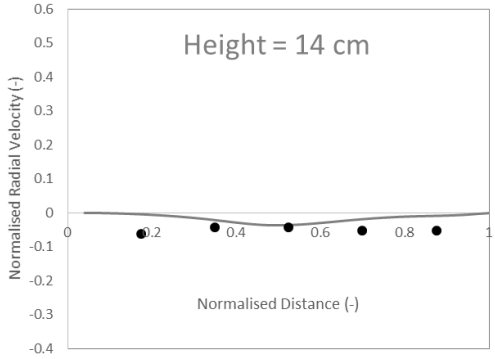

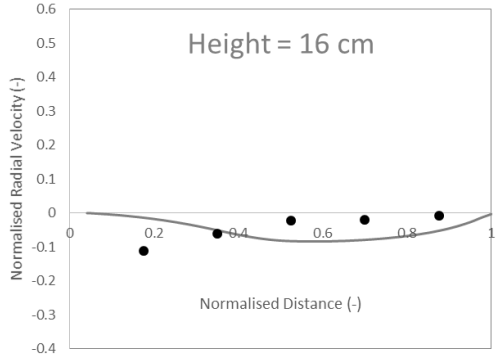

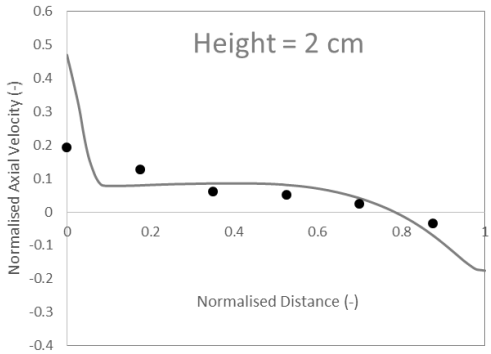
Height = 2 cm
Normalised Axial Velocity (-)
Normalised Distance (-)

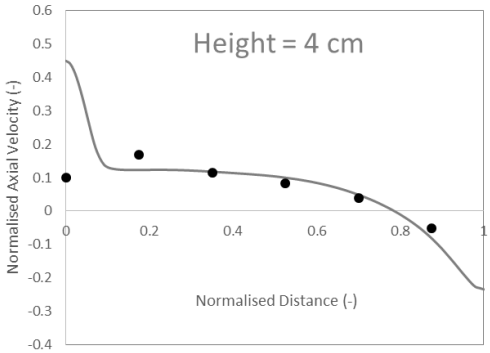
Height = 4 cm
Normalised Axial Velocity (-)
Normalised Distance (-)

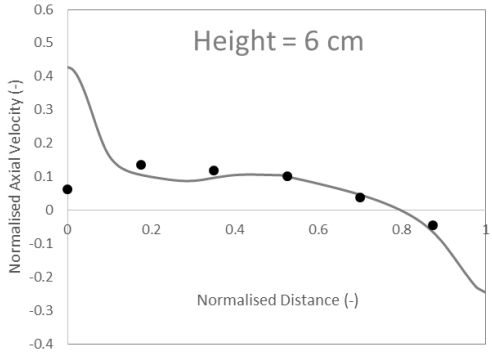
Height = 6 cm
Normalised Axial Velocity (-)
Normalised Distance (-)

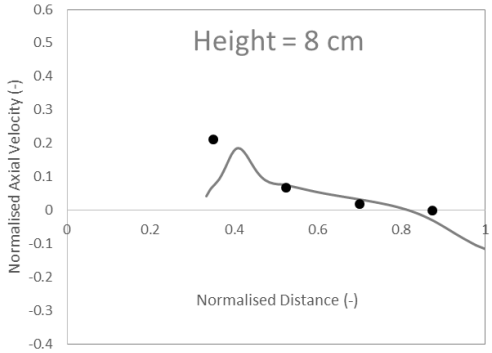
Height = 8 cm
Normalised Axial Velocity (-)
Normalised Distance (-)

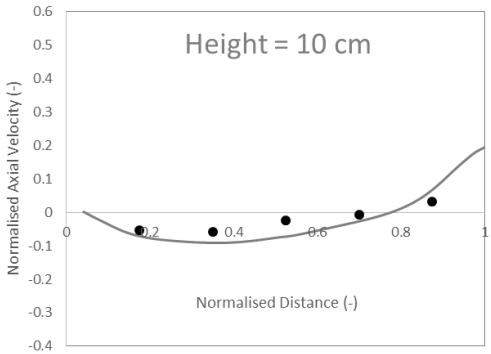
Height = 10 cm
Normalised Axial Velocity (-)
Normalised Distance (-)

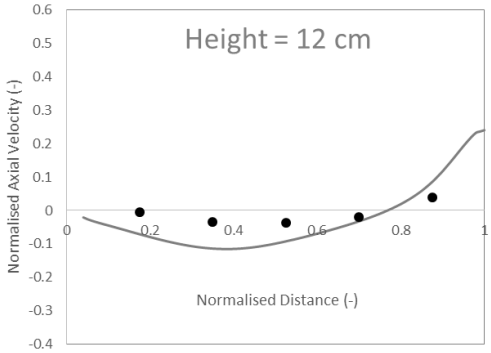
Height = 12 cm
Normalised Axial Velocity (-)
Normalised Distance (-)

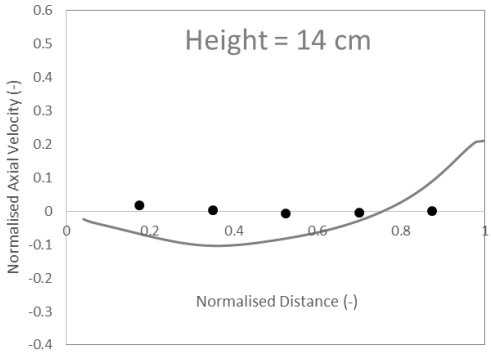
Height = 14 cm
Normalised Axial Velocity (-)
Normalised Distance (-)

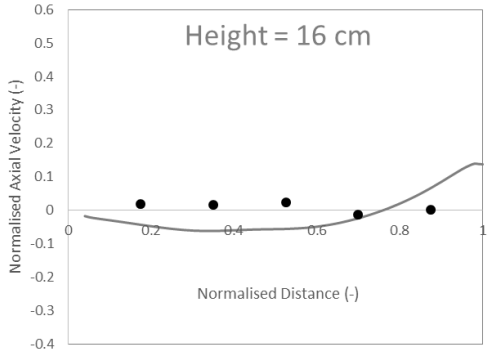
Height = 16 cm
Normalised Axial Velocity (-)
Normalised Distance (-)

Appendix F: Qualitative Comparison of the Experimental and Modelled Liquid-Phase Velocity Profiles at Increasing Tank Height: 400 RPM

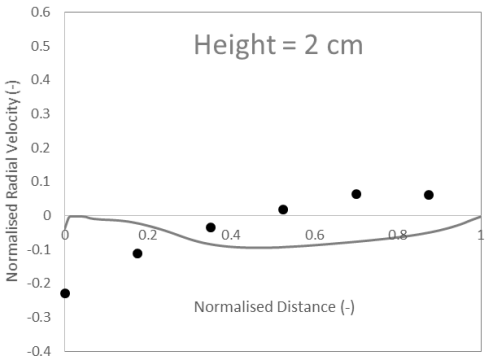

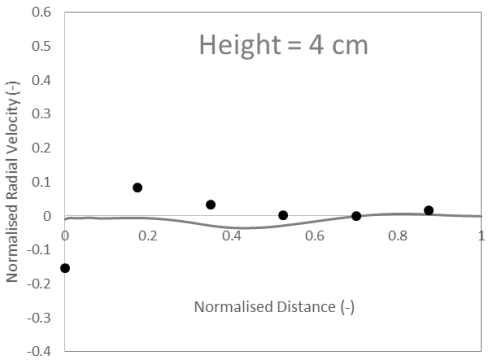

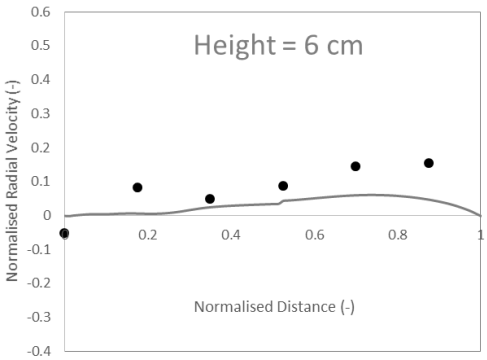

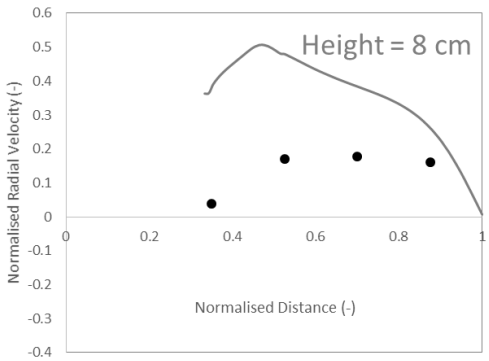

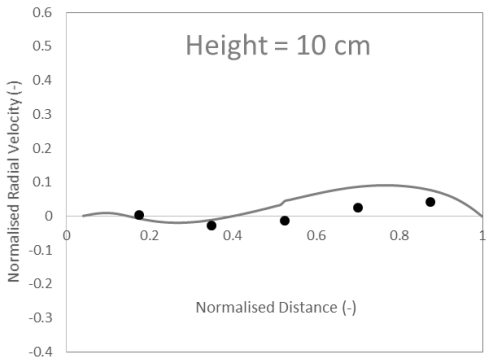

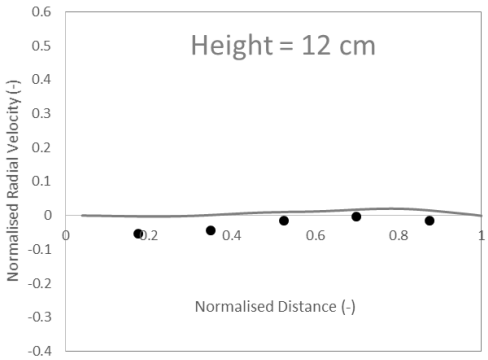

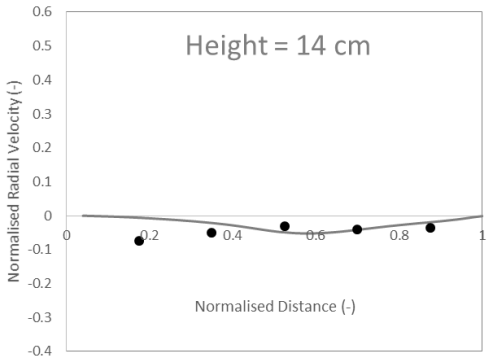

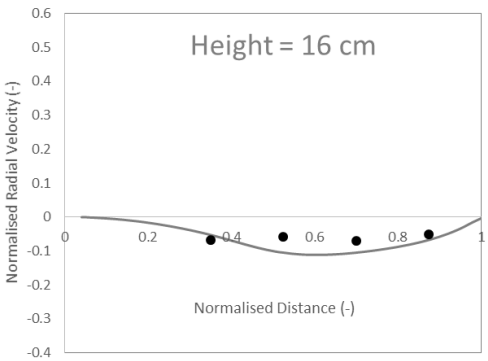

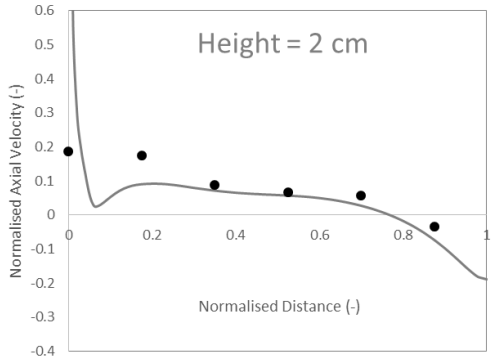
Height = 2 cm
Normalised Axial Velocity (-)
Normalised Distance (-)

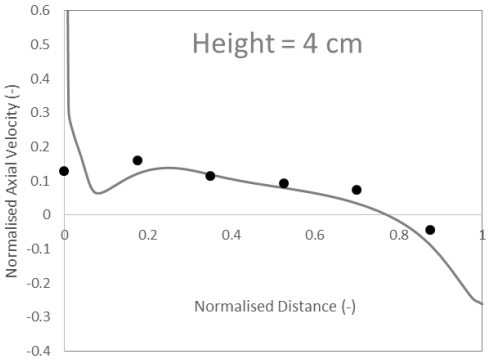
Height = 4 cm
Normalised Axial Velocity (-)
Normalised Distance (-)

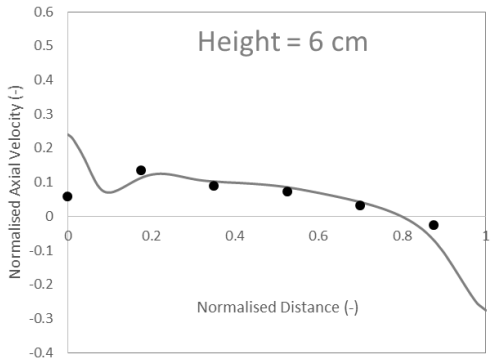
Height = 6 cm
Normalised Axial Velocity (-)
Normalised Distance (-)

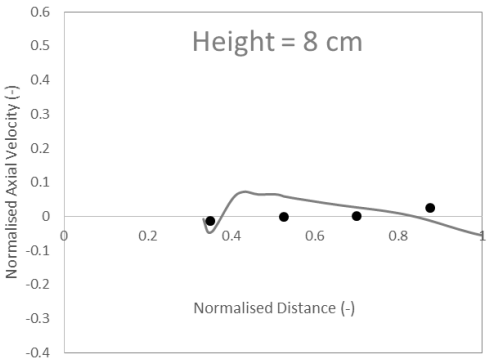
Height = 8 cm
Normalised Axial Velocity (-)
Normalised Distance (-)

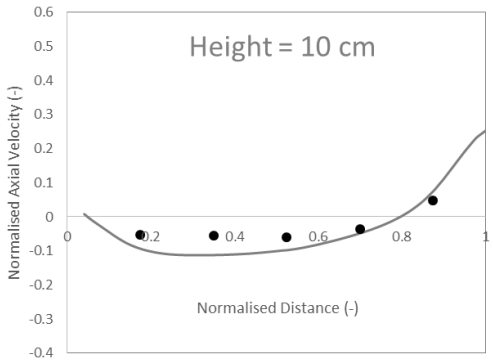
Height = 10 cm
Normalised Axial Velocity (-)
Normalised Distance (-)

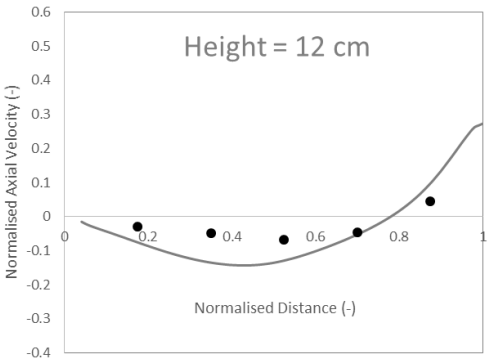
Height = 12 cm
Normalised Axial Velocity (-)
Normalised Distance (-)

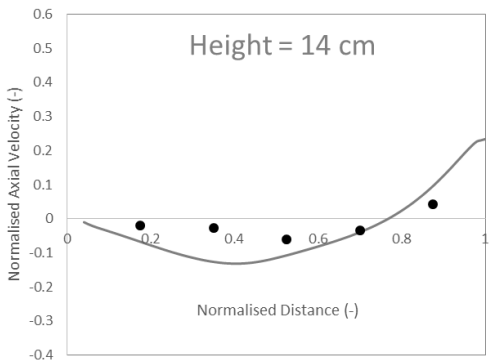
Height = 14 cm
Normalised Axial Velocity (-)
Normalised Distance (-)

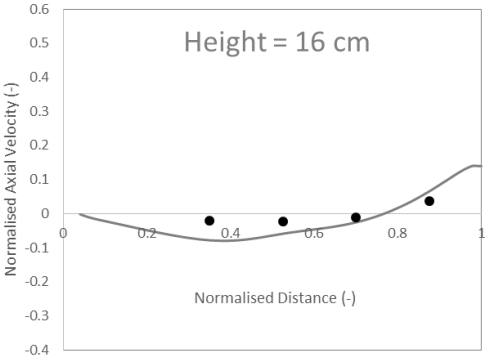
Height = 16 cm
Normalised Axial Velocity (-)
Normalised Distance (-)

Appendix G: MATLAB Code for the Microbubble Sizing Technique

```
clear

ScalingFactor = 1/((757.39/3)/1000);

[File, Path] = uigetfile('*.tif','Select set of
images','MultiSelect','on');

FileTif = strcat(Path,File);
InfoImage=imfinfo(FileTif);
mImage=InfoImage(1).Width;
nImage=InfoImage(1).Height;
NumImage=length(InfoImage);

for i = 1:200

I =  imread(FileTif,'Index',i,'Info',InfoImage);
BW = rgb2gray(I);

C = imcomplement(BW);

D = imbinarize(C, 0.78);
D2 = imfill(D, 'holes');
E = bwareafilt(D2, [50,Inf]);                    %EDIT FACTOR
F = bwpropfilt(E, 'Eccentricity', [0,0.5]);      %EDIT FACTOR
G = bwpropfilt(F, BW, 'MinIntensity', [0,32]);   %EDIT FACTOR

stats = regionprops('table',G, BW,
'Centroid','MajorAxisLength','MinorAxisLength', 'MaxIntensity',
'MeanIntensity', 'Area', 'EquivDiameter');

centers = stats.Centroid;
diameters = mean([stats.MajorAxisLength stats.MinorAxisLength],2);
radii = diameters/2;

Diameter = ScalingFactor*stats.EquivDiameter';

if i==1
   res = Diameter;
else

N = [res Diameter];
res = N;

end

fprintf('Processing Image %i of %i',i, NumImage)
disp(' ')

end

DiameterList = res';
MeanDiameter = mean(res);

disp(' ')
fprintf('Processing Complete')
disp(' ')
fprintf('Mean Diameter = %i um',MeanDiameter)
disp(' ')
fprintf('Sample Size = %i',length(DiameterList))
```

```
disp(' ')

figure;
histogram(DiameterList,10,'BinLimits',[60,180],'Normalization','prob
ability');
yticklabels(yticks*100)
ylabel('Percentage (%)')
xlabel('Bubble Diameter (um)')
```

Appendix H: Microbubble Imaging with Varying Filter Values

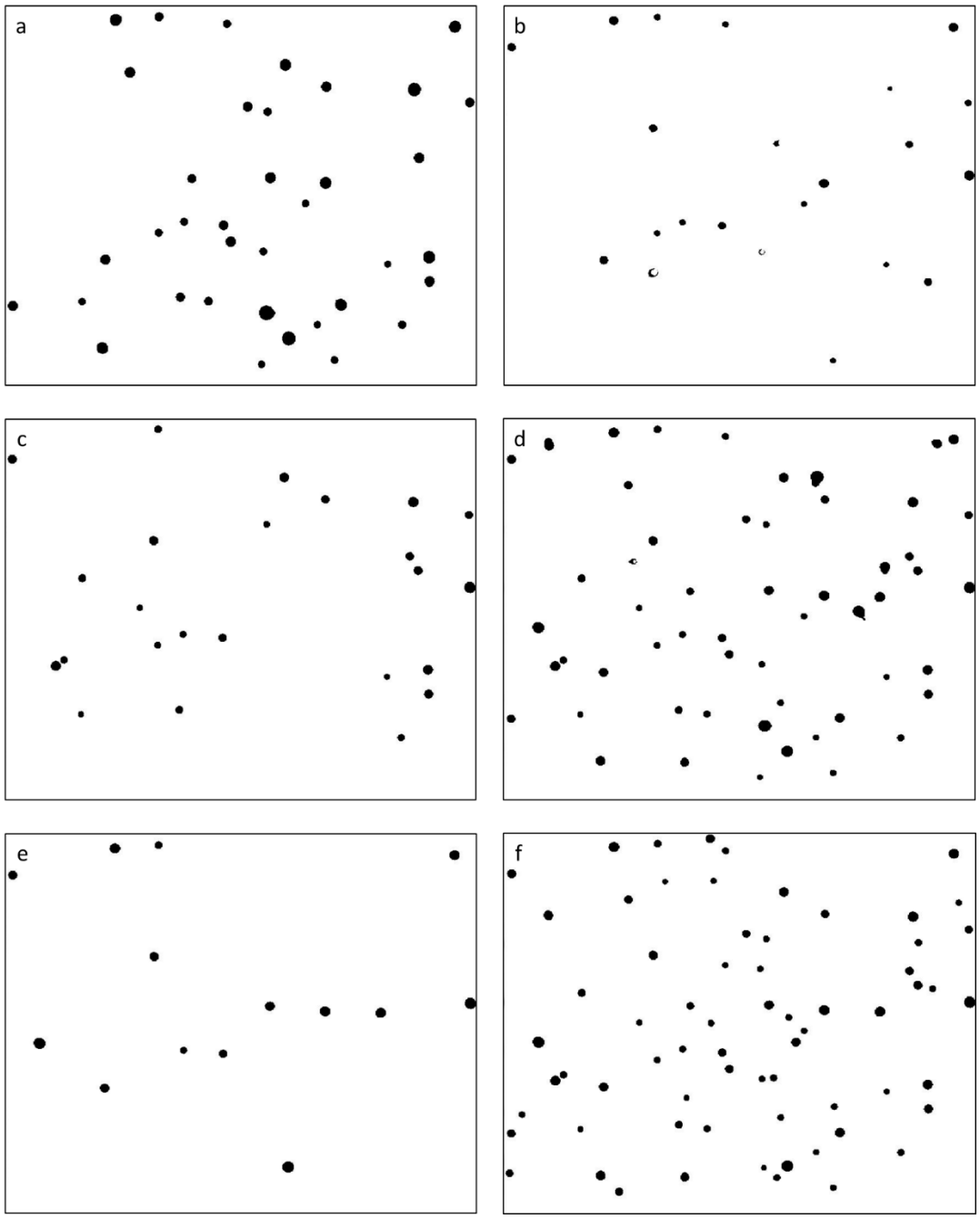

Filtered images are based on the unfiltered image shown in Figure 7-8 a).

a) Threshold light intensity = 0.6

b) Threshold light intensity = 0.85

c) Eccentricity limit = 0.3

d) Eccentricity limit = 0.7

e) Minimum light intensity = 0.25

f) Minimum light intensity = 0.45